Title
Dose-Response Models Reveal Critical Features of Inhibitor Activity and Viral Infection

Author
Webb, Nicholas Eugene

Publication Date
2015

Peer reviewed|Thesis/dissertation

UNIVERSITY OF CALIFORNIA

Los Angeles

Dose-Response Models Reveal Critical Features of Inhibitor Activity and Viral Infection

A dissertation submitted in partial satisfaction of the

requirements for the degree Doctor of Philosophy in

Microbiology, Immunology and Molecular Genetics

by

Nicholas Webb

2015

ABSTRACT OF THE DISSERTATION

Dose-Response Models Reveal Critical Features of Inhibitor Activity and Viral Infection

by

Nicholas Webb

Doctor of Philosophy in Microbiology, Immunology and Molecular Genetics

University of California, Los Angeles, 2015

Professor Benhur Lee, Chair

Over the past 34 years astonishing global efforts have transformed HIV/AIDS from a clinical death sentence into a manageable long-term illness. With approximately 35 million people now living with HIV, our eyes move toward managing and containing HIV infection as a chronic condition on a global scale. Achieving this goal will require the advent of new treatment strategies that target a variety of highly conserved viral features and a more complex analytical framework to assess resistance and transmission potential during treatment as well as to evaluate the potential clinical pathologies of resistant variants.

Contributing to this goal, this dissertation focuses on evaluating novel treatment strategies from two complementary and important perspectives. First, we apply analytical frameworks adapted from biochemistry to more comprehensively asses the therapeutic expectations of emerging immunotherapeutics and novel inhibitor targets. These extensible methods provide a more accurate description of antiviral activity at levels that will be necessary to suppress viral replication and prevent resistance than more traditional potency-based comparisons. Additionally, the mathematical foundation of these methods connects high clinical

expectation to more detailed biochemical mechanisms that present specific criteria to aid in the rational design of more effective therapies.

This analytical framework can, alternatively, be used to understand how a virus responds to the presence of a drug, which will be necessary for assessing how HIV and its pathology might evolve, on a global scale, in the face of widespread treatment. To this end, quantifying infection efficiency and understanding how HIV virion interact with their target cells through extensible mathematical models reveal the impacts that treatment can have on the most fundamental properties of HIV infection. Understanding treatment from the perspective of the virus can aid the design of more potent therapies that pose unsurmountable barriers to resistance and might specifically target transmissibility.

Our results present a unique analysis of the activity of broadly neutralizing HIV antibodies that provides a new dimension to evaluating the clinical expectations of novel immunotherapies in the context of long-term management. This analysis is also used to further distinguish the cytotoxic and antiviral activities of a novel HIV inhibitor class: the disulfide isomerase inhibitors, where we reveal the significant potential of this class as well as specific criteria for the development of stronger and less toxic analogs to boost the diversity of available HIV treatments. We then extend this analytical method to assess the inherent infectious properties of HIV in response to treatment, to evaluate resistance in the more clinical context of target-cell tropism, receptor usage and infectivity.

Managing HIV infection as a long-term condition on a global scale will require more sophisticated efforts in developing and assessing novel treatments in terms of both inhibitor activity and direct viral responses. The methods and experimental strategies presented here are an essential first step to describing the activity of inhibitors and the activity of HIV, itself. Our results illuminate novel mechanistic features that can aid the development of novel treatments specifically suited to contain and control HIV.

The dissertation of Nicholas Webb is approved.

Linda G. Baum.

M. Carrie Miceli

Otto O. Yang

Tom Chou

Benhur Lee, Chair

University of California, Los Angeles

2015

DEDICATION

I dedicate this dissertation to my father, Kenneth F. Webb. My interest in all things quantitative and scientific began at a young age with an Apple][Plus computer, where my father taught me how to program in Basic by command-crashing computer games and exploring the code beneath. My first success in this demanding field was discovering the interrupt code that allowed lower case characters, which were considered unnecessary in this particular model... After we got our first IBM 386 (with turbo boost!), my father taught me Turbo Pascal and the modest capacity of its hard drive quickly boiled over with program modules, the tattered remains of hacked video games and computer bulletin board systems, for which the ringers from all the phones in our house had to be removed. When, in 7th grade, I was caught peering into my school's network-based computer grading system, my father's reaction was very stern: "You're telling me a 7th grader was able to hack into your system? I think that's on you..."

Outside the world of computers, memories of my father are sprinkled with robots made from 2-liter soda bottles, airplanes – lots of airplanes, an entire scale-model village (with working electricity) built entirely from scratch (and mostly hot-glue), a gutted and converted alarm clock used to power a television and nintendo gaming system through automobile cigarette lighters for long drives to our grandparents, and, of course, comically proportioned styrofoam *Jesus Shoes* made for walking across Lake Champlain. Frustrated with the aiming precision required by our new Laser Tag set, my father removed the focusing lens on his weapon and boosted its power, converting it into a Laser Tag bomb with a wide enough radius to tag everyone, including himself, multiple times in one shot. My father's inventiveness and technological creativity, which might also be lovingly described as asinine, was only limited by what we could dig out of industrial dumpsters. My inheritance of these qualities through his parenting, and their maturation through his encouragement, has given me a path in life that satisfies my deepest of curiosities, continually opens my mind to new perspectives and will hopefully, one day, benefit others in a very real and practical way.

Contents

List of Figures

List of Tables

ACKNOWLEDGEMENTS

I would first like to acknowledge and thank my committee chair and mentor, Dr. Benhur Lee (Mount Sinai, Icahn School of Medicine, Professor in the Department of Microbiology and Ward-Coleman Chain in Microbiology) who has not only provided me with exceptional guidance, but who has challenged me in a way that opens my mind to new perspectives. Dr. Lee's mentorship has given direction and practical applicability to my passion in science, helping me to hone my skills and explore the unknown with a more focused and conclusive approach. I'd also like to thank the Lee lab members: Hector Aguilar, Shirley Delair, Patrick Hong, Yao Wang, Fred Vigant, Maggie Chang, Mickey Pentecost, Olivier Pernet, Karina Palomares, Kelechi Chikere, Arnold Park and Shannon Beaty. Although our research covered a vast expanse of topics, the atmosphere curated by Dr. Lee and these wonderful scientists was always highly collaborative and more like a family. Dr. Lee is a strong proponent of openness and through this philosophy, my research has also given rise to a number of collaborations.

My doctoral committee, Dr. Benhur Lee, Dr. Carrie Miceli (University of California, Los Angeles, Professor of Microbiology, Immunology & Molecular Genetics and Co-director for the Center for Duchenne Muscular Distrophy), Dr. Linda Baum (Professor of Pathology and Laboratory Medicine, UCLA), Dr. Tom Chou (University of California, Los Angeles, Professor of Biomathematics), Dr. Otto Yang (University of California, Los Angeles, Professor in the Department of Medicine, Infectious Diseases and Microbiology, Immunology & Molecular Genetics), has supported and inspired me from the day I first interviewed at UCLA in very unique and essential capacities. I'd also like to give special thanks to Dr. Otto Yang, who has generously hosted my research and my person for the last year at UCLA.

Dr. Tom Chou and Dr. Paul Gorry (Professor and Head of the HIV Molecular Pathogenesis Laboratory, Burnet Institute, Melbourne, Australia) were essential to the development of the mathematical methods presented in Chapter 4, their analysis and their interpretation and Dr. Tom Chou was pivotal to the development of the mathematical methods presented

in Chapter 5. I'd like to personally thank Dr. Chou for his support and enthusiastic involvement in my mathematical ventures, and Dr. Gorry for his extremely generous financial support. The research presented in Chapter 4 was recently published: Webb NE, Chikere K, Chou T, Borm K, Sterjovski J, Gorry PR and Lee B. Distinct HIV-1 entry phenotypes are associated with transmission, subtype specificity, and resistance to broadly neutralizing antibodies. *Retrovirology* 2014, 11:48. In addition, the protocols associated with Chapter 4 (Appendix C) are currently in press: Webb NE, Lee B. Quantifying CD4/CCR5 Usage Efficiency of HIV-1 Env Using the Affinofile System. *Methods in Molecular Biology*, 3rd ed. Springer.

I'd like to thank Linda Baum and her post-docs Sandra Thiemann, Jenny Hernandez, Katrin Schaefer and staff Mabel Pang, who were heavily involved in our research of novel disulfide isomerase inhibitors (Chapter 3). Our studies of inhibitor activities also inspired collaborations with Dr. Grace Aldrovandi (University of Southern California, Keck School of Medicine, Professor of Pediatrics, Molecular Microbiology & Immunology and head of the Division of Infectious Diseases at Children's Hospital Los Angeles) and her post-docs Kyle Nakamura and Tom Wilkinson regarding vertical transmission that will soon be published.

Dr. David Montefiori (Duke University, Professor in the Division of Surgical Sciences, Department of Surgery and director of the Laboratory for AIDS Vaccine Research and Development) was the principal collaborator for our research on immunotherapies (Chapter 2) without whom this massive project could never have been completed. I would also like to thank Celia LeBranche, Mira Bilkowska and Amy Peterson for their tireless work and intellectual contributions. The enthusiastic support and efforts of Dr. David Montefiori and his lab were absolutely critical and essential to this project. The results of this project were recently submitted for publication to *Nature Communications*: Webb NE, Montefiori DC and Lee B. (2015). Dose response curve slope helps predict therapeutic potency and breadth of HIV broadly neutralizing antibodies. (in press).

This work was also supported by the Ruth L. Kirschstein National Research Service

Award GM007185 and the NIH (R21 AI092218).

VITA

2005-2007	Laboratory Assistant City College of San Francisco, Chemistry Department
2006	Teaching assistant Microbiology and Cell Biology, City College of San Francisco
2007	Genentech Scholar
2008-2009	Research Assistant Lawrence Berkeley National Laboratory
2009	Bachelor of Science in Chemical Biology University of California, Berkeley
2010	Teaching assistant Introduction to Virology, University of California, Los Angeles
2010-2013	Cellular and Molecular Biology Training Grant Fellow
2012	Teaching assistant Viral Pathogenesis, University of California, Los Angeles

Publications

Schaffer K, **Webb NE**, Hernandez J, Pang M, Lee B and Baum LG. Galectin-9 binds to specific O-glycans on Protein Disulfide Isomerase to retain PDI on the T cell surface. (*in preparation*).

Nakamura KJ, Heath L, Sobrera ER, Decker WD, Wilkinson TA, Semrau K, Sinkala M, Kankasa C, **Webb NE**, Lee B, Thea D, Kuhn L, Mullins JI and Aldrovandi GM. Breast Milk and In Utero Transmission of HIV-1 Select for Envelope Variants with Unique Molecular Signatures. (*in preparation*).

Webb NE, Montefiori DC, Lee B. Dose response curve slope helps predict therapeutic potency and breadth of HIV broadly neutralizing antibodies. *Nature Communications.* (*in press*).

Webb NE, Lee B. Quantifying CD4/CCR5 Usage Efficiency of HIV-1 Env Using the Affinofile System. *Methods in Moleclar Biology,* 3rd ed. Springer. (*in press*)

Chikere K*, **Webb NE***, Chou T, Borm K, Sterjovski J, Gorry PR, Lee B. Distinct HIV-1 entry phenotypes are associated with transmission, subtype specificity and resistance to broadly neutralizing antibodies. *Retrovirology* 2015, 11:40.
**Authors contributed equally*

Salimi H, Roche M, **Webb N**, Gray LR, Chikere K, Sterjovski J, Ellet A, Wesselingh Sl, Ramsland PA, Lee B, Churchill MJ, Gorry PR. Macrophage-tropic HIV-1 variants from brain demonstrate alterations in the way gp120 engages both CD4 and CCR5. *J. Leukoc. Biol.* 2013, 93(1):113-26.

Roche M, Salimi H, Duncan R, Wilkinson BL, Chikere K, Moore MS, **Webb NE**, Zappi H, Sterjovski J, Flynn JK, Ellet A, Gray LR, Lee B, Jubb B, Westby M, Ramsland PA, Lewin SR, Payne RJ, Churchill MJ, Gorry PR. A common mechanism of clinical HIV-1 resistance to the CCR5 antagonist maraviroc despite divergent resistance levels and lack of common gp120 resistance mutations. *Retrovirology* 2013, 10:43.

Holinga GJ, York RL, Onorato RM, Thompson CM, **Webb NE**, Yoon AP, Somorjai GA. An SFG Study of Interfacial Amino Acids at the Hydrophilic SiO2 and Hydrophobic Deuterated Polystyrene Surfaces. *J. Am. Chem. Soc.* 2011, 133:6243-6253.

York RL, Holinga GJ, Somorjai GA. An Investigation of the Influence of Chain Length on the Interfacial Ordering of L-Lysine and L-Proline and Their Homeopeptides and Hydrophobic and Hydrophilic Interfaces Studied by Sum Frequency Generation and Quartz Crystal Microbalance. *Langmuir* 2009, 25:9369-9374. (*acknowledgements*).

Presentations

Webb NE, Lee B. Mechanistic Slope Theories and Antibody Combination Slopes. *Workshop on Combinatorial Immunotherapies.* Los Alamos National Laboratory, Santa Fe, NM. 2015. (*oral presentation*)

Webb NE, Chikere K, Anton P, Baum L, Lee B. Unique Properties of Protein Disulfide Isomerase in HIV-1 Entry. *Cellular and Molecular Biology Training Program, Tri-Campus Symposium.* University of Southern California, Los Angeles, CA, 2013. (*poster*)

Webb NE, Chikere K, Anton P, Baum L, Lee B. Unique Properties of Protein Disulfide Isomerase in HIV-1 Entry. *Keystone Symposia on Molecular and Cellular Biology.* Vancouver, BC. 2012. (*poster*)

CHAPTER 1

Introduction

Since its discovery over 30 years ago, human immunodeficiency virus (HIV) and the pathologies associated with HIV infection have proven a significant challenge to clinical and fundamental science. HIV infection was first reported in the United States as an inexplicable acquired immune deficiency syndrome (AIDS) in young gay men that gave rise to opportunistic infections and death among 48% of the cases reported in its first year[1]. It would take only four years for AIDS to be reported worldwide and 9 years more to be the leading cause of death for all young adults in America[1]. By the turn of the century, AIDS had become the fourth most frequent cause of death worldwide, the most frequent in Africa[1].

The first HIV inhibitor, Zidovudine (AZT), was approved in March of 1987[2], 6 years after HIV/AIDS was first reported. By 1996, seven HIV inhibitors representing three distinct modes of inhibition were available[2], marking the first decrease in reported AIDS cases in the United States[1]. Since then, approximately one hundred HIV treatments have been released under accelerated approval guidelines motivated by the severity of the HIV/AIDS pandemic and response policies such as PEPFAR[3]. The modern arsenal of HIV treatments in the United States now include a total of thirty seven highly successful mono- and combination therapies, demonstrating the rapid pace of a unified, global response.

Although the past 34 years have transformed HIV infection from a morbid certainty into a manageable, chronic condition, roughly 0.5% of the world's population (35 million individuals) now live with HIV[4] (as of 2013). The prevalence of HIV is now disproportionately weighted to developing nations with little access to modern treatments, while drug resistance among populations that do have access to these treatments has been an ongoing problem. Modern public policy and scientific research goals now focus on accessibility, preventing transmission and resistance, vaccination and ultimately curing infection. These goals have proven challenging due to the extraordinary biological properties of HIV, where persistent latency and high mutation rates result in a strong propensity for the emergence of resistant variants. It is critical, therefore, that clinical expectations of new inhibitors and treatment strategies, such as immunotherapy, derived from experimental results *in vitro*, are

both highly predictive and incorporate the effect such treatments may have on the inherent properties of HIV itself.

This dissertation presents the results of four unique research projects aimed at understanding the properties of HIV entry, the first stage in the viral life cycle, and its inhibition. We first introduce an analytical method adapted from the fields of pharmacology and biochemistry to more accurately assess the clinical expectations of novel immunotherapeutics based on experimental results *in vitro* (Chapter 2). We then assess the specific activity of a novel class of entry inhibitors that target disulfide isomerization, a highly conserved process in HIV entry, relative to their potential toxic and contaminant effects to find specific recommendations for the development of next-generation disulfide isomerase inhibitors with improved antiviral activity and reduced cytotoxicity (Chapter 3).

We then change perspectives to describe the effects that inhibitors and immunotherapies can have on the fundamental properties of HIV itself. Infection efficiency can vary significantly among HIV isolates through receptor usage (Chapter 4) and target-cell surface dynamics (Chapter 5). We show that inhibitors and immunotherapies can have a profound influence on the way HIV virion interact with their target cells, which will be important to understanding the pathological properties and replication dynamics of resistant variants. Together, these projects present novel treatment strategies and analytical methods that are specifically geared toward the modern goal of managing HIV infection as a long-term condition on a global scale.

Modern Challenges to HIV Treatment in the Context of Entry

HIV presents unique challenges to finding inhibitor targets and preventing drug resistance. The persistence of HIV infection even during treatment is driven by reservoirs of HIV replication where resting $CD4^+$ T cells with stably integrated proviral DNA support low levels of replication[5]. Cessation of, or poor adherence to antiretroviral treatment then results in a rebound of plasma viremia that are no longer treatment naive and may carry resistance

mutations. Indeed, few viruses are capable of mutating as rapidly as HIV, which possesses a high functional tolerance for mutation[6] despite having a tightly compact genome. This unique capacity results not only in a broad global diversity of HIV isolates, but a diverse quasispecies of isolates within a single patient that can rival the yearly, global diversity of influenza A[6,7]. To understand the complex nature of HIV and the unique challenges this virus poses, we start with the HIV virus particle itself.

Anatomy of the HIV virion. An HIV virion consists of two genomic RNA molecules coated and protected by the viral nucleocapsid protein (NC) (Fig. 1.1a). The HIV capsid forms an additional protective layer that contains proteins involved in the nuclear transport (rev) and transcriptional activation (tat) of the viral genome. The internal space of the virus also contains proteins necessary for infection (reverse transcriptase, integrase and protease), is structurally supported by the matrix protein and is separated from its external environment by a lipid bilayer membrane derived from its parental host cell while budding. The outside of the virion is studded by envelope spikes (Env) that facilitate the attachment and entry of the virion into a new host cell, the first stage of the viral lifecycle. Entry is a highly desirable inhibitor target because Env is exposed and accessible and because entry occurs before the virus has entered its target cell, thus, entry inhibitors do not need to permeate living cells in order to reach their targets.

HIV attachment and entry. Entry is the process by which an HIV virion attaches to, and enters its host cell and is the first task a newborn virion must complete. The translational product of the Env gene is proteolytically cleaved into two glycoprotein subunits: gp120 and gp41, which are non-covalently associated into dimers and then assembled into a non-covalently associated trimer of dimers, or spike, with a 3-fold axis of symmetry (Fig. 1.1a, box). The final spike structure exposes a surface of three gp120 outer domains with three gp41 subunits coiled and tucked along the inner central axis of symmetry, where the N-terminus of gp41 anchors the spike to the viral membrane.

Attachment is driven by gp120 (Fig. 1.1b), where binding to cell-surface CD4 induces conformational changes that expose a co-receptor binding site. The co-receptor binding site recognizes the chemokine receptor CCR5 (for R5-tropic isolates), CXCR4 (for X4-tropic isolates) or either (dual tropic R5/X4 isolates). Co-receptor binding adds to the stability of virion-cell attachment and triggers the release of a fusion peptide in the C-terminus of gp41, which becomes embedded in the cell membrane, forming an irreversible anchor known as the pre-hairpin intermediate (PHI, Fig 1.1b). Massive structural rearrangements in the PHI result in the coordinated twisting and refolding of the three gp41 subunits to form a tight six-hlix bundle (6HB), which locally distorts the viral and cellular membranes with enough energy to induce spontaneous membrane fusion[8,9]. Once fused, the contents of the viral membrane are released into the target-cell cytoplasm, followed by uncoating of the viral RNA, reverse transcription and then integration of viral DNA into the host cell genome.

The vast majority of approved HIV inhibitors target the functions of reverse transcriptase, protease, and recently, integrase, while inhibitors targeting the HIV Env represent a very small proportion of available treatments, due some very unique features of the HIV Env.

Challenges facing entry inhibitors. Entry is an attractive target because it occurs outside the cell, before the viral lifecycle has begun. Although the fundamental mechanism of this process is conserved among all known HIV isolates, the structural details of the HIV Env spike can vary greatly among the quasispecies represented in a single patient[7]. As the only viral protein expressed on the surface of HIV virion, the Env spike is the primary target of humoral immune responses and in response to this, HIV has evolved specific mechanisms to facilitate rapid escape from immune recognition[10,11]. For example, gp120 contains five variable regions (V1-V5) that, together, form the large portion of exposed surface area on the Env spike[12] (Fig. 1.1a, box). These regions can tolerate dramatic changes in both length and amino-acid sequence to evade immune recognition[7]. The variable regions also present glycosylation sites that can be added, removed and re-positioned to form a glycan shield that

masks vulnerable epitopes[13]. Additionally, the tenuous, non-covalent association of gp120 to gp41 can result in gp120 dissociation and shedding, which may then act as an antigenic decoy that triggers humoral responses against viral epitopes not normally present on live virion[14,15].

The high degree of conformational variability in HIV Env presents unique challenges to designing inhibitors and treatments that target entry. For example, the first entry inhibitor, enfuvirtide (ENF) is a small peptide that binds to the PHI, blocking 6HB formation, where resistance can arise from mutations in both the targeted binding site and non-target sites[16,17]. HIV can also develop resistance against co-receptor antagonists that do not directly interact with Env. For example, resistance to maraviroc, which binds to CCR5 and alters its conformation such that gp120 cannot recognize it, comes in the form of an adapted ability, in gp120, to use the MVC-bound form of CCR5[18–20]. Despite these challenges, entry remains a highly desirable therapeutic target as entry inhibitors do not need to permeate cells and can prevent infection before a virion makes contact with its target cell.

How to Hit a Moving Target? Amidst all of the genetic and epigenetic variability of the HIV Env structure, the function of Env in entry is absolutely conserved. Thus, while there are specific regions in gp120 that serve to distract the scent of an immune response, there are also regions that must be structured in a specific way to facilitate entry. This is most evident through the discovery of broadly neutralizing antibodies (bnAbs) that target conserved regions of the Env spike. For example, because the Env must engage cell-surface CD4, the CD4 binding site (CD4bs) in gp120 is relatively conserved and, accordingly, bnAbs directed against epitopes in this region are capable of neutralizing a wide breadth of Env variants[21–24]. The membrane-proximal external region of gp41[25–27] and the gp120/gp41[28–31] interface also present conserved structural elements that are targeted by bnAbs. Even glycan regions in the variable loops can elicit bnAbs with large breadth[32–35].

Novel, conserved targets can also be represented by essential participants in the entry

process, for example, cellular components that might assist in the massive conformational changes in Env during entry (Fig. 1.1b). Like many viruses, the HIV Env contains highly conserved disulfide bonds that form rigid structural elements, stabilizing the native Env structure. Cleavage of these disulfide bonds is an essential part of entry for β, δ and γ retroviruses such as murine leukemia virus (MLV) and human T-lymphotropic virus (HTLV), whose Envs contain classical CXXC disulfide isomerization motifs that cleave local disulfide bonds to trigger fusion[36]. Although the HIV Env does not contain its own CXXC motif, this same mechanism may be at play in the process of HIV entry, driven by cellular DSB exchange proteins such as protein disulfide isomerase (PDI)[37–44].

While the HIV Env certainly represents an extremely dynamic and flexible target, regions that are functionally essential must remain constant and, therefore, can then serve as effective entry inhibitor targets that are insensitive to Env variability.

Assessing the Potential of Novel Entry Inhibitors.

Novel entry inhibitors must first be assessed and characterized *in vitro* before more concrete animal models can be used to reach human trials. Because these experimental systems lack the complexities of a living body, the activity of an inhibitor must be comprehensively assessed to develop clinical expectations that can justify further evaluation. Inhibitor activity is characterized through a dose-response experiment, where inhibition is quantified in terms of inhibitor concentration against a constant viral inoculum. The result is a description of the dose-dependent activity of a drug that can be mathematically reconstructed using a standard dose-response model built from two essential parameters. The EC_{50}, also known as an IC_{50} or median dose (D_m) is a measure of inhibitor strength and specifically describes the concentration of inhibitor needed to achieve 50% inhibition. The slope (m), also known as a Hill slope (H), describes the differential increase or decrease in (rise) inhibition from the median dose set-point. Thus, while IC_{50} (or D_m) anchors a dose-response curve in terms of concentration, the slope (m) describes the pitch, or rise, of the curve.

Classical and modern evaluation of HIV inhibitors. HIV inhibitors are commonly compared by their IC_{50} in the context of pharmacological properties, such as average achievable serum concentrations (C_{ave}) and clearance (e.g. metabolism). Drugs whose IC_{50}s are significantly lower than C_{ave} give high inhibitory quotients (C_{ave}/IC_{50}) and are considered more effective than those with lower inhibitory quotients. Although informative, this strategy does not account for the different pitch or rise in inhibition that drugs may have. For example, among two drugs with the same IC_{50} and pharmacodynamics, one drug may yield a steeper dose-dependent rise, or higher slope, in inhibition than the other, resulting in a greater activity at concentrations above IC_{50}. Both IC_{50} and slope are essential parameters that cannot, alone, describe the dose-response activity of an inhibitor and comparative methods that focus exclusively on any one of these two parameters lack the critical information provided by the other.

A recent retrospective analysis of existing HIV inhibitors revealed that IC_{50} was not as strongly correlated to historical, clinical performance than slope[45,46], demonstrating for the first time in the field that slope is specifically relevant to the inhibition of an exponentially replicating virus. Not only was slope a better indicator of clinical performance, it also provided a more detailed description of inhibitor activity in the context of viral replication[47,48] that can be used to develop novel inhibitors with high slopes and, therefore, greater clinical expectations. These recent studies show that IC_{50} and slope are equally important parameters in developing clinical expectations of inhibitors from *in vitro* experiments.

Alternative criteria for entry inhibitors. Because HIV entry occurs outside the cell, entry inhibitors can have a strong impact on the way HIV virion adapt, during treatment, to interact with their target cells. For example, the CCR5 antagonist, maraviroc, alters the way virion see CCR5 at the cell surface, which in turn, changes the way these virion interact with their target cells[49–51]. These drug-induced changes can come in the form of altered CD4/CCR5 usage efficiency, which describes how HIV virion respond to these recep-

tors specifically, or in the form of more physical properties such as virion distribution, which relates more to the macroscopic behavior of a virus as a population. In this sense, resistance to entry inhibitors can come at the expense of changes in CD4/CCR5 usage efficiency or less efficient, population-based interactions with target cells. Alternatively, resistance may be the result of a greater CD4/CCR5 usage efficiency or more efficient target-cell interactions. Resistance pathways involving changes in CD4/CCR5 usage efficiency[18,50,51] can have profound effects on target-cell tropism and clinical pathology[52–55], while changes in target-cell interaction efficiency can affect replication rates and transmission. It is, therefore, important to understand the effect of an entry inhibitor in terms of inhibitor concentration and also in the context of how a virus might respond to treatment.

Specific Aims.

This dissertation presents four research projects that focus on the major challenges facing HIV research today: controlling and maintaining HIV as a chronic infection and preventing resistance. These goals are addressed through novel analytical frameworks that can be used to develop more accurate clinical expectations of inhibitor activity (Chapter 2) and to comprehensively assess potential viral responses to treatment in terms of CD4/CCR5 usage (Chapter 4) and virus-cell interactions (Chapter 5). These methods are also applied to a novel, highly conserved entry target involving the cleavage of disulfide bonds in Env during entry and identify specific goals for the future development of inhibitors targeting this mechanism, which show great promise (Chapter 3).

We first apply the median effect dose-response model[56] to describe the activity of broadly neutralizing antibodies and develop more comprehensive clinical expectations of bnAbs in the context of immunotherapy that incorporate both IC_{50} and slope (Chapter 2). Our results demonstrate that slope is not only an important property to consider when selecting bnAb candidates for animal and human trials, but this parameter also illuminates potential mechanisms of neutralization that will likely assist in the rational design of more potent

and active immunotherapies. These methods are then extended to evaluate the activity of disulfide isomerase inhibitors (DII) in HIV entry[37–44], which represent a novel and highly conserved target (Chapter 3). Evaluation of DIIs is particularly challenging due to the essential cellular function of disulfide isomerase proteins, where many DIIs can exhibit strong toxic effects. Our results untangle these toxic effects from the inhibitory activities of DIIs against HIV entry to show that although these fist-generation compounds are not yet ready for more advanced trials, they do show great promise. Our results also identify specific goals for the design of next-generation DIIs with increased potency and reduced toxicity.

We then investigate the potential effects of treatment from the perspective of the virus. We present a next-generation Affinofile profiling system and associated viral entry receptor sensitivity assay (VERSA) metrics that we use to evaluate CD4/CCR5 usage efficiency in the context of target-cell tropism, HIV subtypes, transmission and bnAb resistance (Chapter 4). Our results illuminate how these clinical phenotypes are related to more inherent properties of viral infectivity that will be useful for controlling transmission and resistance and assessing the potential clinical pathologies of resistant isolates. Finally, we adapt the median effect dose-response model to the context of viral infection, which reveals that HIV virion exhibit distributive dynamics that influence the infectivity of viral populations (Chapter 5). The impact of CD4/CCR5 expression and entry inhibitors on these dynamics reveal novel properties of infection that may be useful for understanding the replication efficiency of viral isolates during treatment and the expansion and transmission efficiency of resistant variants.

Together, these chapters address the future of managing HIV as a global, long-term illness by introducing more comprehensive analytical methods to assess the clinical potential of novel inhibitor classes and immunotherapies, and through new experimental and analytical techniques that assess the adaptive response of HIV to treatment.

Figures.

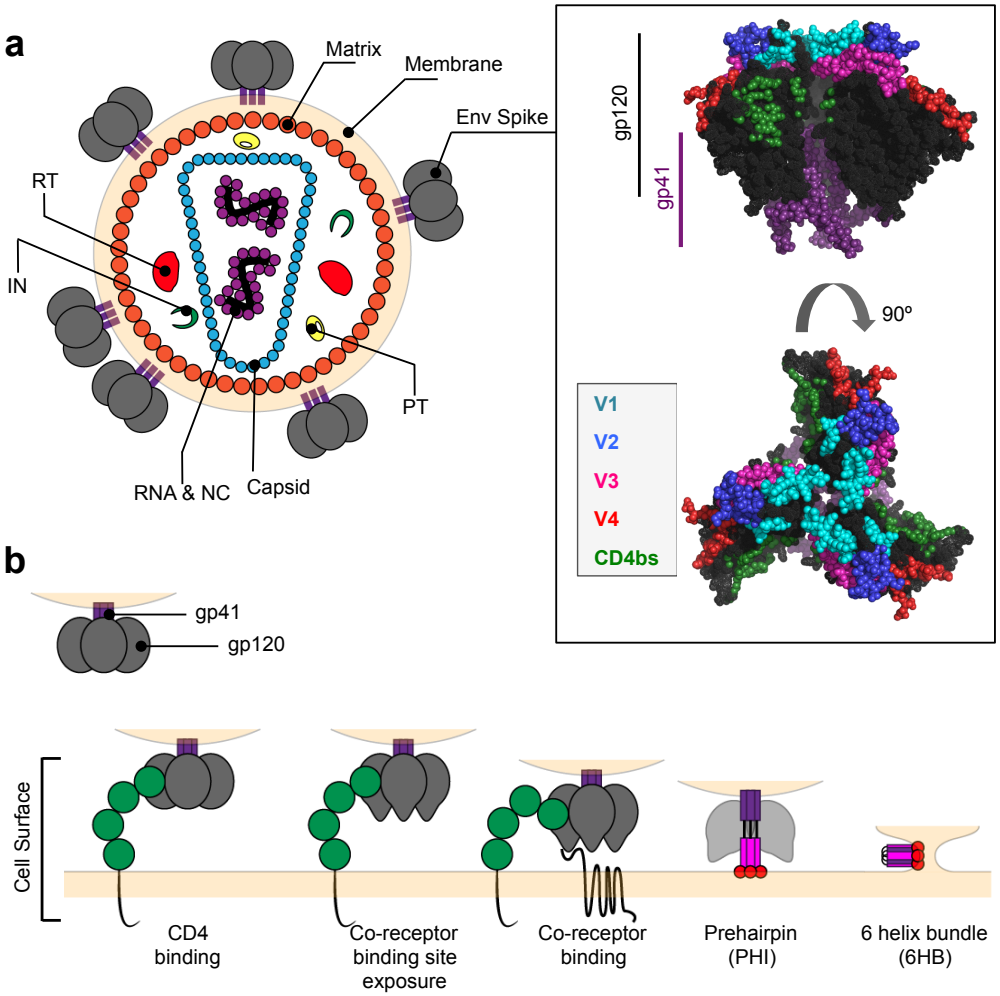

Figure 1.1: Example of the HIV virion, envelope spike and fusion mechanism. The HIV virion (**a**) is composed of two internal compartments containing viral RNA and nucleocapsid (NC), and essential enzymes (reverse transcriptase, RT; integrase, IN; protease, PT). The outer-most compartment is structurally supported by the matrix protein is separated from the external space by a lipid bilayer membrane. The surface of the virion is studded with envelope (Env) spikes that mediate attachment and entry. Side (inset, top) and top (inset, bottom) view of the Env spike (PDB ID 3J5M[57]). The spike is a non-covalently associated trimer of dimers consisting of the attachment glycoprotein 120 (gp120) and fusion glycoprotein 41 (gp41). Variable regions (V1-V4) are shown (cyan, blue, pink and red, respectively) and cover a vast expanse of exposed surface area. The critical CD4 binding site (CD4bs, green) is located between gp120 protomers. (**b**) Entry (left to right) begins when gp120 attaches to CD4, which exposes a co-receptor binding site. Co-receptor biding triggers release of a fusion peptide in gp41 that becomes anchored to the cell membrane to form a pre-hairpin intermediate (PHI). Gp41 HR1 (purple) and HR2 (pink) regions then coil and fold together to form the six-helix bundle (6HB) that induces spontaneous membrane fusion and viral entry.

References

1. A timeline of AIDS. AIDS.gov. <https://www.aids.gov/hiv-aids-basics/hiv-aids-101/aids-timeline/>. last checked Aug. 2015, published 2011.

2. HIV/AIDS History of Approvals. FDA.gov. <http://www.fda.gov/ForPatients/Illness/HIV-AIDS/History/>. last checked Aug. 2015, updated Feb. 2015.

3. FDA Marks 100th HIV/AIDS Drug Authorized for Purchase Under PEPFAR. FDA.gov. <http://www.fda.gov/NewsEvents/Newsroom/PressAnnouncements/ucm185416.htm>. last checked Aug. 2015, Oct. 6, 2009.

4. UN Joint Programme on HIV/AIDS. UNAIDS report on the global AIDS epidemic 2013. November, 2013.

5. T Pierson, J McArthur, and R F Siliciano. Reservoirs for HIV-1: mechanisms for viral persistence in the presence of antiviral immune responses and antiretroviral therapy. *Annu Rev Immunol*, 18:665–708, 2000.

6. Thumbi Ndung'u and Robin A Weiss. On HIV diversity. *AIDS*, 26(10):1255–60, Jun 2012.

7. B Korber, B Gaschen, K Yusim, R Thakallapally, C Kesmir, and V Detours. Evolutionary and immunological implications of contemporary HIV-1 variation. *Br Med Bull*, 58:19–42, 2001.

8. Craig B Wilen, John C Tilton, and Robert W Doms. Molecular mechanisms of HIV entry. *Adv Exp Med Biol*, 726:223–42, 2012.

9. Robert Blumenthal, Stewart Durell, and Mathias Viard. HIV entry and envelope glycoprotein-mediated fusion. *J Biol Chem*, 287(49):40841–9, Nov 2012.

10. Dennis R Burton, Robyn L Stanfield, and Ian A Wilson. Antibody vs. HIV in a clash of evolutionary titans. *Proc Natl Acad Sci U S A*, 102(42):14943–8, Oct 2005.

11. Ralph Pantophlet and Dennis R Burton. GP120: target for neutralizing HIV-1 antibodies. *Annu Rev Immunol*, 24:739–69, 2006.

12. Alan Merk and Sriram Subramaniam. HIV-1 envelope glycoprotein structure. *Curr Opin Struct Biol*, 23(2):268–76, Apr 2013.

13. Xiping Wei, Julie M Decker, Shuyi Wang, Huxiong Hui, John C Kappes, Xiaoyun Wu, Jesus F Salazar-Gonzalez, Maria G Salazar, J Michael Kilby, Michael S Saag, Natalia L Komarova, Martin A Nowak, Beatrice H Hahn, Peter D Kwong, and George M Shaw. Antibody neutralization and escape by HIV-1. *Nature*, 422(6929):307–12, Mar 2003.

14. J P Moore, J A McKeating, R A Weiss, and Q J Sattentau. Dissociation of gp120 from HIV-1 virions induced by soluble CD4. *Science*, 250(4984):1139–42, Nov 1990.

15. R Wyatt, P D Kwong, E Desjardins, R W Sweet, J Robinson, W A Hendrickson, and J G Sodroski. The antigenic structure of the HIV gp120 envelope glycoprotein. *Nature*, 393(6686):705–11, Jun 1998.

16. Michael L Greenberg and Nick Cammack. Resistance to enfuvirtide, the first HIV fusion inhibitor. *J Antimicrob Chemother*, 54(2):333–40, Aug 2004.

17. L Xu, A Pozniak, A Wildfire, S A Stanfield-Oakley, S M Mosier, D Ratcliffe, J Workman, A Joall, R Myers, E Smit, P A Cane, M L Greenberg, and D Pillay. Emergence and evolution of enfuvirtide resistance following long-term therapy involves heptad repeat 2 mutations within gp41. *Antimicrob Agents Chemother*, 49(3):1113–9, Mar 2005.

18. Michael Roche, Martin R Jakobsen, Anne Ellett, Hamid Salimiseyedabad, Becky Jubb, Mike Westby, Benhur Lee, Sharon R Lewin, Melissa J Churchill, and Paul R Gorry.

HIV-1 predisposed to acquiring resistance to maraviroc (MVC) and other CCR5 antagonists in vitro has an inherent, low-level ability to utilize MVC-bound CCR5 for entry. *Retrovirology*, 8:89, 2011.

19. Reem Berro, Per Johan Klasse, Martin R Jakobsen, Paul R Gorry, John P Moore, and Rogier W Sanders. V3 determinants of HIV-1 escape from the CCR5 inhibitors Maraviroc and Vicriviroc. *Virology*, 427(2):158–65, Jun 2012.

20. John P Moore and Daniel R Kuritzkes. A pièce de resistance: how HIV-1 escapes small molecule CCR5 inhibitors. *Curr Opin HIV AIDS*, 4(2):118–24, Mar 2009.

21. Xueling Wu, Zhi-Yong Yang, Yuxing Li, Carl-Magnus Hogerkorp, William R Schief, Michael S Seaman, Tongqing Zhou, Stephen D Schmidt, Lan Wu, Ling Xu, Nancy S Longo, Krisha McKee, Sijy O'Dell, Mark K Louder, Diane L Wycuff, Yu Feng, Martha Nason, Nicole Doria-Rose, Mark Connors, Peter D Kwong, Mario Roederer, Richard T Wyatt, Gary J Nabel, and John R Mascola. Rational design of envelope identifies broadly neutralizing human monoclonal antibodies to HIV-1. *Science*, 329(5993):856–61, Aug 2010.

22. Sunita S Balla-Jhagjhoorsingh, Davide Corti, Leo Heyndrickx, Elisabeth Willems, Katleen Vereecken, David Davis, and Guido Vanham. The N276 glycosylation site is required for HIV-1 neutralization by the CD4 binding site specific HJ16 monoclonal antibody. *PLoS One*, 8(7):e68863, 2013.

23. Johannes F Scheid, Hugo Mouquet, Beatrix Ueberheide, Ron Diskin, Florian Klein, Thiago Y K Oliveira, John Pietzsch, David Fenyo, Alexander Abadir, Klara Velinzon, Arlene Hurley, Sunnie Myung, Farid Boulad, Pascal Poignard, Dennis R Burton, Florencia Pereyra, David D Ho, Bruce D Walker, Michael S Seaman, Pamela J Bjorkman, Brian T Chait, and Michel C Nussenzweig. Sequence and structural convergence of

broad and potent HIV antibodies that mimic CD4 binding. *Science*, 333(6049):1633–7, Sep 2011.

24. Xueling Wu, Tongqing Zhou, Jiang Zhu, Baoshan Zhang, Ivelin Georgiev, Charlene Wang, Xuejun Chen, Nancy S Longo, Mark Louder, Krisha McKee, Sijy O'Dell, Stephen Perfetto, Stephen D Schmidt, Wei Shi, Lan Wu, Yongping Yang, Zhi-Yong Yang, Zhongjia Yang, Zhenhai Zhang, Mattia Bonsignori, John A Crump, Saidi H Kapiga, Noel E Sam, Barton F Haynes, Melissa Simek, Dennis R Burton, Wayne C Koff, Nicole A Doria-Rose, Mark Connors, NISC Comparative Sequencing Program, James C Mullikin, Gary J Nabel, Mario Roederer, Lawrence Shapiro, Peter D Kwong, and John R Mascola. Focused evolution of HIV-1 neutralizing antibodies revealed by structures and deep sequencing. *Science*, 333(6049):1593–602, Sep 2011.

25. Jinghe Huang, Gilad Ofek, Leo Laub, Mark K Louder, Nicole A Doria-Rose, Nancy S Longo, Hiromi Imamichi, Robert T Bailer, Bimal Chakrabarti, Shailendra K Sharma, S Munir Alam, Tao Wang, Yongping Yang, Baoshan Zhang, Stephen A Migueles, Richard Wyatt, Barton F Haynes, Peter D Kwong, John R Mascola, and Mark Connors. Broad and potent neutralization of HIV-1 by a gp41-specific human antibody. *Nature*, 491(7424):406–12, Nov 2012.

26. T Muster, F Steindl, M Purtscher, A Trkola, A Klima, G Himmler, F Rüker, and H Katinger. A conserved neutralizing epitope on gp41 of human immunodeficiency virus type 1. *J Virol*, 67(11):6642–7, Nov 1993.

27. M B Zwick, A F Labrijn, M Wang, C Spenlehauer, E O Saphire, J M Binley, J P Moore, G Stiegler, H Katinger, D R Burton, and P W Parren. Broadly neutralizing antibodies targeted to the membrane-proximal external region of human immunodeficiency virus type 1 glycoprotein gp41. *J Virol*, 75(22):10892–905, Nov 2001.

28. Louise Scharf, Johannes F Scheid, Jeong Hyun Lee, Anthony P West, Jr, Courtney Chen,

Han Gao, Priyanthi N P Gnanapragasam, René Mares, Michael S Seaman, Andrew B Ward, Michel C Nussenzweig, and Pamela J Bjorkman. Antibody 8ANC195 reveals a site of broad vulnerability on the HIV-1 envelope spike. *Cell Rep*, 7(3):785–95, May 2014.

29. Emilia Falkowska, Khoa M Le, Alejandra Ramos, Katie J Doores, Jeong Hyun Lee, Claudia Blattner, Alejandro Ramirez, Ronald Derking, Marit J van Gils, Chi-Hui Liang, Ryan Mcbride, Benjamin von Bredow, Sachin S Shivatare, Chung-Yi Wu, Po-Ying Chan-Hui, Yan Liu, Ten Feizi, Michael B Zwick, Wayne C Koff, Michael S Seaman, Kristine Swiderek, John P Moore, David Evans, James C Paulson, Chi-Huey Wong, Andrew B Ward, Ian A Wilson, Rogier W Sanders, Pascal Poignard, and Dennis R Burton. Broadly neutralizing HIV antibodies define a glycan-dependent epitope on the prefusion conformation of gp41 on cleaved envelope trimers. *Immunity*, 40(5):657–68, May 2014.

30. Claudia Blattner, Jeong Hyun Lee, Kwinten Sliepen, Ronald Derking, Emilia Falkowska, Alba Torrents de la Peña, Albert Cupo, Jean-Philippe Julien, Marit van Gils, Peter S Lee, Wenjie Peng, James C Paulson, Pascal Poignard, Dennis R Burton, John P Moore, Rogier W Sanders, Ian A Wilson, and Andrew B Ward. Structural delineation of a quaternary, cleavage-dependent epitope at the gp41-gp120 interface on intact HIV-1 Env trimers. *Immunity*, 40(5):669–80, May 2014.

31. Jinghe Huang, Byong H Kang, Marie Pancera, Jeong Hyun Lee, Tommy Tong, Yu Feng, Hiromi Imamichi, Ivelin S Georgiev, Gwo-Yu Chuang, Aliaksandr Druz, Nicole A Doria-Rose, Leo Laub, Kwinten Sliepen, Marit J van Gils, Alba Torrents de la Peña, Ronald Derking, Per-Johan Klasse, Stephen A Migueles, Robert T Bailer, Munir Alam, Pavel Pugach, Barton F Haynes, Richard T Wyatt, Rogier W Sanders, James M Binley, Andrew B Ward, John R Mascola, Peter D Kwong, and Mark Connors. Broad and potent HIV-1 neutralization by a human antibody that binds the gp41-gp120 interface. *Nature*, 515(7525):138–42, Nov 2014.

32. Laura M Walker, Sanjay K Phogat, Po-Ying Chan-Hui, Denise Wagner, Pham Phung, Julie L Goss, Terri Wrin, Melissa D Simek, Steven Fling, Jennifer L Mitcham, Jennifer K Lehrman, Frances H Priddy, Ole A Olsen, Steven M Frey, Phillip W Hammond, Protocol G Principal Investigators, Stephen Kaminsky, Timothy Zamb, Matthew Moyle, Wayne C Koff, Pascal Poignard, and Dennis R Burton. Broad and potent neutralizing antibodies from an African donor reveal a new HIV-1 vaccine target. *Science*, 326(5950):285–9, Oct 2009.

33. Laura M Walker, Michael Huber, Katie J Doores, Emilia Falkowska, Robert Pejchal, Jean-Philippe Julien, Sheng-Kai Wang, Alejandra Ramos, Po-Ying Chan-Hui, Matthew Moyle, Jennifer L Mitcham, Phillip W Hammond, Ole A Olsen, Pham Phung, Steven Fling, Chi-Huey Wong, Sanjay Phogat, Terri Wrin, Melissa D Simek, Protocol G Principal Investigators, Wayne C Koff, Ian A Wilson, Dennis R Burton, and Pascal Poignard. Broad neutralization coverage of HIV by multiple highly potent antibodies. *Nature*, 477(7365):466–70, Sep 2011.

34. Hugo Mouquet, Louise Scharf, Zelda Euler, Yan Liu, Caroline Eden, Johannes F Scheid, Ariel Halper-Stromberg, Priyanthi N P Gnanapragasam, Daniel I R Spencer, Michael S Seaman, Hanneke Schuitemaker, Ten Feizi, Michel C Nussenzweig, and Pamela J Bjorkman. Complex-type N-glycan recognition by potent broadly neutralizing HIV antibodies. *Proc Natl Acad Sci U S A*, 109(47):E3268–77, Nov 2012.

35. Mattia Bonsignori, Kwan-Ki Hwang, Xi Chen, Chun-Yen Tsao, Lynn Morris, Elin Gray, Dawn J Marshall, John A Crump, Saidi H Kapiga, Noel E Sam, Faruk Sinangil, Marie Pancera, Yang Yongping, Baoshan Zhang, Jiang Zhu, Peter D Kwong, Sijy O'Dell, John R Mascola, Lan Wu, Gary J Nabel, Sanjay Phogat, Michael S Seaman, John F Whitesides, M Anthony Moody, Garnett Kelsoe, Xinzhen Yang, Joseph Sodroski, George M Shaw, David C Montefiori, Thomas B Kepler, Georgia D Tomaras, S Munir Alam, Hua-Xin Liao, and Barton F Haynes. Analysis of a clonal lineage of HIV-1 en-

velope V2/V3 conformational epitope-specific broadly neutralizing antibodies and their inferred unmutated common ancestors. *J Virol*, 85(19):9998–10009, Oct 2011.

36. Judith M White, Sue E Delos, Matthew Brecher, and Kathryn Schornberg. Structures and mechanisms of viral membrane fusion proteins: multiple variations on a common theme. *Crit Rev Biochem Mol Biol*, 43(3):189–219, 2008.

37. E Fenouillet, R Barbouche, J Courageot, and R Miquelis. The catalytic activity of protein disulfide isomerase is involved in human immunodeficiency virus envelope-mediated membrane fusion after CD4 cell binding. *J Infect Dis*, 183(5):744–52, Mar 2001.

38. Emmanuel Fenouillet, Rym Barbouche, and Ian M Jones. HIV Env reduction postreceptor binding: a new target for AIDS treatment? *Blood*, 104(1):296, Jul 2004.

39. Lisa J Matthias and Philip J Hogg. Redox control on the cell surface: implications for HIV-1 entry. *Antioxid Redox Signal*, 5(1):133–8, Feb 2003.

40. Shuguang Bi, Patrick W Hong, Benhur Lee, and Linda G Baum. Galectin-9 binding to cell surface protein disulfide isomerase regulates the redox environment to enhance T-cell migration and HIV entry. *Proc Natl Acad Sci U S A*, 108(26):10650–5, Jun 2011.

41. R Barbouche, R Miquelis, IM Jones, and E Fenouillet. Protein-disulfide isomerase-mediated reduction of two disulfide bonds of HIV envelope glycoprotein 120 occurs post-CXCR4 binding and is required for fusion. *J. Biol. Chem*, 287(5):3131–6, Jan 31 2003.

42. A Gallina, TM Hanley, R Mandel, M Trahey, CC Broder, GA Viglianti, and HJ Ryser. Inhibitors of protein-disulfide isomerase prevent cleavage of disulfide bonds in receptor-bound glycoprotein 120 and prevent HIV-1 entry. *J. Biol. Chem*, 277((52)):50579–88, Dec 27 2002.

43. W Ou and J Silver. Role of protein disulfide isomerase and other thiol-reactive proteins in HIV-1 envelope protein-mediated fusion. *Virology*, 350(2):406–417, Jul 5 2006.

44. C Finnegan and R Blumenthal. Dissecting HIV fusion: identifying novel targets for entry inhibitors. *Infect Disord Drug Targets*, 6(4):355–67, Dec 2006.

45. Maame Efua S Sampah, Lin Shen, Benjamin L Jilek, and Robert F Siliciano. Dose-response curve slope is a missing dimension in the analysis of HIV-1 drug resistance. *Proc Natl Acad Sci U S A*, 108(18):7613–8, May 2011.

46. Benjamin L Jilek, Melissa Zarr, Maame E Sampah, S Alireza Rabi, Cynthia K Bullen, Jun Lai, Lin Shen, and Robert F Siliciano. A quantitative basis for antiretroviral therapy for HIV-1 infection. *Nat Med*, 18(3):446–51, Mar 2012.

47. Lin Shen, Susan Peterson, Ahmad R Sedaghat, Moira A McMahon, Marc Callender, Haili Zhang, Yan Zhou, Eleanor Pitt, Karen S Anderson, Edward P Acosta, and Robert F Siliciano. Dose-response curve slope sets class-specific limits on inhibitory potential of anti-HIV drugs. *Nat Med*, 14(7):762–6, Jul 2008.

48. Sarah B Laskey and Robert F Siliciano. A mechanistic theory to explain the efficacy of antiretroviral therapy. *Nat Rev Microbiol*, 12(11):772–80, Nov 2014.

49. Kelechi Chikere, Tom Chou, Paul R Gorry, and Benhur Lee. Affinofile profiling: how efficiency of CD4/CCR5 usage impacts the biological and pathogenic phenotype of HIV. *Virology*, 435(1):81–91, Jan 2013.

50. Michael Roche, Martin R Jakobsen, Jasminka Sterjovski, Anne Ellett, Filippo Posta, Benhur Lee, Becky Jubb, Mike Westby, Sharon R Lewin, Paul A Ramsland, Melissa J Churchill, and Paul R Gorry. HIV-1 escape from the CCR5 antagonist maraviroc associated with an altered and less-efficient mechanism of gp120-CCR5 engagement that attenuates macrophage tropism. *J Virol*, 85(9):4330–42, May 2011.

51. Michael Roche, Hamid Salimi, Renee Duncan, Brendan L Wilkinson, Kelechi Chikere, Miranda S Moore, Nicholas E Webb, Helena Zappi, Jasminka Sterjovski, Jacqueline K

Flynn, Anne Ellett, Lachlan R Gray, Benhur Lee, Becky Jubb, Mike Westby, Paul A Ramsland, Sharon R Lewin, Richard J Payne, Melissa J Churchill, and Paul R Gorry. A common mechanism of clinical HIV-1 resistance to the CCR5 antagonist maraviroc despite divergent resistance levels and lack of common gp120 resistance mutations. *Retrovirology*, 10:43, 2013.

52. Paul R Gorry, Joann Taylor, Geoffrey H Holm, Andrew Mehle, Tom Morgan, Mark Cayabyab, Michael Farzan, Hui Wang, Jeanne E Bell, Kevin Kunstman, John P Moore, Steven M Wolinsky, and Dana Gabuzda. Increased CCR5 affinity and reduced CCR5/CD4 dependence of a neurovirulent primary human immunodeficiency virus type 1 isolate. *J Virol*, 76(12):6277–92, Jun 2002.

53. Lachlan Gray, Jasminka Sterjovski, Melissa Churchill, Philip Ellery, Najla Nasr, Sharon R Lewin, Suzanne M Crowe, Steven L Wesselingh, Anthony L Cunningham, and Paul R Gorry. Uncoupling coreceptor usage of human immunodeficiency virus type 1 (HIV-1) from macrophage tropism reveals biological properties of CCR5-restricted HIV-1 isolates from patients with acquired immunodeficiency syndrome. *Virology*, 337(2):384–98, Jul 2005.

54. Hamid Salimi, Michael Roche, Nicholas Webb, Lachlan R Gray, Kelechi Chikere, Jasminka Sterjovski, Anne Ellett, Steve L Wesselingh, Paul A Ramsland, Benhur Lee, Melissa J Churchill, and Paul R Gorry. Macrophage-tropic HIV-1 variants from brain demonstrate alterations in the way gp120 engages both CD4 and CCR5. *J Leukoc Biol*, 93(1):113–26, Jan 2013.

55. Jasminka Sterjovski, Michael Roche, Melissa J Churchill, Anne Ellett, William Farrugia, Lachlan R Gray, Daniel Cowley, Pantelis Poumbourios, Benhur Lee, Steven L Wesselingh, Anthony L Cunningham, Paul A Ramsland, and Paul R Gorry. An altered and more efficient mechanism of CCR5 engagement contributes to macrophage tropism of CCR5-using HIV-1 envelopes. *Virology*, 404(2):269–78, Sep 2010.

56. T C Chou and P Talalay. Quantitative analysis of dose-effect relationships: the combined effects of multiple drugs or enzyme inhibitors. *Adv Enzyme Regul*, 22:27–55, 1984.

57. Dmitry Lyumkis, Jean-Philippe Julien, Natalia de Val, Albert Cupo, Clinton S Potter, Per-Johan Klasse, Dennis R Burton, Rogier W Sanders, John P Moore, Bridget Carragher, Ian A Wilson, and Andrew B Ward. Cryo-EM structure of a fully glycosylated soluble cleaved HIV-1 envelope trimer. *Science*, 342(6165):1484–90, Dec 2013.

CHAPTER 2

Dose Response Curve Slope Helps Predict Therapeutic Potency and Breadth of HIV Broadly Neutralizing Antibodies

The following chapter includes a submitted draft of the following:

Webb NE, Montefiori DC, Lee B. Dose response curve slope helps predict therapeutic potency and breadth of HIV broadly neutralizing antibodies. *Nature Communications*. (*in press*)

Supplementary information is provided in Appendix B.

Introduction

Several regions of the HIV-1 envelope glycoprotein spike are vulnerable to broadly neutralizing antibodies (bnAbs); these regions include the CD4 binding site (CD4bs) of gp120[2,58,70,71], glycan-dependent epitopes in the second and third variable regions (V2 and V3) of gp120[7,46,67,68], linear epitopes in the membrane proximal external region (MPER) of gp41[23,47,73], and glycan-dependent epitopes that bridge gp120 and gp41[6,16,24,57] (Fig. 2.1). This assortment creates opportunities for combinations of bnAbs to target multiple epitopes in an effort to achieve optimal coverage and impede escape[31]. Indeed, the identification and characterization of these bnAbs has generated renewed optimism that novel vaccines can be designed to elicit similar types of antibodies[8,39].

The extraordinary breadth and potency of some of the newer bnAbs also affords promising opportunities for immunotherapy of established infection. Recent proof-of-concept studies with passively delivered bnAbs in HIV-infected humanized mice and simian-human immunodeficiency virus (SHIV)-infected macaques have generated encouraging therapeutic results, especially when combinations of bnAbs were used[3,22,28,29,61]. Moreover, a single infusion with the CD4bs bnAb, 3BNC117, was recently shown to reduce plasma viral load by 0.8-2.5 log10 in chronically infected humans[9]. These therapeutic benefits might be improved in the presence of standard antiretroviral drugs[22] and host autologous neutralizing antibodies[29].

Measurements of bnAb potency and breadth are traditionally determined by the concentration of antibody that inhibits either 50% (IC_{50}) or 80% (IC_{80}) of a fixed virus inoculum in a dose-response single cycle infection assay *in vitro*. While these neutralization thresholds might be sufficient in a prophylactic vaccine setting, where the multiplicity of infection during transmission is relatively low[1,19,33] they fall far below the effective therapeutic dose range that will be required to inhibit multiple logs of virus and impede escape in an infected individual. Another clinically relevant dimension of dose-response curves is slope, which may be a more accurate measure of potency at therapeutically relevant inhibition levels.

Studies with antiretroviral drugs have shown that the slope can be used to more reliably predict clinical outcome than IC_{50} alone. IIP is an additional pharmacodynamic metric that goes further by incorporating both slope and IC_{50} to predict the number of logs of infection reduced at any given concentration of drug in a single round infection assay[59,60]. Together, IC_{50} and slope determine the full range of activity for a given antiretroviral agent, and IIP puts these parameters into a more clinical context. For antiretroviral drugs, the slope of the sigmoidal dose-response curve is related to specific inhibitory mechanisms defined by the cooperative reactivity of inhibitors and their targets[25,32,53,59].

Our results reveal that the neutralization slopes of bnAbs play an important role in forming therapeutic expectations from *in vitro* neutralization curves that complements and extends traditional IC_{50}/IC_{80} based analyses. We also find that slope is more strongly associated with neutralization breadth than IC_{50}. With some exceptions, bnAb slopes generally segregate by epitope class suggesting that like HIV inhibitors, bnAb slopes are also related to specific mechanisms of neutralization, thus, this parameter may aid in the development of novel, highly effective immunotherapies. While both slope and IC_{50} are fundamental properties of bnAb activity *in vitro*, bnAb slopes are rarely considered when predicting therapeutic potency. Our results show that this mechanistic parameter has a significant impact on predicted therapeutic potency and adds a new dimension to the development of novel immunotherapeutics.

Materials and Methods

Virus stocks. Virus stocks were prepared by transfection in 293T cells and titrated in TZM-bl cells as described[42].

Neutralization assay. The neutralizing activity of bnAbs was measured as a function of reductions in luciferase (Luc) reporter gene expression after a single round of infection in TZM-bl cells[42]. TZM-bl cells (also called JC57BL-13) were obtained from the NIH AIDS

Research and Reference Reagent Program, as contributed by John Kappes and Xiaoyun Wu. This is a HeLa cell clone that was engineered to express CD4 and CCR5[51] and to contain integrated reporter genes for firefly luciferase and E. coli beta-galactosidase under control of an HIV-1 LTR[69]. Briefly, a pre-titrated dose of virus was incubated with serial 3-fold dilutions of test sample in duplicate in a total volume of 150 μL for 1 hr at 37oC in 96-well flat-bottom culture plates. Freshly trypsinized cells (10,000 cells in 100 μL of growth medium containing 75 μg mL^{-1} DEAE dextran) were added to each well. One set of 8 control wells received cells + virus (virus control) and another set received cells only (background control). After 48 hours of incubation, 100 μL of cells was transferred to a 96-well black solid plate (Costar) for measurements of luminescence using the Britelite Luminescence Reporter Gene Assay System (PerkinElmer Life Sciences). Assay stocks of molecularly cloned Env-pseudotyped viruses were prepared by transfection in 293T/17 cells (American Type Culture Collection) and titrated in TZM-bl cells as described[42]. This assay has been formally optimized and validated[54] and was performed in compliance with Good Clinical Laboratory Practices, including participation in a formal proficiency testing program[64]. Additional information on the assay and all supporting protocols may be found at: http://www.hiv.lanl.gov/content/nab-reference-strains/html/home.htm.

BnAbs. 3BNC117 and 10-1074 were obtained from Michel Nussenzweig. VRC01 was obtained from John Mascola. PG9, PG16, PGT128 and PGT151 were obtained from Dennis Burton. CH01 and CH31 were obtained from Barton Haynes. HJ16 was obtained from Davide Corti and Antonio Lanzavecchia. 2G12, 2F5 and 4E10 were purchased from PolyMun Scientific (Germany).

Median effect analysis. Slope and IC_{50} values were determined using the median effect method[11]. This method involves a linear transformation of the standard Hill plot (Supplementary Fig. B.1a), where neutralization is represented by a log effect ratio (Equation 2.1) and Supplementary Fig. B.1b). Linear regression was used to determine the slope (m)

and IC_{50} (D_m) values corresponding to the linear slope and x-intercept, respectively, of each curve (Supplementary Fig. B.1b). In all cases, median effect fits were determined from the average of two experimental replicates for each neutralization curve. Dose intersects were calculated according to Equation 2.2 where $D_{m,1}$, m_1, $D_{m,2}$, m_2 are the IC_{50}s and slopes for antibodies 1 and 2 and D_i is the dose where both achieve the same level of neutralization at the same dose. This neutralization level (f_a) is defined in Equation 2.3 in terms of the intersecting dose (D_i) and the slope (m) and IC_{50} (D_m) of either antibody.

Envs that did not reach a minimum 50% neutralization within the range of antibody concentrations used in each neutralization assay were considered non-neutralized as well as Envs with IC_{50} values above 50 μg mL^{-1} (Supplementary Table B.2). In cases where neutralization reached a maximum plateau $< 95\%$ (Supplementary Table B.2 and Supplementary Fig. B.3) a stepwise iterator (perl v5.12.4) was used to fit maximum neutralization (N) to Equation 2.4 using the method of least squares, where f_a is neutralization as a percentage of maximum neutralization, N is maximum neutralization, D is bnAb concentration (μg mL^{-1}), m is slope and D_m is the concentration giving half maximum neutralization. In all cases, the IC_{50} values reported are the concentrations giving 50% maximum neutralization.

$$\log\left(\frac{f_a}{1-f_a}\right) = m\log(D) - m\log(D_m) \tag{2.1}$$

$$D_i = \left[\frac{(D_{m,1})^{m1}}{(D_{m,2})^{m2}}\right]^{\frac{1}{m1-m2}} \tag{2.2}$$

$$f_{ai} = \frac{1}{\left(\frac{D_i}{D_m}\right)^{-m} + 1} \tag{2.3}$$

$$\log\left(\frac{f_a}{N-f_a}\right) = m\log(D) - m\log(D_m) \tag{2.4}$$

IIP analysis. IIPs were calculated using Equation 2.5 as previously described[60], using fitted slope (m) and IC_{50} (D_m) values. See Supplementary Figure B.4 for an illustrative description of IIP.

$$\text{IIP} = \log\left(1 + \left(\frac{D}{D_m}\right)^m\right) \tag{2.5}$$

Slope estimates. Equation 2.6 was used to estimate slope values from publically available IC_{50} and IC_{80} values, where m is slope and log?(4) is the change in the log effect ratio ($\log(f_a/(1-f_a))$, Equation 2.1) between 50 and 80% neutralization. Equation 2.6 was derived from the linear median effect form described by Equation 2.1.

$$m = \frac{\log(4)}{\log(\text{IC}_{80}) - \log(\text{IC}_{50})} \tag{2.6}$$

Comparison of epitope classes. Statistical differences in mean slope between the CD4bs, V2-glycan, V3-glycan, MPER, HM cluster or gp120/gp41 classes were performed using one-way ANOVA in GraphPad Prism 6. The variance of slopes among these classes were equal and followed a normal distribution.

Experimental validation of extrapolated potencies. Extrapolation of inhibitory concentrations using median effect fitted slope and IC_{50} values was investigated experimentally using a modification of the TZM-bl assay described above. Briefly, undiluted stocks of Env-pseudotyped viruses were incubated in the presence and absence of the indicated concentrations of bnAbs for 1 hr at 37°C. Each mixture was then diluted serially 4-fold in quadruplicate for a total of 12 dilutions in 96-well culture plates. TZM-bl cells were added and incubated at 37°C for 48 hours. Infectious viral titer was defined by the fold dilution of Ce1176 virus stock, virus stock + CH31, or virus stock + PG16 mixtures giving 1000 RLU luciferase activity. The dynamic range of this assay was greater than the standard TZM-bl neutralization assay, where we observed a maximum 3.2-log reduction in virus titer

($\approx$ 99.9% neutralization). The change in virus titer reduction between 2x and 10x IC_{80} concentrations for PG16 and CH31 were proportionate to their respective slopes, where the log titer reduction was 2.9-fold higher for CH31 (between 2x and 10x IC_{80}) and the log titer reduction was 1.3-fold for PG16 (between 2x and 10x IC_{80}) (Supplementary Fig. B.2).

Neutralization breadth and breadth correlations. Neutralization breadth was defined as the percentage of Envs on our panel that gave 50%, 80%, 90% or 99% neutralization at concentrations below 50 μg mL^{-1} according to median effect fits. This calculation includes Envs for which no detectible neutralization could be experimentally observed. To accurately represent the correlations of slope, IC_{50} and IC_{80} to 99% neutralization breadth, breadths were re-calculated to exclude Envs that gave no detectible neutralization within the concentration range used in our assay.

Statistical Analysis. Slope and IC_{50} values were determined from linear regression of median effect-transformed neutralization data using Microsoft Excel 2011. Pearson correlations, confidence intervals, t-tests and 1-way ANOVA analyses were conducted using GraphPad Prism 6.

Code availability. In cases where an Env/bnAb combination achieved a maximum plateau in neutralization within our detection limit, a least squares iterative algorithm was used to fit maximum neutralization (N) according to Equation 2.4 using perl v5.12.4. This script is available upon request.

Results

Impact of slope on predicted therapeutic potencies of bnAbs. IC_{50} and IC_{80} are common metrics used to establish clinical expectations of bnAb activity from experimental results *in vitro* and to identify bnAbs with high potential for advancement into clinical trials. While useful, these parameters alone offer only a limited description of neutralization activity.

An additional and often neglected parameter, the dose-response slope, was strongly associated with clinical outcome in the context of small molecule HIV inhibitors, which exhibited a wide range of class-specific and mechanism-specific slopes[25,32,53,60]. To our knowledge, only one previous study examined in any detail the slopes of HIV-1 bnAb dose-response curves, and this was mostly done in the context of assessing the effects of combinations with earlier bnAbs: b12, 2G12 and 2F5[27]. Here we obtained dose-response curve slopes for 14 bnAbs and soluble CD4 (sCD4) assayed in TZM-bl cells against a global panel of 12 molecularly cloned HIV Env-pseudotyped reference viruses[13] (Supplementary Table B.1). To acquire additional positive neutralization results, a subset of bnAbs was assayed against 5 additional Env-pseudotyped reference viruses[34] (Supplementary Table B.1). The bnAbs represented six epitope classes including the CD4bs bnAbs VRC01[34,71], 3BNC117[58], CH31[71] and HJ16[2]; the V2-glycan bnAbs PG9, PG16[67] and CH01[7]; the V3-glycan bnAbs PGT128[68], 10-1074[46] and PGT121[68]; the high mannose cluster (HM cluster) bnAb 2G12[56]; the gp41 MPER bnAbs 2F5, 4E10[47,73] and 10E8[23]; and the gp120/gp41 glycan bnAb PGT151[6].

Dose-response neutralization curves for PG16 (V2-glycan) and CH31 (CD4bs) assayed against four Envs are shown in Figure 2.2a as examples of some of the most dramatic slope differences observed. Regardless of differences in IC_{50} (Fig. 2.2b, top), PG16 exhibited a shallow dose-dependent rise in neutralization relative to the steeper rise seen with CH31 (Fig. 2.2a), which is indicated by the lower dose-response curve slope for PG16 (Fig. 2.2b, bottom; compare blue to orange bars). These results were transformed using the median effect equation[11] (Equation 2.1, Supplementary Fig. B.1, where f_a is percent neutralization, D is antibody concentration, D_m is IC_{50} and m is slope), to give the linear dose-responses shown in Figure 2.2c. This form reveals that for any given Env, the higher slope of CH31 relative to PG16 causes the corresponding neutralization curves to converge toward an intersection point and then diverge as concentration continues to increase. This intersection defines the concentration (D_i, Equation 2.2, where $D_{(m,1)}$, m_1 and $D_{(m,2)}$, m_2 are the IC_{50}s and slopes for PG16 and CH31, respectively) and inhibition level (f_{ai}, Equation 2.3, where D_m and m

are the IC_{50} and slope of either PG16 or CH31) at which both PG16 and CH31 were equally effective against the same Env.

The impact of these intersections on potency is illustrated in Figure 2.2d, where the 50% inhibitory concentration of PG16 was 250- and 1,500-fold lower than CH31 for Envs 25710 and Ce1176, respectively. The potency of CH31 progressively approached that of PG16 for 80% and 90% inhibition, where eventually CH31 was 2,000- and 5-fold more potent than PG16 for 99% inhibition, reflecting the convergence, intersection and divergence of the curves. Median effect extrapolations to 99% inhibition were experimentally verified using a titer reduction assay, where CH31 produced a 3-log reduction in viral titer at 10 times its IC_{80} concentration (42 μg mL^{-1}) compared to PG16, which produced only a 1.9-log reduction in viral titer at 10 times its IC_{80} (0.44 μg mL^{-1}) against Env Ce1176 (Supplementary Fig. B.2). Thus, changes in relative potency at therapeutically relevant bnAb concentrations are the direct result of the slope's differential effect on neutralization. Importantly, these same slope-driven features were strongly associated with the clinical activity of HIV inhibitors, while IC_{50} alone was not correlated to the historical clinical properties HIV inhibitors[53,59].

BnAb classes have characteristic slopes. The IC_{50} and slope values for each bnAb assayed against our entire panel of Envs (Supplementary Table B.1) are shown in Figures 2.3a and 2.3b (see also Supplementary Table B.2), illustrating the full range of values observed in the complete dataset. Virus/bnAb combinations that did not reach at least 50% neutralization at the highest bnAb concentrations tested were excluded due to weak or non-detectable activity. We also note that some neutralization curves exceeded 50% but plateaued below 100% (Supplementary Fig. B.3), indicating that a portion of the virus was refractory to the bnAb. Consistent with previous reports[14,16,24,62,67] we mostly observed such incomplete neutralization for glycan-targeting bnAbs (CH01, PG16, PG9, 2G12 and PGT151). Incomplete neutralization of genetically clonal Env-pseudovirions is likely a manifestation of alternative post-translational modifications giving rise to a heterogenous population of Env

spikes, resulting in an epigenetic mixture of sensitive and resistant virions. Examples are post-translational variability in sequon occupancy[18] and glycan composition[14,52], both of which could profoundly affect bnAbs that either require glycan as part of their epitope, or are subject to glycan shielding. BnAbs that are better able to tolerate this epigenetic variability are more likely to achieve 100% neutralization in the assay. We excluded bnAb/Env combinations that exhibited incomplete neutralization (i.e, curves that plateau below 95%) because their full neutralization potential fell within the measurable range of the assay (< 1 log reduction in infectivity). To compensate for minor assay variance, 95% was used as the upper threshold for plateaus that were considered truly indicative of incomplete neutralization. CH01 exhibited plateaus below 95% neutralization against every Env in our panel, while such plateaus for PG16, PG9, 2G12 and PGT151 were only observed among a minor subset of 1-2 Envs (Supplementary Table B.2).

Collectively, few statistically significant differences in slope were observed within each bnAb epitope class for those bnAb/Env combinations achieving complete neutralization within our detection limits, suggesting that slope is primarily a feature of the target epitope. One exception to this general rule was sCD4, which gave slopes significantly lower than those of the CD4bs bnAb class (0.95 ± 0.3 for sCD4 and 1.37 ± 0.3 for CD4bs bnAbs combined, $p< 0.001$). Although the slopes of PG9 were generally higher than those of PG16, this difference did not reach statistical significance (0.92 ± 0.2 for PG9 and 0.61 ± 0.4 for PG16, $p= 0.08$). No significant correlation between slope and IC_{50} was observed for any bnAb class, reflecting the fundamental independence of these two parameters. However, each class of bnAbs clustered differentially in the landscape of IC_{50} and slope values (Fig. 2.3c). That CD4bs (high slope/moderate IC_{50}, excluding sCD4), V2-glycan (low slope/dispersed IC_{50}), MPER (low slope/high IC_{50}), and V3-glycan (high slope/low IC_{50}) bnAbs clustered into distinct quadrants suggest that bnAbs in each particular class occupy a different phenotypic landscape defined by both IC_{50} and slope. The 10E8 MPER bnAb represents another interesting exception as it exhibited significantly lower IC_{50}s than 4E10 and 2F5 despite having

similar slopes (geometric mean IC_{50} for 10E8 = 0.16 μg mL^{-1} versus 3.5 and 3.6 μg mL^{-1} for 4E10 and 2F5, respectively; $p < 0.001$) (see also Fig. 2.3a and 2.3b).

The slopes of each bnAb epitope class could be further categorized into the three groups (Fig. 2.3d) as those having slopes > 1 (CD4bs, V3 glycan), those having slopes ≈ 1 (HM cluster) and those having slopes < 1 (V2 glycan, gp120/gp41, MPER) with high statistical significance ($p < 0.0001$, 1-way ANOVA). Notably, sCD4 and each bnAb exhibited a range of slope values among the viruses in our panel, indicating that the slope is also Env-dependent. This will be an important consideration when interpreting clinical benefits among a patient population receiving passive bnAb therapy.

CD4-based immunoadhesins. In addition to *bona fide* bnAbs, immunoadhesins consisting of effector domains fused to the IgG Fc region represent a novel class of rationally designed antiviral therapeutics. For example, CD4-Ig consists of the CD4 D1 and D2 domains fused to the Fc domain of IgG1 (IgG1-Fc). Very recently, an enhanced version (eCD4-Ig) was described in which a mimetic peptide derived from the N-terminus of the major HIV coreceptor, CCR5, was fused to the C-terminus of the CD4-Ig Fc domain[17]. eCD4-Ig was able to neutralize an exceptionally broad array of HIV-1 Envs with an increased potency relative to CD4-Ig. We analyzed the dose-response curves of eCD4-Ig and CD4-Ig to determine if differences in slope may account for the enhanced potency of eCD4-Ig and compared these to the slopes and IC_{50}s of the CD4bs bnAbs and sCD4. First order approximations of slopes can be obtained from available IC_{50} and IC_{80} concentrations by using the linear median effect form (Equation 2.6), thus, median effect reduces the complex curvature of the standard sigmoidal Hill curve into a linear form (Fig. 2.2c and Supplementary Fig. B.1) that simplifies mathematical analysis and allows one to approximate slopes from a limited set of available data[11]. Both IC_{50} and IC_{80} values are publicly available for the CD4-based immunoadhesins. Figures 2.4a and 2.4b show the approximated slopes and published IC_{50} values for CD4-Ig and eCD4-Ig. Interestingly, Fig. 2.4a shows that eCD4-Ig does not have a consistently higher

slope compared to CD4-Ig across the panel of Envs analyzed (0.78 ± 0.12 and 0.87 ± 0.21 for CD4-Ig and eCD4-Ig, respectively). Indeed, both the CD4 immunoadhesins and sCD4 all have similar slopes (0.95 ± 0.27 for sCD4). However, eCD4-Ig consistently exhibited a 1.4 log lower IC_{50} compared to CD4-Ig ($p < 0.001$) (Fig. 2.4b). Thus, the enhanced potency of eCD4-Ig relative to CD4-Ig can be attributed to its lower IC_{50}. That the slope does not differ between sCD4, CD4-Ig and eCD4-Ig may also indicate that these mechanisms of inhibition are the same and are predominated by the initial CD4 binding event. Conversely, the higher slopes of CD4bs bnAbs relative to sCD4, CD4-Ig and eCD4-Ig suggest the neutralizing mechanisms of these bnAbs might be distinct from those of the CD4 immunoadhesins.

Neutralization breadth is strongly associated with slope. The overall therapeutic potential of bnAbs will depend on the diversity of HIV isolates that are neutralized within a clinically relevant range of concentration. Breadth is traditionally defined as the percentage of isolates for which a bnAb can achieve 50% or 80% neutralization below a designated concentration, usually 10-50 μg mL^{-1}. Because slope defines the changes in bnAb concentration necessary to increase inhibition, we sought to determine how this property affects neutralization breadth at increasing therapeutic thresholds, rather than simply using IC_{50} and IC_{80} values at a fixed bnAb concentration. Figure 2.5a shows the breadth of each bnAb at increasing thresholds of IC_{50}, IC_{80}, IC_{90} and IC_{99} using median-effect fitted curves. Breadth scores across these increasing thresholds changed more dramatically for bnAbs with characteristically lower slopes (V2-glycan, MPER, gp120/gp41) than for bnAbs with characteristically higher slopes (CD4bs, V3-glycan). The improved and narrow distribution of potencies for 10E8 resulted in a delay of this effect to higher neutralization thresholds, where the extrapolated IC_{99} breadth decreases from 100% to 40%. For isolates that were sensitive to each bnAb ($IC_{50} < 50$ μg mL^{-1}), breadth at the more therapeutically relevant IC_{99} threshold (i.e., potency needed for 2-log inhibition) was strongly associated with slope (Fig. 2.5b). Traditional measures of potency showed moderate association with neutralization breadth

(IC_{80}) or none at all (IC_{50}) (Fig. 2.5c). The MPER bnAbs 4E10 and 2F5, with the exception of 10E8, were excluded from this latter analysis because they exhibited zero breadth at the IC_{99} threshold.

IIP defines clinical expectations using both IC_{50} and slope. The neutralization potency of an antibody can be more completely described when both slope and IC_{50} are used to determine the instantaneous inhibitory potential (IIP). IIP was first used in an explanatory framework that accounted for the marked differences in clinical potency among the extant classes of antiretroviral drugs[59,60] which could not be accounted for by differences in IC_{50} alone. IIP uses both slope and IC_{50} to describe the log decrease by which single round infection is reduced by the antiviral agent at a given concentration (D) *in vitro* (see Equation 2.5, where slope is m and IC_{50} is D_m and Supplementary Fig. B.4). Thus, IIP serves as a more precise therapeutic expectation for any given dose of bnAb than traditional metrics (IC_{50} and IC_{80}).

As an exponential parameter, small differences in slope (m) can lead to large differences in IIP as D increases. As an illustrative example, we calculated the IIP of four bnAbs against a single Env clone (25710) at 10, 50 and 100 μg mL^{-1} (Fig. 2.6a). These four bnAbs from the indicated epitope classes (CD4bs, V2-glycan, and gp120/gp41) also exhibit different m values with this Env. A marked increase in IIP (on a log-scale) is seen as the concentration of bnAb increases, most notably for bnAbs with higher slopes (CH31 and 3BNC117). This pattern is even more apparent when examining the dose response curves shown in Supplementary Figure B.4.

Using Equation 2.5 and the same methodology, we calculated the IIP of the entire panel of bnAbs at 50 μg mL^{-1}, which is a common threshold concentration used to assess the therapeutic potential of bnAbs (Fig. 2.6b). By incorporating both slope and IC_{50}, IIP reveals some striking results. For example, the V3 glycan bnAbs with higher slopes (1.5 ± 0.3) were predicted to reduce viral infectivity by 3 logs more than the MPER bnAbs with lower slopes

(0.8 ± 0.2) (mean IIP 4.9 ± 0.9 for V3 glycan bnAbs versus IIP 1.4 ± 0.6 for MPER bnAbs; $p < 0.0001$). In general, the IIP reflected the slopes (Fig. 2.3b) of each bnAb class except the V2 glycan bnAbs, where the wide range of IC_{50} values (Fig. 2.3a) resulted in an equally wide distribution of IIPs. Indeed, PG16 exhibited one of the highest IIPs (7.6) against Env 703010217, which reflected the characteristically low IC_{50} (0.002 μg mL^{-1}) of PG16 when coupled to an unusually high slope (1.69) for this bnAb (median PG16 slope 0.6 ± 0.4) against this particular Env. The IIPs of the CD4 immunoadhesin reagents (CD4Im) reflected their differences in IC_{50}, where eCD4-Ig achieved a 1.4 log greater reduction in infection than CD4-Ig (IIP$=1.6 \pm 0.7$ for CD4-Ig and 3.0 ± 1.0 for eCD4-Ig, $p < 0.001$). Recall that the IC_{50}s of eCD4-Ig were 1.4 logs lower than those for CD4-Ig but no significant differences in slope were observed (Fig. 2.4). The same was observed for 10E8, which gave geometric mean IC_{50}s that were 1.3 logs lower than 2F5 and 4E10 resulting in $\approx$ 1-log increase in IIP. Altogether, these data suggest that the combination of slope and IC_{50} values reflected in the IIP metric has considerable explanatory potential that can complement and inform the evaluation of the therapeutic efficacy of bnAbs in the same way these three metrics illuminate our understanding of the clinical potency of small molecule inhibitors.

Clinical implications of bnAb slopes. Two studies in humans demonstrated a moderate transient reduction in plasma viremia when 2G12, 2F5 and 4E10 were co-administered immediately prior to treatment-interruption in subjects who began standard antiretroviral therapy (ART) during acute infection[40,65]. Results of a detailed analysis of escape variants in the treated subjects suggested that 2G12 was the only antibody in the combination that exerted pressure on the virus. On the other hand, results of an in-depth analysis showing that escape *in vitro* may be more difficult for 2F5 and 4E10 than for 2G12 suggests that perhaps all three bnAbs were needed for the observed transient effect on viremia[38]. We observed in our dataset moderate but statistically significant differences in slope between 2G12 and the MPER bnAbs 2F5 and 4E10 (2G12 slope $= 1.1 \pm 0.2$; combined 2F5 and

4E10 slopes = 0.83 ± 0.2, p= 0.002). As shown in Figure 2.7a, this moderate difference is compounded at higher neutralization thresholds, such that 2G12 achieves 99% neutralization at an average of 75 μg mL^{-1}, whereas 2F5 and 4E10 required $\geq$ 1 mg mL^{-1}. Figure 2.7b shows the range of 2F5, 4E10 and 2G12 peak/trough plasma concentrations estimated from human trials[40,65]. While the IC_{50}s and IC_{90}s of 2F5 and 4E10 fall within or below this range, only 2G12 remained predominantly within or below this range at IC_{99}. The IIP of these bnAbs against our Env panel at average peak serum concentrations[40,65] provide a more clinical description of expected efficacy, where 2F5 and 4E10 achieved a narrow distribution of moderate IIP (1.64 ± 0.44 and 1.68 ± 0.56 for 2F5 and 4E10 respectively) and 2G12 achieved an IIP > 3 for over half the Envs on our panel that were sensitive to this bnAb (Fig. 2.7c, mean IIP 3.3 ± 1.5). These results illuminate potential mechanisms for the exclusive 2G12 escape observed with this triple therapy in humans, in addition to the relative ease of 2G12 escape *in vitro*[66] and the distinct pharmacokinetic properties of these three bnAbs, where accumulation of 2G12 results in greater concentrations in vivo[40,65]. The higher average IIP of 2G12 against our Env panel suggests this bnAb would likely exert a greater neutralizing activity and selective pressure than 2F5 or 4E10; however, the broad distribution of 2G12 IIP relative to the narrow distribution of MPER IIP also suggest a broader landscape of potential resistance mutations for 2G12, represented by our Env panel. Overall, our results suggest that even subtle differences in slope can give rise to important differences in IIP and clinical outcome.

Three new bnAbs have been evaluated in passive immunotherapy experiments in macaques, each of which exhibited characteristic slopes > 1 in our study. As monotherapy, PGT121 (V3-glycan) was profoundly effective against established SHIV-SF162P3 infection[3], whereas 3BNC117 (CD4bs) and 10-1074 (V3-glycan) were profoundly effective against established SHIV-AD8EO infection[61], resulting in up to 3 log reductions in plasma viremia in each case. Using available published dose-response data, we estimated the slope for PGT121 against the SHIV-SF163P3 challenge stock to be ≈ 2, and the slopes for 3BNC117 and 10-1074

against SHIV-AD8EO challenge stock to be 1.59 and 1.90, respectively. Finally, as mentioned earlier, a single infusion with 3BNC117 was recently shown to reduce plasma viral load in chronically infected humans as long as therapeutic levels were present[9]. While these results further indicate that bnAbs with slopes > 1 are associated with positive clinical outcomes, a paucity of passive immunotherapy data with bnAbs that exhibit lower slopes precludes quantitative verification of their potential clinical benefits at this time.

Discussion

Next generation bnAbs are currently being considered for immunotherapy due to their enhanced potency and breadth of neutralization. In addition to these factors, other considerations such as scale-up manufacturability, safety, pharmacokinetics, immunogenicity and ease of escape, just to name a few, will determine the clinical success of bnAbs. Furthermore, neither breadth nor potency (or any *in vitro* test for that matter) can easily predict the ease of escape and fitness of escape mutations to any particular bnAb in vivo. Indeed, it is unlikely that monotherapy with any one bnAb, no matter how potent or broad, will succeed, especially since all extant bnAbs have known resistance mutations.

Nonetheless, breadth and potency, imperfect surrogate measures as they are of therapeutic efficacy, are critical components of the evaluation of bnAb candidates (or bnAb combinations) for in vivo efficacy trials. Importantly, breadth and potency are traditionally defined by *in vitro* IC_{50} and IC_{80} values that are well below the therapeutic threshold and these metrics only offer a limited, fixed description of bnAb activity. Here we show that dose-response curve slope is a more reliable indicator of bnAb breadth and potency at more therapeutically relevant doses. The current state-of-the-art does not consider the slope parameter when prioritizing which bnAb or combination of bnAbs to advance to human trials. We believe our analysis can complement these increasingly sophisticated efforts[31] and enhance the clinically predictive power of *in vitro* surrogate assays for bnAb potency.

More importantly, inclusion of the established IIP metric, which incorporates both IC_{50}

and slope, adds another clinically relevant dimension to our analysis (Fig. 2.6). The IIP metric has proven utility in predicting the clinical potency of antiretroviral drugs and drug combinations[32,59,60]. It is derived from a pharmacodynamic model that predicts the log decrease in virus infection when the antiviral agent, in this case the bnAb, is extrapolated to a given clinically relevant concentration. Predicted IIPs or IIPave (a more sophisticated metric that includes additional pharmacokinetic parameters such as half-life of the bnAb, but critically still includes the IC_{50} and slope parameters) can help guide the determination of effective dosing ranges and intervals.

Mechanistic explanations for the different bnAb curve slopes will require additional studies. We hypothesize that for the genetically cloned Env pseudovirions used here, slope is at least partially determined by epigenetic heterogeneity within the Env glycoprotein spikes that decorate the virus surface. Examples are variability in sequon occupancy and glycan composition as mentioned above. Target heterogeneity has been invoked to explain the slopes of other ligand-effector units[21] and was suggested to impact the slope of HIV inhibitors, including bnAbs such as b12, 2G12 and 2F5[27]. BnAbs that are better able to tolerate post-translational Env heterogeneity, or whose epitopes are not affected by this, would neutralize all virus particles equally well, resulting in a slope of ≈ 1. BnAbs with a lower threshold of tolerance would exhibit variable neutralization efficiencies across the heterogeneous virus population, resulting in slopes < 1. Here, adequate bnAb concentrations may be capable of neutralizing all virions in the population; however, it is also possible that a minor fraction of virions would completely resist neutralization. Because we excluded all neutralization curves that exhibit incomplete neutralization in our assay, the expected plateau representing the minor fraction of resistant virions would reside outside the range of the assay (e.g., plateau at 99.9% neutralization). Neutralization assays with a wider range of detection will be needed to assess this latter possibility. BnAb slopes might also be determined in part by mechanism of neutralization, such as an ability to act at one or multiple stages of the fusion process[5,12]. BnAbs that are able to inhibit at multiple stages might cooperate to explain in

part dose-response curve slopes > 1.

Collectively our data reveal an association between bnAb epitopes and dose-response slopes that bridge the fields of structural biology and clinical evaluation, and may help to guide the rational design and testing of therapeutically effective antibodies for HIV and other pathogens.

Addendum: Cooperative Basis for Neutralization Slopes

The slope (m) was first formally interpreted by A.V. Hill in 1910[20] as an effector stoichiometry (also see Appendix A) for the oxygen-hemoglobin system, where experimentally measured oxygen binding slopes generally fell within the range of 2 to 3, implying that a hemoglobin molecule has 2 or 3 oxygen binding sites. Crystal structures would definitively prove that there are four hemes and that these slope-based stoichiometric estimates were incorrect. It would later be discovered that the oxygenation of hemoglobin is a cooperative process, where the oxygenation of one heme allosterically increases the affinity of the remaining deoxy-hemes[4,15,49]. The first rigid formulation of this cooperative process was derived by Jacques Monod, Jeffries Wyman and Jean Pierre Changeux in 1965[41] and termed the MWC model. Since then, this form of positive cooperativity and its opposite, negative cooperativitiy, where the binding of a ligand decreases a targets affinity for additional ligands, would be described in a wide variety of biological systems[10,44,45,63].

The simplest mechanism of positive cooperativity is described by Max Perutz[48], whose crystal structures formed the basis of the MWC model, in the context of lamprey hemoglobin (lHb). LHb forms dimers and tetramers in solution through hydrogen bonding between histidine and acidic amino acid side chains (Fig 2.8a, left). The histidine involved in dimerization is also involved in coordinating oxygen to the heme, thus, when one monomer is oxygenated the dimer must dissociate (Fig 2.8a, middle). The histidine of the deoxy monomer is now free and does not require dissociation to coordinate with molecular oxygen, which results in an increased affinity of the newly dissociated heme. This mechanism results in a preferential distribution of oxygen to high affinity lHb monomers which, themselves, are the product of oxygenation. The mechanism for tetrameric human hemoglobin is more complex, involving a rotation and translation of α and β subunits relative to the central axis of symmetry that progressively increase the affinity of deoxy-hemes as the molecule is oxygenated (Fig. 2.8b), but the fundamental oxygen-driven increase in affinity is the same.

Negative cooperativity is the opposite, and is illustrated here using the metabotropic glutamate receptor subtype I (mGluR1) system[63]. This G-coupled protein receptor dimerizes at the cell surface where each of the two glutamate binding sites are in equilibrium between an open an closed conformation (Fig. 2.8c, left). When glutamate binds one of the monomers the closed conformation is stabilized, which then impairs the ability of the second monomer to adopt its own closed state upon glutamate binding (Fig. 2.8, left to right). Thus, although crystal structures can show glutamate in both binding sites, only one site is in the closed position. Mutations in the dimer association region and high ion concentrations can alter this property, allowing both monomers to adopt the closed state and demonstrating that cooperativity is an allosteric process involving the transfer of information from one subunit to another.

Positive and negative cooperativity serve important biological functions. For example, the positive cooperativity of hemoglobin accelerates the oxygenation of any single hemoglobin molecule, ensuring its efficient and rapid ligation when oxygen is abundant. Conversely, negative cooperativity has been reported in several G-protein coupled receptors[36,50,63], which may represent a mechanism of receptor anergy, or alternative signal switching based on extracellular conditions that allow or prevent full ligation by altering cooperativity. Because positive and negative cooperativity are ultimate driven by ligand binding, they may be easily conceptualized as a form of self synergy or self antagonism, respectively. The distributive effect of positive and negative cooperativity is a steep ($m > 1$) or shallow ($m < 1$) concentration-dependent rise in ligation, relative to non-cooperative, random distribution ($m = 1$). In the context of neutralizing antibodies, where neutralization is a function of antibody binding (for antibodies that do neutralize), positive and negative cooperativity would then result in a steep ($m > 1$) or shallow ($m < 1$) rise in neutralization with respect to bnAb concentration, relative to a non-cooperative slope ($m = 1$).

The MWC model proposes specific criteria that define potentially cooperative targets[41]: a) the target must have multiple effector binding sites, b) the target must have at least one

axis of symmetry and c) the target must be composed of identical, associated subunits to facilitate allostery. In the context of broadly neutralizing antibodies, the HIV Env satisfies all of these criteria. As a trimer of identical gp120/gp41 dimers, the HIV Env spike has a central 3-fold axis of symmetry that presents a maximum of three degenerate binding sites for any single Fab. The spatial orientation of degenerate epitopes preclude bivalent binding of an antibody[30] (and references therein), therefore, a single antibody is thought to occupy only one of its three epitopes to yield a maximum stoichiometry of 3 antibody molecules per trimer.

A cooperative interpretation of the slopes observed among our bnAb panel (Fig. 2.3b) is consistent with published binding stoichiometries[72]. For example, the high slopes observed for VRC01 suggest positive cooperativity, which should coincide with an over-abundance of multiply-liganded Env trimers. Accordingly, the trimer-binding stoichiometric estimates of PGV04 (another CD4bs bnAb) and VRC01 are 1.5 and 1.6, respectively. Furthermore, EM analysis revealed a high abundance (44%) of Envs bound by three PGV04 Fabs, consistent with a preferential distribution of PGV04 to trimers that are already bound. The stoichiometric binding estimates of PGT121, PGT122 and PGT123 (V3 glycan bnAbs) were also > 1. Conversely, PG9 and PG16 exhibited low slopes ($m < 1$) that indicate a decreased likelihood of multiply-bound trimers according to the cooperative theory. Both PG16 and PG9 Fab and IgGs yielded unusual trimer binding stoichiometry estimates just under 1[26,72].

The spatial relationship of PG16/PG9 epitopes are unique because all three degenerate binding modes share the same trimer face, thus, negative cooperativity might be driven by a very local form of allostery or steric occlusion[26], which could both prevent additional binding. Interestingly, the gp120-targeting bnAbs exhibiting slopes of negative cooperativity (PG9, PG16, PGT151) are also unique in their preferential recognition of the trimeric Env, relative to monomeric gp120, suggesting that the quartenary stability of HIV Env is highly sensitive to bnAb interactions. The significant difference between the slopes of the CD4bs bnAbs and CD4 immunoadhesins (CD4Im) (Fig 2.4a, in the context of the cooperative

theory, indicate that although these reagents bind to the same general region of HIV Env, they exert very different effects once bound. Accordingly, sCD4 is known to induce massive CD4-like structural changes in Env[43,55] that are not associated with VRC01 binding[35].

While the slopes of our bnAb panel were generally specific to the epitope targeted, we did observe a broad diversity of slopes, for each bnAb, among the different Envs tested. Almost every bnAb had one or two Envs that gave outlier slopes (for example, VRC01, 3BNC117, HJ16, PGT151), suggesting that the major source of slope variability is not the bnAb but the Env. This is also consistent with the cooperative theory where slopes are defined not by the effector, but by the unique structural features of the target, particularly at interfacial regions, as demonstrated in the hemoglobin and mGluR1 systems. The cooperative theory provides a detailed mechanism underlying the clinically relevant slope parameter that will likely be useful in engineering novel immunotherapeutics with higher clinical expectations.

Figures

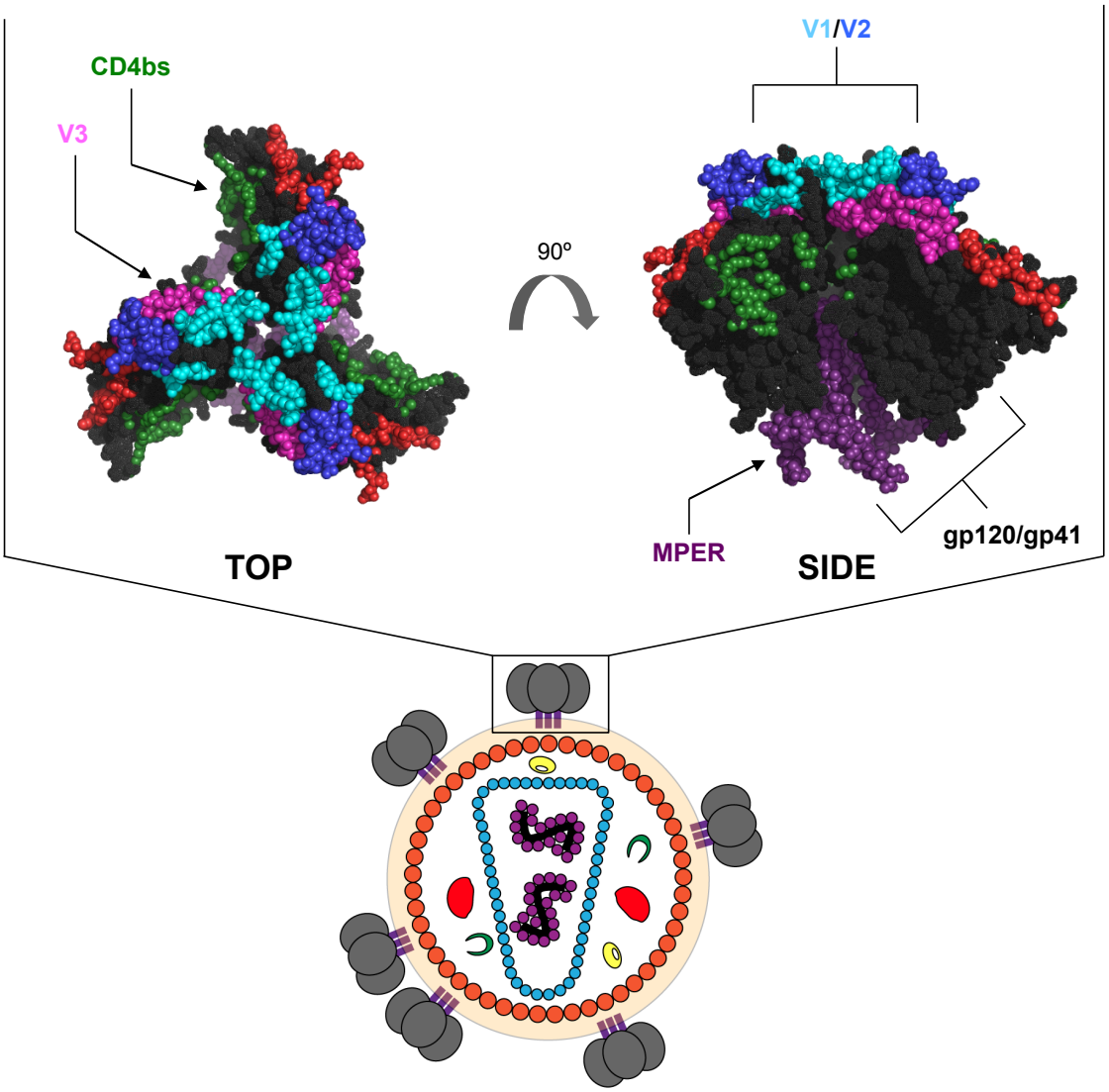

Figure 2.1: Neutralization epitopes on HIV Env. The HIV Env is the only viral protein expressed at the surface of HIV virion (bottom) and is highly immunogenic. Top (left) and side (right) views show major neutralization epitopes. The CD4 binding site (CD4bs, green) lies in a partially exposed region between gp120 protomers. Variable loop 3 (V3, pink) lies along the upper ridge of gp120 while variable loops 1 and 2 (V1 and V2, cyan and blue, respectively) cover the outer-most tip of the trimer. There are no known antibodies that target variable loop 4 (V4, red, shown for reference). Additional epitopes include the membrane-proximal external region of gp41 (MPER, purple) and the external interface between gp120 and gp41 (gp120/41). Crystal structures are from PDB ID 3J5M[37].

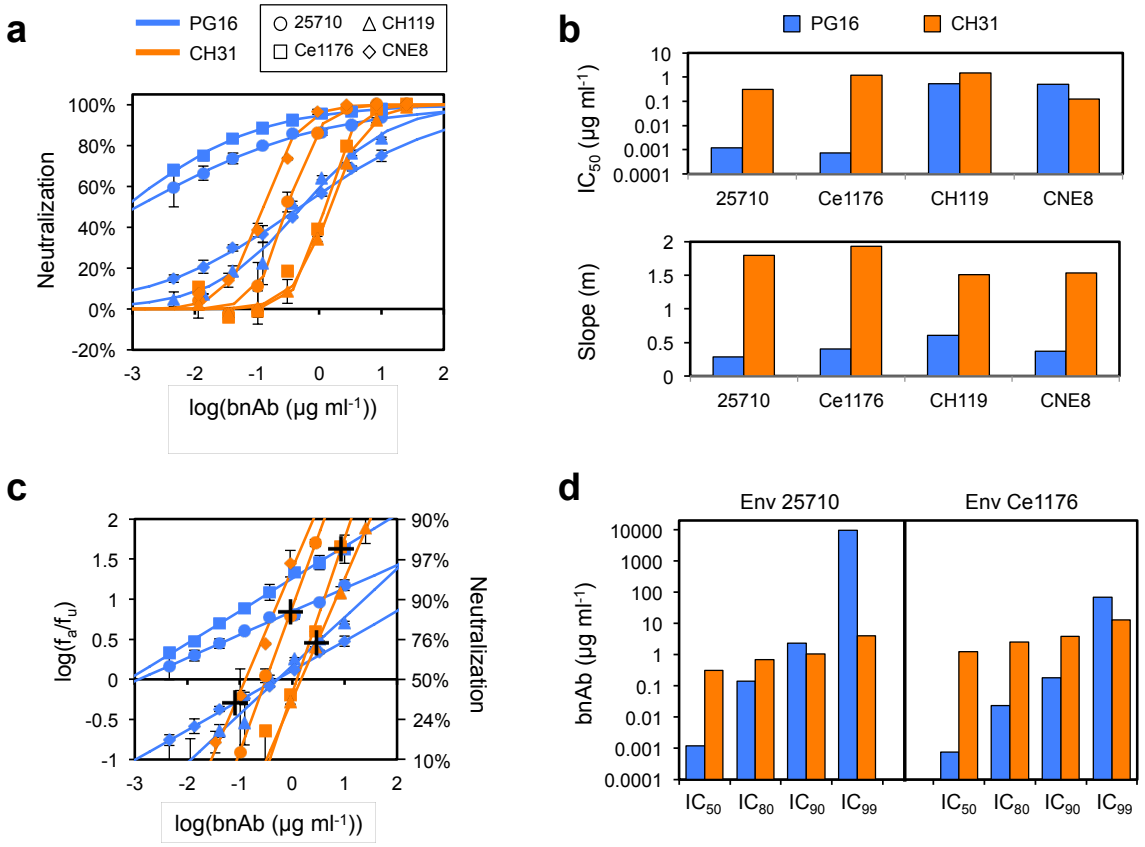

Figure 2.2: Effect of the slope on neutralization and potency. (**a**) Hill plots of neutralization curves for PG16 (blue) and CH31 (orange) against four representative Envs from our panel. (**b**) IC_{50} (top) and slope (bottom) values determined by median effect fitting (Methods). (**c**) Linear median effect plots of neutralization for the same data in panel a, where IC_{50} falls at the x-intercept and slope describes the angle of each curve relative to the x-axis. Intersections (crosses) indicate where both PG16 and CH31 gave the same neutralization at the same concentration for each Env. (**d**) Potencies of PG16 and CH31 against two Envs with the greatest difference in IC_{50}. Data shown are the average of two replicates and error bars indicate s.d.

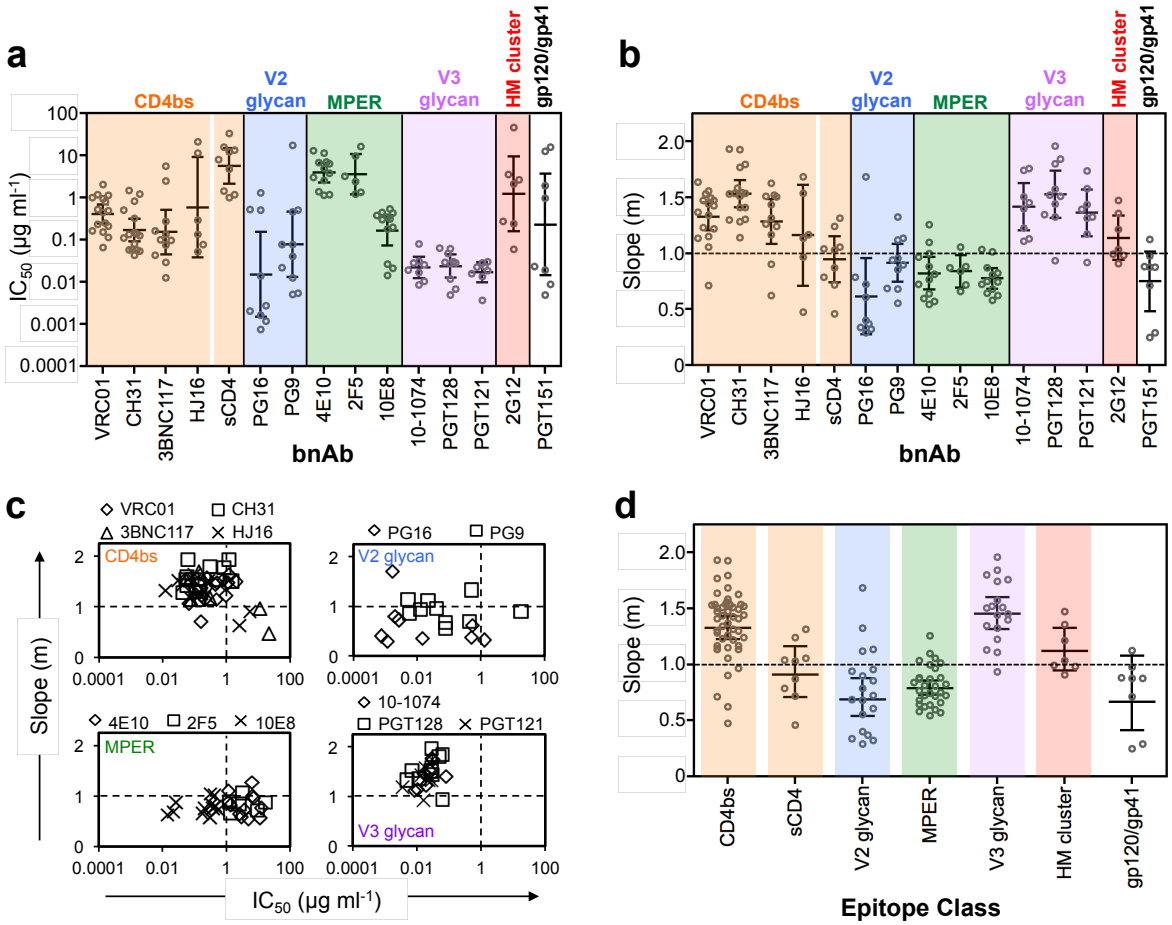

Figure 2.3: Slope and IC_{50} characteristics of bnAb epitope classes. (**a**) IC_{50} and (**b**) slope values of 13 bnAbs (bottom categories) against each Env in our panel (circles). Bars indicate geometric mean IC_{50}s with 95% c.i., or mean slopes with 95% c.i. Antibodies are grouped by epitope class (top categories). (**c**) Landscape of slope and IC_{50} values for CD4bs (top left), V2-glycan (top right), MPER (bottom left) and V3-glycan (bottom right) bnAb classes. Dashed lines indicate quadrants of high/low IC_{50} and high/low slope. (**d**) Slopes of each bnAb epitope class against each Env in our panel. Bars indicate mean and 95% c.i. All data shown are from bnAb/Env combinations that achieved complete neutralization and are derived from median effect fits of two-replicate averages.

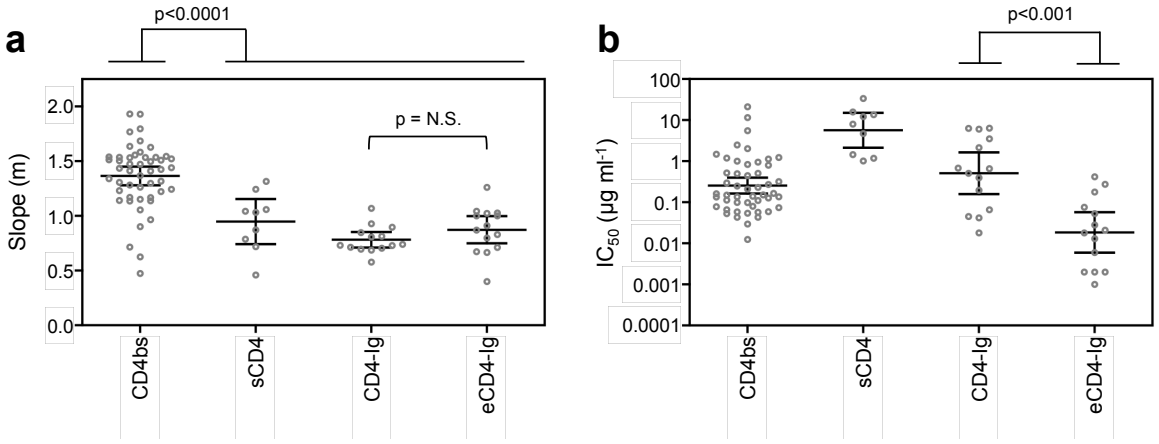

Figure 2.4: Slope and IC_{50} characteristics of CD4 immunoadhesins. . Neutralization slopes (**a**) and IC_{50}s (**b**) of the CD4bs bnAbs combined and CD4 immunoadhesin reagents sCD4, CD4-Ig and eCD4-Ig. Slope and IC_{50} values for CD4bs bnAbs and sCD4 are from Fig. 2 and reproduced here for ease of comparison. Slopes for CD4-Ig and eCD4-Ig were estimated from published IC_{50} and IC_{80} values[17] using Equation 2.6 (Methods). Thus, slopes were only estimated for a subset of Envs (n=14) where discrete IC_{50} and IC_{80} values were reported. Bars represent geometric IC_{50} with 95% c.i. or mean slope with 95% c.i and p-value (one way ANOVA) compares slopes of CD4bs bnAbs to sCD4, CD4-Ig and eCD4-Ig combined.

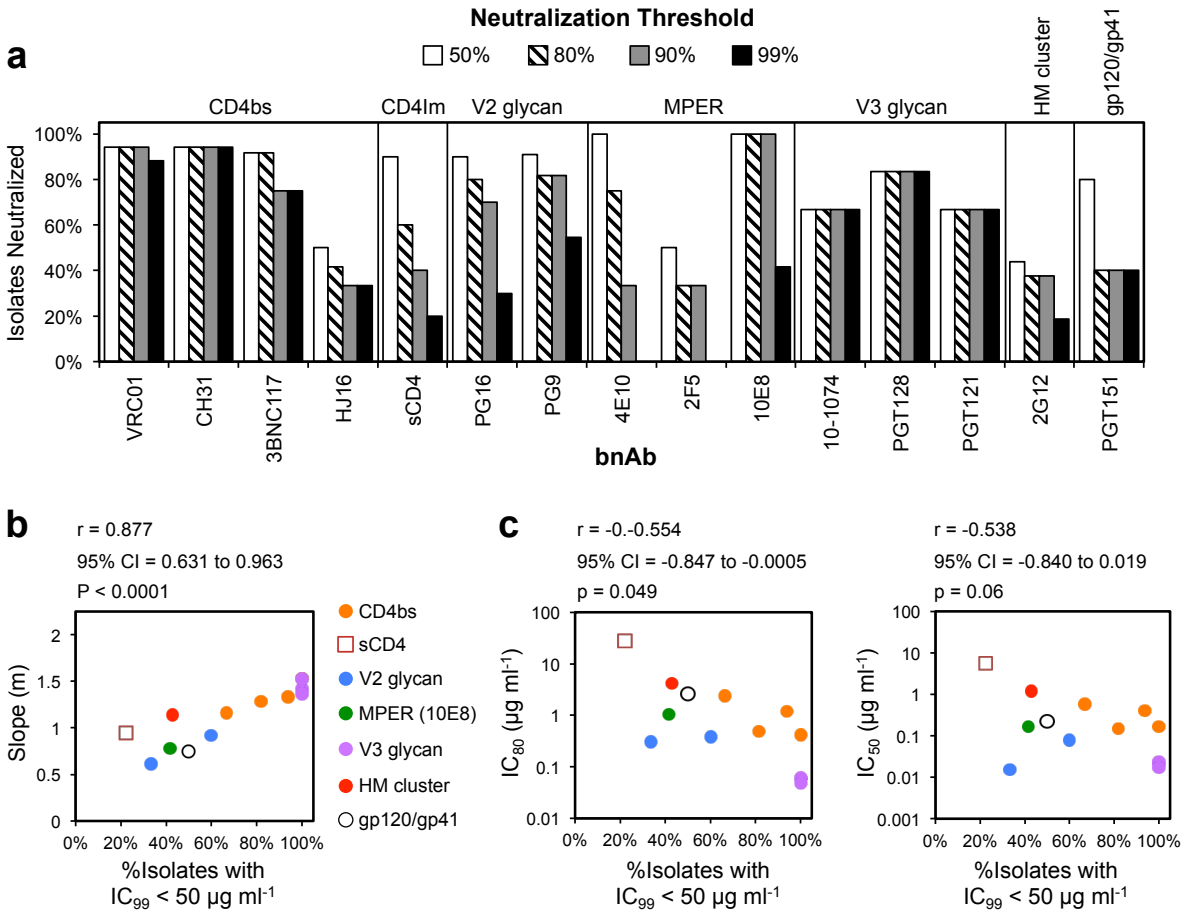

Figure 2.5: Effect of slope on neutralization breadth. (**a**) Neutralization breadths determined from dose-response curves of each bnAb against our total Env panel at increasing neutralization thresholds. A bnAb is considered non-neutralizing for a particular Env at a given inhibitory threshold when the respective inhibitory concentration (IC_{50}, IC_{80}, IC_{90} or IC_{99}) is greater than 50 μg mL^{-1}. Antibodies are ordered by epitope class. Correlations of slope (**b**), IC_{80} (**c**, left) and IC_{50} (**c**, right) to breadth at 99% neutralization for each bnAb, grouped by epitope class (symbols), where breadth excludes Envs giving no detectible neutralization within the parameters of our assay (Methods). Pearson correlations (r), 95% c.i. and associated p values are indicated above each graph.

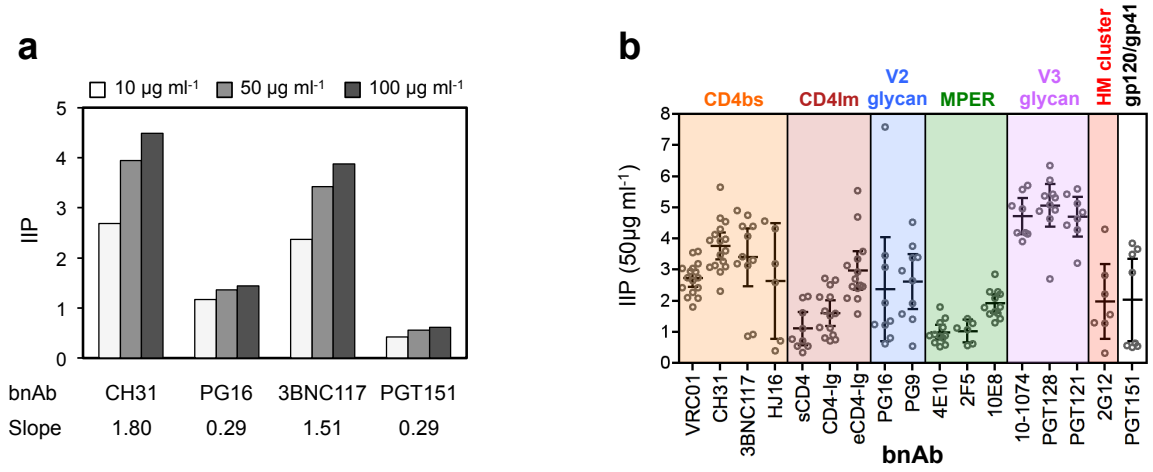

Figure 2.6: Instantaneous inhibitory potential (IIP) incorporates both slope and IC_{50}. (**a**) 10 μg mL^{-1}, 50 μg mL^{-1} and 100 μg mL^{-1} IIPs for CH31, PG16, 3BNC117 and PGT151 against Env 25710 with slopes indicated. (**b**) 50 μg mL^{-1} IIPs for all bnAbs against our Env panel where complete neutralization was observed. Bars indicate mean and 95% c.i.

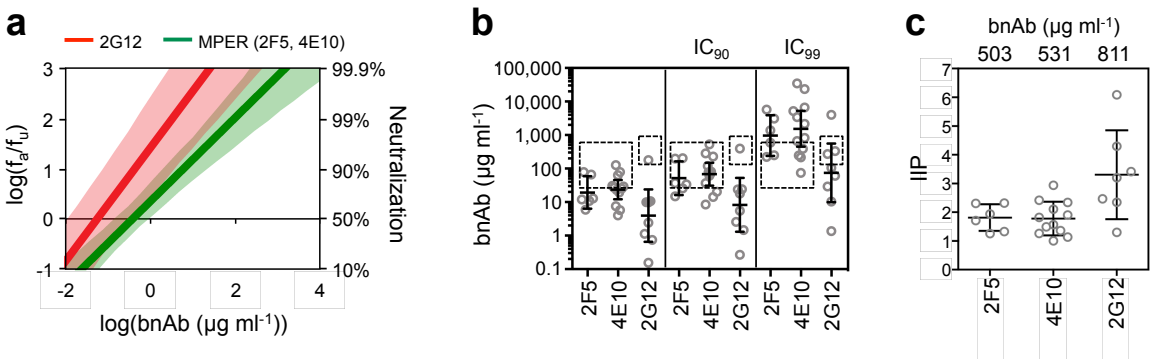

Figure 2.7: Sensitivity of therapeutically relevant potencies to small differences in slope. (**a**) Median effect plot of mean neutralization for 2G12 (red solid line) and MPER bnAbs (4E10 and 2F5 combined, green solid line) determined from the combined median effect curves of these bnAbs against each Env on our panel that was neutralized. Shaded areas indicate the corresponding s.d. (b) IC_{80}, IC_{90} and IC_{99} potencies of 2F5, 4E10 and 2G12 against each Env in our panel (symbols). Bars indicate geometric mean and 95% c.i. Dotted boxes illustrate the range of peak/trough plasma concentrations for each bnAb reported in human trials[40,65]. (c) IIPs of 2F5, 4E10 and 2G12 against our Env panel at average peak serum concentrations reported in human trials[40,65].

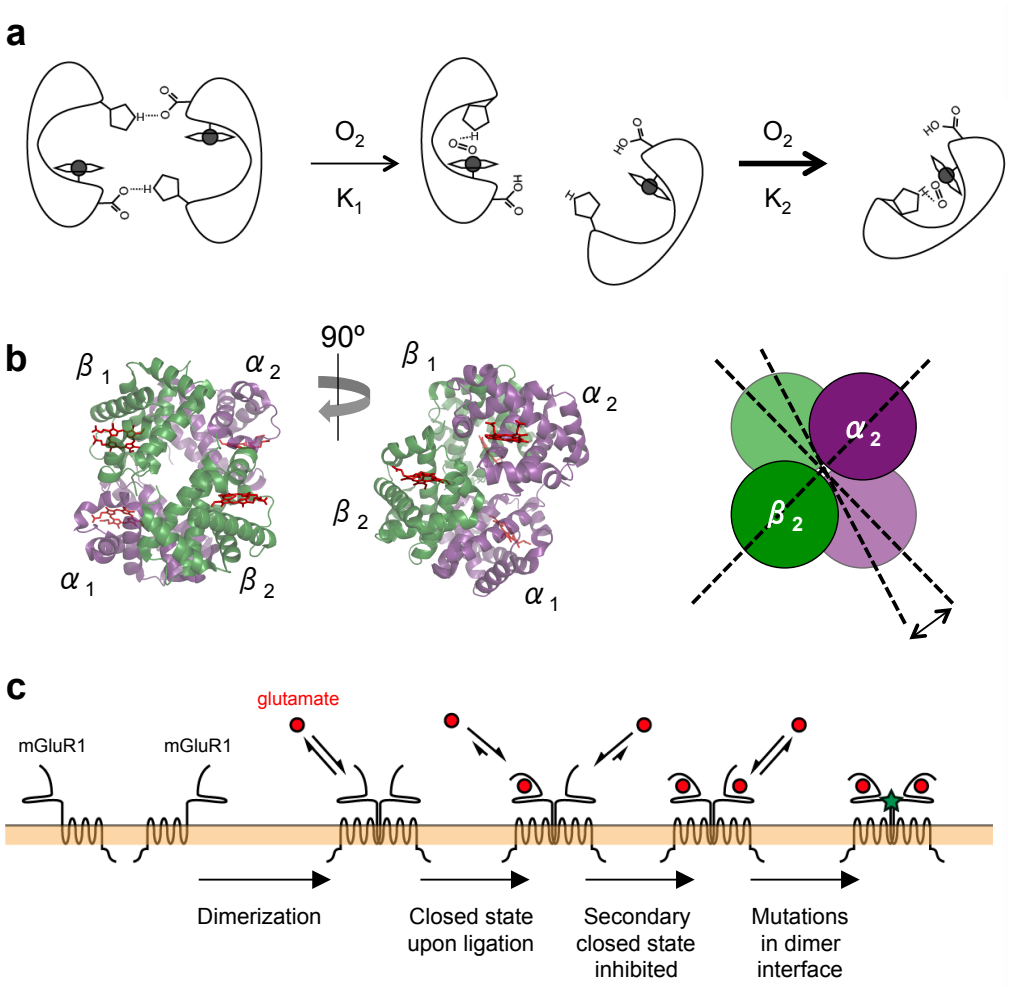

Figure 2.8: Examples of positive and negative cooperativity. (**a**) Lamprey hemoglobin exists as dimers and tetramers associated through hydrogen-bonding interactions between carboxylic amino acid side chains and histidine residues. This occupation of the histidine imidazole moiety prevents its stabilizing coordination with heme-bound oxygen and reduces the overall affinity of the heme (K_1). To stabilize a heme-bound oxygen, the dimers must dissociate, freeing the histidine residues on both monomers, where the histidine on the oxygenated monomer is now coordinated and the free histidine on the deoxy-monomer now confers an increased affinity for oxygen (K_2). (**b**) Front (left) and side (middle) views of the human hemoglobin tetramer composed of identical α and β subunits. Oxygen binding induces a translation and rotation of α_2 and β_2 subunits relative to central axis of symmetry. These subtle conformational changes increase the affinity of unoccupied hemes for partially oxygenated hemoglobin tetramers. (**c**) Negative cooperativity in the mGluR1 system. The mGluR1 receptor dimerizes at the cell surface where each dimer has two glutamate (Glu) binding sites. The first dimer that binds Glu adopts a closed conformation that locks the ligand in place. This closed conformation also allosterically inhibits the closing of the second receptor, allowing the free dissociation of Glu and preventing full dimer ligation. Mutations at the dimer interface and strong ion concentrations allow the second binding site to adopt the closed conformation.

References

1. M.-R. Abrahams, J. A. Anderson, E. E. Giorgi, C. Seoighe, K. Mlisana, L.-H. Ping, G. S. Athreya, F. K. Treurnicht, B. F. Keele, N. Wood, J. F. Salazar-Gonzalez, T. Bhattacharya, H. Chu, I. Hoffman, S. Galvin, C. Mapanje, P. Kazembe, R. Thebus, S. Fiscus, W. Hide, M. S. Cohen, S. A. Karim, B. F. Haynes, G. M. Shaw, B. H. Hahn, B. T. Korber, R. Swanstrom, C. Williamson, CAPRISA Acute Infection Study Team, and Center for HIV-AIDS Vaccine Immunology Consortium. Quantitating the multiplicity of infection with human immunodeficiency virus type 1 subtype C reveals a non-poisson distribution of transmitted variants. *J Virol*, 83(8):3556–67, Apr 2009. doi: 10.1128/JVI.02132-08.

2. S. S. Balla-Jhagjhoorsingh, D. Corti, L. Heyndrickx, E. Willems, K. Vereecken, D. Davis, and G. Vanham. The N276 glycosylation site is required for HIV-1 neutralization by the CD4 binding site specific HJ16 monoclonal antibody. *PLoS One*, 8(7):e68863, 2013. doi: 10.1371/journal.pone.0068863.

3. D. H. Barouch, J. B. Whitney, B. Moldt, F. Klein, T. Y. Oliveira, J. Liu, K. E. Stephenson, H.-W. Chang, K. Shekhar, S. Gupta, J. P. Nkolola, M. S. Seaman, K. M. Smith, E. N. Borducchi, C. Cabral, J. Y. Smith, S. Blackmore, S. Sanisetty, J. R. Perry, M. Beck, M. G. Lewis, W. Rinaldi, A. K. Chakraborty, P. Poignard, M. C. Nussenzweig, and D. R. Burton. Therapeutic efficacy of potent neutralizing HIV-1-specific monoclonal antibodies in SHIV-infected rhesus monkeys. *Nature*, 503(7475):224–8, Nov 2013. doi: 10.1038/nature12744.

4. A. Bellelli. Hemoglobin and cooperativity: Experiments and theories. *Curr Protein Pept Sci*, 11(1):2–36, Feb 2010.

5. J. M. Binley, C. S. Cayanan, C. Wiley, N. Schülke, W. C. Olson, and D. R. Burton. Redox-triggered infection by disulfide-shackled human immunodeficiency virus type 1 pseudovirions. *J Virol*, 77(10):5678–84, May 2003.

6. C. Blattner, J. H. Lee, K. Sliepen, R. Derking, E. Falkowska, A. T. de la Peña, A. Cupo, J.-P. Julien, M. van Gils, P. S. Lee, W. Peng, J. C. Paulson, P. Poignard, D. R. Burton, J. P. Moore, R. W. Sanders, I. A. Wilson, and A. B. Ward. Structural delineation of a quaternary, cleavage-dependent epitope at the gp41-gp120 interface on intact HIV-1 Env trimers. *Immunity*, 40(5):669–80, May 2014. doi: 10.1016/j.immuni.2014.04.008.

7. M. Bonsignori, K.-K. Hwang, X. Chen, C.-Y. Tsao, L. Morris, E. Gray, D. J. Marshall, J. A. Crump, S. H. Kapiga, N. E. Sam, F. Sinangil, M. Pancera, Y. Yongping, B. Zhang, J. Zhu, P. D. Kwong, S. O'Dell, J. R. Mascola, L. Wu, G. J. Nabel, S. Phogat, M. S. Seaman, J. F. Whitesides, M. A. Moody, G. Kelsoe, X. Yang, J. Sodroski, G. M. Shaw, D. C. Montefiori, T. B. Kepler, G. D. Tomaras, S. M. Alam, H.-X. Liao, and B. F. Haynes. Analysis of a clonal lineage of HIV-1 envelope V2/V3 conformational epitope-specific broadly neutralizing antibodies and their inferred unmutated common ancestors. *J Virol*, 85(19):9998–10009, Oct 2011. doi: 10.1128/JVI.05045-11.

8. D. R. Burton, R. Ahmed, D. H. Barouch, S. T. Butera, S. Crotty, A. Godzik, D. E. Kaufmann, M. J. McElrath, M. C. Nussenzweig, B. Pulendran, C. N. Scanlan, W. R. Schief, G. Silvestri, H. Streeck, B. D. Walker, L. M. Walker, A. B. Ward, I. A. Wilson, and R. Wyatt. A Blueprint for HIV Vaccine Discovery. *Cell Host Microbe*, 12(4):396–407, Oct 2012. doi: 10.1016/j.chom.2012.09.008.

9. M. Caskey, F. Klein, J. C. C. Lorenzi, M. S. Seaman, A. P. West, Jr, N. Buckley, G. Kremer, L. Nogueira, M. Braunschweig, J. F. Scheid, J. A. Horwitz, I. Shimeliovich, S. Ben-Avraham, M. Witmer-Pack, M. Platten, C. Lehmann, L. A. Burke, T. Hawthorne, R. J. Gorelick, B. D. Walker, T. Keler, R. M. Gulick, G. Fätkenheuer, S. J. Schlesinger, and M. C. Nussenzweig. Viraemia suppressed in HIV-1-infected humans by broadly neutralizing antibody 3BNC117. *Nature*, Apr 2015. doi: 10.1038/nature14411.

10. J.-P. Changeux. Allostery and the Monod-Wyman-Changeux model after 50 years. *Annu Rev Biophys*, 41:103–33, 2012. doi: 10.1146/annurev-biophys-050511-102222.

11. T. C. Chou and P. Talalay. Quantitative analysis of dose-effect relationships: the combined effects of multiple drugs or enzyme inhibitors. *Adv Enzyme Regul*, 22:27–55, 1984.

12. E. T. Crooks, P. L. Moore, D. Richman, J. Robinson, J. A. Crooks, M. Franti, N. Schülke, and J. M. Binley. Characterizing anti-HIV monoclonal antibodies and immune sera by defining the mechanism of neutralization. *Hum Antibodies*, 14(3-4):101–13, 2005.

13. A. deCamp, P. Hraber, R. T. Bailer, M. S. Seaman, C. Ochsenbauer, J. Kappes, R. Gottardo, P. Edlefsen, S. Self, H. Tang, K. Greene, H. Gao, X. Daniell, M. Sarzotti-Kelsoe, M. K. Gorny, S. Zolla-Pazner, C. C. LaBranche, J. R. Mascola, B. T. Korber, and D. C. Montefiori. Global panel of HIV-1 Env reference strains for standardized assessments of vaccine-elicited neutralizing antibodies. *J Virol*, 88(5):2489–507, Mar 2014. doi: 10.1128/JVI.02853-13.

14. K. J. Doores and D. R. Burton. Variable loop glycan dependency of the broad and potent HIV-1-neutralizing antibodies PG9 and PG16. *J Virol*, 84(20):10510–21, Oct 2010. doi: 10.1128/JVI.00552-10.

15. W. A. Eaton, E. R. Henry, J. Hofrichter, S. Bettati, C. Viappiani, and A. Mozzarelli. Evolution of allosteric models for hemoglobin. *IUBMB Life*, 59(8-9):586–99, 2007. doi: 10.1080/15216540701272380.

16. E. Falkowska, K. M. Le, A. Ramos, K. J. Doores, J. H. Lee, C. Blattner, A. Ramirez, R. Derking, M. J. van Gils, C.-H. Liang, R. Mcbride, B. von Bredow, S. S. Shivatare, C.-Y. Wu, P.-Y. Chan-Hui, Y. Liu, T. Feizi, M. B. Zwick, W. C. Koff, M. S. Seaman, K. Swiderek, J. P. Moore, D. Evans, J. C. Paulson, C.-H. Wong, A. B. Ward, I. A. Wilson, R. W. Sanders, P. Poignard, and D. R. Burton. Broadly neutralizing HIV antibodies define a glycan-dependent epitope on the prefusion conformation of gp41 on cleaved envelope trimers. *Immunity*, 40(5):657–68, May 2014. doi: 10.1016/j.immuni.2014.04.009.

17. M. R. Gardner, L. M. Kattenhorn, H. R. Kondur, M. von Schaewen, T. Dorfman, J. J. Chiang, K. G. Haworth, J. M. Decker, M. D. Alpert, C. C. Bailey, E. S. Neale, Jr, C. H. Fellinger, V. R. Joshi, S. P. Fuchs, J. M. Martinez-Navio, B. D. Quinlan, A. Y. Yao, H. Mouquet, J. Gorman, B. Zhang, P. Poignard, M. C. Nussenzweig, D. R. Burton, P. D. Kwong, M. Piatak, Jr, J. D. Lifson, G. Gao, R. C. Desrosiers, D. T. Evans, B. H. Hahn, A. Ploss, P. M. Cannon, M. S. Seaman, and M. Farzan. AAV-expressed eCD4-Ig provides durable protection from multiple SHIV challenges. *Nature*, 519(7541):87–91, Mar 2015. doi: 10.1038/nature14264.

18. E. P. Go, J. Irungu, Y. Zhang, D. S. Dalpathado, H.-X. Liao, L. L. Sutherland, S. M. Alam, B. F. Haynes, and H. Desaire. Glycosylation site-specific analysis of HIV envelope proteins (JR-FL and CON-S) reveals major differences in glycosylation site occupancy, glycoform profiles, and antigenic epitopes' accessibility. *J Proteome Res*, 7(4):1660–74, Apr 2008. doi: 10.1021/pr7006957.

19. R. E. Haaland, P. A. Hawkins, J. Salazar-Gonzalez, A. Johnson, A. Tichacek, E. Karita, O. Manigart, J. Mulenga, B. F. Keele, G. M. Shaw, B. H. Hahn, S. A. Allen, C. A. Derdeyn, and E. Hunter. Inflammatory genital infections mitigate a severe genetic bottleneck in heterosexual transmission of subtype A and C HIV-1. *PLoS Pathog*, 5(1): e1000274, Jan 2009. doi: 10.1371/journal.ppat.1000274.

20. A. Hill. The possible effects of the aggregation of the molecules of hæmoglobin on its dissociation curves. *J. Physiol.*, 40(Suppl.):iv–vii, January 1910.

21. A. Hoffman and A. Goldberg. The relationship between receptor-effector unit heterogeneity and the shape of the concentration-effect profile: pharmacodynamic implications. *J Pharmacokinet Biopharm*, 22(6):449–68, Dec 1994.

22. J. A. Horwitz, A. Halper-Stromberg, H. Mouquet, A. D. Gitlin, A. Tretiakova, T. R. Eisenreich, M. Malbec, S. Gravemann, E. Billerbeck, M. Dorner, H. Büning, O. Schwartz,

E. Knops, R. Kaiser, M. S. Seaman, J. M. Wilson, C. M. Rice, A. Ploss, P. J. Bjorkman, F. Klein, and M. C. Nussenzweig. HIV-1 suppression and durable control by combining single broadly neutralizing antibodies and antiretroviral drugs in humanized mice. *Proc Natl Acad Sci U S A*, 110(41):16538–43, Oct 2013. doi: 10.1073/pnas.1315295110.

23. J. Huang, G. Ofek, L. Laub, M. K. Louder, N. A. Doria-Rose, N. S. Longo, H. Imamichi, R. T. Bailer, B. Chakrabarti, S. K. Sharma, S. M. Alam, T. Wang, Y. Yang, B. Zhang, S. A. Migueles, R. Wyatt, B. F. Haynes, P. D. Kwong, J. R. Mascola, and M. Connors. Broad and potent neutralization of HIV-1 by a gp41-specific human antibody. *Nature*, 491(7424):406–12, Nov 2012. doi: 10.1038/nature11544.

24. J. Huang, B. H. Kang, M. Pancera, J. H. Lee, T. Tong, Y. Feng, H. Imamichi, I. S. Georgiev, G.-Y. Chuang, A. Druz, N. A. Doria-Rose, L. Laub, K. Sliepen, M. J. van Gils, A. T. de la Peña, R. Derking, P.-J. Klasse, S. A. Migueles, R. T. Bailer, M. Alam, P. Pugach, B. F. Haynes, R. T. Wyatt, R. W. Sanders, J. M. Binley, A. B. Ward, J. R. Mascola, P. D. Kwong, and M. Connors. Broad and potent HIV-1 neutralization by a human antibody that binds the gp41-gp120 interface. *Nature*, 515(7525):138–42, Nov 2014. doi: 10.1038/nature13601.

25. B. L. Jilek, M. Zarr, M. E. Sampah, S. A. Rabi, C. K. Bullen, J. Lai, L. Shen, and R. F. Siliciano. A quantitative basis for antiretroviral therapy for HIV-1 infection. *Nat Med*, 18(3):446–51, Mar 2012. doi: 10.1038/nm.2649.

26. J.-P. Julien, J. H. Lee, A. Cupo, C. D. Murin, R. Derking, S. Hoffenberg, M. J. Caulfield, C. R. King, A. J. Marozsan, P. J. Klasse, R. W. Sanders, J. P. Moore, I. A. Wilson, and A. B. Ward. Asymmetric recognition of the HIV-1 trimer by broadly neutralizing antibody PG9. *Proc Natl Acad Sci U S A*, 110(11):4351–6, Mar 2013. doi: 10.1073/pnas.1217537110.

27. T. J. Ketas, S. Holuigue, K. Matthews, J. P. Moore, and P. J. Klasse. Env-glycoprotein

heterogeneity as a source of apparent synergy and enhanced cooperativity in inhibition of HIV-1 infection by neutralizing antibodies and entry inhibitors. *Virology*, 422(1): 22–36, Jan 2012. doi: 10.1016/j.virol.2011.09.019.

28. F. Klein, A. Halper-Stromberg, J. A. Horwitz, H. Gruell, J. F. Scheid, S. Bournazos, H. Mouquet, L. A. Spatz, R. Diskin, A. Abadir, T. Zang, M. Dorner, E. Billerbeck, R. N. Labitt, C. Gaebler, P. M. Marcovecchio, R.-B. Incesu, T. R. Eisenreich, P. D. Bieniasz, M. S. Seaman, P. J. Bjorkman, J. V. Ravetch, A. Ploss, and M. C. Nussenzweig. HIV therapy by a combination of broadly neutralizing antibodies in humanized mice. *Nature*, 492(7427):118–22, Dec 2012. doi: 10.1038/nature11604.

29. F. Klein, L. Nogueira, Y. Nishimura, G. Phad, A. P. West, Jr, A. Halper-Stromberg, J. A. Horwitz, A. Gazumyan, C. Liu, T. R. Eisenreich, C. Lehmann, G. Fätkenheuer, C. Williams, M. Shingai, M. A. Martin, P. J. Bjorkman, M. S. Seaman, S. Zolla-Pazner, G. B. Karlsson Hedestam, and M. C. Nussenzweig. Enhanced HIV-1 immunotherapy by commonly arising antibodies that target virus escape variants. *J Exp Med*, 211(12): 2361–72, Nov 2014. doi: 10.1084/jem.20141050.

30. J. S. Klein and P. J. Bjorkman. Few and far between: how HIV may be evading antibody avidity. *PLoS Pathog*, 6(5):e1000908, May 2010. doi: 10.1371/journal.ppat.1000908.

31. R. Kong, M. K. Louder, K. Wagh, R. T. Bailer, A. deCamp, K. Greene, H. Gao, J. D. Taft, A. Gazumyan, C. Liu, M. C. Nussenzweig, B. Korber, D. C. Montefiori, and J. R. Mascola. Improving Neutralization Potency and Breadth by Combining Broadly Reactive HIV-1 Antibodies Targeting Major Neutralization Epitopes. *J Virol*, 89(5): 2659–71, Mar 2015. doi: 10.1128/JVI.03136-14.

32. S. B. Laskey and R. F. Siliciano. A mechanistic theory to explain the efficacy of antiretroviral therapy. *Nat Rev Microbiol*, 12(11):772–80, Nov 2014. doi: 10.1038/nrmicro3351.

33. H. Li, K. J. Bar, S. Wang, J. M. Decker, Y. Chen, C. Sun, J. F. Salazar-Gonzalez,

M. G. Salazar, G. H. Learn, C. J. Morgan, J. E. Schumacher, P. Hraber, E. E. Giorgi, T. Bhattacharya, B. T. Korber, A. S. Perelson, J. J. Eron, M. S. Cohen, C. B. Hicks, B. F. Haynes, M. Markowitz, B. F. Keele, B. H. Hahn, and G. M. Shaw. High Multiplicity Infection by HIV-1 in Men Who Have Sex with Men. *PLoS Pathog*, 6(5):e1000890, May 2010. doi: 10.1371/journal.ppat.1000890.

34. M. Li, F. Gao, J. R. Mascola, L. Stamatatos, V. R. Polonis, M. Koutsoukos, G. Voss, P. Goepfert, P. Gilbert, K. M. Greene, M. Bilska, D. L. Kothe, J. F. Salazar-Gonzalez, X. Wei, J. M. Decker, B. H. Hahn, and D. C. Montefiori. Human immunodeficiency virus type 1 env clones from acute and early subtype B infections for standardized assessments of vaccine-elicited neutralizing antibodies. *J Virol*, 79(16):10108–25, Aug 2005. doi: 10.1128/JVI.79.16.10108-10125.2005.

35. Y. Li, S. O'Dell, L. M. Walker, X. Wu, J. Guenaga, Y. Feng, S. D. Schmidt, K. McKee, M. K. Louder, J. E. Ledgerwood, B. S. Graham, B. F. Haynes, D. R. Burton, R. T. Wyatt, and J. R. Mascola. Mechanism of neutralization by the broadly neutralizing HIV-1 monoclonal antibody VRC01. *J Virol*, 85(17):8954–67, Sep 2011. doi: 10.1128/JVI.00754-11.

36. L. E. Limbird and R. J. Lefkowitz. Negative cooperativity among beta-adrenergic receptors in frog erythrocyte membranes. *J Biol Chem*, 251(16):5007–14, Aug 1976.

37. D. Lyumkis, J.-P. Julien, N. de Val, A. Cupo, C. S. Potter, P.-J. Klasse, D. R. Burton, R. W. Sanders, J. P. Moore, B. Carragher, I. A. Wilson, and A. B. Ward. Cryo-EM structure of a fully glycosylated soluble cleaved HIV-1 envelope trimer. *Science*, 342 (6165):1484–90, Dec 2013. doi: 10.1126/science.1245627.

38. A. Manrique, P. Rusert, B. Joos, M. Fischer, H. Kuster, C. Leemann, B. Niederöst, R. Weber, G. Stiegler, H. Katinger, H. F. Günthard, and A. Trkola. In vivo and in vitro

escape from neutralizing antibodies 2G12, 2F5, and 4E10. *J Virol*, 81(16):8793–808, Aug 2007. doi: 10.1128/JVI.00598-07.

39. J. R. Mascola and B. F. Haynes. HIV-1 neutralizing antibodies: understanding nature's pathways. *Immunol Rev*, 254(1):225–44, Jul 2013. doi: 10.1111/imr.12075.

40. S. Mehandru, B. Vcelar, T. Wrin, G. Stiegler, B. Joos, H. Mohri, D. Boden, J. Galovich, K. Tenner-Racz, P. Racz, M. Carrington, C. Petropoulos, H. Katinger, and M. Markowitz. Adjunctive passive immunotherapy in human immunodeficiency virus type 1-infected individuals treated with antiviral therapy during acute and early infection. *J Virol*, 81(20):11016–31, Oct 2007. doi: 10.1128/JVI.01340-07.

41. J. MONOD, J. WYMAN, and J. P. CHANGEUX. ON THE NATURE OF ALLOSTERIC TRANSITIONS: A PLAUSIBLE MODEL. *J Mol Biol*, 12:88–118, May 1965.

42. D. C. Montefiori. Measuring HIV neutralization in a luciferase reporter gene assay. *Methods Mol Biol*, 485:395–405, 2009. doi: 10.1007/978-1-59745-170-3_26.

43. J. P. Moore, J. A. McKeating, R. A. Weiss, and Q. J. Sattentau. Dissociation of gp120 from HIV-1 virions induced by soluble CD4. *Science*, 250(4984):1139–42, Nov 1990.

44. H. N. Motlagh, J. Li, E. B. Thompson, and V. J. Hilser. Interplay between allostery and intrinsic disorder in an ensemble. *Biochem Soc Trans*, 40(5):975–80, Oct 2012. doi: 10.1042/BST20120163.

45. H. N. Motlagh, J. O. Wrabl, J. Li, and V. J. Hilser. The ensemble nature of allostery. *Nature*, 508(7496):331–9, Apr 2014. doi: 10.1038/nature13001.

46. H. Mouquet, L. Scharf, Z. Euler, Y. Liu, C. Eden, J. F. Scheid, A. Halper-Stromberg, P. N. P. Gnanapragasam, D. I. R. Spencer, M. S. Seaman, H. Schuitemaker, T. Feizi, M. C. Nussenzweig, and P. J. Bjorkman. Complex-type N-glycan recognition by potent

broadly neutralizing HIV antibodies. *Proc Natl Acad Sci U S A*, 109(47):E3268–77, Nov 2012. doi: 10.1073/pnas.1217207109.

47. T. Muster, F. Steindl, M. Purtscher, A. Trkola, A. Klima, G. Himmler, F. Rüker, and H. Katinger. A conserved neutralizing epitope on gp41 of human immunodeficiency virus type 1. *J Virol*, 67(11):6642–7, Nov 1993.

48. M. Perutz. *Mechanisms of Cooperativity and Allosteric Regulation in Proteins*. Cambridge University Press, 1 edition, 1990.

49. M. F. Perutz, A. J. Wilkinson, M. Paoli, and G. G. Dodson. The stereochemical mechanism of the cooperative effects in hemoglobin revisited. *Annu Rev Biophys Biomol Struct*, 27:1–34, 1998. doi: 10.1146/annurev.biophys.27.1.1.

50. A. Pizard, J. Marchetti, J. Allegrini, F. Alhenc-Gelas, and R. M. Rajerison. Negative cooperativity in the human bradykinin B2 receptor. *J Biol Chem*, 273(3):1309–15, Jan 1998.

51. E. J. Platt, K. Wehrly, S. E. Kuhmann, B. Chesebro, and D. Kabat. Effects of CCR5 and CD4 cell surface concentrations on infections by macrophagetropic isolates of human immunodeficiency virus type 1. *J Virol*, 72(4):2855–64, Apr 1998.

52. L. K. Pritchard, D. I. R. Spencer, L. Royle, S. Vasiljevic, S. A. Krumm, K. J. Doores, and M. Crispin. Glycan Microheterogeneity at the PGT135 Antibody Recognition Site on HIV-1 gp120 Reveals a Molecular Mechanism for Neutralization Resistance. *J Virol*, 89(13):6952–9, Jul 2015. doi: 10.1128/JVI.00230-15.

53. M. E. S. Sampah, L. Shen, B. L. Jilek, and R. F. Siliciano. Dose-response curve slope is a missing dimension in the analysis of HIV-1 drug resistance. *Proc Natl Acad Sci U S A*, 108(18):7613–8, May 2011. doi: 10.1073/pnas.1018360108.

54. M. Sarzotti-Kelsoe, R. T. Bailer, E. Turk, C.-l. Lin, M. Bilska, K. M. Greene, H. Gao, C. A. Todd, D. A. Ozaki, M. S. Seaman, J. R. Mascola, and D. C. Montefiori. Optimization and validation of the TZM-bl assay for standardized assessments of neutralizing antibodies against HIV-1. *J Immunol Methods*, 409:131–46, Jul 2014. doi: 10.1016/j.jim.2013.11.022.

55. Q. J. Sattentau and J. P. Moore. Conformational changes induced in the human immunodeficiency virus envelope glycoprotein by soluble CD4 binding. *J Exp Med*, 174(2): 407–15, Aug 1991.

56. C. N. Scanlan, R. Pantophlet, M. R. Wormald, E. Ollmann Saphire, R. Stanfield, I. A. Wilson, H. Katinger, R. A. Dwek, P. M. Rudd, and D. R. Burton. The broadly neutralizing anti-human immunodeficiency virus type 1 antibody 2G12 recognizes a cluster of alpha1–¿2 mannose residues on the outer face of gp120. *J Virol*, 76(14):7306–21, Jul 2002.

57. L. Scharf, J. F. Scheid, J. H. Lee, A. P. West, Jr, C. Chen, H. Gao, P. N. P. Gnanapragasam, R. Mares, M. S. Seaman, A. B. Ward, M. C. Nussenzweig, and P. J. Bjorkman. Antibody 8ANC195 reveals a site of broad vulnerability on the HIV-1 envelope spike. *Cell Rep*, 7(3):785–95, May 2014. doi: 10.1016/j.celrep.2014.04.001.

58. J. F. Scheid, H. Mouquet, B. Ueberheide, R. Diskin, F. Klein, T. Y. K. Oliveira, J. Pietzsch, D. Fenyo, A. Abadir, K. Velinzon, A. Hurley, S. Myung, F. Boulad, P. Poignard, D. R. Burton, F. Pereyra, D. D. Ho, B. D. Walker, M. S. Seaman, P. J. Bjorkman, B. T. Chait, and M. C. Nussenzweig. Sequence and structural convergence of broad and potent HIV antibodies that mimic CD4 binding. *Science*, 333(6049):1633–7, Sep 2011. doi: 10.1126/science.1207227.

59. L. Shen, S. Peterson, A. R. Sedaghat, M. A. McMahon, M. Callender, H. Zhang, Y. Zhou, E. Pitt, K. S. Anderson, E. P. Acosta, and R. F. Siliciano. Dose-response curve slope

sets class-specific limits on inhibitory potential of anti-HIV drugs. *Nat Med*, 14(7):762–6, Jul 2008. doi: 10.1038/nm1777.

60. L. Shen, S. A. Rabi, and R. F. Siliciano. A novel method for determining the inhibitory potential of anti-HIV drugs. *Trends Pharmacol Sci*, 30(12):610–6, Dec 2009. doi: 10.1016/j.tips.2009.09.003.

61. M. Shingai, Y. Nishimura, F. Klein, H. Mouquet, O. K. Donau, R. Plishka, A. Buckler-White, M. Seaman, M. Piatak, Jr, J. D. Lifson, D. S. Dimitrov, M. C. Nussenzweig, and M. A. Martin. Antibody-mediated immunotherapy of macaques chronically infected with SHIV suppresses viraemia. *Nature*, 503(7475):277–80, Nov 2013. doi: 10.1038/nature12746.

62. D. Sok, K. J. Doores, B. Briney, K. M. Le, K. L. Saye-Francisco, A. Ramos, D. W. Kulp, J.-P. Julien, S. Menis, L. Wickramasinghe, M. S. Seaman, W. R. Schief, I. A. Wilson, P. Poignard, and D. R. Burton. Promiscuous glycan site recognition by antibodies to the high-mannose patch of gp120 broadens neutralization of HIV. *Sci Transl Med*, 6(236):236ra63, May 2014. doi: 10.1126/scitranslmed.3008104.

63. Y. Suzuki, E. Moriyoshi, D. Tsuchiya, and H. Jingami. Negative cooperativity of glutamate binding in the dimeric metabotropic glutamate receptor subtype 1. *J Biol Chem*, 279(34):35526–34, Aug 2004. doi: 10.1074/jbc.M404831200.

64. C. A. Todd, K. M. Greene, X. Yu, D. A. Ozaki, H. Gao, Y. Huang, M. Wang, G. Li, R. Brown, B. Wood, M. P. D'Souza, P. Gilbert, D. C. Montefiori, and M. Sarzotti-Kelsoe. Development and implementation of an international proficiency testing program for a neutralizing antibody assay for HIV-1 in TZM-bl cells. *J Immunol Methods*, 375(1-2):57–67, Jan 2012. doi: 10.1016/j.jim.2011.09.007.

65. A. Trkola, H. Kuster, P. Rusert, B. Joos, M. Fischer, C. Leemann, A. Manrique, M. Huber, M. Rehr, A. Oxenius, R. Weber, G. Stiegler, B. Vcelar, H. Katinger, L. Aceto,

and H. F. Günthard. Delay of HIV-1 rebound after cessation of antiretroviral therapy through passive transfer of human neutralizing antibodies. *Nat Med*, 11(6):615–22, Jun 2005. doi: 10.1038/nm1244.

66. A. Trkola, H. Kuster, P. Rusert, V. von Wyl, C. Leemann, R. Weber, G. Stiegler, H. Katinger, B. Joos, and H. F. Günthard. In vivo efficacy of human immunodeficiency virus neutralizing antibodies: estimates for protective titers. *J Virol*, 82(3):1591–9, Feb 2008. doi: 10.1128/JVI.01792-07.

67. L. M. Walker, S. K. Phogat, P.-Y. Chan-Hui, D. Wagner, P. Phung, J. L. Goss, T. Wrin, M. D. Simek, S. Fling, J. L. Mitcham, J. K. Lehrman, F. H. Priddy, O. A. Olsen, S. M. Frey, P. W. Hammond, Protocol G Principal Investigators, S. Kaminsky, T. Zamb, M. Moyle, W. C. Koff, P. Poignard, and D. R. Burton. Broad and potent neutralizing antibodies from an African donor reveal a new HIV-1 vaccine target. *Science*, 326(5950): 285–9, Oct 2009. doi: 10.1126/science.1178746.

68. L. M. Walker, M. Huber, K. J. Doores, E. Falkowska, R. Pejchal, J.-P. Julien, S.-K. Wang, A. Ramos, P.-Y. Chan-Hui, M. Moyle, J. L. Mitcham, P. W. Hammond, O. A. Olsen, P. Phung, S. Fling, C.-H. Wong, S. Phogat, T. Wrin, M. D. Simek, Protocol G Principal Investigators, W. C. Koff, I. A. Wilson, D. R. Burton, and P. Poignard. Broad neutralization coverage of HIV by multiple highly potent antibodies. *Nature*, 477(7365): 466–70, Sep 2011. doi: 10.1038/nature10373.

69. X. Wei, J. M. Decker, H. Liu, Z. Zhang, R. B. Arani, J. M. Kilby, M. S. Saag, X. Wu, G. M. Shaw, and J. C. Kappes. Emergence of resistant human immunodeficiency virus type 1 in patients receiving fusion inhibitor (T-20) monotherapy. *Antimicrob Agents Chemother*, 46(6):1896–905, Jun 2002.

70. X. Wu, Z.-Y. Yang, Y. Li, C.-M. Hogerkorp, W. R. Schief, M. S. Seaman, T. Zhou, S. D. Schmidt, L. Wu, L. Xu, N. S. Longo, K. McKee, S. O'Dell, M. K. Louder, D. L. Wycuff,

Y. Feng, M. Nason, N. Doria-Rose, M. Connors, P. D. Kwong, M. Roederer, R. T. Wyatt, G. J. Nabel, and J. R. Mascola. Rational design of envelope identifies broadly neutralizing human monoclonal antibodies to HIV-1. *Science*, 329(5993):856–61, Aug 2010. doi: 10.1126/science.1187659.

71. X. Wu, T. Zhou, J. Zhu, B. Zhang, I. Georgiev, C. Wang, X. Chen, N. S. Longo, M. Louder, K. McKee, S. O'Dell, S. Perfetto, S. D. Schmidt, W. Shi, L. Wu, Y. Yang, Z.-Y. Yang, Z. Yang, Z. Zhang, M. Bonsignori, J. A. Crump, S. H. Kapiga, N. E. Sam, B. F. Haynes, M. Simek, D. R. Burton, W. C. Koff, N. A. Doria-Rose, M. Connors, NISC Comparative Sequencing Program, J. C. Mullikin, G. J. Nabel, M. Roederer, L. Shapiro, P. D. Kwong, and J. R. Mascola. Focused evolution of HIV-1 neutralizing antibodies revealed by structures and deep sequencing. *Science*, 333(6049):1593–602, Sep 2011. doi: 10.1126/science.1207532.

72. A. Yasmeen, R. Ringe, R. Derking, A. Cupo, J.-P. Julien, D. R. Burton, A. B. Ward, I. A. Wilson, R. W. Sanders, J. P. Moore, and P. J. Klasse. Differential binding of neutralizing and non-neutralizing antibodies to native-like soluble HIV-1 Env trimers, uncleaved Env proteins, and monomeric subunits. *Retrovirology*, 11:41, 2014. doi: 10.1186/1742-4690-11-41.

73. M. B. Zwick, A. F. Labrijn, M. Wang, C. Spenlehauer, E. O. Saphire, J. M. Binley, J. P. Moore, G. Stiegler, H. Katinger, D. R. Burton, and P. W. Parren. Broadly neutralizing antibodies targeted to the membrane-proximal external region of human immunodeficiency virus type 1 glycoprotein gp41. *J Virol*, 75(22):10892–905, Nov 2001. doi: 10.1128/JVI.75.22.10892-10905.2001.

CHAPTER 3

Disulfide Isomerization is a Novel HIV-1 Entry Target

Introduction

The wide variety of modern inhibitor classes and combination strategies have dramatically transformed the clinical prospects of HIV patients. No longer a death sentence, HIV infection is now a chronic condition under which patients can live relatively normal and otherwise healthy lives. The persistent nature of HIV infection, however, presents its own challenges such as the emergence of drug resistance. Although modern treatments can maintain undetectable viral loads in patients, low levels of replication and evolution persist that can give rise to resistant variants[1,2]. For example, the first clinically approved entry inhibitor, enfuvirtide (ENF), is a small peptide that blocks 6HB formation by binding to the pre-hairpin intermediate of gp41 (Fig. 1.1) and resistance is acquired through mutations in both the target HR1 and non-target HR2 regions[3,4]. Maraviroc is a CCR5 antagonist approved as a front-line treatment for HIV infection and direct resistance involves an adaptation of HIV Env that recognizes and uses the MVC-bound form of CCR5 as a functional co-receptor[5–7]. Combination therapy has proven to be a very effective strategy, as isolates resistant to one inhibitor have a severely reduced landscape of possible mutations that can also confer resistance to other inhibitors, however, until a *bona fide* cure for HIV is discovered there will always be a need for inhibitors that target novel features of HIV to fight isolates that have become resistant to existing therapies.

Target conservation is an important consideration in the context of drug resistance as highly conserved targets typically have functional roles so essential that even minor escape mutations can render the virus non-infectious. Although enveloped viruses employ a diverse array of specific mechanisms that facilitate target cell entry, these mechanisms have a conserved theme that separates the processes of attachment and fusion through the careful coordination of transition states in Env. In many cases, fusion is triggered by the isomerization or cleavage of rigid disulfide bonds (DSB) in a highly conserved process that can be targeted. For example, many β, δ and γ retrovirus Envs carry their own canonical disulfide

isomerase motifs that trigger 6HB formation, while some α retroviruses and lentiviruses like HIV are thought to employ disulfide isomerase proteins retained at target cell surfaces[8]. In the case of HIV, a significant body of evidence implicates protein disulfide isomerase (PDI) as the cellular component involved in cleaving (reducing) DSBs in HIV Env during entry[9–22].

PDI is an attractive inhibitor target because it is involved with viral entry, a drug-accessible extracellular process and because its involvement is based on the reduction, or cleavage, of at least two of the nine DSBs in HIV gp120[14] whose position and number are conserved among all naturally occurring HIV isolates in the Los Alamos HIV sequence database. However, PDI is essential to cell viability due to its primary role in folding nascent peptides in the endoplasmic reticulum (ER). Most small-molecule PDI inhibitors are both cell-permeable and react in a non-specific way with other members of the broad disulfide isomerase family (such as thioredoxin) as well as non-disulfide, electrophilic moieties. Thus, while PDI inhibitors may target a conserved mechanisms in HIV entry, they may also be highly toxic to living cells. Additionally, more specific PDI reductase inhibitors, such as bacitracin[23], often exhibit contaminant protease activity[24] and exist in a variety of unique isoforms[25] that confound the specific determination of inhibitor efficacy and PDI's role in HIV entry.

The primary aim of this chapter is to distinguish the specific effects of PDI inhibitors against HIV entry from their non-specific, confounding effects, such as toxicity and contamination. In an effort to regulate the reduction/oxidation (redox) potential of the cell surface, we first develop a series of assays to examine the redox state of surface-retained PDI, as only the reduced form of PDI is capable of cleaving DSBs during HIV entry. We then quantify the activity of specific PDI reductase inhibitors against HIV entry relative to their non-specific confounding effects such as contaminant protease activity and cytotoxicity. Our results give promise to the continued development and investigation of novel PDI inhibitors as potential treatments for HIV infection with low resistance potential and reveal specific criteria for the development of more potent, less toxic PDI inhibitor compounds.

Protein disulfide isomerase function and activity. PDI is but one member of a large superfamily of thioredoxin proteins that mediate the reduction, oxidation and isomerization of DSBs on other proteins[26,27]. PDI forms a horseshoe-like shape consisting of four classical thioredoxin fold domains a, b, a' and b' where the ab and b'a' regions are joined by a flexible linker region (x, Fig. 3.1a). While the b' domain is principally involved in substrate binding, the a and a' domains have canonical CXXC DSB isomerization motifs that form two active sites. The N-terminal active site cysteine of the a domain is stabilized as a thiolate anion by the pKa of the local histidine imidazole[28] (Fig, 3.1a, inset).

Although generally inert in solution, DSBs are highly labile in the presence of strong nucleophiles. PDI accepts DSBs from substrates through its nucleophilic N-terminal thiolate, which attacks an electrophilic sulfur in the substrate DSB (Fig. 3.1b). This not only cleaves the substrate DSB to free the linked regions, but results in a new DSB that connects the substrate to PDI's active site. Full DSB transfer is completed when the secondary, C-terminal cysteine performs the same nucleophilic attack on the PDI-substrate DSB. Importantly, this activity is not enzymatic as PDI cannot return to its initial, reduced state until the accepted DSB is transferred elsewhere, through the reverse of this same mechanism.

The direction and thermodynamic properties of PDI activity are governed in the ER by local concentrations of DSB acceptors (glutathione, GSH) and DSB donors (glutathione disulfide, GSSG) where a disproportionate balance of GSSG generated by Ero1 favors the transfer of DSBs to PDI, which then transfers those DSBs to nascent peptides[28]. Although PDI is primarily an ER-resident protein, it is secreted through an unknown pathway and can be retained at cell surfaces[9,29–32]. While the full complement of proteins involved in the surface-retention of PDI is unknown, Galectin-9 (Gal-9), an immunoregulatory lectin[33,34], has been shown to retain PDI at the surface of T-cells[9]. The extracellular milieu is highly oxidizing, and the majority of possible protein substrates already have well-formed DSBs, thus, at the cell surface, PDI primarily acts as a DSB reductase (as described in Fig 3.1b) that regulates a variety of functions including platelet adhesion and lymphocyte migration[9,29–32].

Without a carefully controlled balance of DSB acceptors and donors, ongoing reductase activity at the cell surface requires the continued secretion of reduced, DSB-accepting PDI.

PDI inhibitors come in three general flavors. Small, cell impermeable molecules like 5,5'-dithiobis(2-nitrobenzoic acid) (DTNB) act as DSB donors that readily oxidize reduced PDI, inhibiting reductase activity by saturation. Alternatively, the strong nucleophilicity of the N-terminal thiolate can be exploited by electrophilic alkylating agents like n-ethylmaleimide (NEM, Fig. 3.1c). These reagents trap PDI in an intermediate state that is not electrophilic enough for secondary thiolate attack. PDI antibodies can also be used to prevent substrate binding in a manner that is independent of the PDI active site. While PDI antibodies are highly specific, inhibitors such as DTNB and NEM are reactive toward all proteins of the thioredoxin superfamily and many alkylating agents (like NEM) also react with other nucleophilic moieties such as amine side chains.

Bacitracin is an antimicrobial, cyclic polypeptide that exists as a mixture of at least 11 different isoforms varying in side chain composition and it is also specific inhibitor of PDI reductase, but not oxidase, activity[23,25]. Bacitracin is thought to inhibit PDI through nucleophilic attack of an opened, terminal thiazoline ring with DSBs in the b' and x-linker region of PDI[25], which likely reduces the substrate-binding capacity of the b' domain. Accordingly, the potency of bacitracin against PDI is isoform dependent, as isoforms with the more water-labile keto-thiazole moiety (isoforms H and F) are more active than those with the alternative amino-thiazoline moiety (isoforms A and B). While PDI antibodies, small molecule PDI inhibitors and bacitracin are all known to inhibit HIV infection[11,13–16], the specificity of bacitracin isoforms and potential intracellular, toxic effects of small molecule inhibitors have not been thoroughly investigated. Indeed, the majority of experiments describing bacitracin as an inhibitor of HIV infection employ commercial preparations of unknown isoform composition that may also exhibit a contaminating protease activity[24] against HIV Env or PDI itself. Both protease activity and cytotoxicity can have a strong confounding effect on estimated potencies and can complicate the investigation of PDI's role in HIV entry.

Structural biology of gp120 disulfide bonds. PDI is thought to be important in HIV entry by reducing rigid disulfide bonds in HIV Env to facilitate conformational change. The HIV attachment protein gp120 contains a total of 19 conserved cysteine residues of which 18 are known to pair into 9 highly conserved disulfide bonds (DSB) (Fig. 3.2a and b). The regions between DSBs 3, 4, 7 and 9 form variable loops 1-4 (V1-V4) while DSBs 2 and 8 help form the bridging sheet, which divides the inner, core region of gp120 from the more exposed outer region in the context of the trimeric spike (Fig. 3.2b). V1-V4 form large patches of exposed surface antigen and also provide shifting glycosylation sites that form the glycan shield[35]. The conserved position of the V1-V4 DSBs likely contribute to Envs high functional tolerance for the changes in length, sequence and glycosylation these regions are well known for. Furthermore, DSBs 1 and 5 lie deep within the trimer core near gp41, suggesting important roles in stabilizing the gp120/gp41 interface. Alanine substitution of cysteine residues forming the majority of these DSBs generally result in folding or incorporation defects. Of note, removal of DSBs 2 and 8 yield functional virion that are more sensitive to sCD4 and co-receptor antagonists[36], respectively, indicating a potential role for these DSBs in HIV entry.

The entry mechanism involves a highly concerted and tightly regulated series of conformational changes in gp120. Chemical cleavage of the DSBs in gp120 follow a progressive trend that spans a 10,000-fold range of reductant concentration (β-mercaptoethanol)[14], thus, each DSB exhibits a unique redox potential and susceptibility to cleavage. Accordingly, the two major stages of attachment: CD4 and co-receptor binding, are associated with a progressive reduction of up to two DSBs in monomeric gp120[14]. Disulfide reducing proteins such as PDI and thioredoxin (Trx) are known to interact with monomeric gp120 at critical sites near DSBs 3, 4, 8 and are capable of reducing DSBs 1, 2, 4, 8 and 9[37,38], in solution and in the absence of cells. Both PDI and Trx have been implicated as critical components of entry that facilitate DSB reduction[11,13–16,37], which in turn, is thought to facilitate the gp120 structural transitions that must occur during entry[14]. Whether PDI, Trx or any

other disulfide reductase can serve as a primary clinical target will depend on the specific environmental circumstances that govern their secretion and cell-surface retention in the context of inflammation[9,33], T-cell activation and the trimeric, glycosylated Env. Thus, the finding that PDI can be retained by an immunoregulatory lectin[9] connects specific cellular mechanisms that facilitate entry to the broader context of pathology. These data offer a novel perspective where the conformational changes that occur in Env during entry might be viewed as a progressive decomposition, or unraveling, of gp120 as opposed to a transition between rigidly defined structural states. Most importantly, the functional necessity of these DSBs and their cleavage during entry make them prime targets for entry inhibitors that are likely to have a very low resistance potential.

Specific Aims. The function performed by PDI at the cell surface is highly generalized as an overall local redox potential, thus, surface PDI reductase activity is not specifically directed toward HIV entry but represents a local chemical environment that facilitates entry. The role of disulfide isomerization in HIV entry is largely supported by inhibition experiments using bacitracin or non-specific thiol alkylating agents and DSB donors[9,11,13–16] as well as the direct measurement of DSB cleavage on monomeric gp120[14]. To date, no study has described the essential connection between overall cell-surface redox potential and HIV entry, which will be necessary to understand the broader context of inflammatory states and HIV entry susceptibility, particularly in the event that multiple or alternative disulfide reductases are involved. Furthermore, the toxic effects of membrane permeable PDI inhibitors and protease contaminants found in commercial bacitracin have not been thoroughly described in the context of HIV entry.

The first aim of this study is to lay the groundwork for tools that can be used to assess overall cell-surface redox potential, which will be essential for understanding potential connections between inflammatory states and entry susceptibility that have been described[9,33]. Through these studies we describe a novel phenotype of surface PDI expression that is rel-

evant to quantifying the importance of PDI activity in HIV entry. The second aim of this study is to assess the inhibitory activities of a commercial bacitracin mixture, two purified bacitracin isoforms representing both the more PDI-active keto-thiazole and less active amino-thiazoline terminal moieties (isoforms F and A, respectively) as well as a novel, specific inhibitor of PDI: 16F16, which was discovered in a screen of compounds that prevent huntington protein misfolding[39]. Finally, these inhibitory activities are compared to their toxic and potential contaminant effects to formally address the specific effects of PDI inhibition against HIV entry. Our results help to clarify ongoing specificity issues in the field[24] and give promise to the continued development of novel, cell impermeable PDI inhibitors as potential HIV therapeutics.

Materials and Methods

Cells and reagents. All cells were cultured in RPMI 1640 medium supplemented with 10% fetal bovine serum (v/v) and 100μg/mL penicillin and streptomycin. CEM, and PM1 cells were a kind gift from Linda Baum (UCLA, Dept. of Pathology and Laboratory Medicine). Monocyte-derived macrophages (MDM) were produced from Ficoll-purified PBMCs cultured for 5 days in culture medium supplemented with 50 ng/mL granulocyte macrophage colony-stimulating factor. Recombinant human Galectin-9 was purchased from R&D systems (Cat #2045-GA). 5,5'-dithiobis(2-nitrobenzoid acid) (DTNB, Cat #D218200), Tris(2-carboxyethyl) phosphine (TCEP, Cat #646547) and n-ethylmaleimide (NEM, Cat #E3876) and biotin maleimide (Cat #B1267) were purchased from Sigma Aldrich. Bacitracin mixture (Bac-STD, Cat#B0125) and bacitracin A isoform (BacA-Vet, VETRANAL^{TM} grade, Cat #31626) were purchased from Sigma Aldrich while the purified A (BacA-Evo, Cat#B015) and F (BacF-Evo, Cat #B021) were purchased from TOKU-E. 16F16[39] was purchased from Sigma Aldrich (Cat #SML0021). PDI antibody (clone RL77) was purchased from AbCam (Cat #ab5484). Gal-9 antibody (clone ECA8) was purchased from MBL International (Cat #D192-3).

Galectin-9 treatment and flow cytometry. Recombinant human Galectin-9 was added to cells in culture to achieve a final concentration of 0.1μM after which cells were incubated for 2 hours at 37°C. All flow staining samples (Galectin-9 treated and untreated) were washed twice in PBS supplemented with 10% (v/v) fetal bovine serum and stained for 1 hour at 4°C with 1:100X RL77 (PDI), Gal-9 antibody or 0.5mM biotin maleimide. After two additional washes, cells were stained with fluorescent-labeled secondary PE-anti mouse (PDI and Gal-9) or streptavidin-APC (thiols) for 1 hour at 4°C, washed and then fixed in 2% paraformaldehyde.

Cell-surface reductase activity. Cell surface reductase activity was measured using a modified Ellman's protocol[40]. Ellman's reagent (2mM DTNB with 50mM sodium acetate in water) was prepared fresh before each use and diluted 1:10 in Tris buffer (pH 8.0). A minimum of 2.5×10^5 cells were pelleted at 1250rpm for 5 minutes and washed with PBS twice. Cells were resuspended in 200-300μL diluted Ellman's reagent and incubated at room temperature for 10 minutes. Cells were pelleted and 90μL supernatant was transferred to transparent 384-well plates. 412nm absorbance was read using a TECAN Infinite® microplate reader.

Virus production and inhibitor assays. HIV Envelopes BaL.26 and III_B were obtained through the HIV AIDS Reagent Program, Division of AIDS, NIAID, NIH. Envelopes were pseudotyped using the pSG3$^{\Delta env}$ backbone (AIDS Reagent Program) where Gaussia Luciferase was cloned in place of HIV Nef (pSG3$^{\Delta env}$Gluc). Pseudovirus was prepared by co-transfection of 293T cells with a 1:1 molar ratio of pSG3$^{\Delta env}$Gluc and either BaL.26 or IIIB Env DNA using BioT transfection reagent according to manufacturer protocols (Bioland Scientific, Paramount, CA). 72 hours post-transfection viral supernatant was collected and clarified by centrifugation at 1250rpm for 5 minutes at 4°C. Virus samples were quantified by titration on Ghost Hi-R5 cells as described previously[41].

Inhibition assays. Cells were treated with inhibitors for 10 minutes at room temperature and inoculated with pseudovirus at a multiplicity of infection of 0.2. Treated and inoculated cells were centrifuged at 2,000rpm for 2 hours at 37°C, washed, and resuspended in fresh culture medium. Cells were cultured for 48 hours at 37°C. 10μL culture supernatant was combined with 10μL Gaussia Lysis Buffer (GLB: 50mM Tris-HCL, pH 7.5, 20% glycerol (v/v), 0.1% TritonX-100 (v/v) and 10mM DTT) in black 96-well plates. Gaussia luciferase activity was measured using Coelenterazine substrate according to manufacturer's specifications (NEB, Ipswich, MA). Gaussia luciferase-catalyzed bioluminescence was read using a TECAN Infinite® microplate reader with an integration time of 8 seconds.

Inhibitor toxicity assays. Toxicity was measured using the Pierce LDH Cytotoxicity Assay Kit (Thermo Scientific, Carlsbad, CA) according to the manufacturer's protocol. Briefly, 50μL culture supernatant was transferred to a clear 96-well plate and 50μL lyophilizate reaction mixture was added and incubated for 30 minutes at room temperature. After adding 50μL stop solution absorbance was read at 490nm and 680nm using a TECAN Infinite® microplate reader.

Results

Retention and modulation of PDI activity at the cell surface. Although PDI is considered an ER-resident protein, it is also secreted to the cell surface where it creates a localized DSB reducing environment[42] that activates membrane-bound integrins to facilitate cell adhesion and migration[9,29–32]. This reducing environment is also thought to reduce DSBs in gp120 to facilitate entry[9–22]. PDI exhibits both an oxidase (DSB forming) and reductase (DSB cleaving) activity where only the reductase activity participates in HIV entry. It is, therefore, necessary to distinguish between surface-bound, reducing PDI and total surface-bound PDI.

We first set out to develop a series of tools that could be used to modulate and quantify

cell-surface reductase activity in the more chemically descriptive context of redox potential. 5,5'-Dithiobis(2-nitrobenzoic acid) (DTNB, or Ellman's reagent[40]) is a cell-impermeable disulfide reductase indicator containing two absorbing 2-nitro-5-thiobenzoate (TNB^-) moieties covalently linked by a highly electrophilic disulfide bond. When reduced, the two TNB^- moieties are released and absorb at a stoichiometric ratio of 2 TNB^- for each reduced disulfide bond. To calibrate this system, PM1 cells were treated with the DSB-specific phosphine reducing agent tris(2-carboxyethyl)phosphine (TCEP) or the thiol alkylating agent n-ethylmaleimide (NEM). Figure 3.3a and b illustrate how TCEP and NEM treatment results in an increase or decrease in DTNB-detected surface thiols. DTNB reduction at the cell surface is calibrated to the concentration-dependent reduction of DTNB by cysteine, thus, yielding a chemically defined reference point of cell-surface redox potential. Relative to untreated cells, reduction of the PM1 cell surface by TCEP resulted in a 1.3 to 1.4-fold increase in surface cysteine equivalents while NEM alkylation of free thiols resulted in a 3-fold (1×10^6 PM1 cells) and 13-fold (0.5×10^6 PM1 cells) decrease (Fig. 3.3c). Galectin-9 was previously reported to retain PDI at the surface of T-cells[9]. Accordingly, treatment of monocyte derived macrophages (MDM) with Gal-9 resulted in a 2.8-fold increase in surface reductase activity (Fig. 3.3d), suggesting that Gal-9 also retains reductase-active PDI at the surface of macrophages.

The Gal-9 mediated retention of PDI serves as both an experimental strategy that can be used to modulate cell-surface reductase activity and connects the role of PDI in HIV entry to a broader context of inflammation and pathology. Exogenous Gal-9 was retained at the surface of PM1 and CEM T-cell lines while monocyte derived macrophages (MDM) endogenously expressed low levels of surface Gal-9 (Figure 3.4a). Unlike previous reports[9], we observed that PDI was only expressed at the surface of a minor subpopulation of cells (Fig. 3.4b, middle). While Gal-9 did not increase the surface expression of PDI ubiquitously, it did result in a 2-3 fold increase in the size of the PDI^+ population (Fig. 3.4b, right) without dramatically changing the quantity of PDI expressed.

Although Gal-9 only increased the size of the minor PDI^+ subpopulation, exogenous Gal-9 was ubiquitously retained at the surface of PM1 cells and could be removed after washing with 100mM lactose (Fig 3.4c, left). The Gal-9 mediated increase in the PDI^+ population was also lactose-dependent (Fig 3.4c, middle), suggesting that this effect is both Gal-9 specific and temporary. Interestingly, Gal-9 treatment caused an increase in surface thiols, indicative of reductase activity, that was not restricted to the PDI^+ population (Fig 3.4c, right). Furthermore, the removal of Gal-9 with lactose and its associated decrease in the PDI^+ population did not result in a decrease in total cell-surface thiols. These results suggest that Gal-9 has a long-lasting and ubiquitous reductive effect on the PM1 surface.

Although highly sensitive and specific to disulfide reduction, our reductase activity assay cannot distinguish an increase in average surface reductase activity from the increases in the activity of a minor PDI^+ subpopulation. Therefore, the utility and accuracy of this assay depends on the uniform increase in PDI expression that has been reported[9]. Our results describe an alternative phenotype, where Gal-9 increases the size of the PDI^+ subpopulation without causing a ubiquitous increase in the quantity of PDI retained. Because Gal-9 was also associated with a ubiquitous, long-lasting change in the redox potential of PM1 surfaces, it is possible that either a) other disulfide reductases are retained by Gal-9 at the surface of PDI^- cells or b) alternative isoforms of PDI are being retained that could not be detected with the PDI antibody used. These alternative isoforms and heterogenous phenotypes may be the result of cell culture heterogeneity.

We attempted to isolate the PDI^+ subpopulation by obtaining six single-cell clones of the parental PM1 culture. Although we observed the same phenotype, the native size of the PDI^+ population was much lower and Gal-9 treatment resulted in a much more dramatic increase in the size of this population than the parental culture (Fig. 3.5a). However, none of the clones exhibited a ubiquitous Gal-9 mediated increase in total surface PDI. We also found that Gal-9 treatment had significant toxic effects, likely related to its biological role in stimulating T-cell apoptosis[33,34]. In one experiment, Gal-9 had a dramatic effect

on flow cytometry collection rates of the PM1 clones, which can serve as a crude estimate of toxicity (Fig 3.5b). In conjunction with this, Gal-9 caused a dramatic change in the light scattering properties of these clones (Fig 3.5c) that may also be indicative of apoptotic effects. Gal-9 toxicity was confirmed by direct cell counts after treatment (Fig. 3.5d), where Gal-9 resulted in a 40% decrease in survival for the parental PM1 culture and 40% to 60% decrease in survival for PM1 clones A, C and F. Although not quantified, Gal-9 mediated toxicity was observed for the CEM and Jurkat cell lines as well.

Taken together, these results agree with previous reports[33] that Gal-9 has a long-lasting and ubiquitous effect on the disulfide redox state of a cell surface, however, our results also suggest that PDI may not be the only disulfide reductase retained by Gal-9 or that alternative isoforms of PDI may be at play. Single-cell cloning could not isolate the Gal-9 refractory PDI^- population or the native PDI^+ population. Instead, all single-cell clones resembled the parental cell culture, suggesting that the Gal-9/PDI phenotype may be the result of epigenetic heterogeneity and/or cell culture conditions. These observations introduce significant complications to experimental approaches aimed at understanding the Gal-9/PDI axis in HIV entry. Although Gal-9 does cause a ubiquitous shift in cell-surface redox potential, this shift could not be associated with PDI specifically. Furthermore, the toxicity observed after Gal-9 treatment leaves open the possibility that enhanced PDI retention may be the result of increased secretion of PDI mediated by large-scale apoptotic effects *in vitro*, which may not be conducive to HIV replication *in vivo*.

PDI Inhibitors are Active Against HIV-1 Entry. The toxicity of Gal-9 and heterogeneous surface retention of PDI precluded the use of Gal-9 to modulate cell-surface PDI retention in the context of HIV entry. However, a variety of inhibitors, specific to PDI and not other thioredoxin family members, can be used to directly interrogate this system. Bacitracin is cyclic polypeptide antimicrobial agent that also acts as a specific inhibitor of PDI reductase activity[23]. Commercial preparations of bacitracin contain a mixture of at least 11

dominant isoforms that vary in their antimicrobial activity, amino acid composition and in a terminal moiety that has been identified as either an amino-thiazoline (isoforms A, B1-B3) or keto-thiazole (isoforms F, H1-H3) ring. This terminal moiety is though to be in equilibrium between a closed and open ring state, where the open ring form exposes a free thiol capable of reducing DSBs in the b' or x-linker region of PDI to inhibit PDI substrate binding[25]. 16F16 is a cell-permeable, small-molecule inhibitor, specific to PDI, discovered in a screen of compounds that inhibit huntington protein misfolding[39]. This compound acts as a thiol alkylating agent in much the same way as NEM, where a highly electrophilic chloroacetyl moiety forms a covalent bond with the PDI active site to prevent further reductase activity[39]. Thus, the inhibitory activity of bacitracin and 16F16 against PDI is driven not by binding affinity, but by the redox potential of their reactive moieties.

We first assessed the activity of a standard commercial bacitracin (Bac-STD) mixture and a commercially purified bacitracin A isoform (BacA-Vet). Both the mixture and purified isoform were active against X4 (III_B) and R5 (BaL) tropic HIV using PM1 and CEM cell lines (Fig. 3.6a). BacA-Vet was slightly more potent than the Bac-STD mixture and also had a higher inhibitory slope (Table 3.1). A more direct comparison of potency could not be obtained due to the fact that the isoform composition of the Bac-STD mixture is unknown. Although the commercial availability of purified bacitracin isoforms is extremely limited, we were able to acquire small quantities of purified bacitracin A and bacitracin F isoforms (BacA-Evo and BacF-Evo, respectively) from a different manufacturer. These samples were 2-4 fold more potent than Bac-STD and BacA-Vet (Table 3.1). Importantly, these bacitracin preparations also exhibited much higher slopes of inhibitory activity, indicating a greater potency at therapeutically relevant inhibitory levels (see Chapter 2). Bac-STD was also active against infection of MDM by the R5-tropic BaL isolate, although a sufficient fit of its inhibitory slope could not be obtained (Table 3.1).

Comparing the potencies of these commercially available bacitracin preparations was problematic due to their unknown composition. While the isoform composition of Bac-

STD is wholly unknown, the BacA-Evo and BacF-Evo preparations were specified by their manufacturers to be 99% pure. Unfortunately, the manufacturer could not provide any evidence of purity. We were able to obtain HPLC chromatograms confirming that the BacA-Vet preparation was 76% pure, however, the identity and composition of the remaining fraction could not be specified. While we cannot directly compare these potencies with certainty, the general range of potencies observed in our results falls between 0.4 to 2mg/mL. Interestingly, both the bacitracin F and A isoforms tested here exhibited similar inhibitory activity, suggesting that both the amino-thiazoline and keto-thiazole forms are equally active.

16F16 was active against both R5 and X4-tropic isolates using PM1 and CEM cells as well as MDM (Fig. 3.6b and c). While the IC_{50}s for bacitracin were on the scale of mg/mL, 16F16 was generally 100 times more potent, with IC_{50}s in the μM range (Fig. 3.6c, right and Table 3.1). 16F16 also exhibited inhibitory slopes that were similar to the more purified forms of bacitracin (2.3-2.7, Table 3.1), however, this slope was dramatically lower with MDM (0.8, Fig. 3.6c, left and Table 3.1). While the increased potency of 16F16 relative to bacitracin may be the result of its more electrophilic moiety and direct mechanism against the PDI active site, the similarity in slope between the purified bacitracin isoforms (A and F) and 16F16 suggest similar mechanisms of HIV entry inhibition, consistent with their specificity for PDI.

Unlike the majority of slope-related topics in this dissertation, the cooperative interpretation of these inhibitory slopes is not justified because the inhibitory mechanisms of bacitracin and 16F16 are not driven by reversible binding. Instead, the slope likely reflects a critical threshold of inhibited PDI molecules that are required to prevent entry[43], thus, the slopes reported here suggest that one to two reducing PDI molecules are necessary to facilitate HIV entry, consistent with the proposed involvement of at least two reduced DSBs in this process[14]. The lower IC_{50} of 16F16 suggest that direct inhibition of the PDI active site is more potent against HIV entry than the inhibition of PDI substrate binding proposed for bacitracin. Further development of 16F16-like inhibitors with better tuned redox potential

and electrophilicity may bring life to a novel class of HIV inhibitors that target this highly conserved entry mechanism.

Toxicity and Contamination of PDI-Specific Inhibitors. The potential contaminant and toxic effects of PDI inhibitors have not yet been described in the context of HIV entry. Bacitracin is produced by *Bacillus subtilis var* Tracy and commercially prepared through chemical extraction techniques that can leave unwanted contaminants. Evidence of serine protease contamination in some commercially available preparations[24] suggest that the inhibitory effects of bacitracin against PDI and HIV entry may not be bacitracin-specific. Furthermore, the use of small-molecule PDI inhibitors that are membrane-permeable, such as 16F16, can inhibit intracellular PDI to produce toxic side effects or result in improper folding of infection reporter proteins.

To assess potential serine protease contamination, we incubated recombinant human PDI with Bac-STD and BacA-Vet (Fig. 3.7a). Bac-STD exhibited strong protease activity capable of degrading PDI in only 20 minutes (compare lanes 1 and 2), while BacA-Vet did not result in any discernible protease activity even after a 60 minute incubation (compare lanes 1 and 3), similar to the BacA-Evo and BacF-Evo preparations (data not shown). Bacitracin is a small, thermostable polypeptide, while proteases are sensitive to thermal denaturing. After boiling, the protease activity of the Bac-STD preparation was eliminated (compare lanes 1 and 2 with lane 4), suggesting that this activity is temperature sensitive and likely due to protease contamination. Boiling caused a slight increase in Bac-STD IC_{50} against HIV infection, suggesting that the protease activity of this preparation may have had a confounding effect on HIV entry (Table 3.1). Interestingly, boiling also increased the slope of Bac-STD to levels that were similar to the other, protease-free preparations, while boiling had no dramatic effect on the slope of BacA-Vet (Table 3.1). The changes in slope observed for Bac-STD suggest that while contaminant protease activity may have conferred an increase in apparent potency, it has a negative impact on slope. This may

be consistent with a stoichiometric, critical threshold interpretation of the slope[43], where the protease contaminant, when unaccounted for in a dose-response analysis, reduces the inhibitory stoichiometry of bacitracin by reducing the quantity of active PDI molecules.

The bacitracin preparations also exhibited significant toxic activity with TD_{50}s falling within a 2-3 fold range if their IC_{50}s (Table 3.1). The cell-permeable 16F16 exhibited toxic activity within the same range despite being more potent than bacitracin (Table 3.1). While the inhibitory and toxic effects of 16F16 do overlap (Fig. 3.7b), up to 60% inhibition was observed before any measurable toxic activity. To analyze the balance of toxic and inhibitory effects for 16F16 more directly, we pre-treated CEM cells for 114, 60 and 26 minutes before washing and spinoculating with HIV III_B. Toxicity was measured directly after a 120 minute spinoculation and infection was measured 48 hours later from the same experimental samples. We compared these results to the standard 16F16 treatment during spinoculation, also performed in the same experiment (spin, Figure 3.7c). Pre-treatment with 16F16 for as little as 20 minutes was sufficient to obtain a full inhibition curve from which slopes of inhibition and toxicity, and an IC_{50} and TD_{50} values could be fit (Fig 3.7c). Both the inhibitory and toxic potency of 16F16 were proportionately time-dependent, indicating both a higher inhibitory and toxic potency with longer treatment times. The best separation between IC_{50} and TD_{50} was obtained while 16F16 was present only during spinoculation (Fig 3.7c, left, spin) and was associated with an increased TD_{50} and not a decreased IC_{50} relative to the pre-treatment equivalent (114 min). This suggests that spinoculation may exacerbate the toxic effect of 16F16 after pre-treatment.

While the slopes of inhibitory activity for 16F16 were time-dependent, the slopes of toxic activity were not (Fig. 3.7c, right). In all cases, the inhibitory slopes for 16F16 were higher than its toxicity slopes, indicating a greater dose-dependent increase in inhibition relative to toxicity. This is illustrated in Figure 3.7d, where the rise in inhibitory activity for both the 114 minute pre-treatment and treatment during spinoculation was much greater than the rise in toxic activity. This is consistent with the difference between inhibiting a limited

quantity of accessible, surface-bound PDI and inducing cytotoxic effects by inhibiting large quantities of intracellular, ER-resident PDI. The increase in slope associated with longer pre-treatment (Fig 3.7c, right) is likely due to continued secretion of reducing, cell-surface PDI during spinoculation in the absence of 16F16, which necessarily results in an increased apparent stoichiometry of inhibition. Accordingly, 16F16 treatment during spinoculation exhibited an inhibitory slope similar to the shortest pre-treatment (26 minutes), suggesting an estimated 30 minute turnover rate for the regeneration of entry-active, reduced PDI. While these interesting differences between inhibitory and toxic slopes are not sufficient to justify direct clinical applications, they do indicate a high potential for novel, cell impermeable analogs.

We have identified that protease contamination of commercially available bacitracin preparations may be a significant confounder in examining the role of PDI in HIV entry by altering the apparent mechanism of inhibition. In addition to contamination, Bac-STD, its purified BacA-Vet isoform and 16F16 exhibited toxic activity that coincided with their inhibitory activity. The toxic activity of 16f16, however, showed a weaker dose-dependent strength that its inhibitory activity, consistent with the cell surface-specific role of PDI in HIV entry. Although toxicity and inhibition were closely related, our results give promise to the development of cell-impermeable analogs of 16F16-like compounds. Importantly, both the keto-thiazole and amino-thiazoline isoforms of bacitracin (F and A, respectively) were active against HIV entry, thus, it is likely that most bacitracin isoforms will also be active, as these are the two predominant terminal moieties. The potencies of bacitracin and 16F16 are not driven by binding affinity but by their fine-tuned redox potential. Our results, therefore, present redox potential and cell permeability as two well-defined criteria for the design of novel analogs with greater efficacy and clinical potential.

Discussion

The enthusiasm for PDI inhibitors as novel HIV therapeutics is well warranted as PDI acts on one of the most conserved structural elements in HIV Env to facilitate entry. Indeed, the potential for PDI-based antivirals extends well beyond HIV[8]. PDI is but one component in a larger system that defines the environmental redox potential of a cell surface, which in turn, may be a critical component of entry susceptibility. The connection between Gal-9, PDI retention and HIV entry[9] emphasizes the complex and dynamic nature of cell-surface redox potential in the context of cellular responses to inflammatory stimuli. That PDI is only one member of a large superfamily of proteins capable of reducing DSBs at the cell surface suggests that the role of DSB reduction in HIV entry might first be defined in terms of non-specific cell-surface redox potential as opposed to specific PDI activity. To this end, we show that DTNB can be used to quantify the redox potential of a cell surface in terms of reducing cysteine equivalents.

Previous studies have thoroughly demonstrated a ubiquitous increase in total cell-surface PDI after treatment with Gal-9[9]. We describe an alternative phenotype, where culture conditions can give rise to a heterogenous population of cells that a) natively express PDI at their surface, b) only express surface PDI after Gal-9 treatment or c) do not express detectible levels of surface PDI with or without Gal-9 treatment. These findings are not directly contradictory, as Gal-9 did enhance total surface thiols suggesting that other disulfide reductases may be involved. These results further affirm the dynamic nature of cell-surface PDI retention, which can be heavily influenced by culture conditions. We also observed that Gal-9 exhibited severe toxic effects on the CEM, PM1 and Jurkat T-cell lines. Together, the alternative Gal-9 induced PDI expression phenotype and the toxicity of Gal-9 precluded its use as a positive effector of PDI surface retention for further experiments.

The bacitracin mixture (Bac-STD) and purified isoforms A and F (BacA-Vet, BacA-Evo and BacF-Evo) were all active against HIV entry with similar inhibitory slopes, when

contaminant protease activity was eliminated. 16F16, which alternatively inhibits the PDI active site directly, exhibited inhibitory slopes similar to bacitracin and in all cases these slopes were independent of co-receptor tropism and target-cell type (except for MDM). These results are consistent with the stoichiometric translation of inhibitor-to-PDI and PDI-to-entry activity, indicating that approximately 2 PDI active sites and, therefore, 2 reduced DSBs are required for HIV entry[14]. That the apparent stoichiometry of 16F16 depends on pre-treatment duration further emphasizes the dynamic nature of cell-surface redox potential, which is likely the result of continuous PDI secretion.

Although bacitracin and 16F16 exhibited overlapping profiles of toxicity and inhibition, our results bring to light the importance of compound purity and simultaneous measurements of both toxic and inhibitory effects as well as the technical complexity of investigating HIV inhibitors that target such essential components of cell function. In total, our data reveal two important criteria for the further development of PDI inhibitors in HIV treatment. First, understanding the environmental circumstances that regulate cell-surface redox activity in the specific context of HIV entry will solidify the connection between immunological responses and entry susceptibility, as has been demonstrated for Gal-9[9]. Second, our data suggest that inhibitors directed specifically against the PDI active site such as 16F16, although toxic, show great promise, as the toxic response showed a weaker dose-dependent strength than inhibition. The toxicity and inhibitory activity of such compounds might be synthetically tuned by including charged spectator moieties that reduce membrane permeability and by adjusting the nucleophilic strength of PDI-reactive moieties.

As DSB reduction is a conserved feature of entry for many viruses, PDI inhibitors are an important and novel antiviral strategy with low resistance potential. Clinically effective PDI inhibitors may be cheaper and more stable for broad distribution than existing inhibitors and potential immunotherapies. Alternatively, such inhibitors might be used as inexpensive, topical agents to prevent HIV transmission in a way that does not promote resistance to existing therapies. PDI inhibitors have a broad clinical applicability that warrants the further

development of less toxic and more cell-surface specific compounds.

Figures

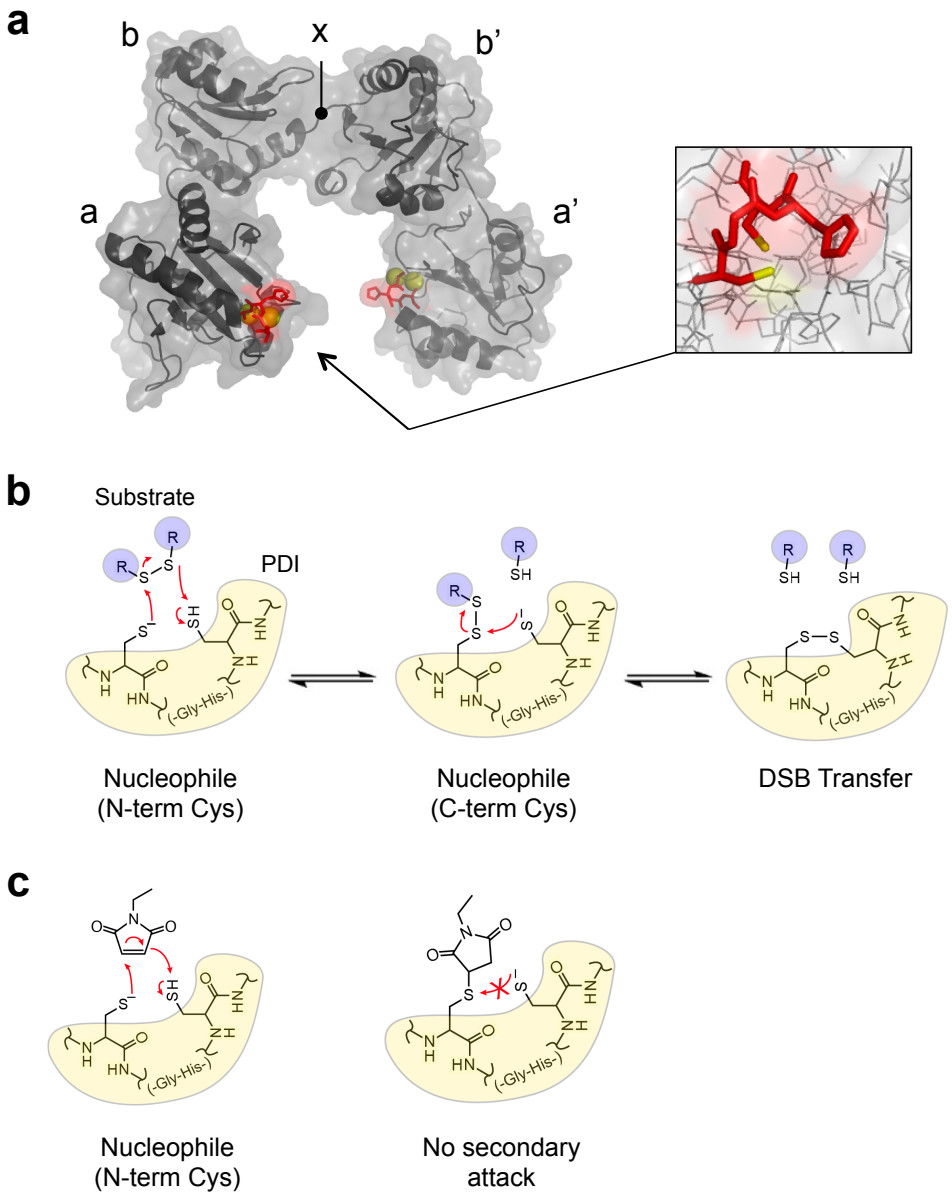

Figure 3.1: Structure, function and inhibition of PDI. (**a**) Crystal structure of human PDI[44] (PDB ID 4EKZ) with labeled catalytically active a and a' domains, substrate binding b' domain, b domain and x-linker region. CGHC active sites are shown in red with sulfur atoms represented as yellow spheres. Thiolate state of N-terminal cysteine side chain is stabilized by proton exchange with the local histidine residue (inset). (**b**) Reducing mechanism of PDI. N-terminal cysteine thiolate attacks on of two electrophilic sulfurs forming the substrate DSB (left), resulting in a mixed PDI-substrate disulfide bond (middle). Full DSB exchange occurs when that secondary, C-terminal cysteine reacts with the N-terminal cysteine of PDI in the mixed DSB. (**c**) Alkylation and inhibition of PDI by NEM involves the same nucleophilic attack of the N-terminal PDI thiolate (left). The resulting bond does not have sufficient electrophilic strength to for secondary attack (right).

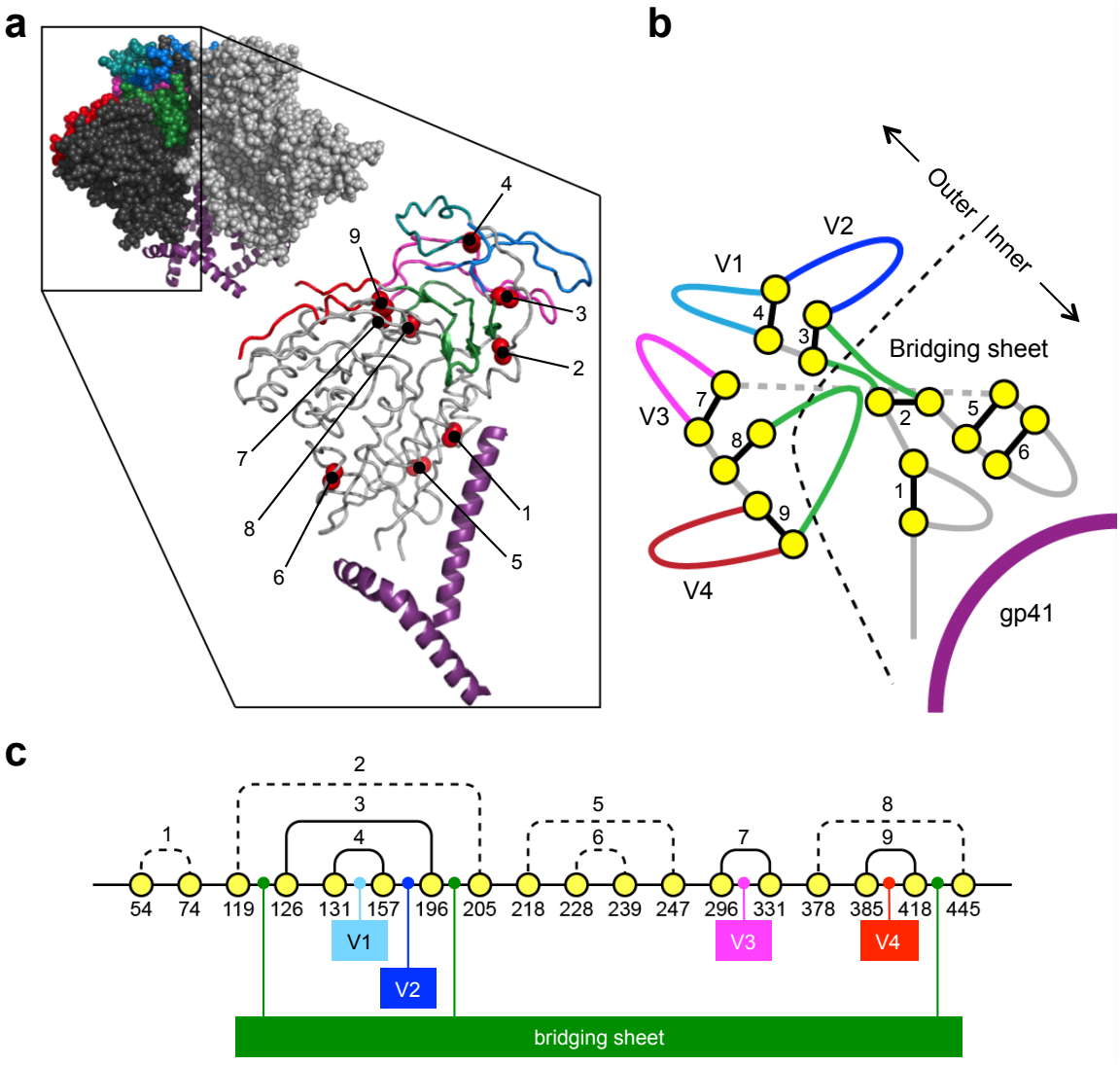

Figure 3.2: Structural characteristics of DSBs in HIV Env. (**a**, top left) Crystal structure of the BG505.SOSSIP HIV Env trimer[45] (PDB ID 3J5M) indicating variable loops V1 (cyan), V2 (blue), V3 (magenta) and V4 (red), bridging sheet (green) and gp41 (purple helices). (bottom right) A single gp120/gp41 protomer (PDB ID 3J5M) illustrates the location of DSBs 1-9 (red spheres) with V1-V4, bridging sheet and gp41 indicated. (**b**) 2-dimensional illustration of cysteines (yellow circles) and DSB positions (black lines) relative to the linear peptide backbone (grey and colored lines), bridging sheet (green), V1-V4 (cyan, blue, pink and red, respectively) and gp41 with inner and outer domains indicated. (**c**) Linear representation of DSB patterns in HIV gp120. Cysteines are shown as yellow circles along the linear peptide backbone extending from left to right. DSB-connections between cysteine residues are indicated by arched bridges and cysteines forming the base of loops that extend into the gp120 core are dashed while cysteines forming the base of exposed loops are solid (V1-V4). Cysteine positions are numbered below the yellow circles.

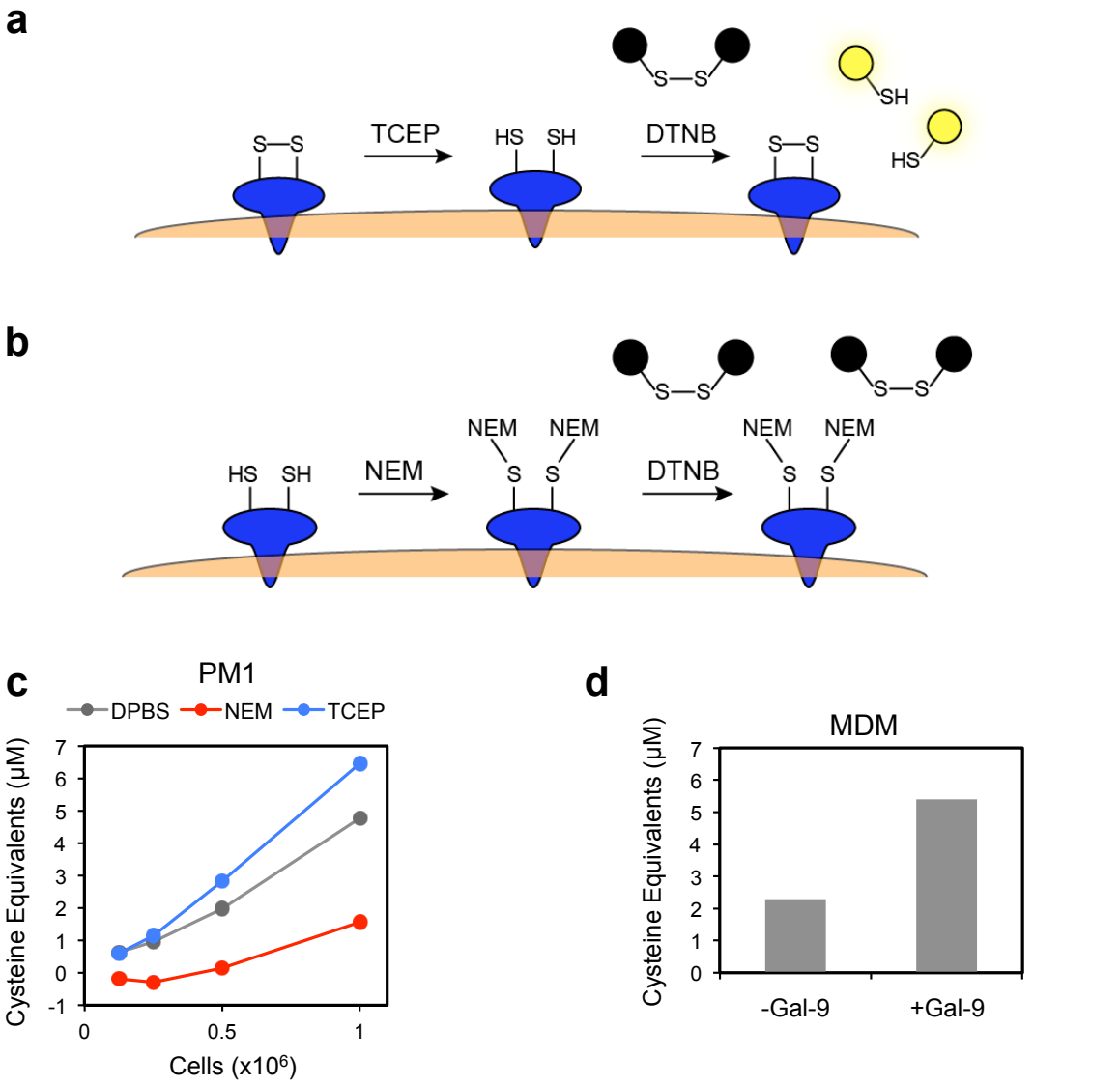

Figure 3.3: Modulation of surface disulfide redox activity. Use of DTNB as an indicator of cell-surface DSB redox state (**a** and **b**). Reduction of cell-surface thiols by the phosphine reducing agent TCEP (**a**) results in the transfer of DSBs from DTNB to the cell surface and an increase in DTNB absorbance. Alkylation of cell-surface thiols by NEM prevents transfer of DSBs from DTNB to the cell surface, preventing indicator absorbance (**b**). (**c**) TCEP-reduction (blue) and NEM-alkylation of PM1 cell surfaces are indicated by an increase and decrease in cell-surface cysteine equivalents measured by DTNB, respectively, and are dependent on the quantity of cells tested. Data represent a single experiment. (**d**) MDM treated with Gal-9 show a 3-fold increase in cell-surface cysteine equivalents. Data are representative of at least two replicates.

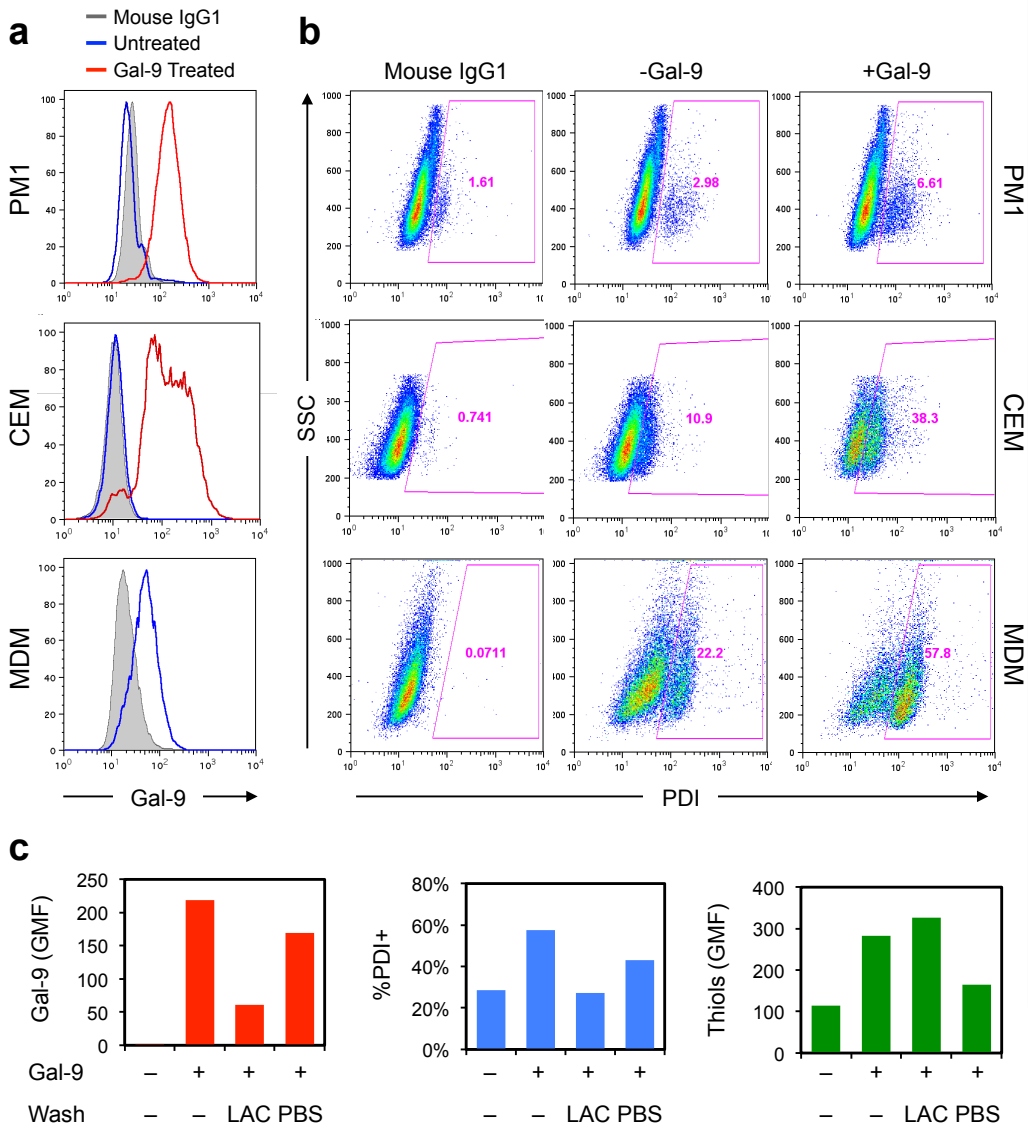

Figure 3.4: Cell surface Gal-9 and PDI retention phenotypes. (**a**) Cell-surface Gal-9 expression for PM1 and CEM cell lines untreated (blue) or treated with exogenous Gal-9 (red) and untreated MDM, with isotype controls (grey shaded). Data represent a single experiment. (**b**) PDI expression for PM1, CEM and MDM showing isotype control (left), untreated (middle) and Gal-9 treated (right) PDI surface expression phenotypes. Values shown are the %PDI+ cells of the live cell population. Data are representative of 2-3 replicates.

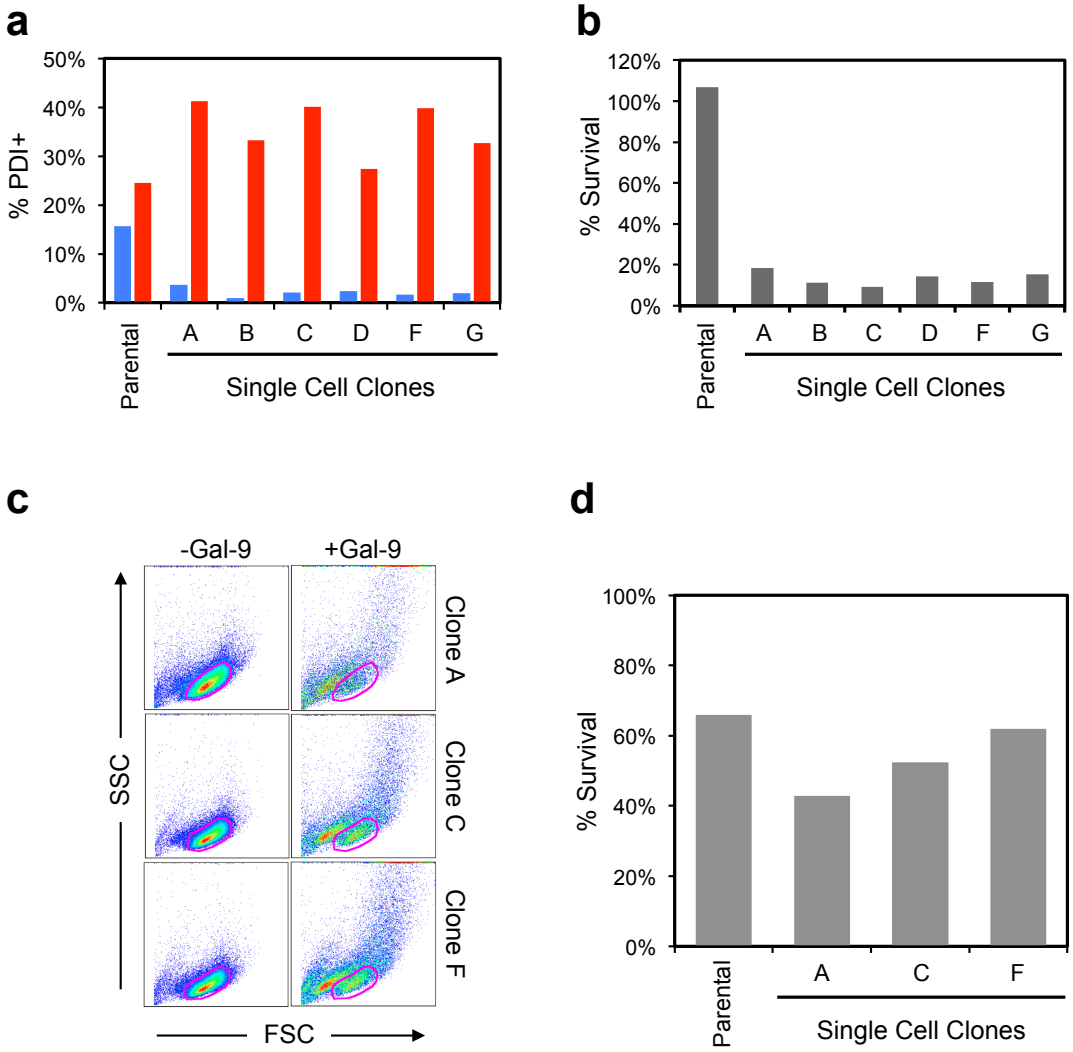

Figure 3.5: PDI expression and Gal-9 toxicity of PM1 single cell clones. (**a**) Expression of PDI for parental PM1 culture and single cell clones with (red) and without (blue) exogenous Gal-9 treatment. (**b**) Flow-based survival estimates for parental and single cell PM1 clones after Gal-9 treatment from the same experiment in panel a. (**c**) Representative examples of shifts in the light scattering properties induced by Gal-9 treatment for PM1 single cell clones A, C and F. (**d**) Survival of parental and A, C, F PM1 clones immediately after Gal-9 treatment determined by cell counting. All data represent a single replicate.

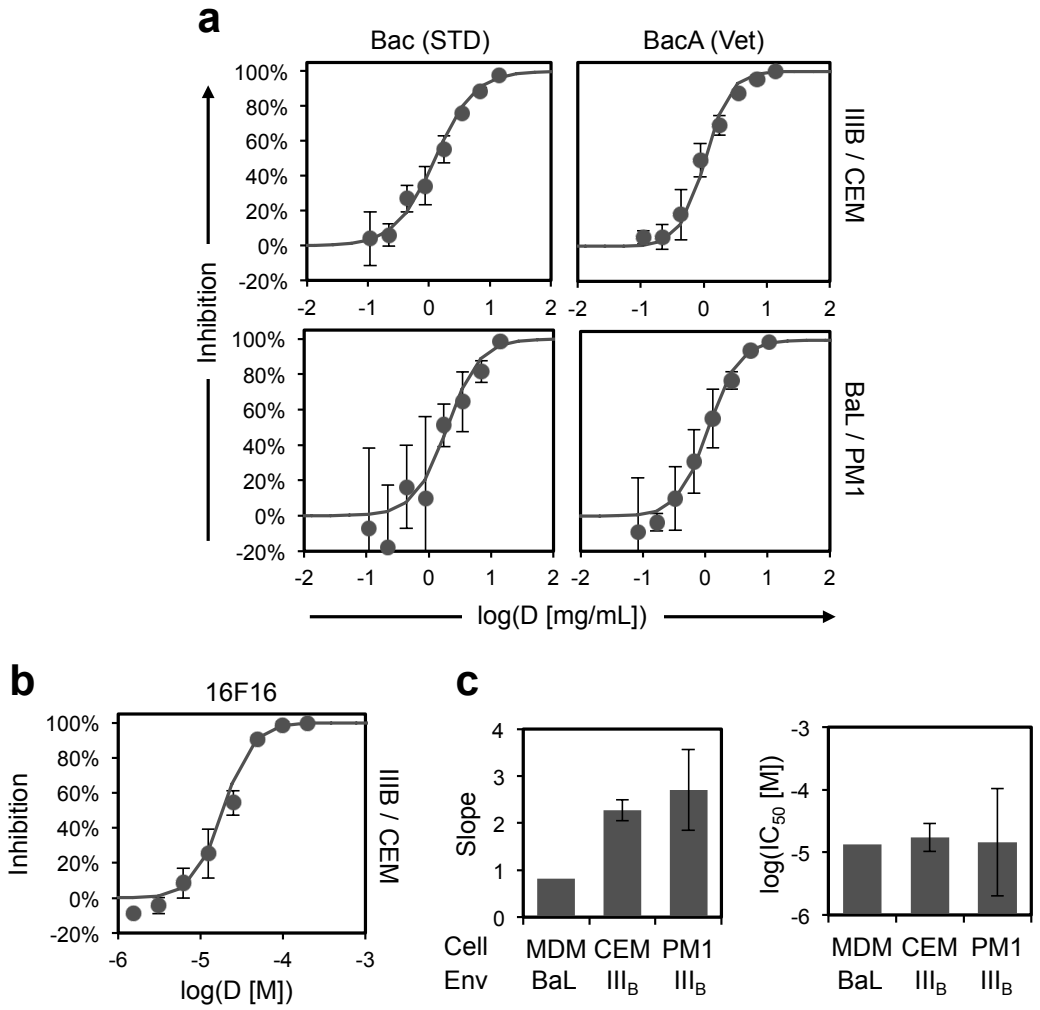

Figure 3.6: Inhibitory activity of bacitracin and 16F16. (**a**) Inhibition of III_B with CEM (top) and BaL with PM1 (bottom) by bacitracin mixture (Bac-STD, left) or purified isoform A (BacA-Vet, right). Data are the average of three replicates and bars show standard deviation. (**b**) Inhibition of III_B with CEM cells by the PDI-specific inhibitor 16F16 (data shown are the average of three replicates and bars indicate standard deviation). (**c**) slopes and IC_{50}s of 16F16 with indicated cells and Envs. Where shown, bars indicate standard deviation of 2-4 replicates.

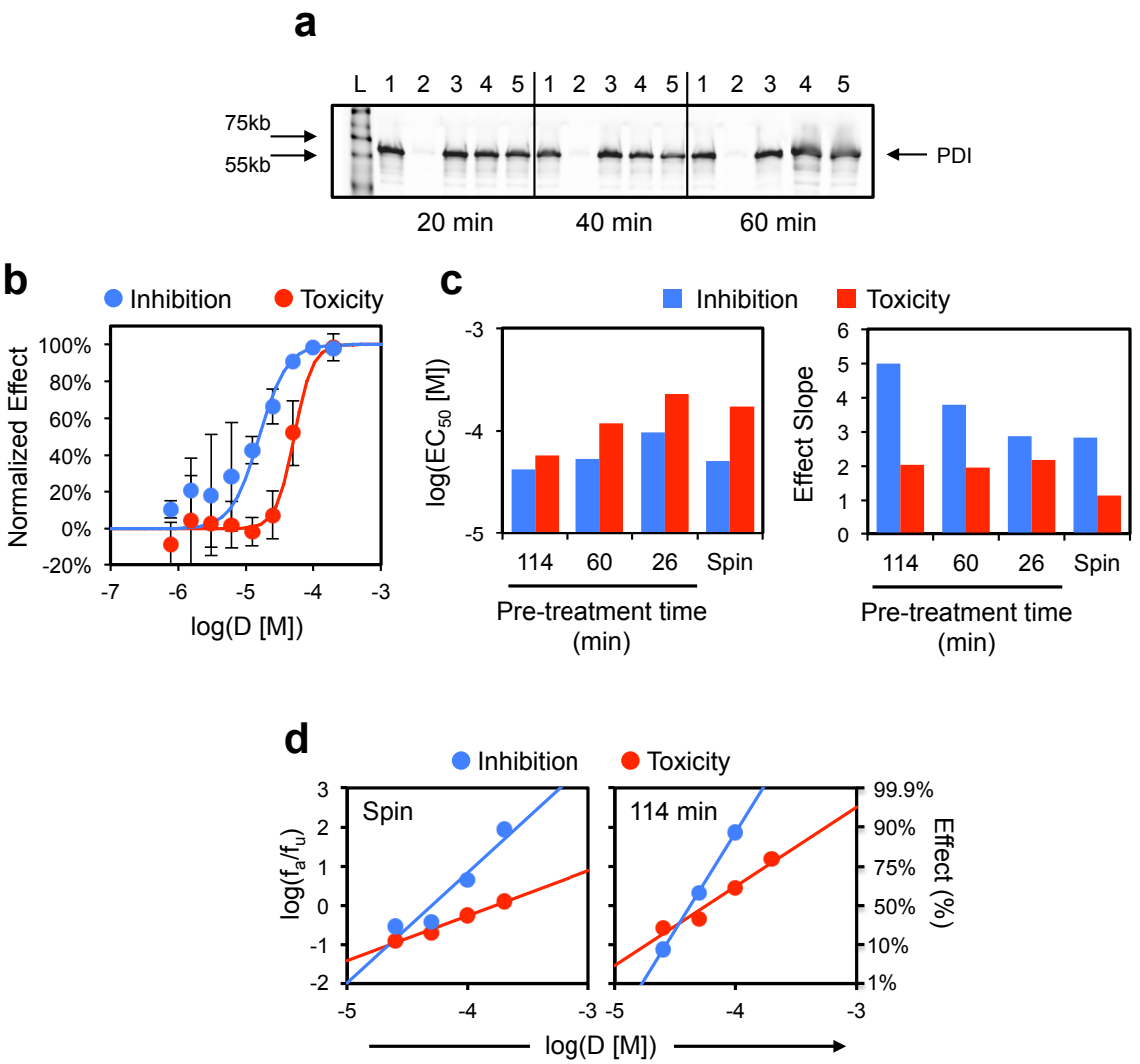

Figure 3.7: Toxicity of bacitracin and 16F16. (**a**) Western blot of recombinant human PDI incubated with 1: PBS, 2: Bac-STD, 3: BacA-Vet, 3: boiled Bac-STD and 4: boiled BacA-Vet. (**b**) Comparison of inhibitory (blue) and toxic (red) activity for 16F16 on CEM cells with HIV III_B. (**c**) comparison of EC_{50}s (left) and effect slopes (right) of inhibition (blue) and toxicity (red) for CEM cells pre-treated with 16F16 (114, 60, 26 min) or treated with 16F16 during spinoculation (spin) with HIV III_B. (**d**) Median effect plots of inhibitory (blue) and toxic (red) activity for 16F16 treatment during spinoculation (left) and after 114 minute pre-treatment followed by spinoculation (right). Data for panels a, c and d represent a single experiment and data for panel b is the average of triplicate measurements (error bars indicate standard deviation).

Tables

Table 3.1: Inhibitory and Toxic Activity of PDI Inhibitors in HIV-1 Entry.

Inhibitor	**Treatment**	**Cell**	**Env**	**Slope**	**IC_{50}[1]**	**TD_{50}[1]**
Bac-STD[2]	None	CEM	III_B	1.36	1.26	≈5
Bac-STD[2]	None	PM1	BaL	1.65	1.95	≈5
Bac-STD[2]	Boiled	CEM	III_B	2.48	2.75	N.D.
BacA-Vet[3]	None	CEM	III_B	2.19	1.05	≈5
BacA-Vet[3]	None	PM1	BaL	1.81	1.14	≈4
BacA-Vet[3]	None	PM1	III_B	2.53	1.03	≈4
BacA-Vet[3]	None	MDM	BaL	N.F.	≈1.7	N.D.
BacA-Vet[3]	Boiled	CEM	III_B	1.86	1.11	N.D.
BacA-Evo[4]	None	CEM	III_B	2.40	0.40	N.D.
BacF-Evo[5]	None	CEM	III_B	2.07	0.43	N.D.
16F16	None	PM1	III_B	2.7	15μM	45μM
16F16	None	CEM	III_B	2.3	17μM	47μM
16F16	None	MDM	BaL	0.8	13μM	35μM

[1]IC_{50} and TD_{50} are reported in units of mg/mL unless specified

[2]Bacitracin isoform mixture (Sigma Aldrich)

[3]Vetranal grade Bacitracin A isoform (Sigma Aldrich)

[4]Purified Bacitracin A isoform (EvoPure)

[5]Purified Bacitracin F isoform (EvoPure)

N.D.: Not Done

N.F.: A sufficient fit of slope could not be obtained, IC_{50}s were interpolated

References

1. Pleuni S Pennings. HIV Drug Resistance: Problems and Perspectives. *Infect Dis Rep*, 5(Suppl 1):e5, Jun 2013.

2. Eric S Daar and Douglas D Richman. Confronting the emergence of drug-resistant HIV type 1: impact of antiretroviral therapy on individual and population resistance. *AIDS Res Hum Retroviruses*, 21(5):343–57, May 2005.

3. Michael L Greenberg and Nick Cammack. Resistance to enfuvirtide, the first HIV fusion inhibitor. *J Antimicrob Chemother*, 54(2):333–40, Aug 2004.

4. L Xu, A Pozniak, A Wildfire, S A Stanfield-Oakley, S M Mosier, D Ratcliffe, J Workman, A Joall, R Myers, E Smit, P A Cane, M L Greenberg, and D Pillay. Emergence and evolution of enfuvirtide resistance following long-term therapy involves heptad repeat 2 mutations within gp41. *Antimicrob Agents Chemother*, 49(3):1113–9, Mar 2005.

5. Michael Roche, Martin R Jakobsen, Anne Ellett, Hamid Salimiseyedabad, Becky Jubb, Mike Westby, Benhur Lee, Sharon R Lewin, Melissa J Churchill, and Paul R Gorry. HIV-1 predisposed to acquiring resistance to maraviroc (MVC) and other CCR5 antagonists in vitro has an inherent, low-level ability to utilize MVC-bound CCR5 for entry. *Retrovirology*, 8:89, 2011.

6. Reem Berro, Per Johan Klasse, Martin R Jakobsen, Paul R Gorry, John P Moore, and Rogier W Sanders. V3 determinants of HIV-1 escape from the CCR5 inhibitors Maraviroc and Vicriviroc. *Virology*, 427(2):158–65, Jun 2012.

7. John P Moore and Daniel R Kuritzkes. A pièce de resistance: how HIV-1 escapes small molecule CCR5 inhibitors. *Curr Opin HIV AIDS*, 4(2):118–24, Mar 2009.

8. Judith M White, Sue E Delos, Matthew Brecher, and Kathryn Schornberg. Structures

and mechanisms of viral membrane fusion proteins: multiple variations on a common theme. *Crit Rev Biochem Mol Biol*, 43(3):189–219, 2008.

9. Shuguang Bi, Patrick W Hong, Benhur Lee, and Linda G Baum. Galectin-9 binding to cell surface protein disulfide isomerase regulates the redox environment to enhance T-cell migration and HIV entry. *Proc Natl Acad Sci U S A*, 108(26):10650–5, Jun 2011.

10. Emmanuel Fenouillet, Rym Barbouche, and Ian M Jones. Cell entry by enveloped viruses: redox considerations for HIV and SARS-coronavirus. *Antioxid Redox Signal*, 9(8):1009–34, Aug 2007.

11. HJ Ryser, EM Levy, R Mandel, and GJ DiSciullo. Inhibition of human immunodeficiency virus infection by agents that interfere with thiol-disulfide interchange upon virus-receptor interaction. *Proc. Natl. Acad. Sci. USA*, 91(10):4559–63, May 10 1994.

12. E Fenouillet, R Barbouche, J Courageot, and R Miquelis. The catalytic activity of protein disulfide isomerase is involved in human immunodeficiency virus envelope-mediated membrane fusion after CD4 cell binding. *J Infect Dis*, 183(5):744–52, Mar 2001.

13. A Gallina, TM Hanley, R Mandel, M Trahey, CC Broder, GA Viglianti, and HJ Ryser. Inhibitors of protein-disulfide isomerase prevent cleavage of disulfide bonds in receptor-bound glycoprotein 120 and prevent HIV-1 entry. *J. Biol. Chem*, 277((52)):50579–88, Dec 27 2002.

14. R Barbouche, R Miquelis, IM Jones, and E Fenouillet. Protein-disulfide isomerase-mediated reduction of two disulfide bonds of HIV envelope glycoprotein 120 occurs post-CXCR4 binding and is required for fusion. *J. Biol. Chem*, 287(5):3131–6, Jan 31 2003.

15. Emmanuel Fenouillet, Rym Barbouche, and Ian M Jones. HIV Env reduction postreceptor binding: a new target for AIDS treatment? *Blood*, 104(1):296, Jul 2004.

16. I Markovic, TS Stanchev, KH Fields, LJ Tiffany, M Tomic, CD Weiss, CC Broder, K Strebel, and KA Clouse. Thiol/disulfide exchange is a prerequisite for CXCR4-tropic HIV-1 envelope-mediated T-cell fusion during viral entry. *Blood*, 103(5):1586–94, Mar 1 2004.

17. Iman Azimi, Lisa J Matthias, Rob J Center, Jason W H Wong, and Philip J Hogg. Disulfide bond that constrains the HIV-1 gp120 V3 domain is cleaved by thioredoxin. *J Biol Chem*, 285(51):40072–80, Dec 2010.

18. MJ Papandreou, R barbouche, R Guieu, S Rivera, J Fantini, M Khrestchatisky, IM Jones, and E Fenouillet. Mapping of domains on HIV envelope protein mediating association with calnexin and protein-disulfide isomerase. *J. Biol. Chem*, 285(18):13788–96, Apr 30 2010.

19. Maola M G Khan, Siro Simizu, Ngit Shin Lai, Makoto Kawatani, Takeshi Shimizu, and Hiroyuki Osada. Discovery of a small molecule PDI inhibitor that inhibits reduction of HIV-1 envelope glycoprotein gp120. *ACS Chem Biol*, 6(3):245–51, Mar 2011.

20. C Finnegan and R Blumenthal. Dissecting HIV fusion: identifying novel targets for entry inhibitors. *Infect Disord Drug Targets*, 6(4):355–67, Dec 2006.

21. HJ Ryser and R Fluckiger. Progress in targeting HIV-1 entry. *Drug Discov. Today*, 10(16):1085–94, Aug 15 2005.

22. J Billington, T P Hickling, G H Munro, C Halai, R Chung, G G Dodson, and R S Daniels. Stability of a receptor-binding active human immunodeficiency virus type 1 recombinant gp140 trimer conferred by intermonomer disulfide bonding of the V3 loop: differential effects of protein disulfide isomerase on CD4 and coreceptor binding. *J Virol*, 81(9):4604–14, May 2007.

23. Anna-Riikka Karala and Lloyd W Ruddock. Bacitracin is not a specific inhibitor of protein disulfide isomerase. *FEBS J*, 277(11):2454–62, Jun 2010.

24. S Rogelj, K J Reiter, L Kesner, M Li, and D Essex. Enzyme destruction by a protease contaminant in bacitracin. *Biochem Biophys Res Commun*, 273(3):829–32, Jul 2000.

25. Nina Dickerhof, Torsten Kleffmann, Ralph Jack, and Sally McCormick. Bacitracin inhibits the reductive activity of protein disulfide isomerase by disulfide bond formation with free cysteines in the substrate-binding domain. *FEBS J*, 278(12):2034–43, Jun 2011.

26. Peter A Jordan and Jonathan M Gibbins. Extracellular disulfide exchange and the regulation of cellular function. *Antioxid Redox Signal*, 8(3-4):312–24, 2006.

27. Jun Lu and Arne Holmgren. The thioredoxin superfamily in oxidative protein folding. *Antioxid Redox Signal*, 21(3):457–70, Jul 2014.

28. F Hatahet and LW Ruddock. Protein disulfide isomerase: a critical evaluation of its function in disulfide bond formation. *Antioxid. Redox Signal.*, 11(11):2807–50, Nov 2009.

29. David W Essex. Redox control of platelet function. *Antioxid Redox Signal*, 11(5):1191–225, May 2009.

30. D A Lawrence, R Song, and P Weber. Surface thiols of human lymphocytes and their changes after in vitro and in vivo activation. *J Leukoc Biol*, 60(5):611–8, Nov 1996.

31. B Sahaf, K Heydari, LA Herzenberg, and LA Herzenberg. Lymphocyte surface thiol levels. *Proc. Natl. Acad. Sci. USA*, 100(7):4001–5, Apr 1 2003.

32. Bita Sahaf, Kartoosh Heydari, Leonard A Herzenberg, and Leonore A Herzenberg. The extracellular microenvironment plays a key role in regulating the redox status of cell surface proteins in HIV-infected subjects. *Arch Biochem Biophys*, 434(1):26–32, Feb 2005.

33. Shuguang Bi, Lesley A Earl, Linsey Jacobs, and Linda G Baum. Structural features of galectin-9 and galectin-1 that determine distinct T cell death pathways. *J Biol Chem*, 283(18):12248–58, May 2008.

34. Mitsuomi Hirashima, Yumiko Kashio, Nozomu Nishi, Akira Yamauchi, Tada-atsu Imaizumi, Toshiro Kageshita, Naoki Saita, and Takanori Nakamura. Galectin-9 in physiological and pathological conditions. *Glycoconj J*, 19(7-9):593–600, 2004.

35. Xiping Wei, Julie M Decker, Shuyi Wang, Huxiong Hui, John C Kappes, Xiaoyun Wu, Jesus F Salazar-Gonzalez, Maria G Salazar, J Michael Kilby, Michael S Saag, Natalia L Komarova, Martin A Nowak, Beatrice H Hahn, Peter D Kwong, and George M Shaw. Antibody neutralization and escape by HIV-1. *Nature*, 422(6929):307–12, Mar 2003.

36. Eelco van Anken, Rogier W Sanders, I Marije Liscaljet, Aafke Land, Ilja Bontjer, Sonja Tillemans, Alexey A Nabatov, William A Paxton, Ben Berkhout, and Ineke Braakman. Only five of 10 strictly conserved disulfide bonds are essential for folding and eight for function of the HIV-1 envelope glycoprotein. *Mol Biol Cell*, 19(10):4298–309, Oct 2008.

37. Kathrin Reiser, Katrien O François, Dominique Schols, Tomas Bergman, Hans Jörnvall, Jan Balzarini, Anna Karlsson, and Mathias Lundberg. Thioredoxin-1 and protein disulfide isomerase catalyze the reduction of similar disulfides in HIV gp120. *Int J Biochem Cell Biol*, 44(3):556–62, Mar 2012.

38. Marie-Jeanne Papandréou, Rym Barbouche, Régis Guieu, Santiago Rivera, Jacques Fantini, Michel Khrestchatisky, Ian M Jones, and Emmanuel Fenouillet. Mapping of domains on HIV envelope protein mediating association with calnexin and protein-disulfide isomerase. *J Biol Chem*, 285(18):13788–96, Apr 2010.

39. Benjamin G Hoffstrom, Anna Kaplan, Reka Letso, Ralf S Schmid, Gregory J Turmel, Donald C Lo, and Brent R Stockwell. Inhibitors of protein disulfide isomerase suppress apoptosis induced by misfolded proteins. *Nat Chem Biol*, 6(12):900–6, Dec 2010.

40. G L ELLMAN. Tissue sulfhydryl groups. *Arch Biochem Biophys*, 82(1):70–7, May 1959.

41. A Mörner, A Björndal, J Albert, V N Kewalramani, D R Littman, R Inoue, R Thorstensson, E M Fenyö, and E Björling. Primary human immunodeficiency virus type 2 (HIV-2)

isolates, like HIV-1 isolates, frequently use CCR5 but show promiscuity in coreceptor usage. *J Virol*, 73(3):2343–9, Mar 1999.

42. R Mandel, H J Ryser, F Ghani, M Wu, and D Peak. Inhibition of a reductive function of the plasma membrane by bacitracin and antibodies against protein disulfide-isomerase. *Proc Natl Acad Sci U S A*, 90(9):4112–6, May 1993.

43. Sarah B Laskey and Robert F Siliciano. A mechanistic theory to explain the efficacy of antiretroviral therapy. *Nat Rev Microbiol*, 12(11):772–80, Nov 2014.

44. Chao Wang, Wei Li, Jinqi Ren, Jingqi Fang, Huimin Ke, Weimin Gong, Wei Feng, and Chih-Chen Wang. Structural insights into the redox-regulated dynamic conformations of human protein disulfide isomerase. *Antioxid Redox Signal*, 19(1):36–45, Jul 2013.

45. Dmitry Lyumkis, Jean-Philippe Julien, Natalia de Val, Albert Cupo, Clinton S Potter, Per-Johan Klasse, Dennis R Burton, Rogier W Sanders, John P Moore, Bridget Carragher, Ian A Wilson, and Andrew B Ward. Cryo-EM structure of a fully glycosylated soluble cleaved HIV-1 envelope trimer. *Science*, 342(6165):1484–90, Dec 2013.

CHAPTER 4

Distinct HIV-1 Entry Phenotypes are Associated with Transmission, Subtype Specificity, and Resistance to Broadly Neutralizing Antibodies

The following chapter includes a reprint of the following:

Chikere K*, **Webb NE***, Chou T, Borm K, Sterjovski J, Gorry PR, Lee B. Distinct HIV-1 entry phenotypes are associated with transmission, subtype specificity and resistance to broadly neutralizing antibodies. *Retrovirology* 2015, 11:40.

Supplementary figures, tables, and additional files are provided in Appendix D.

Introduction

The clinical expectations of inhibitors are derived from *in vitro* experimental results that describe an inhibitor's activity in terms of its concentration through potency (IC_{50}) and a dose-dependent differential effect (slope). Inhibitors also effect the natural behavior of a virus either directly, through the perturbations an inhibitor imposes on the viral lifecycle, or adaptively, through changes in infectious behavior that are uniquely associated with resistant isolates. For example, the CCR5 antagonist maraviroc (MVC) fundamentally alters the way HIV recognizes CCR5, where resistant isolates adapt the unique ability to use MVC-bound CCR5 as a functional co-receptor by binding to alternative regions[1–4]. This unique adaptation does not always manifest as a loss in sensitivity to the drug as some of these isolates can use MVC-bound CCR5 with low efficiency, leading to treatment failure while remaining sensitive in the classical sense[1]. This phenotype, therefore, is not clearly described in terms of inhibitor concentration but is, instead, more comprehensively defined by the efficiency with which an isolate uses CD4 and CCR5.

HIV entry is a highly complex, concerted mechanism involving two receptors (CD4 and co-receptor, CCR5 or CXCR4) and two viral proteins (gp120 and gp41). Attachment and entry efficiency, therefore, depend on a variety of factors including receptor stoichiometry, binding affinity and transition state kinetics. CCR5-tropic HIV isolates exhibit unique and independent responses to CD4 and CCR5 expression[5] that have been connected to clinically relevant phenotypes such as transmission[6,7], target cell tropism[8–10], and neuropathology[8,11–13], thus, understanding the effect that a drug has on the efficiency of CD4/CCR5 usage can bring to light novel therapeutic strategies that are mindful of the potential pathologies associated with altered CD4/CCR5 usage efficiency during long-term treatment.

Initially, studies aimed at measuring the CD4/CCR5 usage phenotypes of HIV Envs were limited to high and low CD4/CCR5 surface densities[14–16], offering a more qualitative understanding of CD4/CCR5 usage efficiency. Over the last decade, our laboratory has developed

a novel, clonal cell line that allows dual and independent induction of up to 25 distinct and clinically relevant combinations of cell-surface CD4 and CCR5 expression, termed Affinofile cells[9,17]. A matrix of Affinofile cells expressing unique combinations of CD4/CCR5 are infected to generate a CD4/CCR5-dependent infectivity profile (see Appendix C). This cell line is accompanied by mathematical methods that distill these infectivity matrices into three Viral Entry Receptor Sensitivity Assay (VERSA) metrics[5,17] describing overall infectivity (mean infectivity, M), a balance of CD4/CCR5 dependence (angle, θ) and CD4/CCR5 responsiveness (amplitude, Δ). These metrics connect CD4/CCR5 usage efficiency, an inherent viral property, to unique pathological phenotypes[5] and resistance adaptations[1–4].

We recently improved this system to include a dual enhanced GFP (eGFP) and gaussia luciferase (GLuc) reporter linked by an internal ribosomal entry site (IRES) that allows infectivity profiles to be measured using full-length, unmodified molecular viral clones via. flow cytometry or non-destructive supernatant sampling, termed GGR Affinofile cells[18]. This enhanced system was accompanied with standardized, high-throughput protocols and improved biophysical interpretations of the associated VERSA matrics (Appendix C). This chapter focuses on the optimization of this new GGR system and the revised interpretation of VERSA metrics in the context of specific point mutants with known CD4/CCR5 usage phenotypes, HIV subtypes, transmission and antibody resistance.

The biophysical interpretation of VERSA metrics. An full 5x5 infectivity matrix consists of GGR Affinofile cells induced to express 25 distinct combinations of CD4 and CCR5, ranging from 2,000 to 150,000 and 1,500 to 25,000 antibody binding sites per cell (ABS/cell), respectively, that are reflect the wide variety of CD4 and CCR5 expression on HIV target cells[9,17]. All distinct combinations are infected with an equal viral inoculum to produce a 3-dimensional profile of infectivity with CD4 expression along the x-axis, CCR5 along the y-axis and infectivity along the z-axis. When CD4 and CCR5 expression are normalized these data are fit to a 2-dimensional surface function $F(x, y)$ (Equation 4.1).

$$F(x,y) = a_0 + a_1x + a_2y + a_3xy + a_4x^2 + a_5y^2 \tag{4.1}$$

This surface is distilled into three parameters that describe the inherent CD4/CCR5-dependence and infectivity of the isolate being analyzed. Overall infectivity (M) is defined by the total area under the surface using Equation 4.2.

$$M = \int_0^1 dx \int_0^1 dy \quad F(x,y) \tag{4.2}$$

CD4 and CCR5 usage is defined by two parameters derived from the gradient, $\nabla F(x,y)$ (Equation 4.3) of this surface, which traces the path of the steepest increase in infection from minimum to maximum CD4/CCR5 expression. The sensitivity vector ($\vec{S}$) is the unit steepness, or amplitude of $\nabla F(x,y)$ (Equation 4.4) while θ (Equation 4.5) is the angle of $\nabla F(x,y)$ relative to the CD4 (y) axis. Thus, X4-tropic isolates exhibit low, CD4-dependent angles that do not respond to increasing levels of CCR5 while CD4-independent isolates exhibit high, CCR5-dependent angles that do not respond strongly to increasing levels of CD4[17].

$$\nabla F(x,y) = \hat{x}\frac{\delta F(x,y)}{\delta x} + \hat{y}\frac{\delta F(x,y)}{\delta y} \tag{4.3}$$

$$\vec{S} = \int_0^1 dx \int_0^1 dy \frac{\nabla F(x,y)}{|\nabla F(x,y)|} = S_x\hat{x} + S_y\hat{y} \tag{4.4}$$

$$\theta = \tan^{-1}\left(\frac{S_y}{S_x}\right) \tag{4.5}$$

Of these three parameters defined above, M and θ are conceptually intuitive as they describe the overall infectivity observed across all levels of CD4/CCR5 expression (M) and the specific ratio of CD4/CCR5 expression that yields the greatest response in infectivity (θ). In this sense, θ is interpreted as a balance of an isolate's dependence on both CD4 and

CCR5 from a discrete stoichiometric perspective. This parameter is not directly equal to the stoichiometric requirements of CD4/CCR5 during entry as the stability of transition-state kinetics also contribute to θ. For example, low CCR5 expression may result in slower diffusion of cell-surface CCR5 to sites of CD4-Env conjugates that increases the likelihood of entry failure.

While the angle (θ) of the sensitivity vector ($\vec{S}$) describes the ratio of CD4 and CCR5 generating the greatest response, the amplitude of this vector ($|\vec{S}|$ or Δ) describes the strength of that response. For example, a two-fold increase in CD4/CCR5 expression at the ratio defined by θ may yield a two-fold increase in infection, indicating a proportionate response, or a 0.5 or 3-fold increase in infection, indicating a disproportionate response. By comparison, isolates exhibiting higher Δ indicate a steeper response at the optimal CD4/CCR5 ratio, which has two important consequences. Because M describes the set-point of overall infectivity, Δ necessarily describes the amplitude of response from that baseline. Isolates exhibiting higher Δ and equal M will naturally be a) more infectious at higher levels of the optimal CD4/CCR5 ratio and, conversely, b) less infectious at lower levels of this optimal ratio. Importantly, because Δ is the amplitude of the most responsive θ, all other possible ratios of CD4/CCR5 will, by definition, exhibit a lower amplitude. Thus, the comparison of Δ between isolates must take into account both the differential nature of this parameter relative to M and within the context of θ.

Together, M, θ and Δ provide a simplified framework for comparing the overall infectivity, CD4/CCR5 dependence and sensitivity of HIV isolates[5]. The mathematical methods presented here were made available in an automated, web-based platform[17]. This interface was updated to generate unique and informative graphical representations produced in scalar vector graphics (SVG) format, which will become available in the next public version.

Future development of VERSA metrics. The existing VERSA metrics (M, θ and Δ) are highly descriptive but difficult to attribute to specific, well defined biophysical properties.

The mathematical VERSA framework and associated metrics are, however, synonymous to the more extensible median effect model. For example, Δ describes the response of an isolate to its most preferred ratio of CD4 and CCR5 (given by θ) and as such, Δ is directly analogous to a median effect slope when measured across proportionate increases in CD4/CCR5 expression at the ratio of θ.

Median effect can be used to describe CD4/CCR5 dependence in terms of EC_{50}, where, for example, the EC_{50} surface expression of CCR5 can be described in terms of CD4 expression, and vice versa. Likewise, changes in responsiveness to CCR5 expression, given by the median effect slope (m), can be assessed across varying levels of CD4. When combined, the new surface function $f(x, y)$ recapitulates the total interdependence of CD4 and CCR5 through parameters with clear biophysical meaning, such as affinity/efficiency (through EC_{50}s) and stoichiometry/cooperativity (through slopes) (see Appendix A).

The median effect model offers the practical advantage of a linearized representation of infectivity responses to varying levels of CD4 and CCR5, where infectivity is described in terms of a log infectivity ratio (see Appendix A) instead of an effect-based Hill representation with complex curvatures. Thus, this model is amenable to linear manipulations, allowing the infectivity ratio across varying levels of CCR5 expression to be described in terms of a CD4-dependent slope and EC_{50} (Equation 4.6, where $f_{R,B}$ is the CCR5-dependent effect ratio, m_B is the CD4-dependent slope, B is CCR5 expression and $D_{m,B}$ is the CD4-dependent EC_{50} of CCR5.

$$\log(f_{R,B}) = m_B \log(B) - m_B \log(D_{m,B}) \tag{4.6}$$

Both the slope (m_B) and EC_{50} ($D_{m,B}$) of CCR5 are then represented by CD4-dependent functions (Equations 4.7a and 4.7b, respectively).

$$m_B = f_1([\text{CD4}]) \qquad (4.7\text{a}) \qquad\qquad D_{m,B} = f_2([\text{CD4}]) \qquad (4.7\text{b})$$

These CD4-dependent functions f_1 and f_2 then describe complementary features of

CD4/CCR5 usage. For example, f_2 ($D_{m,B}$) describes CD4-dependent changes in CCR5 EC_{50} that are probabilistic in nature, related to binding affinity and rote usage efficiency while f_1 describes the more dynamic interplay of CD4/CCR5 usage in a cooperative context. In this new model, θ is now more rigidly defined as the ratio of CD4 and CCR5 EC_{50}s that produce the greatest slope.

The existing VERSA metrics are, in most ways, directly synonymous to the EC_{50} and slope-based parameters of this new model, therefore, the advantage of this new analytical framework lies in the more extensible interpretation of its parameters. Although we have not yet finalized a complete median effect-based adaptation of VERSA metrics, this strategy expands the interpretive contexts of CD4 and CCR5 usage from a more clinical perspective, in terms of infectivity, to more detailed and well-defined biophysical properties.

Specific aims. The goal of this chapter is to first *scharacterize the new GGR system* using specific point mutations in the JR-CSF isolate that confer well described phenotypes associated with CD4/CCR5 usage. For example, the S142N variant was isolated after passage onto PBMCs, Molt-4 and Sup-T1 cell lines and is able to infect cells expressing very low levels of CCR5. These phenotypes are then connected to target cell tropism through our VERSA metrics, which provide distilled CD4/CCR5 usage characteristics. We then *demonstrate the utility of these metrics in the novel contexts of transmission, subtype specificity, and resistance to broadly neutralizing antibodies.* Concurrent with our published results, we further *refine the biophysical interpretations of the existing metrics*, which has lead to a *new formulation* based on the more extensive physical parameters given by the media effect model.

Results

Background

Human immunodeficiency virus type 1 (HIV-1) enters target cells through the stepwise interaction of its envelope glycoproteins (Env) with CD4 and a coreceptor, either CCR5 or CXCR4. Receptor binding induces a series of conformational changes that results in fusion pore formation and virus/cell membrane fusion [1]. Acutely transmitted viruses invariably use CCR5 (R5) regardless of the subtype. Furthermore, although CXCR4-using (X4, R5X4) viruses can emerge in approximately 40-50% of late stage HIV-1 subtype B infections [2,3], most HIV-1 infected subjects, particularly those with subtype A and C viruses [4-6], progress to late stages of infection despite exclusively harboring R5 viruses.

While many viral and host factors contribute to HIV-1 progression, there is a strong body of evidence that supports some Env determinants of pathogenicity. For example, in patients with R5 viruses, isolates from late stages of infection have a greater capacity to infect macrophages [7-9], which correlates with more efficient usage of the low levels of CD4 and CCR5 expressed on these cells [9-13]. These late stage R5 isolates can also cause increased levels of cell-cell fusion [14] and CD4+ T-cell apoptosis [15]. Late stage brain isolates have also been shown to utilize low levels of CD4 and/or CCR5 for entry [16-24]. Therefore, viruses capable of exploiting limiting levels of CD4 and/or CCR5 may have expanded target cell tropism with pathological consequences [24-26]. Furthermore, viruses that are resistant to the CCR5 antagonists vicriviroc (VVC) and maraviroc (MVC) exhibit a reduced ability to use lower levels of CCR5 compared to their non-resistant counterparts [27-29]. Finally, the recent characterization of transmitter/founder (T/F) Envs has indicated that these R5 variants enter and replicate in activated primary T-cells but not macrophages [30], underscoring the increasingly evident notion that CCR5 usage is not equivalent to macrophage-tropism [5,31]. Together, these studies show that the efficiency with which a viral Env engages CD4 and/or CCR5 can have an influence on pathogenicity, disease progression and resistance to CCR5 antagonists [5,32,33]. Therefore, a more refined understanding of how Env-CD4/CCR5 usage develops and differs under alternate evolutionary histories will inform the development and use of HIV-1 vaccines and therapeutics that target HIV-1 entry.

The Affinofile system, based on a CD4 and CCR5 dual-inducible cell line, permits quantitative characterization of HIV-1 infection across 24–48 distinct combinations of CD4/CCR5 expression levels [34]. Multiple groups have used this receptor affinity profiling system (Affinofile) to reveal unique CD4/CCR5 usage efficiencies associated with distinct pathophysiological phenotypes. These studies have shed light on the nature of CCR5-inhibitor resistance [27-29,35-37], the relationship between CD4/CCR5 usage and cellular tropism as well as disease pathogenesis [38], and CD4/CCR5 usage interdependence (reviewed in [39]). Using this system, the infectivity of an Env under 24–48 distinct combinations of CD4 and CCR5 expression is compiled and summarized as three metrics that collectively describe a distinct profile of CD4 and CCR5 usage. Biological insights are gained by comparing the Affinofile metrics of different Envs. Affinofile metrics can be extracted from infectivity data by an automated web-based computational platform [34].

Comprehensive infectivity profiling requires the examination of each Env under multiple distinct combinations of CD4/CCR5 expression levels. To gain further insights into HIV-1 entry phenotypes associated with distinct pathophysiologies, and to examine a larger panel of Envs from distinct cohorts, we engineered a higher throughput, second generation Affinofile system that would: (1) improve the robustness of the infectivity data obtained, (2) ease the process of data sampling and analysis by permitting sequential time-point sampling of the infected cell supernatant without the need for end-point lysis, and (3) allow infectivity measurements without requiring a virus-associated reporter gene while retaining compatibility with any HIV-1 proviral backbone used for Env pseudo typing. To this end, we transduced Affinofile cells with a Tat- and Rev-dependent reporter engineered to express green fluorescent protein (GFP) and secrete *Gaussia* luciferase into the supernatant upon infection. This Gaussia luciferase-GFP reporter (GGR) Affinofile cell line now permits simple and rapid detection of HIV-1 infection by serial sampling a small volume of supernatant for Gaussia luciferase activity, while also taking full advantage of the CD4 and CCR5 inducibility of the original Affinofile cells.

In this study, we validate our new GGR Affinofile system, and use this improved, higher throughput GGR Affinofile system to reveal distinct Env phenotypes associated with acute transmission, subtype specificity and neutralization resistance.

Results

Generation and characterization of the GGR Affinofile cell line

We modified a previously published Tat/Rev-dependent vector [40,41] by cloning the *Gaussia* luciferase (GLuc) gene upstream of an eGFP reporter gene, linked via an internal ribosomal entry site (IRES) (Figure 1A). Judiciously placed splice donor and acceptor sites, in addition to the Rev-responsive element (RRE) placed downstream of the eGFP reporter gene, ensures that only the full-length, unspliced reporter mRNA will be translated in the presence of Tat and Rev, which is provided by commonly used HIV-1 reporter vectors and replication-competent HIV-1. Lentiviral VSV-G pseudotypes containing this

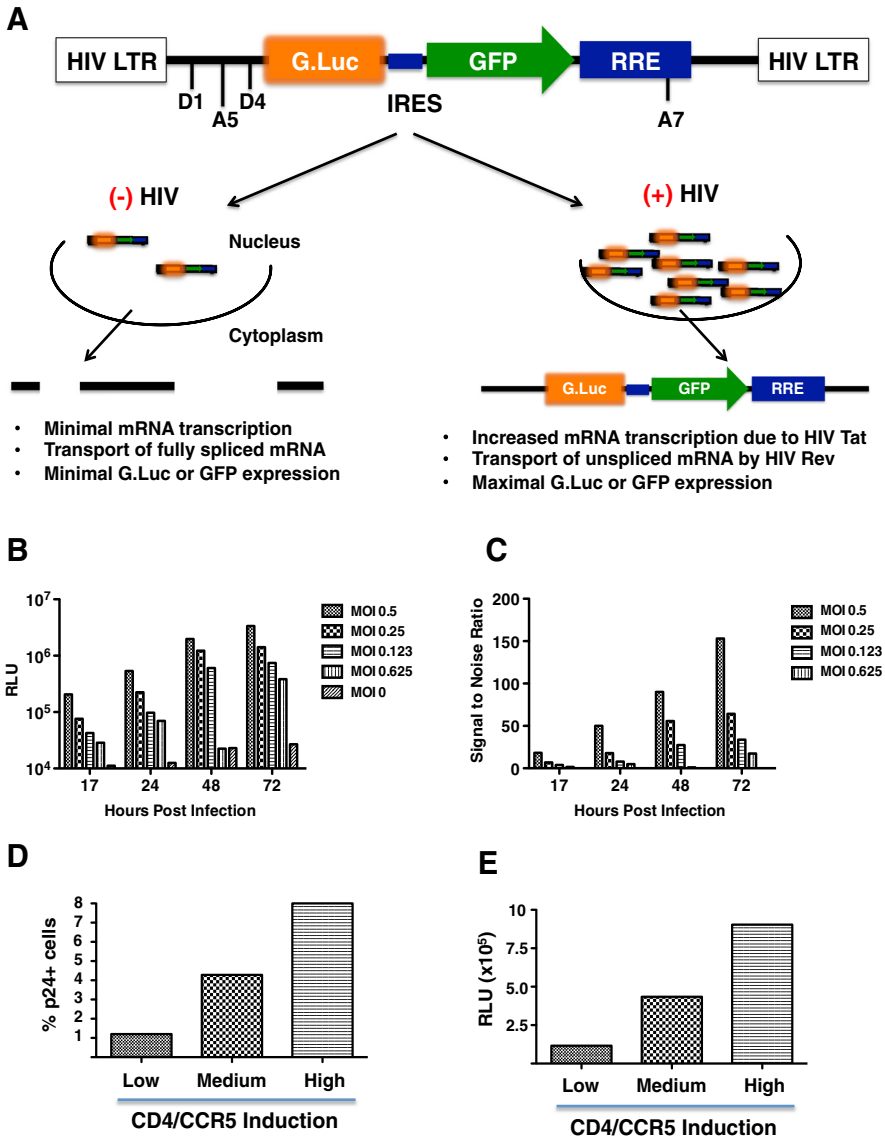

Figure 1 Generation and characterization of the GGR Affinofile Cell Line. (A) Schema of the tat-rev dependent *Gaussia* luciferase (gLuc)-IRES-GFP reporter vector as described in the text. **(B)** and **(C)** GGR cells were maximally induced with doxycyline (Doxy, 4ng/ml) and ponasterone A (PonA, 4 μM) at the time of their seeding in 96-well plates. 16–21 hours post-seeding/induction, cells were infected with wt JR-CSF virus at varying multiplicities of infection (MOI). The titer of the virus was previously determined on stable CD4/CCR5-expressing GHOST cells where CD4/CCR5 levels are non-limiting. At 17, 24, 48, and 72 hpi, 10 μL (out of 150) of the infected cell supernatant was removed and analyzed for gLuc activity as per manufacturer's instructions. Luciferase activity (measured as relative light units, RLU), and the corresponding signal:noise ratios at each data point are shown in **(B)** and **(C)**, respectively. Mock-infected cell supernatant served as the background signal. **(D)** and **(E)** GGR cells were induced at high (3.2ng/mL Doxy, 2 μM PonA), medium (1.6ng/mL Doxy, 1μm PonA), and low (0.4ng/mL Doxy, 0.25μM PonA) levels, and infected as above with pseudotyped virus at an MOI of 0.25. Three days post-infection, supernatant was collected and analyzed for gluc expression **(E)**, while cells from each well were individually processed for intracellular p24 staining **(D)** as described in methods. Data shown is representative of two independent experiments.

*G*Luc-e*G*FP *R*eporter (GGR) vector were used to transduce early passage Affinofile cells. Stable *GGR* Affinofile cell lines with optimal properties were single cell cloned as described in methods.

To determine the ability of GGR Affinofile cells to detect HIV-1 infection, we infected a stable clone of GGR Affinofile cells (at maximum CD4/CCR5 induction) using a range of viral inoculums (JR-CSF, MOI = 0.5 – 0.0625) and serially sampled the infected cell culture supernatant for GLuc activity. GLuc activity could be detected at 20-fold above background as early as 17 hpi depending on the amount of viral inoculum used

(Figure 1B-C). Furthermore, we observed that GLuc activity in the infected culture supernatant mirrored the level of infection as reported by intracellular p24 staining (Figure 1D-E), especially at low MOIs (e.g. 0.2) that ensure a single infectious event per cell.

Defining the parameters that impact the infectivity metrics used for profiling HIV-1 entry efficiency

We previously demonstrated that R5 virus infection of Affinofile cells across a spectrum of CD4 and CCR5 expression levels generated an infectivity profile (Figure 2A) that can be fitted by the surface function $F(x, y)$ to give the surface plot shown in Figure 2B. $F(x, y)$ describes the infectivity response as a function of CD4 and CCR5 cell surface expression levels [34]. The salient features of this surface function can be captured by three biophysically meaningful parameters illustrated in Figure 2B and C: the mean infectivity level M (Figure 2B), and the angle and amplitude of the sensitivity vector ($\vec{S}$) representing the gradient of the surface function $F(x, y)$ on a 2-D plot (Figure 2C). Mean infectivity (M) expresses the overall infectivity observed across all levels of CD4 and CCR5

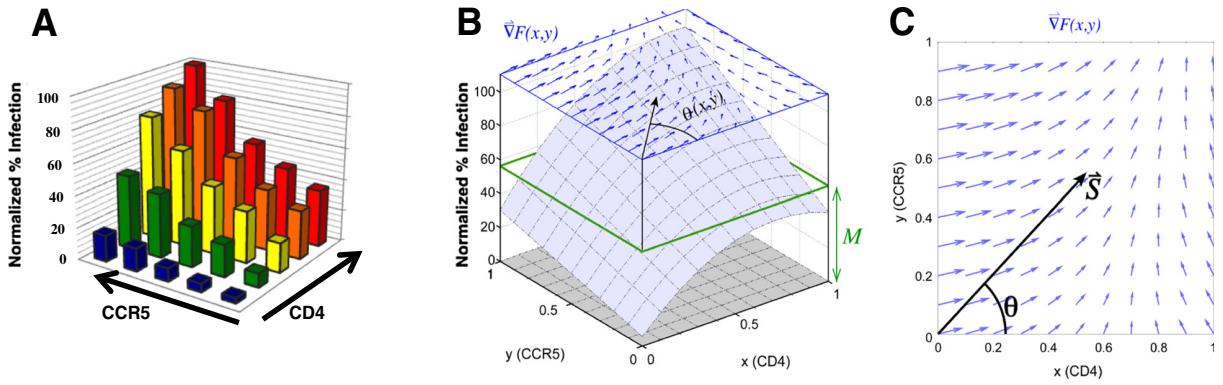

The surface function $F(x, y)$ is the best-fit surface plot that describes the relative infectivity of an envelope at varying levels of CD4 and CCR5.

M **The mean infectivity**, M, provides a rough estimate of the overall entry efficiency; it is the mean of the normalized function $F(x, y)$ across the entire range of CD4 (x) and CCR5 (y) surface expression levels represented by the x-y plane.

$\vec{S}$ The gradient of $F(x, y)$ is represented by a **sensitivity vector** in the 2-D plot shown in Fig. 2C. The vector has two metrics: **theta** (θ): the angle of the gradient path relative to the CD4 axis; and **Delta** (Δ): the magnitude or steepness of that gradient.

θ **The angle of the sensitivity vector** (**theta,** θ) measures whether the infectivity of a given Env is more responsive to changes in cell surface levels of CD4 (as θ approaches 0° on the x-axis) or CCR5 (as θ approaches 90° on the y-axis).

Δ **The amplitude of the sensitivity vector** (**Delta,** Δ) measures the amplitude of infectivity response along the gradient; that is, the overall "steepness" of the $F(x, y)$ gradient, complementing the angle of this path defined by θ.

Figure 2 Defining the limiting parameters of sensitivity vector metrics used for profiling HIV-1 entry efficiency. (A) Infectivity of a primary subtype B R5-virus monitored across 25 distinct combinations of CD4 and CCR5 expression levels. The normalized infectivity profile is shown as a 3-D bar graph with the luciferase activity obtained at the highest CD4 and CCR5 induction level set at 100%. **(B-C)** The surface function $F(x, y)$ is used to fit the infectivity data as previously described [34]. The resulting 3-D surface plot can be represented by three metrics that reflect distinct phenotypic properties of the infecting virus envelope: **(B)** the mean infectivity level (M), and **(C)** the angle (θ) and amplitude (Δ) of the sensitivity vector $\vec{S}$ that describes the envelope's response to varying levels of CD4 and CCR5. For clarity, the operational definitions of these metrics, and what they measure with respect to the infectious phenotype of Env, are also indicated. Note that while we have changed the nomenclature of these Affinofile metrics to more intuitively reflect the Env properties they are intended to describe, the fundamental definitions are the same as in Johnston et al. (Ref [34]). Thus, "mean induction" is now termed "mean infectivity", and vector "magnitude" is now termed vector "amplitude".

expression. The gradient of $F(x, y)$ is fit by the sensitivity vector ($\vec{S}$) shown in Figure 2C, representing both the stoichiometric combination of CD4 and CCR5 with the greatest impact on entry across the entire surface (θ) and the magnitude of that impact (Δ) illustrated by the vector field in Figure 2C. For example, a relative increase in θ, driven by a shift in the gradient toward the CCR5 axis (Figure 2C), indicates a greater responsiveness to CCR5. The magnitude of this shifted responsiveness may be comparatively larger (increased Δ) or smaller (decreased Δ), indicating a relative increase in CCR5 usage efficiency or a decrease in both CD4 and CCR5 usage efficiency, respectively. The operational definitions of these parameters are indicated in the panels below Figure 2A-C. Their mathematical definitions and formulations have been reviewed recently [39]. Together, these three metrics quantitatively describe the phenotypic behavior of a given viral envelope in response to changes across a spectrum of CD4 and CCR5 expression levels.

Similar to regular Affinofile cells, GGR Affinofile cells can be used to characterize a range of distinct Env phenotypes (see Additional file 1: Figure S1A-C) and the infectivity profile of each Env can be represented by the set of three metrics (Additional file 1: Figure S1D-F). Notably, all three metrics (θ, Δ, M) for a given Env can be represented on a polar plot and are highly reproducible under standardized conditions (Additional file 1: Figure S1G).

Affinofile metrics illuminate the phenotype of functionally well-characterized point mutants

To further define the biological meaning of the three Affinofile metrics, we examined three point mutants in JR-CSF with well-described effects on CD4 and CCR5 binding. S142N [42] and E153G [43] are both V1 loop mutations that increase the ability of JR-CSF to enter cells with low levels of CCR5 [20,25] or CD4, respectively, while K421D is a "bridging sheet" mutant that reduces the affinity of gp120 for CCR5 [44,45]. Viruses pseudotyped with wild type (wt) JR-CSF, or with S142N or K421D Env mutants were produced and titrated first on Ghost-R5 cells. An equivalent MOI (0.2) of each pseudotype was then used to infect GGR Affinofile cells expressing 25 distinct combinations of CD4 and CCR5 levels. We are cognizant that viral titers are cell-type dependent, but we reasoned that normalizing the infectious inoculum on GGR Affinofile cells using titers obtained from infecting Ghost-R5 cells (where CD4/CCR5 levels are non-limiting) would fairly reveal biologically relevant differences in entry efficiencies when CD4/CCR5 levels do become limiting under certain induction conditions on GGR Affinofile cells.

Compared to wt JR-CSF (Figure 3A), the S142N mutant exhibited enhanced entry at every level of CCR5 at or above a specific threshold level of CD4 (0.4 ng/ml Doxy) (Figure 3B, compare the rows of green, yellow, orange and red bars along the CCR5 axis with Figure 3A). A similar increase in infection was observed for E153G, particularly at low CD4 expression (compare blue and green bars in Figure 3C to A), whereas the K421D mutant showed inefficient entry at low CCR5 levels regardless of how much CD4 was present (Figure 3D, note the low infectivity at 0 and 0.25 μM PonA (<20% of maximum) even when CD4 was maximally induced). S142N was more responsive to changes in CCR5 levels than wt JR-CSF, and this phenotype was reflected as an increase in from 30.5° to 38° for wt JR-CSF and S142N, respectively. Recall that a relative increase or decrease in vector angle indicates that an Env's infectivity is more responsive to changes in levels of CCR5 or CD4, respectively. A summary of the Affinofile metrics is given in Figure 3E, and illustrated in the polar plots below Figures 3A-D.

For S142N, the ability to use CCR5 efficiently also enhanced its infectivity at any given level of CD4; thus, the overall level of infection across the entire matrix of CD4/CCR5 expression is higher. This overall increase in infectivity is reflected in the increase in M from 20 to 40.3 for wt JR-CSF and S142N, respectively (Figure 3E, and also graphically represented by the size of the circle in the polar plot below Figure 3B). This combination of an increase in θ and M support the conclusion that S142N uses CCR5 more efficiently.

E153G, which putatively confers the ability to use low levels of CD4, also exhibited an increased M (32.1) compared to wt JR-CSF (20.1), illustrating that these mutations, both attributed to usage of low CD4 or CCR5 expression, have a broad impact on infectivity across all combinations of CD4 and CCR5. This highlights the inter-dependence of CD4 and CCR5 usage as, for example, a higher CD4 binding affinity is likely to increase the success of gp120-CCR5 engagement. E153G exhibited a stronger response to CCR5 expression than CD4 compared to wt JR-CSF, which is reflected in an increased angle (38°, Figure 3E), matching the same responsive phenotype observed for S142N. That E153G would necessarily result in a lower, or more CD4-responsive, angle than wt JR-CSF or S142N is not obvious given the proposed indirect mechanism by which this mutation primes Env to use low levels of CD4. E153G is positioned distal to the CD4 binding site at the apex of the Env trimer and also results in a higher neutralization sensitivity to the V3 loop conformational Mab 447-52D [43]. Our data supports the conclusion of Clapham and colleagues, that the ability to use low levels of CD4 attributed to E153G is not the direct result of CD4 engagement, but the result of a more fluid and successful transition to CCR5 recognition due to the mutation's effect on V1/V2 mobility [43]. These results

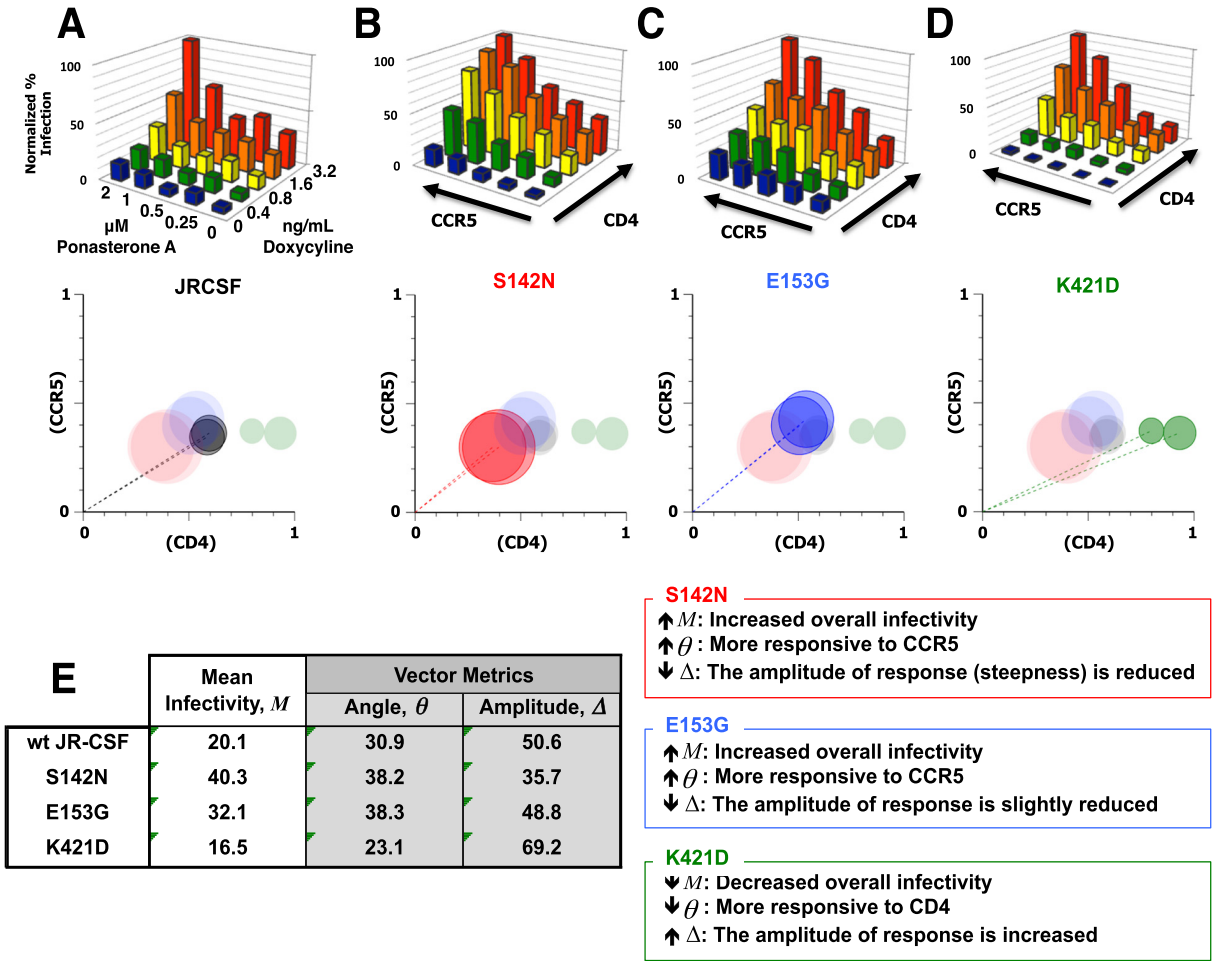

E

	Mean Infectivity, M	Vector Metrics	
		Angle, θ	Amplitude, Δ
wt JR-CSF	20.1	30.9	50.6
S142N	40.3	38.2	35.7
E153G	32.1	38.3	48.8
K421D	16.5	23.1	69.2

Figure 3 Sensitivity vector metrics further illuminate the phenotype of well-characterized point mutants. (A) Infectivity profile of wt JR-CSF (R5) envelope, and three point mutants: **(B)** S142N, **(C)** E153G and **(D)** K421D, previously shown to enhance or perturb CCR5 or CD4 usage with polar plots (beneath) representing the metrics obtained from mathematical analysis of the infectivity profiles **(A-C)**. The vector angle (θ) is the angle between the x-axis and the dotted line. The vector amplitude (Δ) is represented by the length of the dotted line. The mean infectivity (M) is represented by the size of the circle. Data shown is a representative of two experiments. **(E)** Table of the average Affinofile metrics obtained from **(A-D)** and graphically shown in polar plots beneath **(A-D)**. Boxes next to **(E)** describe the phenotypes indicated by each metric relative to wt JR-CSF. The infectivity profile of each Env was independently repeated twice.

extend the phenotype originally ascribed to E153G, visible as an increased infectivity at low levels of CD4 relative to wt JR-CSF (compare blue and green bars in Figure 3C to A), into a more complex interplay of both CD4 and CCR5 that supports the role of this mutation in facilitating CCR5 recognition.

In contrast, K421D exhibited inefficient entry at low levels of CCR5, which is consistent with the known role of this K421 bridging sheet residue in mediating coreceptor interactions [44,45]. Interestingly, at high CCR5 levels (2 and 1 µM PonA), K421D responded more dramatically to increasing levels of CD4 than wt JR-CSF (Figure 3C). These phenotypic properties are reflected by a decrease in θ (30.9° to 23.1° for wt JR-CSF and K421D, respectively), and a concomitant increase in Δ (50.6 to 69.2 for wt and K421D, respectively) (Figure 3D and E). Just as an increase in θ indicates that the S142N and E153G Envs are more responsive to changes in levels of CCR5 expression when compared to wt JR-CSF, a decrease in θ indicates that the K421D Env is more responsive to changes in CD4 levels. The increase in amplitude for K421D is apparent because the differential magnitude of response is markedly greater for K421D at the highest CCR5 and CD4 levels, which is related to the relative lack of infectivity response at low CD4/CCR5 levels. Recall that the amplitude measures the "steepness" of the steepest direction along the surface function $F(x,y)$ used to fit the infectivity data (Figure 2, box). Overall, the mean infectivity (M) for K421D was only moderately decreased compared to wt JR-CSF (16.5 vs 20.1, Figure 3D and E). This likely reflects a balance between the lack of infectivity observed at low CD4/CCR5 levels, and the compensatory increase in the magnitude of K421D's infectivity

response at high CD4/CCR5 levels. These results, collectively, reveal that high levels of CD4/CCR5 may compensate for the inefficient entry exhibited by the K421D mutation at low CCR5 levels. A summary of these metric comparisons and their meaning is included next to Figure 3E.

Affinofile infectivity profile and metrics reflect biologically relevant differences in T-cell tropism

To determine how these Affinofile metrics reflect the ability of a viral Env to infect primary CD4+ T-cells, we infected total PBMCs with pseudotyped luciferase reporter viruses bearing wt JR-CSF, S142N or the K421D Env mutants. Figure 4A shows that the S142N virus infected PBMCs better than wt JR-CSF while the K421D virus exhibited the lowest level of infection. This pattern reflected the θ and M metrics of the respective viruses, as the limiting parameter on primary CD4+ T-cells are the levels of CCR5 (low), not CD4 (high).

Next, we infected CD3/CD28 stimulated CD4+ T-cells with wt JR-CSF, S142N or the K421D Env pseudotyped virus, and assessed the infection of the indicated CD4+ T-cell subsets (Figure 4B) via intracellular p24 staining

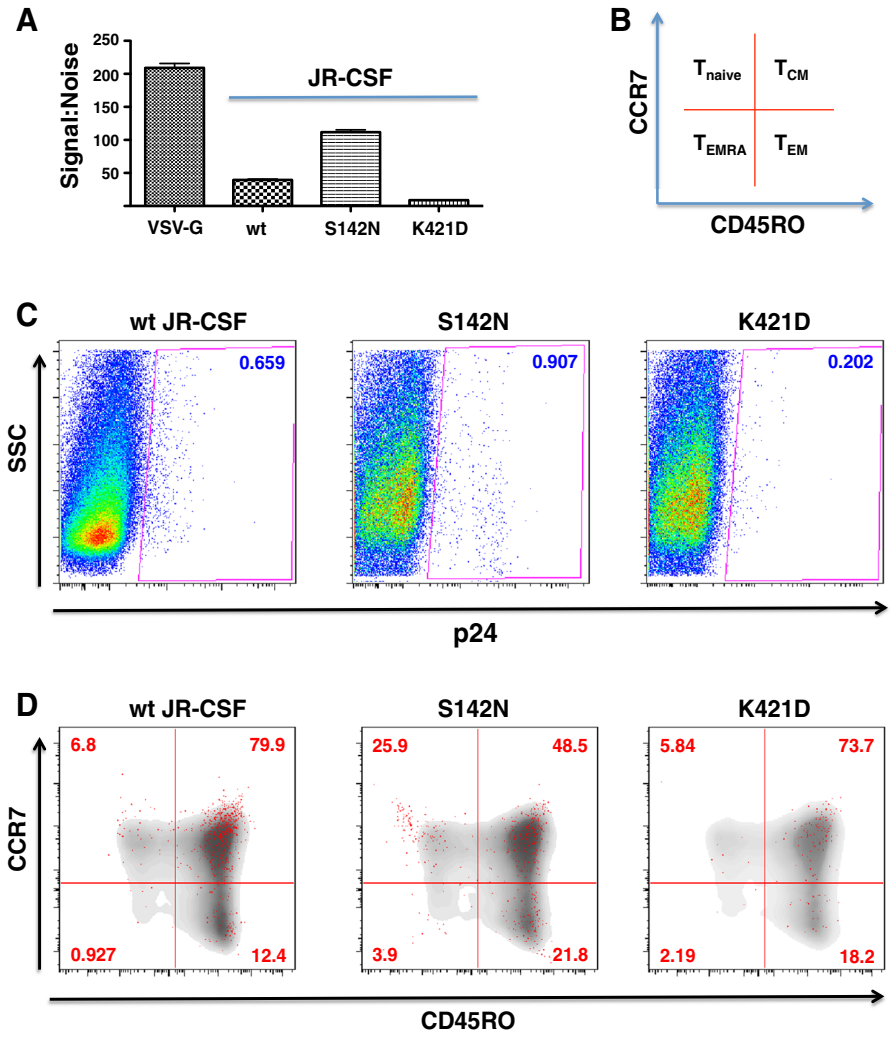

Figure 4 Sensitivity vector metrics reflect biologically relevant differences in T cell subset tropism. (A) Total PBMCs were infected with luciferase reporter pseudotypes bearing wt, S142N, or K421D JR-CSF envelopes. VSV-G pseudotypes were used as positive controls. All infections (except for VSV-G) could be inhibited by maraviroc (>95%). Error bars represent ranges between two experiments. **(B)** Scheme for using CCR7 (PE-Cy7) and CD45RO (FITC) to identify the following T-cell subsets: Naïve (CCR7+ CD45RO-), Central Memory (T_{CM}, CCR7+ CD45RO+), Effector Memory (T_{EM}, CCR7- CD45RO+), and Effector Memory RA (T_{EMRA}, CCR7- CD45RO-). **(C)** and **(D)** CD8-depleted PBMCs were infected with the indicated pseudotyped viruses at an MOI of 20 (as titered on Ghost-R5 cells). Three days post-infection, cells were analyzed by multi-color flow cytometry. **(C)** Infected cells were identified by intracellular p24 staining using PE-conjugated KC57 Mab. **(D)** Uninfected T-cell subset distribution is shown in grey density plot, while infected p24+ cells are overlaid as the red dots. The percent of total p24+ cells are indicated in each quadrant. All infections could be inhibited by maraviroc (>90%). Data shown here is a representative of two independent donors.

and multiparametric FACS analysis three days post-infection. The overall levels of infection, as determined by the percentage of p24+ cells, were consistent with the luciferase reporter results observed in Figure 4A, with S142N infecting the greatest proportion of cells and K421D the lowest (Figure 4C). In most cases, the majority of p24+ cells were CD4+ T-central memory cells (T_{CM}, CCR7 + CD45RO+), with the remainder comprising the effector memory subset (T_{EM}, CCR7-CD45RO+) or the naïve T-cell subset (T_{naive}, CCR7 + CD45RO-) (Figure 4D). It is unclear whether the small number of p24+ cells found in CD4+ T-effector RA + cells (T_{EMRA}, CCR7-CD45RO-) represents a reproducibly infectable population since CD4+ T_{EMRA} cells are thought to be non-permissive for R5 virus infection [46].

Interestingly, the S142N mutant demonstrated not only an increase in overall infectivity, but also an altered pattern of cellular tropism. Compared to wt JR-CSF, the S142N mutant infected almost 4-fold more naïve T-cells (25.9% vs 6.8%) and 2-fold more T_{EM} cells (21.8% vs 12.4%). As a consequence, S142N infected fewer T_{CM} cells compared to wt JR-CSF (48.5% vs 79.9%) (Figure 4D). Although K421D infected fewer CD4+ T-cells, the CD4+ T-cell subset distribution resembled that of wt JR-CSF infection. Thus, the differential ability to use CCR5 as quantified by the GGR Affinofile assay is reflected in the differential ability of the wt and mutant JR-CSF Envs (S142N) to infect CD4+ T-cell subsets where relatively high and uniform CD4 expression is coupled to relatively low and variable CCR5 expression [20,46]. Our results indicate that the distinct entry efficiencies quantified by our GGR Affinofile system reflect the biologically relevant contributions of CD4 and CCR5 usage to primary CD4+ T-cell subset tropism.

Affinofile metrics reveal differences in CD4/CCR5 usage efficiencies between chronic and transmitter/founder derived Envs

An accumulating body of evidence indicates that the majority of primary infections are established by a single viral clone [47-49]. To discern whether relevant differences in entry efficiencies exist between T/F and chronic Envs, we used the GGR Affinofile system to examine the infectivity of T/F Envs (isolated from acutely infected Feinberg stage II or III patients) [50], and compared their Affinofile GGR metrics (θ, Δ, M) with those from a standard panel of chronic Envs. The specific clones used are indicated in [see Additional file 2: Table S1]. The infectivity of each T/F and chronic Env was examined at 25 distinct CD4/CCR5 expression levels [see Additional file 3: Figure S2A-B], and their infectivity metrics (Figure 5A-C) were obtained via VERSA as described in methods.

Figure 5A shows that T/F Envs have a median θ that is significantly lower than that of chronic Envs (15° vs 25°, p = 0.0003), and that this lower θ was associated with a lower Δ (vector amplitude) (Figure 5C). This correlation indicates a diminished responsiveness (lower Δ) that is weighted toward CD4 (lower θ), meaning T/F Envs take advantage of increases in CD4 expression less efficiently than Chronic Envs. The decreased responsiveness to CD4 is most evident at lower, more physiological levels of CCR5 expression, illustrated in Figure 5D and E. The wedge plot in Figure 5F summarizes the distinct T/F and chronic Env phenotypic differences in and observed within the cohort of subtype B Envs examined. Finally, the 2-D contour plots of the averaged infectivity between T/F and chronic Envs across the spectrum of CD4/CCR5 expression levels corroborate the differences indicated by their infectivity metrics: that at low to moderate levels of CCR5 (0–0.5 μM Pon), even the highest level of CD4 allowed only moderate entry levels (40-60%) for the T/F Envs (Figure 5G, compare upper right quadrants). This phenotype is consistent with the observation that T/F Envs, despite being universally CCR5-using, are almost always primary T-cell tropic (high CD4/low CCR5) and not macrophage-tropic (low CD4/high CCR5) [30]. We confirmed that all six of these R5 T/F Envs are indeed non-macrophage-tropic (Figure 5H).

Affinofile metrics reveal that HIV-1 Envs exhibit subtype-specific differences in CD4/CCR5 usage efficiencies

We next used the GGR Affinofile cells to characterize a panel of 28 subtype A, B, C and D Envs [see Additional file 4: Table S2]. As might be expected from a diverse panel of subtype Envs, there was a high degree of intra- and inter-subtype variability in all three metrics (Figure 6A). An additional figure shows the infectivity profile for each subtype Env examined [see Additional file 5: Figure S3]. Despite this variability, significant differences in CD4/CCR5 usage patterns between HIV-1 subtypes can be appreciated. For example, subtype C Envs had the highest θ and M values (Figure 6A), indicating that this subtype, as a group, used CCR5 more efficiently than Envs from other HIV-1 subtypes. The aggregate infectivity data confirms that subtype C Envs do, indeed, achieve a higher level of infection in response to increasing CCR5 levels, especially when CD4 levels are limiting (Figure 6B, compare the lower left quadrants). Interestingly, when CCR5 levels are low, subtype C Envs exhibited markedly reduced levels of infectivity compared to Envs from other HIV-1 subtypes, even at the highest CD4 levels (Figure 6B, compare upper right quadrants). Although this subtle nuance is not captured in Δ, infectivity profiles serve as an alternative method that adds depth to the existing algorithm. Finally, Envs from both HIV-1 subtypes A and C have significantly higher M values than subtype B Envs (Figure 6A). The polar plot in Figure 6C shows that subtype C envelopes can be clearly distinguished from other subtype envelopes based on their and metrics even if the amplitudes (Δ) do not differ significantly between the subtypes.

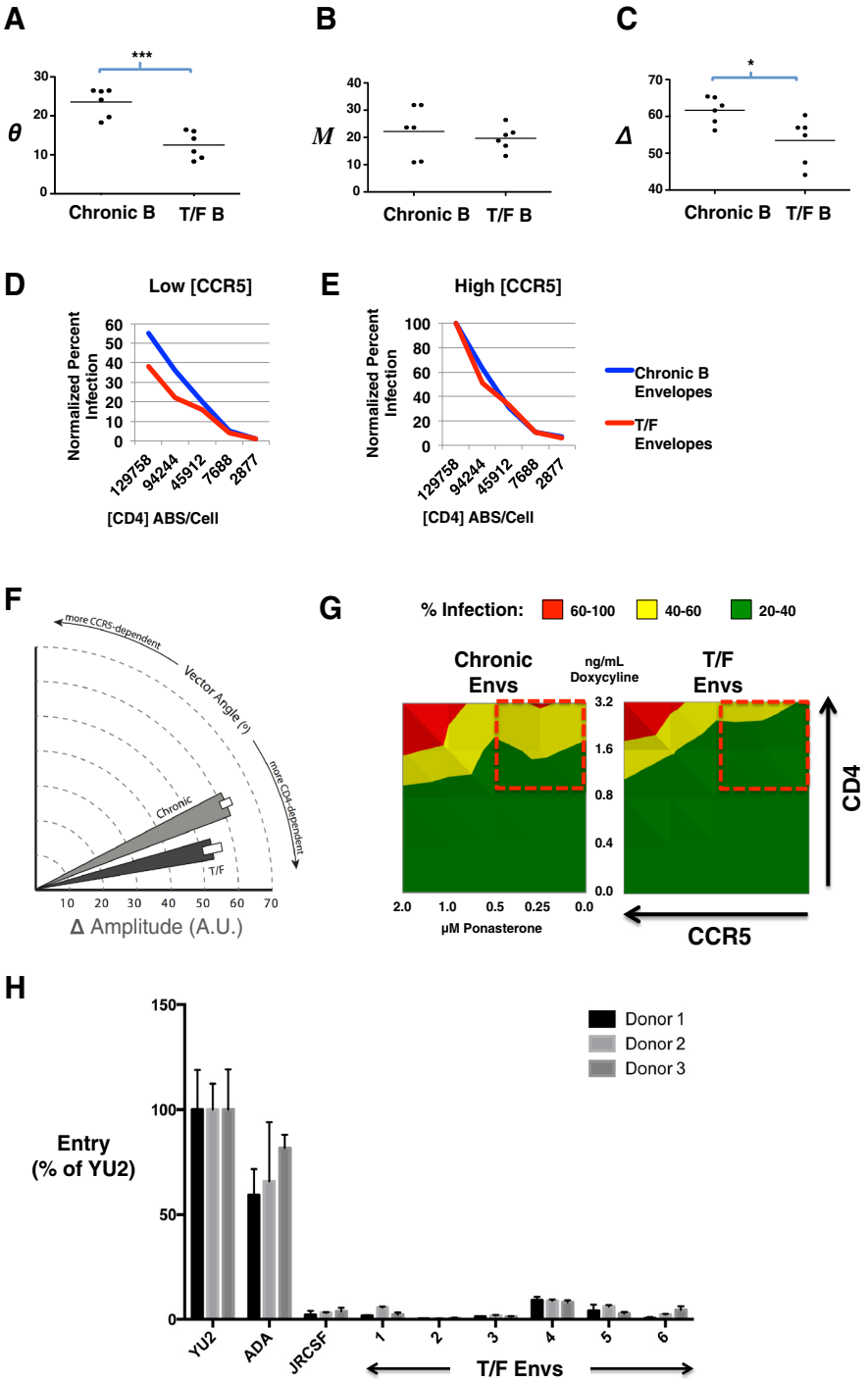

Figure 5 (See legend on next page.)

(See figure on previous page.)
Figure 5 Sensitivity vector metrics reveal differences in CD4/CCR5 usage efficiencies between Transmitter/Founder (T/F) and chronic envelopes. Normalized infection data using T/F and chronic Env clones were analyzed using VERSA. **(A)** Vector angle, (θ), **(B)** mean infectivity (M), and **(C)** vector amplitude (Δ) values were obtained for each Env clone. Each Env was profiled twice, in triplicate, across 25 combinations of CD4/CCR5 expression. Average metrics of 6 individuals from each group (T/F or chronic, N=12) are shown, each group consisting of 900 data points. The median value of each metric for the T/F and chronic Env cohorts is marked by a line. p values were generated by the non- parametric unpaired t test (***p = 0.0003; *p = 0.05). **(D** and **E)** The normalized infectivity for the chronic (blue line) and T/F envelopes (red line) are averaged, and compared as a group at **(D)** low and **(E)** high levels of CCR5 expression, across varying levels of CD4 as indicated. **(F)** Wedge plot of the average angle and amplitude (+/− S.D.) obtained for T/F (dark grey) versus chronic envelopes (light grey). **(G)** The infectivity profile of individual T/F and chronic Envs (from Additional file 5: Figure S3) were averaged to form their respective group profile. 2-D contour plots representing the averaged infectivity profiles of T/F and chronic envelopes are shown. **(H)** T/F Envs and macrophage tropic (YU2, ADA) and non-macrophage tropic (JRCSF) R5 Envs were used to produce Env pseudotyped luciferase reporter viruses, which were subsequently titrated on JC53 cells. Monocyte derived macrophages were inoculated with equivalent infectious units of each reporter virus, and luciferase activity measured in cell lysates at 72hrs post infection. Results of infection in 3 independent donors are shown. Results are means of triplicate wells, and error bars represent standard deviations.

Affinofile profiling reveals that resistance to broadly neutralizing antibodies also results in reduced entry efficiency

Recent technological advancements have resulted in the cloning and characterization of numerous broadly neutralizing antibodies (BNabs) with increased potency and breath of coverage compared to the "classical" BNAbs such as b12, 2G12 and 2F5. PG9/PG16 and VRC01 represent two of the major classes of these "next generation" BNabs with non-overlapping epitopes [51-53]. Despite the breath and potency of these BNAbs, single point mutations, N160K and N279/280A, can confer resistance to PG9/PG16 and VRC01, respectively [51,53]. N160 and N279/280 are highly conserved residues across HIV-1 subtypes [See Additional file 6: Figure S4A], which suggest that these residues are under selective pressure.

To determine potential entry efficiency consequences related to these BNab resistance mutations we generated resistant N160K and N279/280A mutants in 24 Envs representing subtypes A through D, and examined their CD4/CCR5 entry efficiencies using the GGR Affinofile system. Figure 7A, B and C, shows the mean infectivity profiles for wt Envs (n = 12, 3 each from subtype A-D), and their respective isogenic N160K, and N279/280A mutants, each Env examined across 25 distinct CD4/CCR5 expression levels. An additional figure shows the individual infectivity profile for all 36 Envs examined [see Additional file 6: Figure S4]. The PG9/PG16 (N160K) and VRC01 (N279/280A) resistance mutations reduce the efficiency of entry; both requiring higher levels of CD4 and CCR5 to achieve similar levels of infection as their wt counterparts. This can be appreciated by comparing the CD4/CCR5 expression level combinations that give rise to low levels of infection (green areas), or conversely, those that give rise to the highest level of infection (red areas), between the wt and mutant Envs (Figure 7A-C). This reduced entry efficiency phenotype across all subtypes tested is quantitatively reflected in the values, where the average M for PG9/PG16 and VRC01 resistant mutants is lower than that of their wt counterparts (Figure 7D and E). However, due to marked variability when comparing across all HIV-1 subtypes, only the difference between VRC01 resistance mutants and wt reached significance (p = 0.007). Our results suggest that resistance to BNAbs comes at the cost of reduced HIV-1 entry efficiency, and provides one functional explanation for the high conservation of these residues across HIV-1 subtypes. Both these reasons bode well for vaccine design that will elicit these kinds of BNAbs.

Discussion

The Affinofle system and associated VERSA metrics have provided investigators a more quantitative method to characterize viral entry efficiency as a function of CD4 and CCR5 expression. Quantitative comparisons of these three VERSA metrics—Mean infectivity (M), Vector Angle (θ) and Amplitude (Δ)—have facilitated our understanding of how CD4/CCR5 usage efficiencies correspond to distinct Env phenotypes associated with resistance to CCR5-inhibitors, and the myriad of *in vitro* or *in vivo* selective pressures that result in differential or altered cell tropism [28,34,36,37,39,54-56].

Efficiency of CD4/CCR5 usage and T cell subset tropism

A critical feature of our GGR Affinofile system is the ability to distill the aggregate entry phenotype of Env into three metrics. Here, we demonstrate that these VERSA metrics reflect biologically relevant phenotypes for wt JR-CSF Env, and two point mutants (S142N and K421D) known to modulate its affinity for CCR5, and the complex interplay of CD4 and CCR5 usage associated with mutations that affect conformational transitions (E153G). Specifically, S142N, which had larger θ and M values relative to wt JR-CSF, also infected total PMBCs better. This increase infectivity may be due to an expanded CD4+ T-cell subset tropism as S142N pseudotyped virions infected a larger portion of naïve T-cells relative to their wild-type counterparts (Figure 4C, 25.9% vs 6.8%). Intriguingly, naïve T-cells have undetectable levels of CCR5 by FACS

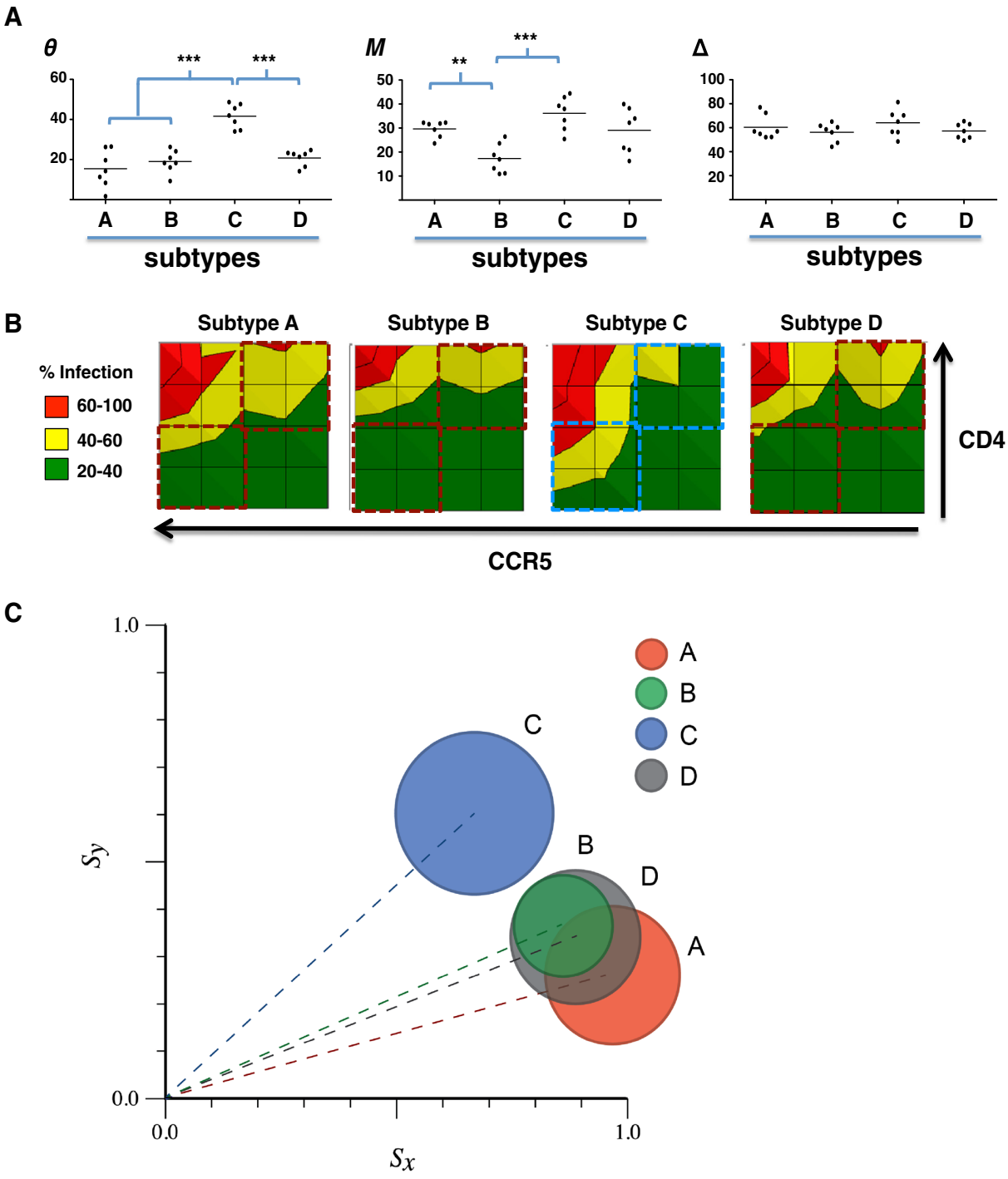

Figure 6 HIV envelopes exhibit subtype-specific differences in CD4/CCR5 usage efficiencies. (A) Normalized infection data from each subtype A, B, C and D envelope clones (n = 28) were analyzed by VERSA. The vector metrics were averaged for at least two independent infections (with a variance <5%) for each envelope in each subtype group. Vector angle (*θ*), mean infectivity (*M*), and vector amplitude (Δ) values for each envelope are shown as grouped by subtypes. P values were generated by the non- parametric unpaired *t* test ($p^{***} < 0.005$, $^{**}p < 0.05$). **B)** 2-D contour plots of the average infectivity profile for each subtype, generated and color coded as in Figure 4G. The colored dashed square boxes compare the infectivity differences noted between subtype C (blue) Envs and others (red) in the lower left (LL) and upper right (UR) quadrants. Each Env clone was independently profiled twice. **(C)** Polar plot of the averaged sensitivity vectors obtained from each subtype, generated as in Figure 3E.

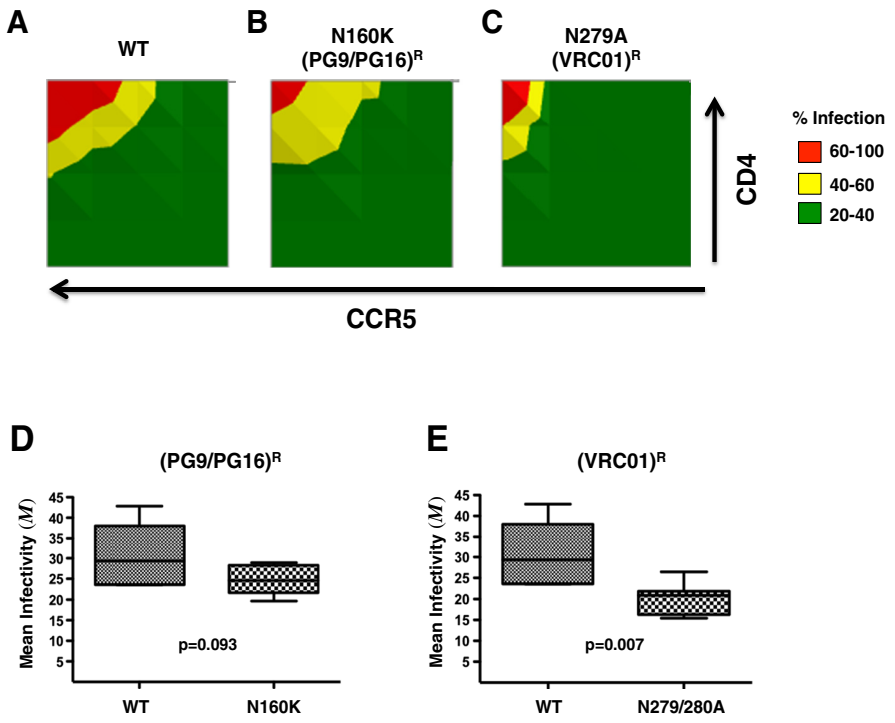

Figure 7 Affinofile profiling reveals that resistance to broadly neutralizing antibodies (BNAbs) also results in reduced entry efficiency. **(A-C)** N160K and N279/280A mutations were engineered into a random sample of 12 subtype A-D Envs. The resultant $(PG9/PG16)^R$ and $(VRC01)^R$ resistant Envs were assayed for CD4 and CCR5 usage efficiency along with their parental BNAb sensitive Envs. GGR Affinofile profiling was performed as previously described. 2-D contour plots of the averaged infectivity profiles for **(A)** WT, **(B)** $(PG9/PG16)^R$, and **(C)** $(VRC01)^R$ Envs are shown. The infectivity profile for the individual Envs are shown in supplementary Figure S5. Axes and color-codes are identical to previous contour plots. **(D-E)** The median values and interquartile ranges of the Mean infectivity (*M*) are shown for $(PG9/PG16)^R$ or $(VRC01)^R$ resistant Envs compared to their WT counterparts. P values calculated via a non-parametric paired *t*-test.

[47,57,58], much like the CCR5 "FACS-negative" T-cell lines (Molt 4 and SupT1) that the S142N Env virus is known to infect in a CCR5-dependent manner [25]. Conversely, K421D, which had the smallest θ and M values, also infected PBMCs with the least efficiency, and lacked the expanded tropism seen with the S142N mutant.

Our GGR/Affinofile system can interrogate an Env phenotype across a fuller fitness landscape than traditional assays. The ability to evaluate infectivity across a broad spectrum of CD4 and CCR5 expression levels underscores the innate inter-dependence of CD4 and CCR5 levels in the context of infection. For example, although the enhanced macrophage tropism of the E153G mutant was originally attributed to increased CD4 binding affinity and more efficient infection on cells expressing low levels of CD4, our Affinofile assay describes an Env that is more responsive to changes in CCR5 than wt JR-CSF ($\theta = 38.3°$ and 30.9° respectively, Figure 3E). Our results complement and expand published results on E153G, and provide direct support for the proposed effect of E153G on V1/V2 loop flexibility, which can affect exposure of both the CD4 and CCR5 binding sites. The latest structural evidence also supports such a model [59].

What is the utility of being able to quantify the efficiency of CD4/CCR5 usage through a set of standardized metrics? For S142N, the ability to use lower levels of CD4 and CCR5 for entry correlates with its expanded tropism for naïve CD4+ T cells. HIV-1 preferentially infects memory, rather than naïve CD4+ T cells [60-62]. However, loss of naïve T-cells is also clearly associated with immune system decline and disease progression, but is thought to be due to secondary factors such as lymph node fibrosis, which destroys the regenerative niche required for maintaining naïve T-cells [63,64]. To our knowledge, the infection of naïve T-cells in lymph nodes of late stage patients have not been directly examined. Since late stage R5 isolates are also more efficient at using low levels of CD4 and CCR5 for entry [12,65], it is possible that infection of naïve T-cells by late stage R5 Envs might contribute to the diminishment seen. Currently, macrophage-tropism is widely used as a surrogate measure for R5 Envs that can use low levels of CD4 and/or CCR5 for entry [66], but it is not clear whether macrophage-tropic Envs also have an expanded tropism for naïve CD4+ T-cells. Use of our GGR Affinofile system and VERSA metrics to characterize extended panels of R5 macrophage-tropic and R5 non-

macrophage tropic Envs will help shed light on this important issue related to R5 Env pathogenesis. Intriguingly, even a binary read-out, such as an increased ability to infect $CD4^{low}/CCR5^{high}$ relative to $CD4^{high}/CCR5^{high}$ Affinofile cells, has been observed in CSF-derived R5 Envs from a patient many months *before* the patient developed HIV-1 associated dementia [67]. Thus, it would also be of interest to determine the VERSA metrics of R5 Envs from a broader array of longitudinal cohorts to evaluate whether a certain pattern of VERSA metrics is predictive of pathogenicity or disease progression.

T/F and chronic Envs

~70-80% of heterosexual or IV drug use HIV-1 transmission cases are established by a single transmitted/founder (T/F) virus clone [50,68-71]. Concerted efforts have been made to discern genotypic and phenotypic differences between T/F and chronic Envs, since such differences may inform vaccine design, shed light on the biology of HIV-1 transmission and pathogenesis, or facilitate development of strategies to prevent HIV-1 transmission [47,48]. While T/F Envs are enriched in genotypic features such as an overall reduction in the number of potential N-linked glycosylation sites (PNGS) [72], no unique genetic signatures can be ascribed only to T/F Envs. Phenotypic differences between T/F and chronic Envs also appear subtle: no overt differences were found in multiple assays such as entry/fusion efficiency into cells expressing high or low levels of CD4/CCR5, infection of CD4+ T-cell subsets, dendritic cell mediated *trans*-infection, and sensitivity to entry inhibitors [73-77]. However, moderate increases in sensitivity to neutralization by the CD4 binding site antibody b12, and more marked resistance to sCD4 inhibition, have been reported for some cohorts of subtype B T/F Envs relative to chronic Envs [75,76].

Our Affinofile profiling of a small panel of subtype B T/F and chronic Envs reveals moderate but significant differences in the CD4/CCR5 usage efficiencies. The differences are subtle, but the combination of θ and Δ clearly distinguishes the T/F Envs from the chronic Envs (Figure 5F). These data also indicate that T/F Envs are less efficient at using CD4, as a diminished responsiveness (lower Δ) is associated with CD4 (lower θ) without a significant change in overall infectivity (M) (Figures 5A, B and C). The implied decrease in CD4 usage efficiency exhibited by the T/F Envs in our study is consistent with the aforementioned cohort of T/F Envs with increased resistance to sCD4 neutralization [76]. However, sensitivities to sCD4 or b12 neutralization are surrogate markers for CD4 utilization, and neither directly measures the true entry phenotype of a virus with regards to CD4/CCR5 usage efficiency. sCD4 sensitivity does not always correlate with gp120-CD4 binding affinity ([78] and references therein), and b12 neutralization can be affected by epitope changes that don't affect CD4 binding [79]. For example, T/F Envs are enriched for the loss of a particular N-glycan site, mediated by *not* having a Thr at position 415 (T415X), that allows better access to key b12 binding residues at positions 417–419 [72]. Thus, the increased sensitivity to b12 neutralization may be associated with a genetic signature (T415X) enriched in T/F Envs, rather than being a general property of T/F Envs *per se*. In our cohort, there is no obvious relationship with sensitivity to b12 or sCD4 neutralization even though all but one T/F Env has the T415X signature [see Additional file 2: Table S1]. Yet, infectivity profiling across the full spectrum of CD4/CCR5 expression levels and VERSA metrics were able to reveal differences in entry phenotypes between T/F and chronic Envs. Clearly, our findings need to be extended by examination of larger groups. However, recent evidence suggests that T/F envs and chronic Envs can differ in their ability to use the maraviroc bound form of CCR5, but this phenotype is more obviously revealed only on $CD4^{high}/CCR5^{high}$ Affinofile cells [80]. The ability to use the MVC-bound form of CCR5 in this case is likely a surrogate marker for an expanded promiscuity in the use of CCR5 conformations. These results are consistent with our current findings and suggest that the full Affinofile profiling may have the requisite sensitivity to reveal subtle but real differences in Env phenotypes related to HIV-1 transmission.

The pattern of responses to CD4 and CCR5 observed using the Affinofile system and their correlation to infection on primary cells with different CD4 and CCR5 expression levels are naturally sensitive to alternate CCR5 conformations and post-translational modifications [81-89] that may or may not support entry. To achieve the most representative measure of CCR5 in the context of HIV entry, expression is quantified in terms of cell-surface epitopes specifically recognized by the broadly and potently neutralizing CCR5 Mab 2D7, a biologically relevant, surrogate measure of the majority of CCR5 that is accessible and functional as bona fide entry coreceptors [90]. However, we cannot rule out that some Envs can use qualitatively different conformations of CCR5 that are not represented by 2D7 antibody binding sites.

Subtype Env specific differences

Subtype C viruses, in pure or recombinant forms, comprise the majority of HIV-1 infections worldwide, and are associated with heterosexual transmission. Subtype Envs do exhibit phenotypic differences as evidenced by a significant correlation between CCR5 and FPRL1 usage for subtype A and C Envs, and between CCR5 and CCR3 usage only for subtype B Envs [91,92]. These differences in alternate coreceptor usage in highly permissive NP2/CD4/CoR cells likely reflects the different evolutionary histories of the subtype Envs, and is more apt to be a surrogate marker for the efficiency of CCR5 usage or the use of a specific conformation of CCR5.

Subtype C Envs are indeed transmitted more efficiently *in utero* than subtype A or D Envs [93]. Thus, it seems reasonable to intuit that subtype C Envs are more efficient in cell entry and/or transmission. However, in vitro and ex vivo assays indicate that viruses bearing subtype C Envs are invariably outcompeted by other subtype Envs in PBMC outgrowth assays [94-96]. This decrease in replicative fitness presents an explanatory conundrum that may be illuminated by our Affinofile data. Our GGR Affinofile profiling results indicate that the average subtype C Env used CCR5 more efficiently than the other subtype Envs, but this was only true at low to moderate levels of CD4 (Figure 6B, compare lower left quadrants). Future refinements of the metric algorithm can provide more detail to these subtle nuances. At high levels of CD4 but lower (more physiologic) levels of CCR5 such as would be present on activated PBMCs (Figure 6B, compare upper right quadrants), subtype C Envs are *less* efficient at entry. The difference in entry efficiencies between subtype C and the other subtype Envs, reflected in the UR and LL quadrants of their infectivity profile (Figure 6B), might provide an explanatory framework that accounts for both the decreased replicative fitness observed in vitro (on activated PBMCs), and the notion that subtype C Envs must be more efficient at entry and/or transmission at some level. The VERSA metrics and infectivity profiles in Figure 6 quantify a genuine phenotypic difference between subtype C and other subtype Envs, and can serve as a reference point for future studies into their physiological correlates. Despite the small number of Envs examined (n = 28, 7 for each subtype), these are well-characterized reference subtype Envs, chosen carefully to represent acute/early infection isolates, so as to compare the Env phenotypes that might be specific to each subtype before disease stage-specific selective pressures come into play [see Additional file 4: Table S2].

BNAb resistance mutations

Our Affinofile profiling suggests that mutations in Env that confer resistance to at least two BNAbs come at a fitness cost. This is perhaps not surprising since the mutated residues N160 and N279/280 are themselves highly conserved amongst HIV-1 subtypes suggesting that selective pressures are at play. Nevertheless, we engineered mutations into 12 Envs from 4 different subtypes, and observed a general trend that N279/280A $(VRC01)^R$ mutations, and to a lesser extent, the N160K $(PG9/PG16)^R$ mutations decrease the mean infectivity without a significant impact on the other two VERSA metrics. While the $(VRC01)^R$ mutation near the CD4bs was likely to affect entry efficiency, it was not clear that the $(PG9/PG16)^R$ mutation would. Indeed, the impact on entry efficiency is much greater for the $(VRC01)^R$ mutation compared to the $(PG9/PG16)^R$. It remains to be seen if resistant mutations to the latest generation of BNAbs all come at a fitness cost or whether they are epitope dependent. We recognize that our results regarding the impact of BNAb resistant mutations on entry efficiency need to be confirmed and expanded with a larger set of mutants and antibodies. Our GGR Affinofile system provides an appropriately high throughput methodology to facilitate such future studies. The results from these further studies might inform the engineering of the most appropriate immunogen that will elicit the BNAbs that will best constraint the development of resistance.

Conclusions

In sum, Affinofile profiling not only interrogates the functional plasticity of HIV-1 Env in response to a spectrum of CD4 and CCR5 expression levels, it provides and distills the multi-dimensional data that captures this functional plasticity. Thus, Affinofile profiling may be a more sensitive method for discerning subtle but real differences in entry phenotypes that are not detected by other standard assays for evaluating CD4/CCR5 usage efficiency. A database of carefully curated VERSA metrics will help standardize the phenotypic characteristics of Envs from multiple cohorts and facilitate future studies into pathophysiology associated with Env phenotypes. We are currently creating a panel of GGR Affinofile cell lines that express alternate coreceptors as well as hybrid and mutant CCR5 that will help extend and refine such studies.

Methods

Virus production

Envelopes and the SG3Δenv vector were obtained through the NIH AIDS and Research and Reference Reagent Program. Details and provenance of all envelopes used are given in Additional file 2: Table S1 and Additional file 4: Table S2. Pseudovirons were generated by cotransfection of 293T cells with Env-deleted SG3Δenv vector and Env expressing vector at a 3:1 ratio with Bioline Bio T transfection reagent. 72 hours post transfection, viral supernatant was collected, clarified by low speed centrifugation and stored at −80°C. The number of infectious virus particles was determined by titration on Ghost HI-R5 cells, as described previously [97].

CD4 and CCR5 cell surface expression

CD4 and CCR5 surface expression levels were determined by quantitative flow cytometry (qFACS) as described previously [34,39].

GGR vector cloning

pNL-GFP-RRE was obtained through the NIH AIDS Research and Reference Reagent Program [40,41]. pNL-GFP-RRE was digested with SacI and SalI. The *Gaussia* luciferase gene was PCR amplified from pCMV-Gluc (Promega). The PCR product was digested with SacI and

SalI and subsequently ligated into the precut pNL-GFP-RRE vector to form pNL-GGR.

GGR virus production

GGR-expressing lentiviral transducing viruses were produced by cotransfection of 293T cells with pNL-GGR vector, pCMVΔR8.2, and pVSV-G at a ratio of 10:10:1, respectively, using the calcium phosphate method. Two days post transfection the viral supernatant was collected, clarified by low speed centrifugation, and filtered through a .45μM filter. Viral supernatant was then concentrated by ultracentrifugation at 32,000 x g for 90 minutes and stored at -80C.

GGR single cell cloning

Affinofile cells were seeded into a 48 well plate at 5 X 10^4 per well. 24 hours later cells were infected with 1 μg (p24 equivalents) of VSV-G pseudotyped GGR virus. Infected cells were then spinoculated for 2 hours at 37 degrees and 770 x g. Cells were washed once with PBS and replenished with fresh D10/B media. Cells were allowed to grow in a 10cm culture dish for three weeks, by splitting and replenishing media every 2–3 days. Single cell clones were then obtained by limiting dilution into 96-well plates. Single cell clones were passaged for three weeks, and clones with stable integration of the pNL-GGR vector were screened for optimal signal to noise ratio of *Gaussia* luciferase activity in the supernatant upon infection with JR-CSF virus. Selected clones were then screened for ones that still maintained a robust CD4 and CCR5 inducible response to doxycycline and ponasterone A.

T cell infection

Leukopacks from healthy uninfected donors were obtained from the virology core at the UCLA CFAR. For purification of CD4+ T-cells, buffy coats containing peripheral blood mononuclear cells (PBMC) were first Ficoll-purified, and CD8+ T cells were depleted using Invitrogen CD8 Dynabeads. CD8 depleted PBMCs were incubated in RPMI supplemented with IL-2, 20% FCS and stimulated with CD3/CD28 coupled Dynabeads (Invitrogen) for three days. Three days post-stimulation, cells were washed twice and infected with indicated virus. Infection was synchronized by spinoculation for 2 hours at 2,000 rpm (770x *g*) at 4°C. After spinoculation, infectious media was replaced with fresh media. Three days post infection cells were collected and stained for T-cell subset markers CD4 (RPT-4), CD3 (OKT3), CCR7 (3D12) CD45RA (Hl100) (Ebiosciences), and intracellular p24 (KC57, BD Pharmingen).

GGR affinofile assay

GGR Affinofile cells were seeded in a 96 well plate at 2 X 10^4 cells/well. Simultaneously, cell surface expression of CD4 and CCR5 was induced with 0 to 4.0 ng/mL of Doxycycline and/or 0 to 2 μM of Ponasterone A, respectively. 18hrs later the induction media was removed. Each well of cells was then inoculated with HIV-1 at an MOI of 0.25, as determined on Ghost R5 cells. The cells were then spinoculated (770 x *g*) for 2 hours at 37° C. Infectious supernatant was then replaced with fresh D10 media (DMEM with 10% FBS and 1% Pen/Strep). At the indicated timepoints (hours post-infection) used in the various assays, 10 μl of supernatant was combined with 10 μl of substrate detection buffer (SDB: 50mM Tris–HCl (pH 7.5), 20% glycerol, 0.1% TritonX-100, 10mM DTT). The supernatant and SDB mix was assayed for *Gaussia* luciferase (GLuc) activity using Coelenterazine substrate in 96-well black plates according to manufacturer's instructions (NEB, Ipswich, MA). GLuc-catalyzed bioluminescence was detected on the TECAN Infinite® M1000 microplate reader via luminescence scanning with an integration time of 8 seconds. All test were done with mararviroc controls to confirm exclusive CCR5 coreceptor usage.

Data analysis

The Affinofile infectivity metrics were derived from raw or normalized data using the VERSA (Viral Entry Receptor Sensitivity Analysis) computational platform as previously described [34]. The considerations for the use of raw versus normalized data, and the limitations of each have been extensively reviewed [39].

Additional files

Additional file 1: Figure S1. Isolates with different CD4 and CCR5 usage can be represented by distinct 3-D surface plots. GGR Affinofile cells induced to express 25 different combinations of CD4 and CC5 were infected with the (A) "CD4-independent" R5 SIV316, (B) R5X4 89.6, or (C) X4 IIIB pseudotyped viruses. The SIV 316 infection profile indicated that SIV 316 is much more sensitive to changes in CCR5 levels, and is relatively insensitive to varying CD4 levels. Conversely, the HIV IIIB infectivity profile indicated a phenotype that was dependent on changes in CD4, but was relatively insensitive to changes in CCR5. This phenotype can be attributed to the use of low levels of CXCR4 present on the HEK293 cells, the parental derivative of GGR Affinofile cells. The 89.6 virus demonstrated an infectivity profile that was equally sensitive to changes in CD4 and CCR5 levels. The distinct infectivity profiles for each Env demonstrated in A-C can be mathematically transformed into the corresponding 3-D surface plots shown in D-F. These three envelopes represent the diverse range of infectivity profiles that can be demonstrated in GGR Affinofile cells. (G) A polar plot representing the three metrics describing the infectivity profiles of the three viruses is shown. SIV316 has a vector angle closest to 90 degrees indicating a greater infective response to CCR5 expression and reflecting the CD4-independence of this Env. Conversely, HIV IIIB has a vector angle closest to zero degrees, endorsing an X4 tropism that is manifested as CCR5 independence. 89.6 has a vector angle of ~45 degrees indicating that it is equally sensitive to changes in CD4 and CCR5 levels. Each circle represents one independent experiment profiling infectivity across 25 distinct CD4/CCR5 expression levels.

Additional file 2: Table S1. List of T/F and chronic envelopes.

Additional file 3: Figure S2. Infectivity profiles of Chronic and T/F Envelopes. The infectivity profile for individual chronic (A) and T/F (B) derived envelopes across a spectrum of CD4 and CCR5 expression levels

were generated and plotted as described in the Materials and Methods. One representative experiment out of two is shown. Each infectivity data point was performed in triplicate. The contour plots are arranged from highest to lowest mean infectivity (*M*), from left to right. (C) T/F Envs and macrophage tropic (YU2, ADA) and non-macrophage tropic (JRCSF) R5 Envs were used to produce Env pseudotyped luciferase reporter viruses, which were subsequently titrated on JC53 cells. Monocyte derived macrophages were inoculated with equivalent infectious units of each reporter virus, and luciferase activity measured in cell lysates at 72hrs post infection. Results of infection in 3 independent donors are shown. Results are means of triplicate wells, and error bars represent standard deviations.

Additional file 4: Table S2. List of subtype envelopes.

Additional file 5: Figure S3. Infectivity profiles of Subtype A-D Envelopes. The infectivity profile for indivudal Subtype A, Subtype B, Subtype C and Subtype D derived Envs (A-D, respectively) across a spectrum of CD4 and CCR5 expression levels were generated and plotted as described in the Materials and Methods. One representative experiment out of at least two is shown. The contour plots are arranged from highest to lowest mean infectivity (*M*), from left to right.

Additional file 6: Figure S4. Infectivity profiles of $(PG9/PG16)^R$ or $(VRC01)^R$ Envs. (A) Consensus and/or predicted ancestral Env sequences from subtypes A-D were obtained from the Los Alamos HIV sequence database (http://www.hiv.lanl.gov), and the amino acid sequences from the relevant regions aligned. Arrows highlight location of conserved residues where single point mutations were engineered to confer PG9/16 (N160K) or VRC01 (N279/280A) resistance. (B-D) 2-D contour plots of the infectivity profile for individual Envs are shown for the wild-type parental WT (A), and the corresponding N160K (B), and N279/280A (C) mutants. Subtype specific Envs (A1-3, B1-3, C1-3) refer to the Env clones listed in Additional file 4: Table S2. Axes and color-codes are identical to previous contour plots. Contour plots are ordered based on the *M* values of the parent Env (highest to lowest, from left to right).

Competing interests
The authors declare they have no competing interests.

Authors' contributions
KC generated the system, performed the major experiments, and drafted the manuscript. NEW helped with the analysis, wrote some of the programs for data presentation, and finalized the figures and text for submission. TC formulated the mathematical analysis and VERSA metrics, and helped in interpreting the data. KB and JS performed the confirmatory assays on primary cells. PRG participated at all stages of the manuscript, providing invaluable input during multiple revisions. BL conceived of the study, and participated in its design and coordination and helped to draft the manuscript. All authors read and approved the final manuscript.

Acknowledgements
BL and KC acknowledge seed grant and fellowship support from the UCLA AIDS Institute and the UCLA Center for AIDS Research (AI028697). Development of the Affinofile system was supported by NIH grant R21 AI092218 (BL), and NSF grant DMS-1021818 (TC). PRG is the recipient of an Australian Research Council Future Fellowship (FT2), and is supported by grants from the Australian National Health and Medical Research Council (1006543 and 1022066), and acknowledges the contribution to this work of the Victorian Operational Infrastructure Support Program received by the Burnet Institute. KC and NEW are supported by fellowships from the Microbial Pathogenesis (NIH T32 AI07323) and Cellular & Molecular Biology Training Grants (NIH T32 GM007185), respectively. We thank Anne Ellett for assistance with macrophage infection assays.

Author details
[1]Department of Microbiology, Immunology, and Molecular Genetics, Los Angeles, USA. [2]Department of Biomathematics, University of California at Los Angeles, Los Angeles, CA, USA. [3]Center for Biomedical Research, Burnet Institute, Melbourne, VIC, Australia. [4]Department of Infectious Diseases, Monash University, Melbourne, VIC, Australia. [5]Department of Microbiology and Immunology, University of Melbourne, Melbourne, VIC, Australia. [6]Department of Microbiology, Icahn School of Medicine at Mount Sinai, One Gustave L. Levy Place, #1124, New York, NY 10029, USA.

Received: 20 January 2014 Accepted: 3 June 2014
Published: 23 June 2014

References
1. Wilen CB, Tilton JC, Doms RW: **Molecular mechanisms of HIV entry.** *Adv Exp Med Biol* 2012, **726:**223–242.
2. Connor RI, Sheridan KE, Ceradini D, Choe S, Landau NR: **Change in coreceptor use correlates with disease progression in HIV-1–infected individuals.** *J Exp Med* 1997, **185:**621–628.
3. Bjorndal A, Deng H, Jansson M, Fiore JR, Colognesi C, Karlsson A, Albert J, Scarlatti G, Littman DR, Fenyo EM: **Coreceptor usage of primary human immunodeficiency virus type 1 isolates varies according to biological phenotype.** *J Virol* 1997, **71:**7478–7487.
4. Spira S, Wainberg M, Loemba H, Turner D, Brenner B: **Impact of clade diversity on HIV-1 virulence, antiretroviral drug sensitivity and drug resistance.** *J Antimicrob Chemoth* 2003, **51:**229–240.
5. Gorry PR, Ancuta P: **Coreceptors and HIV-1 Pathogenesis.** *Curr HIV/AIDS Rep* 2010, **8:**45–53.
6. Jakobsen MR, Cashin K, Roche M, Sterjovski J, Ellett A, Borm K, Flynn J, Erikstrup C, Gouillou M, Gray LR, Saksena NK, Wang B, Purcell DF, Kallestrup P, Zinyama-Gutsire R, Gomo E, Ullum H, Ostergaard L, Lee B, Ramsland PA, Churchill MJ, Gorry PR: **Longitudinal analysis of CCR5 and CXCR4 usage in a cohort of antiretroviral therapy-naive subjects with progressive HIV-1 subtype C infection.** *PLoS One* 2013, **8:**e65950.
7. Trkola A, Dragic T, Arthos J, Binley JM, Olson WC, Allaway GP, Cheng-Mayer C, Robinson J, Maddon PJ, Moore JP: **CD4-dependent, antibody-sensitive interactions between HIV-1 and its co-receptor CCR-5.** *Nature* 1996, **384:**184–187.
8. Blaak H, Ran LJ, Rientsma R, Schuitemaker H: **Susceptibility of in vitro stimulated PBMC to infection with NSI HIV-1 is associated with levels of CCR5 expression and beta-chemokine production.** *Virology* 2000, **267:**237–246.
9. Li S, Juarez J, Alali M, Dwyer D, Collman R, Cunningham A, Naif HM: **Persistent CCR5 utilization and enhanced macrophage tropism by primary blood human immunodeficiency virus type 1 isolates from advanced stages of disease and comparison to tissue-derived isolates.** *J Virol* 1999, **73:**9741–9755.
10. Tuttle DL, Anders CB, Aquino-De Jesus MJ, Poole PP, Lamers SL, Briggs DR, Pomeroy SM, Alexander L, Peden KW, Andiman WA, Sleasman JW, Goodenow MM: **Increased replication of non-syncytium-inducing HIV type 1 isolates in monocyte-derived macrophages is linked to advanced disease in infected children.** *AIDS Res Hum Retrov* 2002, **18:**353–362.
11. Smit TK, Wang B, Ng T, Osborne R, Brew B, Saksena NK: **Varied tropism of HIV-1 isolates derived from different regions of adult brain cortex discriminate between patients with and without AIDS dementia complex (ADC): evidence for neurotropic HIV variants.** *Virology* 2001, **279:**509–526.
12. Gray L, Sterjovski J, Churchill M, Ellery P, Nasr N, Lewin SR, Crowe SM, Wesselingh SL, Cunningham AL, Gorry PR: **Uncoupling coreceptor usage of human immunodeficiency virus type 1 (HIV-1) from macrophage tropism reveals biological properties of CCR5-restricted HIV-1 isolates from patients with acquired immunodeficiency syndrome.** *Virology* 2005, **337:**384–398.
13. Gorry PR, Francella N, Lewin SR, Collman RG: **HIV-1 envelope-receptor interactions required for macrophage infection and implications for current HIV-1 cure strategies.** *J Leukoc Biol* 2014, **95:**71–81.
14. Sterjovski J, Churchill MJ, Ellett A, Gray LR, Roche MJ, Dunfee RL, Purcell DFJ, Saksena N, Wang B, Sonza S, Wang B, Sonza S, Wesselingh SL, Karlsson I, Fenyo EM, Gabuzda D, Cunningham AL, Gorry PR: **Asn 362 in gp120 contributes to enhanced fusogenicity by CCR5-restricted HIV-1 envelope glycoprotein variants from patients with AIDS.** *Retrovirology* 2007, **4:**89.
15. Wade J, Sterjovski J, Gray L, Roche M, Chiavaroli L, Ellett A, Jakobsen MR, Cowley D, da Fonseca Pereira C, Saksena N, Wang B, Purcell DF, Karlsson I, Fenyö EM, Churchill M, Gorry PR: **Enhanced CD4+ cellular apoptosis by CCR5-restricted HIV-1 envelope glycoprotein variants from patients with progressive HIV-1 infection.** *Virology* 2010, **396:**246–255.
16. Chang J, Jozwiak R, Wang B, Ng T, Ge YC, Bolton W, Dwyer DE, Randle C, Osborn R, Cunningham AL, Saksena NK: **Unique HIV type 1 V3 region sequences derived from six different regions of brain: region-specific**

evolution within host-determined quasispecies. *AIDS Res Hum Retrov* 1998, **14:**25–30.
17. Choe H, Farzan M, Sun Y, Sullivan N, Rollins B, Ponath PD, Wu L, Mackay CR, LaRosa G, Newman W, Gerard N, Gerard C, Sodroski J: **The beta-chemokine receptors CCR3 and CCR5 facilitate infection by primary HIV-1 isolates.** *Cell* 1996, **85:**1135–1148.
18. Hill CM, Kwon D, Jones M, Davis CB, Marmon S, Daugherty BL, DeMartino JA, Springer MS, Unutmaz D, Littman DR: **The amino terminus of human CCR5 is required for its function as a receptor for diverse human and simian immunodeficiency virus envelope glycoproteins.** *Virology* 1998, **248:**357–371.
19. Hoffman TL, Doms RW: **HIV-1 envelope determinants for cell tropism and chemokine receptor use.** *Mol Membr Biol* 1999, **16:**57–65.
20. Lee B, Sharron M, Montaner LJ, Weissman D, Doms RW: **Quantification of CD4, CCR5, and CXCR4 levels on lymphocyte subsets, dendritic cells, and differentially conditioned monocyte-derived macrophages.** *Proc Natl Acad Sci U S A* 1999, **96:**5215–5220.
21. Korber BT, Kunstman KJ, Patterson BK, Furtado M, McEvilly MM, Levy R, Wolinsky SM: **Genetic differences between blood- and brain-derived viral sequences from human immunodeficiency virus type 1-infected patients: evidence of conserved elements in the V3 region of the envelope protein of brain-derived sequences.** *J Virol* 1994, **68:**7467–7481.
22. Martín-García J, Cao W, Varela-Rohena A, Plassmeyer ML, González-Scarano F: **HIV-1 tropism for the central nervous system: brain-derived envelope glycoproteins with lower CD4 dependence and reduced sensitivity to a fusion inhibitor.** *Virology* 2006, **346:**169–179.
23. Ogert RA, Ba L, Hou Y, Buontempo C, Qiu P, Duca J, Murgolo N, Buontempo P, Ralston R, Howe JA: **Structure-function analysis of human immunodeficiency virus type 1 gp120 amino acid mutations associated with resistance to the CCR5 coreceptor antagonist vicriviroc.** *J Virol* 2009, **83:**12151–12163.
24. Peters P, Dueñas-Decamp MJ, Sullivan WM, Clapham PR: **Variation of macrophage tropism among HIV-1 R5 envelopes in brain and other tissues.** *J NeuroImmune Pharm* 2007, **2:**32–41.
25. Dejucq N, Simmons G, Clapham PR: **Expanded tropism of primary human immunodeficiency virus type 1 R5 strains to CD4(+) T-cell lines determined by the capacity to exploit low concentrations of CCR5.** *J Virol* 1999, **73:**7842–7847.
26. Pakarasang M, Wasi C, Suwanagool S, Chalermchockcharoenkit A, Auewarakul P: **Increased HIV-DNA load in CCR5-negative lymphocytes without viral phenotypic change.** *Virology* 2006, **347:**372–378.
27. Pugach P, Ray N, Klasse PJ, Ketas TJ, Michael E, Doms RW, Lee B, Moore JP: **Inefficient entry of vicriviroc-resistant HIV-1 via the inhibitor-CCR5 complex at low cell surface CCR5 densities.** *Virology* 2009, **387:**296–302.
28. Roche M, Jakobsen MR, Sterjovski J, Ellett A, Posta F, Lee B, Jubb B, Westby M, Lewin SR, Ramsland PA, Churchill MJ, Gorry PR: **HIV-1 escape from the CCR5 antagonist maraviroc associated with an altered and less-efficient mechanism of gp120-CCR5 engagement that attenuates macrophage tropism.** *J Virol* 2011, **85:**4330–4342.
29. Roche M, Salimi H, Duncan R, Wilkinson BL, Chikere K, Moore MS, Webb NE, Zappi H, Sterjovski J, Flynn JK, Lewin SR, Payne RJ, Churchill MJ, Gorry PR: **A common mechanism of clinical HIV-1 resistance to the CCR5 antagonist maraviroc despite divergent resistance levels and lack of common gp120 resistance mutations.** *Retrovirology* 2013, **10:**43.
30. Salazar-Gonzalez JF, Salazar MG, Keele BF, Learn GH, Giorgi EE, Li H, Decker JM, Wang S, Baalwa J, Kraus MH, Parrish NF, Shaw KS, Guffey MB, Bar KJ, Davis KL, Ochsenbauer-Jambor C, Kappes JC, Saag MS, Cohen MS, Mulenga J, Derdeyn CA, Allen S, Hunter E, Markowitz M, Hraber P, Perelson AS, Bhattacharya T, Haynes BF, Korber BT, Hahn BH, *et al*: **Genetic identity, biological phenotype, and evolutionary pathways of transmitted/founder viruses in acute and early HIV-1 infection.** *J Exp Med* 2009, **206:**1273–1289.
31. Arrildt KT, Joseph SB, Swanstrom R: **The HIV-1 env protein: a coat of many colors.** *Curr HIV/AIDS Rep* 2012, **9:**52–63.
32. Mosier DE: **How HIV changes its tropism: evolution and adaptation?** *Curr Opin HIV AIDS* 2009, **4:**125–130.
33. Duenas-Decamp MJ, Peters PJ, Repik A, Musich T, Gonzalez-Perez MP, Caron C, Brown R, Ball J, Clapham PR: **Variation in the biological properties of HIV-1 R5 envelopes: implications of envelope structure, transmission and pathogenesis.** *Future Virol* 2010, **5:**435–451.
34. Johnston SH, Lobritz MA, Nguyen S, Lassen K, Delair S, Posta F, Bryson YJ, Arts EJ, Chou T, Lee B: **A quantitative affinity-profiling system that reveals distinct CD4/CCR5 usage patterns among human immunodeficiency virus type 1 and simian immunodeficiency virus strains.** *J Virol* 2009, **83:**11016–11026.
35. Roche M, Jakobsen MR, Ellett A, Salimiseyedabad H, Jubb B, Westby M, Lee B, Lewin SR, Churchill MJ, Gorry PR: **HIV-1 predisposed to acquiring resistance to maraviroc (MVC) and other CCR5 antagonists in vitro has an inherent, low-level ability to utilize MVC-bound CCR5 for entry.** *Retrovirology* 2011, **8:**89.
36. Pfaff JM, Wilen CB, Harrison JE, Demarest JF, Lee B, Doms RW, Tilton JC: **HIV-1 resistance to CCR5 antagonists associated with highly efficient use of CCR5 and altered tropism on primary CD4+ T cells.** *J Virol* 2010, **84:**6505–6514.
37. Agrawal-Gamse C, Lee FH, Haggarty B, Jordan APO, Yi Y, Lee B, Collman RG, Hoxie JA, Doms RW, Laakso MM: **Adaptive mutations in a human immunodeficiency virus type 1 envelope protein with a truncated V3 loop restore function by improving interactions with CD4.** *J Virol* 2009, **83:**11005–11015.
38. Salimi H, Roche M, Webb N, Gray LR, Chikere K, Sterjovski J, Ellett A, Wesselingh SL, Ramsland PA, Lee B, Churchill MJ, Gorry PR: **Macrophage-tropic HIV-1 variants from brain demonstrate alterations in the way gp120 engages both CD4 and CCR5.** *J Leukoc Biol* 2013, **93:**113–126.
39. Chikere K, Chou T, Gorry PR, Lee B: **Affinofile profiling: how efficiency of CD4/CCR5 usage impacts the biological and pathogenic phenotype of HIV.** *Virology* 2013, **435:**81–91.
40. Wu Y, Beddall MH, Marsh JW: **Rev-dependent lentiviral expression vector.** *Retrovirology* 2007, **4:**12.
41. Wu Y, Beddall MH, Marsh JW: **Rev-dependent indicator T cell line.** *Curr HIV Res* 2007, **5:**394–402.
42. Boyd MT, Simpson GR, Cann AJ, Johnson MA, Weiss RA: **A single amino acid substitution in the V1 loop of human immunodeficiency virus type 1 gp120 alters cellular tropism.** *J Virol* 1993, **67:**3649–3652.
43. Musich T, Peters PJ, Duenas-Decamp MJ, Gonzalez-Perez MP, Robinson J, Zolla-Pazner S, Ball JK, Luzuriaga K, Clapham PR: **A conserved determinant in the V1 loop of HIV-1 modulates the V3 loop to prime Low CD4 Use and macrophage infection.** *J Virol* 2011, **85:**8.
44. Reeves JD: **Sensitivity of HIV-1 to entry inhibitors correlates with envelope/coreceptor affinity, receptor density, and fusion kinetics.** *Proc Natl Acad Sci U S A* 2002, **99:**16249–16254.
45. Rizzuto CD: **A conserved HIV gp120 glycoprotein structure involved in chemokine receptor binding.** *Science* 1998, **280:**1949–1953.
46. Oswald-Richter K, Grill SM, Leelawong M, Tseng M, Kalams SA, Hulgan T, Haas DW, Unutmaz D: **Identification of a CCR5-expressing T cell subset that is resistant to R5-tropic HIV infection.** *PLoS Pathog* 2007, **3:**e58.
47. Virgin HW, Walker BD: **Immunology and the elusive AIDS vaccine.** *Nature* 2010, **464:**224–231.
48. Haase AT: **Targeting early infection to prevent HIV-1 mucosal transmission.** *Nature* 2010, **464:**217–223.
49. Grivel J-C, Shattock RJ, Margolis LB: **Selective transmission of R5 HIV-1 variants: where is the gatekeeper?** *J Transl Med* 2010, **9:**S6.
50. Keele BF, Giorgi EE, Salazar-Gonzalez JF, Decker JM, Pham KT, Salazar MG, Sun C, Grayson T, Wang S, Li H, Wei X, Jiang C, Kirchherr JL, Gao F, Anderson JA, Ping LH, Swanstrom R, Tomaras GD, Blattner WA, Goepfert PA, Kilby JM, Saag MS, Delwart EL, Busch MP, Cohen MS, Montefiori DC, Haynes BF, Gaschen B, Athreya GS, Lee HY, *et al*: **Identification and characterization of transmitted and early founder virus envelopes in primary HIV-1 infection.** *Proc Natl Acad Sci U S A* 2008, **105:**7552–7557.
51. Walker LM, Phogat SK, Chan-Hui PY, Wagner D, Phung P, Goss JL, Wrin T, Simek MD, Fling S, Mitcham JL, Lehrman JK, Priddy FH, Olsen OA, Frey SM, Hammond PW, Principal Investigators PG, Kaminsky S, Zamb T, Moyle M, Koff WC, Poignard P, Burton DR: **Broad and potent neutralizing antibodies from an African donor reveal a new HIV-1 vaccine target.** *Science* 2009, **326:**285–289.
52. Zhou T, Georgiev I, Wu X, Yang Z-Y, Dai K, Finzi A, Kwon YD, Scheid JF, Shi W, Xu L, Yang Y, Zhu J, Nussenzweig MC, Sodroski J, Shapiro L, Nabel GJ, Mascola JR, Kwong PD: **Structural basis for broad and potent neutralization of HIV-1 by antibody VRC01.** *Science* 2010, **329:**811–817.
53. Li Y, O'Dell S, Walker LM, Wu X, Guenaga J, Feng Y, Schmidt SD, McKee K, Louder MK, Ledgerwood JE, Graham BS, Haynes BF, Burton DR, Wyatt RT, Mascola JR: **Mechanism of neutralization by the broadly neutralizing HIV-1 monoclonal antibody VRC01.** *J Virol* 2011, **85:**8954–8967.
54. Trkola A, Lassen KG, Lobritz MA, Bailey JR, Johnston S, Nguyen S, Lee B, Chou T, Siliciano RF, Markowitz M, Arts EJ: **Elite suppressor–derived HIV-1 envelope glycoproteins exhibit reduced entry efficiency and kinetics.** *Plos Pathog* 2009, **5:**e1000377.

55. Tilton JC, Wilen CB, Didigu CA, Sinha R, Harrison JE, Agrawal-Gamse C, Henning EA, Bushman FD, Martin JN, Deeks SG, Doms RW: **A maraviroc-resistant HIV-1 with narrow cross-resistance to other CCR5 antagonists depends on both N-terminal and extracellular loop domains of drug-bound CCR5.** *J Virol* 2010, **84:**10863–10876.
56. Jiang C, Parrish NF, Wilen CB, Li H, Chen Y, Pavlicek JW, Berg A, Lu X, Song H, Tilton JC, Pfaff JM, Henning EA, Decker JM, Moody MA, Drinker MS, Schutte R, Freel S, Tomaras GD, Nedellec R, Mosier DE, Haynes BF, Shaw GM, Hahn BH, Doms RW, Gao F: **Primary infection by a human immunodeficiency virus with atypical coreceptor tropism.** *J Virol* 2011, **85:**10669–10681.
57. Bleul CC, Wu L, Hoxie JA, Springer TA, Mackay CR: **The HIV coreceptors CXCR4 and CCR5 are differentially expressed and regulated on human T lymphocytes.** *Proc Natl Acad Sci U S A* 1997, **94:**1925–1930.
58. Mo H, Monard S, Pollack H, Ip J, Rochford G, Wu L, Hoxie J, Borkowsky W, Ho DD, Moore JP: **Expression patterns of the HIV type 1 coreceptors CCR5 and CXCR4 on CD4+ T cells and monocytes from cord and adult blood.** *AIDS Res Hum Retrov* 1998, **14:**607–617.
59. Merk A, Subramaniam S: **HIV-1 envelope glycoprotein structure.** *Curr Opin Structual Biol* 2013, **23:**8.
60. Benito JM, Zabay JM, Gil J, Bermejo M, Escudero A, Sanchez E, Fernandez-Cruz E: **Quantitative alterations of the functionally distinct subsets of CD4 and CD8 T lymphocytes in asymptomatic HIV infection: changes in the expression of CD45RO, CD45RA, CD11b, CD38, HLA-DR, and CD25 antigens.** *J Acquir Immune Defic Syndr Hum Retrovirol* 1997, **14:**128–135.
61. Helbert MR, Walter J, L'Age J, Beverley PC: **HIV infection of CD45RA + and CD45RO + CD4+ T cells.** *Clin Exp Immunol* 1997, **107:**300–305.
62. Spina CA, Prince HE, Richman DD: **Preferential replication of HIV-1 in the CD45RO memory cell subset of primary CD4 lymphocytes in vitro.** *J Clin Invest* 1997, **99:**1774–1785.
63. Silvestri G, Zeng M, Southern PJ, Reilly CS, Beilman GJ, Chipman JG, Schacker TW, Haase AT: **Lymphoid tissue damage in HIV-1 infection depletes naïve T cells and limits T cell reconstitution after antiretroviral therapy.** *Plos Pathog* 2012, **8:**e1002437.
64. Schacker TW, Brenchley JM, Beilman GJ, Reilly C, Pambuccian SE, Taylor J, Skarda D, Larson M, Douek DC, Haase AT: **Lymphatic tissue fibrosis is associated with reduced numbers of naive CD4+ T cells in human immunodeficiency virus type 1 infection.** *Clin Vaccine Immunol* 2006, **13:**556–560.
65. Kwa D, Vingerhoed J, Boeser B, Schuitemaker H: **Increased in vitro cytopathicity of CC chemokine receptor 5-restricted human immunodeficiency virus type 1 primary isolates correlates with a progressive clinical course of infection.** *J Infect Dis* 2003, **187:**1397–1403.
66. Duncan CJA, Sattentau QJ: **Viral determinants of HIV-1 macrophage tropism.** *Viruses* 2011, **3:**2255–2279.
67. Cullen BR, Schnell G, Joseph S, Spudich S, Price RW, Swanstrom R: **HIV-1 replication in the central nervous system occurs in Two distinct cell types.** *Plos Pathog* 2011, **7:**e1002286.
68. Salazar-Gonzalez JF, Bailes E, Pham KT, Salazar MG, Guffey MB, Keele BF, Derdeyn CA, Farmer P, Hunter E, Allen S, Derdeyn CA, Farmer P, Hunter E, Allen S, Manigart O, Mulenga J, Anderson JA, Swanstrom R, Haynes BF, Athreya GS, Korber BT, Sharp PM, Shaw GM, Hahn BH: **Deciphering human immunodeficiency virus type 1 transmission and early envelope diversification by single-genome amplification and sequencing.** *J Virol* 2008, **82:**3952–3970.
69. Kearney M, Maldarelli F, Shao W, Margolick JB, Daar ES, Mellors JW, Rao V, Coffin JM, Palmer S: **Human immunodeficiency virus type 1 population genetics and adaptation in newly infected individuals.** *J Virol* 2008, **83:**2715–2727.
70. Haaland RE, Hawkins PA, Salazar-Gonzalez J, Johnson A, Tichacek A, Karita E, Manigart O, Mulenga J, Keele BF, Shaw GM, Hahn BH, Allen SA, Derdeyn CA, Hunter E: **Inflammatory genital infections mitigate a severe genetic bottleneck in heterosexual transmission of subtype a and C HIV-1.** *Plos Pathog* 2009, **5:**e1000274.
71. Masharsky Alexey E, Dukhovlinova Elena N, Verevochkin Sergei V, Toussova Olga V, Skochilov Roman V, Anderson Jeffrey A, Hoffman I, Cohen Myron S, Swanstrom R, Kozlov Andrei P: **A substantial transmission bottleneck among newly and recently HIV-1–infected injection drug users in St Petersburg.** *Russia J Infect Dis* 2010, **201:**1697–1702.
72. Gnanakaran S, Bhattacharya T, Daniels M, Keele BF, Hraber PT, Lapedes AS, Shen T, Gaschen B, Krishnamoorthy M, Li H, Decker JM, Salazar-Gonzalez JF, Wang S, Jiang C, Gao F, Swanstrom R, Anderson JA, Ping LH, Cohen MS, Markowitz M, Goepfert PA, Saag MS, Eron JJ, Hicks CB, Blattner WA, Tomaras GD, Asmal M, Letvin NL, Gilbert PB, Decamp AC, *et al*: **Recurrent signature patterns in HIV-1 B clade envelope glycoproteins associated with either early or chronic infections.** *Plos Pathog* 2011, **7:**e1002209.
73. Isaacman-Beck J, Hermann EA, Yi Y, Ratcliffe SJ, Mulenga J, Allen S, Hunter E, Derdeyn CA, Collman RG: **Heterosexual transmission of human immunodeficiency virus type 1 subtype C: Macrophage tropism, alternative coreceptor use, and the molecular anatomy of CCR5 utilization.** *J Virol* 2009, **83:**8208–8220.
74. Alexander M, Lynch R, Mulenga J, Allen S, Derdeyn CA, Hunter E: **Donor and recipient envs from heterosexual human immunodeficiency virus subtype C transmission pairs require high receptor levels for entry.** *J Virol* 2010, **84:**4100–4104.
75. Wilen CB, Parrish NF, Pfaff JM, Decker JM, Henning EA, Haim H, Petersen JE, Wojcechowskyj JA, Sodroski J, Haynes BF, Montefiori DC, Tilton JC, Shaw GM, Hahn BH, Doms RW: **Phenotypic and immunologic comparison of clade B transmitted/founder and chronic HIV-1 envelope glycoproteins.** *J Virol* 2011, **85:**8514–8527.
76. Ochsenbauer C, Edmonds TG, Ding H, Keele BF, Decker J, Salazar MG, Salazar-Gonzalez JF, Shattock R, Haynes BF, Shaw GM, Hahn BH, Kappes JC: **Generation of transmitted/founder HIV-1 infectious molecular clones and characterization of their replication capacity in CD4 T lymphocytes and monocyte-derived macrophages.** *J Virol* 2011, **86:**2715–2728.
77. Parrish NF, Wilen CB, Banks LB, Iyer SS, Pfaff JM, Salazar-Gonzalez JF, Salazar MG, Decker JM, Parrish EH, Berg A, Hopper J, Hora B, Kumar A, Mahlokozera T, Yuan S, Coleman C, Vermeulen M, Ding H, Ochsenbauer C, Tilton JC, Permar SR, Kappes JC, Betts MR, Busch MP, Gao F, Montefiori D, Haynes BF, Shaw GM, Hahn BH, Doms RW: **Transmitted/founder and chronic subtype C HIV-1 Use CD4 and CCR5 receptors with equal efficiency and Are Not inhibited by blocking the integrin α4β7.** *Plos Pathog* 2012, **8:**e1002686.
78. Haim H, Si Z, Madani N, Wang L, Courter JR, Princiotto A, Kassa A, DeGrace M, McGee-Estrada K, Mefford M, Gabuzda D, Smith AB 3rd, Sodroski J: **Soluble CD4 and CD4-mimetic compounds inhibit HIV-1 infection by induction of a short-lived activated state.** *Plos Pathog* 2009, **5:**e1000360.
79. Sterjovski J, Churchill MJ, Ellett A, Wesselingh SL, Ramsland PA, Gorry PR: **Structural elements of primary CCR5-using HIV-1 gp120 proteins influencing sensitivity and resistance to the broadly neutralizing monoclonal antibody b12.** *Virology* 2012, **432:**394–404.
80. Parker ZF, Iyer SS, Wilen CB, Parrish NF, Chikere KC, Lee FH, Didigu CA, Berro R, Klasse PJ, Lee B, Moore JP, Shaw GM, Hahn BH, Doms RW: **Transmitted/founder and chronic HIV-1 envelope proteins are distinguished by differential utilization of CCR5.** *J Virol* 2013, **87:**2401–2411.
81. Lee B, Sharron M, Blanpain C, Doranz BJ, Vakili J, Setoh P, Berg E, Liu G, Guy HR, Durell SR, Parmentier M, Chang CN, Price K, Tsang M, Doms RW: **Epitope mapping of CCR5 reveals multiple conformational states and distinct but overlapping structures involved in chemokine and coreceptor function.** *J Biol Chem* 1999, **274:**9617–9626.
82. Berro R, Klasse PJ, Lascano D, Flegler A, Nagashima KA, Sanders RW, Sakmar TP, Hope TJ, Moore JP: **Multiple CCR5 conformations on the cell surface are used differentially by human immunodeficiency viruses resistant or sensitive to CCR5 inhibitors.** *J Virol* 2011, **85:**8227–8240.
83. Thiele S, Steen A, Jensen PC, Mokrosinski J, Frimurer TM, Rosenkilde MM: **Allosteric and orthosteric sites in CC chemokine receptor (CCR5), a chimeric receptor approach.** *J Biol Chem* 2011, **286:**37543–37554.
84. Baribaud F, Edwards TG, Sharron M, Brelot A, Heveker N, Price K, Mortari F, Alizon M, Tsang M, Doms RW: **Antigenically distinct conformations of CXCR4.** *J Virol* 2001, **75:**8957–8967.
85. Nakano Y, Monde K, Terasawa H, Yuan Y, Yusa K, Harada S, Maeda Y: **Preferential recognition of monomeric CCR5 expressed in cultured cells by the HIV-1 envelope glycoprotein gp120 for the entry of R5 HIV-1.** *Virology* 2014, **452–453:**117–124.
86. Fenyö EM, Esbjörnsson J, Medstrand P, Jansson M: **Human immunodeficiency virus type 1 biological variation and coreceptor use: From concept to clinical significance.** *J Intern Med* 2011, **270:**520–531.
87. Flegler AJ, Cianci GC, Hope TJ: **CCR5 conformations are dynamic and modulated by localization, trafficking and G protein association.** *PLoS One* 2014, **9:**e89056.
88. Ketas TJ, Kuhmann SE, Palmer A, Zurita J, He W, Ahuja SK, Klasse PJ, Moore JP: **Cell surface expression of CCR5 and other host factors influence the**

inhibition of HIV-1 infection of human lymphocytes by CCR5 ligands. *Virology* 2007, **364:**281–290.
89. Melikyan GB, Platt EJ, Kabat D: **The role of the N-terminal segment of CCR5 in HIV-1 Env-mediated membrane fusion and the mechanism of virus adaptation to CCR5 lacking this segment.** *Retrovirology* 2007, **4:**55.
90. Wu L, LaRosa G, Kassam N, Gordon C, Heath H, Ruffing N, Chen H, Humblias J, Samson M, Parmentier M, Moore JP, Mackay CR: **Interaction of chemokine receptor CCR5 with its ligands: multiple domains for HIV-1 gp120 binding and a single domain for chemokine binding.** *J Exp Med* 1997, **186:**8.
91. Nedellec R, Coetzer M, Shimizu N, Hoshino H, Polonis VR, Morris L, Martensson UE, Binley J, Overbaugh J, Mosier DE: **Virus entry via the alternative coreceptors CCR3 and FPRL1 differs by human immunodeficiency virus type 1 subtype.** *J Virol* 2009, **83:**8353–8363.
92. Cashin K, Jakobsen MR, Sterjovski J, Roche M, Ellett A, Flynn JK, Borm K, Gouillou M, Churchill MJ, Gorry PR: **Linkages between HIV-1 specificity for CCR5 or CXCR4 and in vitro usage of alternative coreceptors during progressive HIV-1 subtype C infection.** *Retrovirology* 2013, **10:**98.
93. Renjifo B, Gilbert P, Chaplin B, Msamanga G, Mwakagile D, Fawzi W, Essex M: **Preferential in-utero transmission of HIV-1 subtype C as compared to HIV-1 subtype A or D.** *AIDS* 2004, **18:**1629–1636.
94. Abraha A, Nankya IL, Gibson R, Demers K, Tebit DM, Johnston E, Katzenstein D, Siddiqui A, Herrera C, Fischetti L, Shattock RJ, Arts EJ: **CCR5- and CXCR4-tropic subtype C human immunodeficiency virus type 1 isolates have a lower level of pathogenic fitness than other dominant group M subtypes: implications for the epidemic.** *J Virol* 2009, **83:**5592–5605.
95. Ball SC, Abraha A, Collins KR, Marozsan AJ, Baird H, Quinones-Mateu ME, Penn-Nicholson A, Murray M, Richard N, Lobritz M, Zimmerman PA, Kawamura T, Blauvelt A, Arts EJ: **Comparing the ex vivo fitness of CCR5-tropic human immunodeficiency virus type 1 isolates of subtypes B and C.** *J Virol* 2003, **77:**1021–1038.
96. Marozsan AJ, Moore DM, Lobritz MA, Fraundorf E, Abraha A, Reeves JD, Arts EJ: **Differences in the fitness of Two diverse wild-type human immunodeficiency virus type 1 isolates Are related to the efficiency of cell binding and entry.** *J Virol* 2005, **79:**7121–7134.
97. Morner A, Bjorndal A, Albert J, Kewalramani VN, Littman DR, Inoue R, Thorstensson R, Fenyo EM, Bjorling E: **Primary human immunodeficiency virus type 2 (HIV-2) isolates, like HIV-1 isolates, frequently use CCR5 but show promiscuity in coreceptor usage.** *J Virol* 1999, **73:**2343–2349.

References

1. Michael Roche, Hamid Salimi, Renee Duncan, Brendan L Wilkinson, Kelechi Chikere, Miranda S Moore, Nicholas E Webb, Helena Zappi, Jasminka Sterjovski, Jacqueline K Flynn, Anne Ellett, Lachlan R Gray, Benhur Lee, Becky Jubb, Mike Westby, Paul A Ramsland, Sharon R Lewin, Richard J Payne, Melissa J Churchill, and Paul R Gorry. A common mechanism of clinical HIV-1 resistance to the CCR5 antagonist maraviroc despite divergent resistance levels and lack of common gp120 resistance mutations. *Retrovirology*, 10:43, 2013.

2. John C Tilton, Craig B Wilen, Chukwuka A Didigu, Rohini Sinha, Jessamina E Harrison, Caroline Agrawal-Gamse, Elizabeth A Henning, Frederick D Bushman, Jeffrey N Martin, Steven G Deeks, and Robert W Doms. A maraviroc-resistant HIV-1 with narrow cross-resistance to other CCR5 antagonists depends on both N-terminal and extracellular loop domains of drug-bound CCR5. *J Virol*, 84(20):10863–76, Oct 2010.

3. Michael Roche, Martin R Jakobsen, Jasminka Sterjovski, Anne Ellett, Filippo Posta, Benhur Lee, Becky Jubb, Mike Westby, Sharon R Lewin, Paul A Ramsland, Melissa J Churchill, and Paul R Gorry. HIV-1 escape from the CCR5 antagonist maraviroc associated with an altered and less-efficient mechanism of gp120-CCR5 engagement that attenuates macrophage tropism. *J Virol*, 85(9):4330–42, May 2011.

4. Michael Roche, Martin R Jakobsen, Anne Ellett, Hamid Salimiseyedabad, Becky Jubb, Mike Westby, Benhur Lee, Sharon R Lewin, Melissa J Churchill, and Paul R Gorry. HIV-1 predisposed to acquiring resistance to maraviroc (MVC) and other CCR5 antagonists in vitro has an inherent, low-level ability to utilize MVC-bound CCR5 for entry. *Retrovirology*, 8:89, 2011.

5. Kelechi Chikere, Tom Chou, Paul R Gorry, and Benhur Lee. Affinofile profiling: how

efficiency of CD4/CCR5 usage impacts the biological and pathogenic phenotype of HIV. *Virology*, 435(1):81–91, Jan 2013.

6. Li-Hua Ping, Sarah B Joseph, Jeffrey A Anderson, Melissa-Rose Abrahams, Jesus F Salazar-Gonzalez, Laura P Kincer, Florette K Treurnicht, Leslie Arney, Suany Ojeda, Ming Zhang, Jessica Keys, E Lake Potter, Haitao Chu, Penny Moore, Maria G Salazar, Shilpa Iyer, Cassandra Jabara, Jennifer Kirchherr, Clement Mapanje, Nobubelo Ngandu, Cathal Seoighe, Irving Hoffman, Feng Gao, Yuyang Tang, Celia Labranche, Benhur Lee, Andrew Saville, Marion Vermeulen, Susan Fiscus, Lynn Morris, Salim Abdool Karim, Barton F Haynes, George M Shaw, Bette T Korber, Beatrice H Hahn, Myron S Cohen, David Montefiori, Carolyn Williamson, Ronald Swanstrom, and CAPRISA Acute Infection Study and the Center for HIV-AIDS Vaccine Immunology Consortium. Comparison of viral Env proteins from acute and chronic infections with subtype C human immunodeficiency virus type 1 identifies differences in glycosylation and CCR5 utilization and suggests a new strategy for immunogen design. *J Virol*, 87(13):7218–33, Jul 2013.

7. Zahra F Parker, Shilpa S Iyer, Craig B Wilen, Nicholas F Parrish, Kelechi C Chikere, Fang-Hua Lee, Chuka A Didigu, Reem Berro, Per Johan Klasse, Benhur Lee, John P Moore, George M Shaw, Beatrice H Hahn, and Robert W Doms. Transmitted/founder and chronic HIV-1 envelope proteins are distinguished by differential utilization of CCR5. *J Virol*, 87(5):2401–11, Mar 2013.

8. Hamid Salimi, Michael Roche, Nicholas Webb, Lachlan R Gray, Kelechi Chikere, Jasminka Sterjovski, Anne Ellett, Steve L Wesselingh, Paul A Ramsland, Benhur Lee, Melissa J Churchill, and Paul R Gorry. Macrophage-tropic HIV-1 variants from brain demonstrate alterations in the way gp120 engages both CD4 and CCR5. *J Leukoc Biol*, 93(1):113–26, Jan 2013.

9. Sarah B Joseph, Kathryn T Arrildt, Adrienne E Swanstrom, Gretja Schnell, Benhur Lee, James A Hoxie, and Ronald Swanstrom. Quantification of entry phenotypes of

macrophage-tropic HIV-1 across a wide range of CD4 densities. *J Virol*, 88(4):1858–69, Feb 2014.

10. Jasminka Sterjovski, Michael Roche, Melissa J Churchill, Anne Ellett, William Farrugia, Lachlan R Gray, Daniel Cowley, Pantelis Poumbourios, Benhur Lee, Steven L Wesselingh, Anthony L Cunningham, Paul A Ramsland, and Paul R Gorry. An altered and more efficient mechanism of CCR5 engagement contributes to macrophage tropism of CCR5-using HIV-1 envelopes. *Virology*, 404(2):269–78, Sep 2010.

11. P R Gorry, G Bristol, J A Zack, K Ritola, R Swanstrom, C J Birch, J E Bell, N Bannert, K Crawford, H Wang, D Schols, E De Clercq, K Kunstman, S M Wolinsky, and D Gabuzda. Macrophage tropism of human immunodeficiency virus type 1 isolates from brain and lymphoid tissues predicts neurotropism independent of coreceptor specificity. *J Virol*, 75(21):10073–89, Nov 2001.

12. Paul R Gorry, Joann Taylor, Geoffrey H Holm, Andrew Mehle, Tom Morgan, Mark Cayabyab, Michael Farzan, Hui Wang, Jeanne E Bell, Kevin Kunstman, John P Moore, Steven M Wolinsky, and Dana Gabuzda. Increased CCR5 affinity and reduced CCR5/CD4 dependence of a neurovirulent primary human immunodeficiency virus type 1 isolate. *J Virol*, 76(12):6277–92, Jun 2002.

13. J Martín, C C LaBranche, and F González-Scarano. Differential CD4/CCR5 utilization, gp120 conformation, and neutralization sensitivity between envelopes from a microglia-adapted human immunodeficiency virus type 1 and its parental isolate. *J Virol*, 75(8):3568–80, Apr 2001.

14. S L Kozak, E J Platt, N Madani, F E Ferro, Jr, K Peden, and D Kabat. CD4, CXCR-4, and CCR-5 dependencies for infections by primary patient and laboratory-adapted isolates of human immunodeficiency virus type 1. *J Virol*, 71(2):873–82, Feb 1997.

15. E J Platt, N Madani, S L Kozak, and D Kabat. Infectious properties of human immun-

odeficiency virus type 1 mutants with distinct affinities for the CD4 receptor. *J Virol*, 71(2):883–90, Feb 1997.

16. E J Platt, K Wehrly, S E Kuhmann, B Chesebro, and D Kabat. Effects of CCR5 and CD4 cell surface concentrations on infections by macrophagetropic isolates of human immunodeficiency virus type 1. *J Virol*, 72(4):2855–64, Apr 1998.

17. Samantha H Johnston, Michael A Lobritz, Sandra Nguyen, Kara Lassen, Shirley Delair, Filippo Posta, Yvonne J Bryson, Eric J Arts, Tom Chou, and Benhur Lee. A quantitative affinity-profiling system that reveals distinct CD4/CCR5 usage patterns among human immunodeficiency virus type 1 and simian immunodeficiency virus strains. *J Virol*, 83(21):11016–26, Nov 2009.

18. Kelechi Chikere, Nicholas E Webb, Tom Chou, Katharina Borm, Jasminka Sterjovski, Paul R Gorry, and Benhur Lee. Distinct HIV-1 entry phenotypes are associated with transmission, subtype specificity, and resistance to broadly neutralizing antibodies. *Retrovirology*, 11:48, 2014.

CHAPTER 5

Cooperativity is a Novel Property of HIV-1 Infection *in vitro*

Introduction

Inhibitors can have dramatic effects on the inherent properties of viral attachment and entry, such as CD4 and CCR5 usage[1–5]. Inhibitors might also have an impact on the more general infectious behavior of a virus. Inhibitor activities are traditionally measured in terms of inhibitor concentration against a constant quantity of viral input, which, while useful, does not describe how the fundamental mechanism of infection and entry might respond to the presence of the inhibitor. An entry inhibitor may reduce the overall infection efficiency of a virus by blocking a certain proportion of infectious events or, alternatively, it may change the way in which a population of virion interact with and become distributed among their target cells. While effector distribution has been an important concept in the fields of pharmacology and biochemistry for over half a century[6], these same principles have not yet been applied to the context of viral infectivity.

The classical, interpretive model of viral infection is binary, where a single virion results in either one infected cell or no infection at all. This interpretation is woven into the very core of practical virology, where the mathematical methods used to quantify infectious virion in virus samples are explicitly defined by either the interpolation of an infectious endpoint (50% probability of a single infected cell given by the method of Reed and Muench[7] and the Spearman-Karber method[8–10]) or by a direct and proportionate linear continuity between infected cells and virus sample volume[11–15], which will be defined in this chapter as the infectious titer model. These methods ultimately represent a fundamental assumption that is central to our interpretation of viral infectivity, viral replication and inhibitor efficacy that is: infectious virion are equally and randomly distributed among their target cells.

Effector distribution is a key issue in the fields of pharmacology and biochemistry, where target molecules having multiple effector binding sites can exhibit allosteric, cooperative effects[6,16]. These cooperative properties are fundamental to many complex and simple biological systems[16–18] and manifest as a distributive phenomenon defined in reference to

non-cooperative, random distribution (see Chapter 2). Although a cell-surface is much more complex than a classical cooperative protein, virion attached to the cell surface can have a strong impact on the distribution of CD4 and co-receptor[19–23] that might alter the way additional virion interact with an engaged surface. In this sense, virion exhibiting negative cooperativity are preferentially distributed to cells that are unengaged by other virion. This decreases the probability that multiple virion will engage the same cell, relative to random distribution, which then increases the number of cells that a population of virion can produce. Conversely, a population of virion exhibiting high, positive cooperativity will preferentially engage cells that are already engaged by other virion, representing a highly inefficient mode of distribution that results in less overall infection.

The clinical significance of infectious cooperativity is rooted in the fact that viral replication depends not on the total number of virion present, but on the amount of infection those virion produce. In this context, negative infectious cooperativity represents the most efficient distribution of virion in terms of infection that is then expected to yield a faster rate of replication than virion that are non-cooperative or exhibit positive cooperativity. Thus, cooperativity allows two virion populations, of equal size, to generate different amounts of infection, which may be important in the clinical context of viral replication and expansion.

The goal of this chapter is to determine whether cooperativity is a significant phenomenon in HIV infection *in vitro* and, if so, to develop an analytical framework that can be used to investigate its potential clinical significance. Our results show that *in vitro*, HIV entry is a process of negative cooperativity and that this cooperativity is strong enough to invalidate traditional models of infection that are rooted in random-distribution[7–15]. As a distributive phenomenon, negative cooperativity was strongly associated with cell-surface CD4/CCR5 expression, consistent with the fact that HIV virion can induce rapid co-localization of CD4 and CCR5 at the cell surface within the time-frame of entry[19–23]. We then extend these concepts to develop an analytical framework that highlights the impact of infectious cooperativity in the context of maraviroc resistance. These results show that cooperativity

is an important part of HIV attachment and entry that may have strong clinical significance.

Assessing the significance of cooperativity in HIV entry. Cooperativity is readily measured through a standard dose-response experiment, which is described in detail in Chapter 2 and Appendix A. Briefly, an effector (virus) is titrated and the resulting dose-dependent effect (infection) is measured for each dilution. The differential rise in effect for any given change in dose, measured by the dose-response slope (m), then indicates non-cooperativity ($m = 1$), positive cooperativity ($m > 1$) or negative cooperativity ($m < 1$). These slopes are explicitly calculated by fitting the experimental dose-response data to either the Hill equation[24] or its equivalent, the median effect equation[25].

While these dose-response models are the gold standard for characterizing the dose-dependent activity of many systems, from target-ligand binding to receptor signaling, inhibitors and immunotherapeutics (see Chapter 2), the applicability of a standard dose-response model has not yet been determined in the context of viral infection. The classical interpretation of viral infection assumes that virion are randomly distributed among their target cells, thus, the process of viral infection is generally considered non-cooperative.

The interaction with and distribution of virion to target cells is a complex process involving binding affinities, receptor/co-receptor usage efficiency and cell-surface dynamics. None of these properties are explicitly accounted for in the classical models of infection, which assume a non-cooperative, random distribution of virion to target cells. The interaction of a single virion with its target cell can induce profound changes in the composition of a cell surface, such as the redistribution of CD4 and CCR5/CXCR4 to sites of viral attachment[19–23]. These effects are likely to manifest as a cooperative distribution of virion, giving slopes $\neq 1$, that are not accommodated by the non-cooperative assumption of classical infection models which assume a titration slope of 1.

Because cooperativity has not yet been explored in the context of infection, our first goal is to determine whether HIV infection exhibits cooperative or non-cooperative behavior,

where cooperativity is quantified by the median effect slope (m) after fitting this model to experimental HIV titration results. Experimentally, the cooperativity of slopes falling near 1 can be ambiguous, for example, a slope of 1.01 can indicate a very weak positive cooperativity or non-cooperativity and may be represented equally well by cooperative and non-cooperative models of infection. Therefore, we define the significance of cooperativity in relation to the non-cooperative assumption, by determining the range of slope values that cannot be accommodated by assuming non-cooperativity.

We introduce three models based on the assumptions they make regarding cooperativity, their widespread use in the field of virology, biochemistry and pharmacology and the fact that all three models are intended to recapitulate the experimental results of a virus titration, where cooperativity manifests as a steep ($m > 1$) or shallow ($m < 1$) rise in infection relative to the non-cooperative assumption ($m = 1$). The infectious titer model (IT) is the simplest representation of a viral titration curve, which assumes a strict linear proportionality between viral input and infection[12–15]. This model is adapted to give the Poisson titer model (PT), which specifically accounts for random virion distribution but not cooperativity. Finally, we adapt the median effect model[25] to the context of viral titration to give a median effect titer (MT) model, which allows for positive, negative and non-cooperativity.

The significance of cooperativity is assessed by comparing how well each model represents experimental virus titration data through their correlation coefficients (R^2). In the previous example, a slope of 1.01 is considered non-cooperative only when the cooperative (MT) and non-cooperative (IT, PT) models achieve similar representative accuracy (R^2), indicating that the experiment is appropriately represented by the non-cooperative assumption and that no additional information is gained by allowing for cooperativity. Alternatively, a slope of 1.01 can be considered cooperative if the non-cooperative (IT, PT) models exhibit a clear representative deficiency, giving low R^2 relative to the cooperative MT model. Each of the three models presented here contain one quantitative parameter that can be used to quantify the infectious virion in a sample while the cooperative MT model contains an additional slope

parameter (m) that permits positive, negative and non-cooperativity.

The infectious titer model. The infectious titer (IT) model is most commonly used to quantify the infectious material of a virus sample[11–15] in terms of transducing or infectious units (IU). This model assumes a strict linear proportionality between viral input and infection (Equation 5.1a), where each infected cell is defined as a single IU to obtain an infectious titer (T, Equation 5.1b), where f_a is the percent of infected cells, V is the volume of virus sample (in mL), C is the total number of cells available for infection and T is the infectious titer (in IU/mL). The linear proportionality of this model inherently assumes that IU are randomly distributed, in a singular fashion, to their target cells.

$$f_a = \frac{T \times C}{V} \qquad (5.1a) \qquad\qquad T = \frac{f_a \times C}{V} \qquad (5.1b)$$

This representation is problematic because, for example, if viral input exceeds the total cell count (C), Equation 5.1a predicts that more than 100% of the cells can be infected. This doesn't naturally occur because as viral input increases, so too does the distribution of IU to target cells. Thus, the IT model cannot accommodate the statistical distribution of multiple IU to a single cell in any capacity. This deficiency is partially corrected by imposing a specific limit to the validity of this model: the liner range of infection (LRI). The LRI is defined by the Poisson equation as the range of f_a giving a negligible probability that any single infected cell was infected by > 1 IU (Equation 5.2, where p_n is the probability of any single cell being infected by n IU and M is the multiplicity of infection (IU per cell)). For example, when 50% infection is observed, Equation 5.2 predicts that 30% of those infected cells were derived from > 1 IU, thus, a calculation of T (Equation 5.1b) where $f_a = 50\%$ is a severely underestimated count of IU, and the IT model is not valid. Conversely, when 20% infection is observed, this probability is reduced to 10% and continues to drop as observed infection (f_a) deceases. For this reason, the LRI is typically defined as $0 < f_a \leq 20\%$ (or lower maximum thresholds), where Ts from all virus sample dilutions giving infection within this range are averaged to further minimize the distributive deficiency of the IT model.

$$p_n = \frac{M^n \times e^{-M}}{n!} \tag{5.2}$$

The Poisson titer model. Equation 5.2 itself can be used to describe the relationship between viral input and infection while specifically accounting for random distribution, thus, this model is not restricted to an LRI like the IT model. Normalized, percent infection (f_a) is the macroscopic average of any single cell being infected by 1 or more IU, therefore, the total percent infection observed equals the sum probability that any cell will be infected by any number of IU (Equation 5.3, where f_a is the percentage of infected cells, $p_{n>0}$ is the probability that any cell will be infected by $n > 0$ IU, and M is the multiplicity of infection in terms of IU per cell).

$$f_a = p_{n>0} = \sum_{n=1}^{\infty} \frac{M^n \times e^{-M}}{n!} = 1 - e^{-M} \tag{5.3}$$

Equation 5.3 can be used to represent the relationship between viral input and infection by recognizing that M is the multiplicity of infection given by IU per cell (C) and that the quantity of IU at any given volume of a virus sample is equal to the infectious titer times the volume used (IU= $T_p \times V$, where T_p specifically denotes the infectious titer given by this Poisson model and V is the volume of sample). Infection (f_a) is then represented in terms of a Poisson model titer (T_p), a sample volume (V) and a number of cells (C) with Equation 5.4a and the Poisson titer (T_p) is given by a rearrangement of the same equation (Equation 5.4b).

$$f_a = 1 - e^{-\frac{T_p V}{C}} \qquad \text{(5.4a)} \qquad\qquad T_p = \frac{C}{V} \ln\left(\frac{1}{1 - f_a}\right) \qquad \text{(5.4b)}$$

Importantly, the relationship between viral input and infection given by Equations 5.4a and 5.4b are not subject to an LRI like the IT model and explicitly assume the random distribution of IU represented by the Poisson equation (Equation 5.2).

The median effect titer model. The relationship between an effector quantity (or dose, D), and its resulting effect (f_a) is most commonly described by a standard dose-response model given by the Hill equation[24] or its normalized equivalent, the median effect equation[25] (Equation 5.5, where m is slope and D_m is median dose). Both are derived from a randomly distributed target-ligand binding equilibrium[24] (see Appendix A) where the slope (m) was originally thought to represent ligand stoichiometry. In the mid 1960's the phenomenon of non-random, cooperative distribution and its impact on slope was first formulated based on extensive biochemical and crystallographic experiments using hemoglobin[6,26,27]. Since then, cooperative distribution has been described in a diverse variety of both simple and complex target-effector systems[17,18], where positive cooperativity gives $m > 1$, negative cooperativity gives $m < 1$ and non-cooperativity gives $m = 1$, regardless of the underlying stoichiometry.

$$\left(\frac{f_a}{1-f_a}\right) = \left(\frac{D}{D_m}\right)^m \tag{5.5}$$

Positive and negative cooperativity describe a preferential distribution of effectors to partially liganded or non-liganded targets, respectively, relative to random distribution. This distributive phenomenon has a significant impact on the *apparent* stoichiometry of an effector, which necessarily increases when that effector is preferentially distributed to liganded targets and decreases when the effector is preferentially distributed to non-liganded targets (relative to random distribution). In this sense, cooperativity manifests specifically through m, which no longer indicates a true effector stoichiometry but, instead, is a measure of the degree of positive ($m > 1$) or negative ($m < 1$) cooperativity based on how far this value falls from the non-cooperative $m = 1$.

The median effect equation is used to represent the relationship between an effector dose (D) and its resulting normalized effect (f_a), such as a virus titration experiment, through two parameters. The slope (m) measures the cooperativity of the system and the median dose (D_m) is a quantitative measure of the effector (the dose need to achieve 50% effect). These parameters are most readily fit to experimental results through the linear log transformation

of Equation 5.5 shown in Equation 5.6.

$$\log\left(\frac{f_a}{1-f_a}\right) = m\log(D) - m\log(D_m) \tag{5.6}$$

Because the concentration, or titer of a virus sample is unknown until the fitting is complete, D and D_m adopt units of virus sample volume (mL), thus, we change the notation of these variables to V and V_m, respectively, to indicate that they are volumes. The previously defined IT and PT models have only one parameter, which is associated with the quantity of IU in the virus sample. To ensure that these three models are compared in equal footing, it was necessary to derive a formal IU quantity from the median effect equation. A formal titer can be derived from V_m, which indicates the volume of virus sample required to yield 50% infection. We assume that each infected cell is representative of a single IU (as with the IT and PT models) so that a formal median effect titer (T_m) is then given by the number of cells infected ($C/2$) divided by a sample volume of V_m (Equation 5.7a). Solving the median effect equation (Equation 5.5) for infection (f_a) and substituting T_m gives an expression for how much infection is expected of a given volume (V) of a virus sample with a given median effect titer (T_m), slope (m) and cell count (C).

$$T_m = \frac{C}{2V_m} \qquad \text{(5.7a)} \qquad\qquad f_a = \frac{1}{\left(\frac{2VT_m}{C}\right)^{-m}+1} \qquad \text{(5.7b)}$$

Together, Equations 5.7a and 5.7b represent a virus titration curve through the same quantitative titer value as the IT and PT models, where an extra parameter (m) allows for cooperativity. We define this as the median effect titer (MT) model. It should be noted that the random distribution given by the Poisson equation (for IT and PT models), and the random distribution represented by a the median effect model (where $m = 1$) are fundamentally different (e.g. the IT and PT models are not equal to the MT model when $m = 1$). For this reason, the estimated MT model titer (T_m) is roughly one-half of the IT and PT model titers (T and T_p, respectively), when all three models agree (see Appendix E). We also note that neither the PT nor the MT model are confined by an LRI like the IT

model is.

Specific aims. Our first aim is to quantify the prevalence and significance of infectious cooperativity in HIV infection *in vitro*. This will be done by comparing how well the non-cooperative assumption (IT and PT models) represent a compilation of experimental titration data relative to the cooperative MT model. Titrations giving similar correlations to experimental data (R^2) for all three models are compared to the MT model slope, an indicator of cooperativity, to identify the range of slopes that qualify as non-cooperative. This range is then derived mathematically (Appendix E) and compared to the experimental correlations of each model.

The potential clinical significance of cooperativity is that it allows an equal quantity of virus to produce more or less infected cells, where negative cooperativity results in greater infection. Negative infectious cooperativity is likely based on changes in CD4/CCR5 distribution at the cell surface during viral attachment[19–23], which would leave a large portion of the cell surface bare of CD4/CCR5. Low CD4/CCR5 expression may exacerbate this phenotype as a greater proportion of total surface CD4/CCR5 would be redistributed to the site of attachment, relative to very high CD4/CCR5 expression. To investigate this potential mechanism, we use the GGR Affinofile cell line[28] to determine whether the strength of negative cooperativity increases as CD4/CCR5 expression decreases.

To further investigate the clinical correlates of infectious cooperativity, we develop an analytical strategy that quantifies changes in infection when infectious viral input is equalized. This is applied to isolates that are sensitive and partially resistant to the CCR5 antagonist, maraviroc (MVC), to determine how MVC effects the cooperative distribution of virion to target cells.

Our results define a specific range of slopes ($1 \leq m \leq 1.35$) where the non-cooperative assumption was appropriate and beyond which, the non-cooperative models achieved significantly lower R^2 than the cooperative MT model. In total, we observed a 78% prevalence of

cooperativity. We show that negative infectious cooperativity is a function of CD4/CCR5 expression consistent with the cooperative theory and the impact that attachment can have on cell-surface CD4/CCR5 distribution. This is brought into a more clinical context by showing that MVC reduces the negative cooperativity of sensitive isolates but has no effect on partially resistant isolates. Although limited, our results show that cooperativity is an important phenomenon *in vitro* with potential clinical significance.

Materials and Methods

Cells and virus production. Ghost Hi-R5 cells were obtained from the NIH AIDS Reagent Program and cultured in DMEM supplemented with 10% fetal bovine serum and 100μg/mL hygromycin. HIV Envelopes BaL.26, MI18, MI28, MI29, MI24, MI38, MI39, MI32, MI33, MI21, JR-CSF, PVO, 6535, TRJ and the HIV backbone plasmid pSG3$^{\Delta\text{env}}$ were obtained through the NIH AIDS Reagent Program. Envelopes 24S, 24R, 17S and 17R were obtained from Paul Gorry and Envs 4051C and 4051P were obtained from Ron Swanstrom. A full list of the HIV Envs used is given in Appendix E, Table E.1. HIV pseudotypes were prepared by co-transfection of 293T cells with a 1:1 molar ratio of pSG3$^{\Delta\text{env}}$Gluc and Env DNA using BioT transfection reagent according to manufacturer protocols (Bioland Scientific, Paramount, CA). 72 hours post-transfection viral supernatant was collected and clarified by centrifugation at 1250rpm for 5 minutes at 4°C.

Viral titration. Ghost Hi-R5 cells were plated at a density of 2×10^5 to 3.5×10^5 cells/well onto 24-well plates or 5×10^3 cells/well on 96-well plates and incubated for 24 hours to promote adherence. GGR cells were cultured in DMEM supplemented with 10% dialyzed fetal bovine serum and 50μg/mL Blasticidin S HCl. GGRs were plated onto 24 or 96-well plates at similar densities and cultured for 24 hours prior to inducing with 3ng/mL or 0.2ng/mL doxycycline (CD4 Hi and CD4 Lo, respectively) and 3μM or 0.5μM ponasterone A (CCR5 Hi and CCR5 Lo, respectively) ponasterone A. GGR cells were incubated for another

18-20 hours to allow complete induction of CD4 and CCR5 expression. An extensive review of protocols associated with the GGR cells can be found in Appendix C). HIV pseudotype samples were serial diluted and cell cultures inoculated followed by centrifugation at 2,000 rpm for 2 hours at 37°C. Inoculant was removed, fresh culture media added and cells were incubated for 48 hours prior to fixing and quantifying infectivity via. GFP fluorescence using flow cytometry.

Maraviroc treatment. Viral titrations were performed as described after treatment with 0, 0.4 or 3.3μM maraviroc for 30 minutes at 37°C.

Results

HIV exhibits negative cooperativity *in vitro*. To assess the potential significance of cooperativity in HIV infection, we compiled a total of 37, R5-tropic HIV pseudotype titration experiments performed on Ghost R5 cells using the same spinoculation protocol, where infection was measured by flow cytometry. These titrations represented a total of 21 HIV Envs (Supplementary Table E.1). Because the IT model is restricted by an LRI, the data were filtered to exclude all dilutions of sample giving $> 20\%$ infection (the upper boundary of the LRI) and giving $< 0.5\%$ infection (representing a generous instrumental detection limit). For each titration experiment, the parameters of the IT (T), PT (T_p) and MT (T_m and m) models were calibrated from the filtered data using Equations 5.1b, 5.4b and 5.7a, respectively. The calibrated parameters of each model, for all titration experiments are shown in Figure 5.1 (and Supplementary Table E.2). Both the IT and PT models gave very similar estimated titers, while the MT model titers were, on average, half the value estimated by the IT and PT models (Fig 5.1a), however, the IT and PT model titers fell within a range of 8-fold higher and 2-fold lower than the MT model titer.

Figure 5.1b shows the MT model slopes, which indicate positive ($m > 1$), negative ($m < 1$) or non-cooperativity ($m \approx 1$). We observed a wide range of slopes between

$0.7 < m < 1.7$ while the majority of slopes were less than 1, indicating a possible strong prevalence for negative cooperativity. We also observed a significant correlation between the MT model slope parameter and the ratio of IT and PT titers to the MT titers, that could be approximated by a power function (Fig. 5.1c), consistent with the fact that the MT model contains an additional, exponential slope parameter. It can be shown that the IT and PT titers are expected to be roughly 2-fold larger than an MT titer under agreeable, non-cooperative conditions (see Appendix E). Accordingly, the fitted power function gives a two-fold greater IT and PT titer when $m = 1.008$, consistent with the non-cooperative convergence of all three models when $m \approx 1$. Thus, under non-cooperative conditions ($m \approx 1$), all three models agree as to the quantity of infectious material present in each sample, however, the ratio of IT and PT titers, relative to MT titer, are inversely proportional to MT slope.

To assess the significance of these potential cooperative slopes, the fitted parameters of each model (T, T_p, T_m and m) were then used to back-calculate how much infection each titration experiment should have seen, according to each model. Figure 5.2a shows two examples that demonstrate this process. All three models provided accurate estimates of infection for experiment ID #10 (Fig. 5.2a, left), giving R^2 values of 0.995, 0.995 and 0.996 (IT, PT and MT models, respectively). This particular experiment exhibited an MT slope of 1.06, indicating a non-cooperative mode of infection that is consistent with the high R^2 values of all three models. Conversely, experiment ID #11 (Fig. 5.2a, right) gave a low slope ($m = 0.70$) indicating negative cooperativity that was accurately represented by the MT model ($R^2 = 0.956$). The IT and PT models could not match the shallow rise in infection that was experimentally observed (compare blue and green IT and PT predictions to filled circles in Fig. 5.2a), resulting in low R^2 (0.864 and 0.884, respectively). The consequence of the poor IT and PT fits is a 3-fold overestimate of infection, where the IT and PT models predict 28% and 32% infection, respectively, when only 11% infection was observed (Fig. 5.2a, right). These examples demonstrate that a slope of $m = 0.70$ has a dramatic impact

on the accuracy with which the non-cooperative assumption is able to represent these data and, therefore, an MT model slope of $m = 0.70$ is indicative of negative cooperativity and not non-cooperativity.

The R^2 values for each model among all titration experiments are shown in Figure 5.2b. Both the IT and PT models gave a wide spread of R^2 averaging 0.933 $\pm$ 0.012 and 0.940 $\pm$ 0.013, respectively. The MT model gave the highest and most narrow range of R^2 (0.986 $\pm$ 0.004) that was significantly different from both the IT and PT models ($p< 0.0001$ and $p< 0.001$, respectively), indicating that the MT model, overall, represents the experimental titration of these virus samples with greater accuracy.

To determine the range of slopes that can be considered cooperative or non-cooperative, we found a strong association between MT slope and IT/PT model R^2 (Fig. 5.2c, left and right, respectively). While the MT model R^2 is consistent for all slopes, the IT and PT model R^2 progressively decrease as m increases or decreases away from $m = 1$ and, importantly, the R^2 of all three models converge at $m = 1$. This relationship was so strong that it could be simulated directly by using theoretical titration data generated from the median effect equation and different slopes (Fig. 5.2c, solid lines), indicating that the the IT and PT R^2 values are specifically the result of a slope-based representative deficiency and not experimental error. We evaluated a range of slopes near 1 that can be considered non-cooperative in two ways. First, this range was evaluated mathematically (Appendix E) as $1 \geq m \geq 1.35$ where the IT and PT models yield R^2 that are lower than those of the MT model with statistical significance ($p= 0.0002$ and $p= 0.003$ for IT and PT R^2, respectively). A more narrow range was represented by experiments with IT and PT model R^2 values falling below the range of MT model R^2 values (0.98 ± 0.02), where slopes outside the range of $0.91 \leq m \leq 1.06$ gave IT and MT model R^2 below 0.96. We conclude that the prevalence of cooperativity was 62%, where only 38% of these experiments (with slopes in the range of 0.96 to 1.06) could be equally represented by the cooperative MT and non-cooperative IT and PT models.

The consequence of the non-cooperative assumption engrained in the IT and PT models is shown in Figure 5.2d. At low levels of observed infection (between the range of $0.5\% < f_a < 5\%$), the ratio of expected to observed infection for all three models were centered at 1, thus, on average, all of the models can accurately represent very low levels of infection. It should be noted, however, that although all three models give good predictions on average, the MT model exhibited a much lower spread of expected/observed infection (0.96 ± 0.22, 0.97 ± 0.22 and 1.01 ± 0.11 for IT, PT and MT models within the range of $0.5\% < f_a < 5\%$ infection). As the range of observed infection increases, however, the expectations of the IT and PT models progressively diverge from the amount of infection that was observed. Between the range of 10% to 15% infection the IT and PT models begin to over-predict infection (expected/observed ratios of 1.4 ± 0.4 and 1.3 ± 0.3, respectively) with statistical significance ($p< 0.0001$ for IT and PT models across all ranges of infection, one-way ANOVA), while the MT model remains consistently accurate (1.04 ± 0.08). This reflects the results shown in Figure 5.2a (right), where the shallow rise in observed infection could not be accommodated by these non-cooperative models, resulting in a predicted 32% infection when only one third of that was observed.

We define an approximate range of slopes ($0.96 \leq m \leq 1.06$) that can be considered non-cooperative as the two non-cooperative models achieved a similar representative quality as the cooperative MT model. Outside this range, the non-cooperative IT and PT models fail to describe viral titration with equal R^2 as the cooperative MT model, suggesting that the 62% of titrations exhibiting slopes outside this range were cooperative. We conclude from these data that cooperativity is a frequent phenomenon in HIV infection *in vitro* and that this phenomenon is strong enough to cause significant overestimations of infection when non-cooperativity is assumed. In total, our results suggest that the fundamental assumption of non-cooperative, random distribution in HIV infection, at least *in vitro*, is not generalizable.

Infectious cooperativity is dependent on CD4/CCR5 expression. Cooperativity describes a preferential, non-random distribution of ligands, or virion, that is, according to the cooperative theory, driven by changes in target cell avidity caused by the interaction of a virion with its target cell. When viral attachment decreases the avidity of a cell surface the likelihood than another, unattached and free-floating virion will engage the same cell surface is also decreased – instead, those free virion are more likely to attach to the unengaged cell surfaces that exhibit a higher avidity. This change in avidity, mediated by viral attachment, is most likely the result of rapid, virion-induced redistribution of CD4 and co-receptor molecules at the cell surface. For example, binding of gp120 to CD4, CCR5 and CXCR4 can induce rapid sub-surface activity that redistributes CD4 and co-receptor to the site of attachment[19–23]. While this mechanism ensures a maximum availability of CD4 and co-receptor at the attachment site to facilitate fusion, it is also likely to have a strong negative impact on the avidity of that cell surface for additional virion, which is consistent with the high prevalence of negative cooperativity we observe.

To more closely investigate this possible mechanism, we employed the GGR Affinofile cell line[28,29] (and see Chapter 4) to determine whether infectious cooperativity is dependent on CD4/CCR5 expression. At low CD4/CCR5 expression, the redistribution of CD4/CCR5 to the site of attachment should cause a very dramatic change in CD4/CCR5 availability outside the site of attachment, while at high CD4/CCR5 expression this change should be minimal. The more dramatic decrease in available receptors outside the attachment site, given by low CD4/CCR5 expression, should then increase the strength of negative cooperativity and reduce the slope of viral titration. Thus, we expect CD4/CCR5 expression and slope to be directly proportional.

This mechanism is also fundamentally and inseparably related to CD4 and CCR5 usage efficiency, thus, we chose an HIV isolate for whom the CD4 and CCR5 usage properties have been well characterized[28] (also see Chapter 4), the JR-CSF S142N point mutant. This R5-tropic isolate is able to infect cells with very low levels of CCR5[30], which is more thoroughly

described by its VERSA metrics[28]. S142N exhibits a more CCR5-dependent response in infectivity through an increased VERSA angle, θ (30.9° and 38.2° for WT and S142N) and a higher overall mean infectivity, M (20.1% and 40.3% for WT and S142N). S142N also exhibits a weaker, overall responsiveness to changes in CD4/CCR5 expression than WT JR-CSF through a lower response amplitude, Δ (50.6 and 35.7 for WT and S142N, respectively). Because S142N has a weaker overall response to changes in CD4/CCR5 expression (Δ) and a higher set-point of infectivity (M), the change in infection with respect to increases and decreases in CD4/CCR5 expression are weaker than its WT counterpart, thus, this Env is more infectious than WT JRCSF when CD4/CCR5 expression is low. Cooperativity may give an alternative, complementary perspective of this phenotype.

JRCSF S142N was titrated onto Ghost R5 cells expressing non-limiting (NL) levels of CD4 and CCR5 as well as GGR cells expressing maximum (Hi) and mimimum (Lo) combinations of CD4 and CCR5. These titration curves were analyzed using the cooperative MT model to obtain estimated titers (T_m) and slopes (m) (Fig. 5.3a and b). The highest titer was estimated using Ghost R5 cells ($T_m = 46 \times 10^3$ IU/mL), while maximally induced CD4/CCR5 (Hi/Hi) GGR cells estimated a lower titer ($T_m = 23 \times 10^3$ IU/mL), concordant with a lower relative quantity of CD4/CCR5 expression. On GGR cells expressing high levels of CCR5, the estimated titer of S142N did not respond to changes in CD4 expression, while a dramatic decrease in titer is associated more specifically with decreases in CCR5 expression, in agreement with the CCR5 dependence of this isolate given by the VERSA θ metric. The greatest change in estimated titer, a 10-fold decrease, was associated with a decreased CCR5 expression when CD4 was Lo, suggesting that limited CD4 expression exacerbates the CCR5-dependence of S142N.

The slopes of each titration curve are shown in Figure 5.3b. By far, Ghost R5 cells expressing non-limiting levels of CD4 and CCR5 gave the most non-cooperative slope ($m = 0.96$) while all levels of CD4/CCR5 induction on GGR cells gave slopes much lower than any of the 37 titrations we have analyzed on Ghost R5 cells (Fig. 5.1b). Little to no change

in slope was observed upon changes in CD4 expression when CCR5 was Hi, or with changes in CCR5 expression when CD4 was Hi. However, when CD4 was Lo, there was a dramatic decrease in slope associated with decreased CCR5 expression ($m = 0.70$ and 0.50 for CCR5 Hi and CCR5 Lo, respectively).

To understand the consequence of this changing slope, we developed a novel analytical method to compare infection across a normalized infectious viral input. A fair comparison of infectivity cannot be obtained by evaluating infection in terms of viral input volume or Ghost R5 titer because the titers of this single virus sample were dependent on CD4/CCR5 expression (Fig. 5.3a). For example, GHR5 cells estimated the highest titer because they express the highest levels of CD4/CCR5 and, accordingly, the titer of this sample was 22-fold lower on GGR cells expressing low levels of CD4/CCR5. Thus, reduced CD4/CCR5 expression resulted in a 22-fold decrease in the quantity of virion detected, but does not assess the infectious capacity, or quality of the virion that *did* infect. To assess infection in terms of the quantity of virion that successfully infected, we normalized viral input volume by the estimated titers under each condition to obtain an MOI-based comparison of infectivity (Fig. 5.3c).

JRCSF S142N exhibited a greater MOI-based infectivity on CD4 Hi GGR cells, relative to Ghost R5 cells, at both Hi and Lo CCR5 expression (Fig. 5.3c, left). Interestingly, the dramatic increase in MOI-based infectivity between Ghost R5 cells and GGRs expressing Hi CD4 and Hi CCR5 is associated with a 2-fold decrease in estimated titer, while the negligible difference in MOI infectivity between GGRs expressing Hi levels of CD4 and Hi to Lo levels of CCR5 is accompanied by a greater 3.5-fold decrease in titer (compare infected cells in Fig. 5.3c, left to respective titers in Fig. 5.3a). These results show a lack of response to CCR5 expression, on an MOI basis, when CD4 is expressed at maximal levels on GGR cells despite an overall 3.5-fold decrease in effective titer. Conversely, the MOI infectivity of this isolate was more sensitive to CCR5 expression when CD4 was minimally expressed (Fig. 5.3c, right). Again, relative to Ghost R5 cells, a greater MOI infectivity was observed on GGR

cells when CD4 was Lo and CCR5 was Hi, however, a further increase in MOI infectivity was observed when CCR5 was reduced. This increased MOI infectivity was associated with the most dramatic, 10-fold decrease in estimated titer, suggesting that although less virion can be detected due to decreased CD4/CCR5 expression, the virion that are detected can generate up to 2.3-fold more infection when CCR5 expression is minimal and 7.1-fold more infection than on Ghost R5 cells, at an effective MOI of approximately 0.4 (Fig 5.3c, right, dashed lines).

The MOI infectivities shown in Figure 5.3c reflect the changing cooperativities of infection for each condition (Fig 5.3b). While S142N exhibited a non-cooperative slope ($m \approx 1$) when titrated on Ghost R5 cells, this same virus sample exhibited strong negative cooperativity when titrated onto GGR cells ($m \leq 0.7$ for all CD4/CCR5 combinations). A decrease in slope was observed when CD4 was Lo and CCR5 expression was reduced ($m = 0.7$ to 0.5 for CCR5 Hi and CCR5 Lo), suggesting that although minimal CD4/CCR5 expression caused a dramatic 22-fold decrease in estimated titer, relative to Ghost R5 cells, it also increased the negative cooperativity and distribution efficiency of the virion that do manage to infect, resulting in a 7-fold greater MOI-based infectivity, relative to Ghost R5 cells and a 2-fold increase in infectivity relative to the same GGR cells, expressing higher levels of CCR5.

These results are consistent with the well documented ability of JRCSF S142N to efficiently infect cells with very low levels of CCR5 expression[28,30]. Our analysis further explicates this phenotype by suggesting that this Env is more infectious, on an MOI basis, when CCR5 is low, consistent with the adaptation of S142N from PBMCs to Molt-4 and finally Sup-T1 cells[30], which express vanishingly low levels of CCR5[31]. Our results also show that the titration slope of this Env is proportional to CD4/CCR5 expression, where a non-cooperative slope of 0.96 was observed on Ghost R5 cells and a strong negative cooperativity ($m = 0.5$) was observed on GGR cells expressing low levels of CD4 and CCR5. Our analysis further distinguishes changes in infection probability, given by an estimated titer, from the infectious capacity or quality of the virion that manage to infect.

Cooperativity in drug resistance. As a distributive phemonenon relating to the interactions between virion and their target cells, an increasing negative cooperativity (and decreased titration slope) was associated with reduced CD4/CCR5 expression. Maraviroc (MVC) is a CCR5 antagonist that alters the conformation of CCR5 in such a way that it cannot be recognized by the HIV Env as a functional co-receptor[32,33]. Resistance, while maintaining R5-tropism, is given by an adaptation in gp120 that recognizes alternative regions of CCR5 that are unaffected by the drug, thus, resistant isolates can use the MVC-bound form of CCR5[1–3]. Because resistant isolates engage a different region of CCR5, they may not trigger dramatic changes in CD4/CCR5 distribution that we associate, here, with negative cooperativity. HIV BaL is a standard, R5-tropic laboratory strain isolated from infant lung tissue[34] and is naive to MVC treatment. The envelopes of isolates 17S and 17R were sequenced from a single patient before MVC treatment (17S) and after treatment failure (17R)[3]. While 17S is sensitive to MVC treatment, 17R exhibits a unique form of weak resistance where it is able to use the MVC-bound form of CCR5 with low efficiency by recognizing an alternative region. 17R can be inhibited by MVC, but it cannot be completely inhibited due to the use of MVC-bound CCR5, resulting in a maximum percent inhibition (MPI) effect[3]. To evaluate the potential significance of cooperativity in MVC resistance, we titrated BaL, 17S and 17R Env pseudotypes onto Ghost R5 cells in the presence or absence of MVC.

Figure 5.4a shows the experimental results from titrations of these Envs with no MVC, 0.4μM MVC and 3.3μM MVC. Both BaL and 17S showed substantial decreases in infection with respect to virus sample volume, while the volume-dependent infection of 17R was only slightly reduced at the highest concentration of MVC. The sensitivity of each isolate can be described in terms of the estimated titer under each condition (Fig. 5.4b), where MVC reduced the effective titer of all isolates. MVC caused greater reductions in titer for BaL and 17S, up to 70% (3.3μM MVC), and much smaller reductions in titer for the partially resistant 17R isolate (13% and 50% for 0.4 and 3.3μM MVC, respectively). These reductions

in estimated titer represent the proportion of infectious events that could have occurred (100% titer with no MVC) but were instead, outright inhibited by the drug, resulting in a loss of countable virion.

Cooperativity, given by the slope parameter (m) adds a new dimension to the range of possible effects MVC might have on these isolates. Figure 5.4c shows the slopes of each isolate in the presence and absence of MVC. Both the treatment naive BaL and 17S isolates exhibited increases in slope that were proportionate to MVC concentration, indicating that MVC induced a more positive cooperativity. The partially resistant 17R isolate exhibited no change in slope, even at 3.3μM MVC, which reduced the effective titer of this virus by 50%.

Although MVC was able to outright block infectious events for all three isolates, cooperativity adds an additional phenotype, where MVC might change the properties of the virion that managed to escape inhibition. For example, 3.3μM MVC blocked 70% of the BaL pseudotype from infecting (given by the titer reduction), but does MVC alter how much infection the remaining, uninhibited 30% can produce? In essence, do the same number of uninhibited, infecting virion generate the same amount of infection in the presence and absence of MVC? Or does MVC not only impact the number of countable virion, but also the infectious quality, or capacity of those virion? To answer this question, we normalized viral input (Fig. 5.4a) by the titers at for each isolate at each MVC concentration to obtain MOI-based infectivity plots. Thus, the virion that were outright blocked by MVC activity are excluded from this analysis, allowing infection to be compared for each condition in terms of an equalized quantity of countable, infecting virion.

Figure 5.4d compares the normalized, MOI-based infectivity of each isolate in the presence and absence of MVC. Both BaL and 17S exhibit a reduced MOI-based infectivity that was proportionate to MVC concentration. For example, at an effective MOI of approximately 0.015, the highest concentration of MVC resulted in a 3.8-fold decrease in BaL infection and a 2.5-fold decrease in 17S infection. This suggests that MVC has a two-pronged activity

against these isolates. First, MVC outright inhibits a certain proportion of infectious virion and second, the virion that do manage to infect in the presence of MVC cannot generate as much infection as the same quantity of virion do in the absence of MVC. Conversely, the partially resistant 17R isolate did not exhibit a reduced MOI-based infectivity at any concentration of MVC even though 3.3μM MVC was able to outright inhibit 50% of these virion. Thus, while this isolate is partially sensitive to inhibition, MVC does not reduce the infectious quality of 17R virion as it does with the treatment naive 17S and BaL isolates.

The MVC-induced decreases in MOI-based infectivity for BaL and 17S are the direct result of an MVC-dependent increase in slope and positive cooperativity, as a more positive cooperativity indicates a greater probability for multiple virion to attach to the same cell and, thus, less overall infection. This may be driven by the fact that MVC inhibits infection after virion engage cell-surface CD4, thus, the virion that are inhibited have already begun attachment and are not free to find another cell, which increases the effective stoichiometry of virion to infected cells. That this does not occur for the partially resistant, 17R isolate is in agreement with the known ability of 17R to use CCR5-bound MVC, thus, MVC has no effect on the fundamental entry mechanism of 17R outside of a MVC-bound CCR5 usage efficiency, which is reflected in the decreased titer and is not a differential slope property.

These results suggest that infectious cooperativity may have clinical significance, where unique entry inhibitor activities might be measured as an increase in cooperativity that might accelerate the effect of treatment on viral replication *in vivo*. Conversely, isolates exhibiting no change in infectious cooperativity in the presence of a drug might indicate a propensity for resistance indicated by the fact that the drug has no effect on the mechanism of virion distribution and attachment.

Discussion

The classical, binary notion that an infectious virion can only give rise to a single cell that is either infected or not infected is surely true in the most limited context, involving one cell and

one virion. However, this perspective does not account for the emergent dynamics of viral populations. Indeed, random distribution was the core assumption for most target-effector systems until a concrete formulation of cooperativity was available[6]. The assumptions of the IT model reflect this classical concept, where a direct and linear proportionality between viral input and infection is expected that leaves no room for any form of distribution other than one virion per cell. The imposition of a linear range onto the IT model minimizes the resulting error, but does not correct this fundamental deficiency. Conversely, the PT model, which specifically accounts for the random distribution of virion, represents a significantly improved perspective. Although both positive and negative cooperativity have been described in great detail for a variety of biological systems, an understanding of this phenomenon has been generally confined to the fields of biochemistry and pharmacology. Cooperativity is a strong possibility for all target-effector systems involving targets with multiple effector sites, such as the myriad of potential fusion sites presented by HIV target cells. Our results strongly suggest that the basic process of attachment and entry *in vitro* is more dynamic than random distribution can allow. Whether cooperativity extends to more complex systems *in vivo* remains to be seen. Here, we present the first step: a complete analytical framework to investigate the significance of cooperativity in the context of clinically relevant viral phenotypes.

Cooperativity is specifically driven by the impact an effector has on its target, from the perspective of other effectors. In the classical context of hemoglobin, positive cooperativity is driven by oxygen-induced conformational changes that increase the affinity of deoxy-hemes. By analogy, the predominantly negative cooperativities observed here are likely driven by the impact a single virion has on the distribution of CD4/CCR5 at the cell surface, within the limited time-frame of entry. Signaling through CD4 and CCR5/CXCR4 by gp120 is known to have a dramatic and rapid effect on the co-localization of these receptors to sites of entry[19–23]. This process likely decreases the probability of multiple virion engaging the same cell by increasing the local density of CD4/CCR5 at the expense of total surface

CD4/CCR5 density, that is, colocalization may leave the rest of the cell surface bare of potential fusion sites. This may result in a lower surface avidity for virion-engaged cells relative to virion-free cells and, therefore, a non-random distribution of virion consistent with negative cooperativity. We point out that the slope also has a stoichiometric interpretation, however, slopes less than 1 would indicate that a single virion is capable of infecting multiple cells, which violates the logical, limiting stoichiometry of infection. Thus, the predominantly negative cooperativities observed in our data preclude a purely stoichiometric interpretation.

This proposed mechanism is consistent with the CD4/CCR5-dependent cooperativities of JRCSF S142N. Co-localization of CD4/CCR5 likely has a strong impact on total surface density when CD4/CCR5 expression is low (Fig 5.5a), causing a strong negative cooperativity. This effect, however, may not be as dramatic when CD4/CCR5 are expressed at very high levels on GGR cells or at non-limiting levels on Ghost R5 cells, thus, a weaker negative cooperativity or non-cooperativity is expected (Fig. 5.5b). The result of strong negative cooperativity was a dramatic 7.1-fold increase in the amount of infection generated by an equalized quantity of infecting, countable virion concomitant with a 10-fold reduction in titer. Importantly, the non-cooperative IT and PT models could not represent the strong negative coopeartivities observed here and fundamentally do not allow a virus to exhibit different levels of MOI-based infectivity, thus, these models do not permit this type of analysis.

While the CD4/CCR5-dependent decrease in estimated titer for S142N was associated with a more negative cooperativity and a greater MOI-based infectivity, the MVC-sensitive BaL and 17S isolates showed the opposite phenotype. The inhibition of infectious virion decreased the estimated titer of these samples but, instead, resulted in a more positive cooperativity and a decrease in MOI-based infectivity. These results may be both stoichiometric and cooperative, where MVC may inhibit both a) the successful entry of an attached virion and b) the redistribution of surface CD4/CCR5 by preventing Env-CCR5 engagement. Interestingly, while the sensitive 17S isolate exhibited negative cooperativity in the absence

of MVC, the partially resistant 17R isolate was equally non-cooperative in the absence and presence of MVC. Resistance of the 17R isolate is attributed to mutations in the V3 loop, which allow Env to recognize alternative regions of CCR5 that are not affected by MVC[3,5]. Our results suggest that recognition of this alternative site might not trigger CD4/CCR5 co-localization, resulting in non-cooperativity whether MVC is present or not.

Many additional, experimental factors contribute to infectivity slopes, such as the specific ratio of envelope and backbone DNA used to pseudotype HIV virion, spinoculation and temperature (data not shown). While we were able to minimize these confounding factors by analyzing only R5-tropic HIV pseudotype samples titrated onto Ghost R5 cells via. spinoculation, we did observe some high variability in slope and titer among different preparations of the same pseudotypes (Supplementary Table E.2). To avoid such complications in an appropriate time-frame, the data shown regarding MVC resistance and CD4/CCR5 expression represented only a single replicate. To further clarify the potential variability in slope and titer, we titrated a single BaL pseudotype virus 15 times over the course of 7 months using the same spinoculation protocol, where this sample gave a highly consistent titer (log 5.3 IU/mL, 95% c.i. log 5.2 to log 5.35 IU/mL). The slope of this virus was also consistent ($m = 0.84 \pm 0.05$) and indicative of negative cooperativity. While the experimental variability in slope observed for this isolate was well below the changes in slope presented in the context of MVC resistance and CD4/CCR5 usage, we acknowledge that these data lack sufficient reproducibility, at the moment, to draw concrete conclusions.

Although the time frame of this dissertation did not permit a more thorough explication of these phenotypes or the specific biological mechanisms of cooperativity in HIV infection, we were able to show that cooperative infection is a frequent and significant phenomenon and we were able to develop a complete analytical framework to facilitate further investigation. That negative cooperativity was strongest using GGR cells expressing more biologically relevant levels of CD4 and CCR5 (relative to Ghost R5 cells) suggests that this phenomenon may be an important component of target cell tropism *in vivo*. The clinical significance of

cooperativity will likely be related to the fact that this phenomenon allows an equal quantity of virions to produce more or less infected cells than expected, given the classical modality of random distribution. Conditions that increase negative cooperativity may have a powerful influence on replication rates, which depend on the amount of infection a population of virion can produce as opposed to the actual quantity of virion present. This is highly relevant in clinical contexts of viral expansion, such as transmission and resistance, which are initiated by very low quantities of viral input and where small differences in the infectious quality of a virus is expounded over generations of infection and adaptation.

Figures

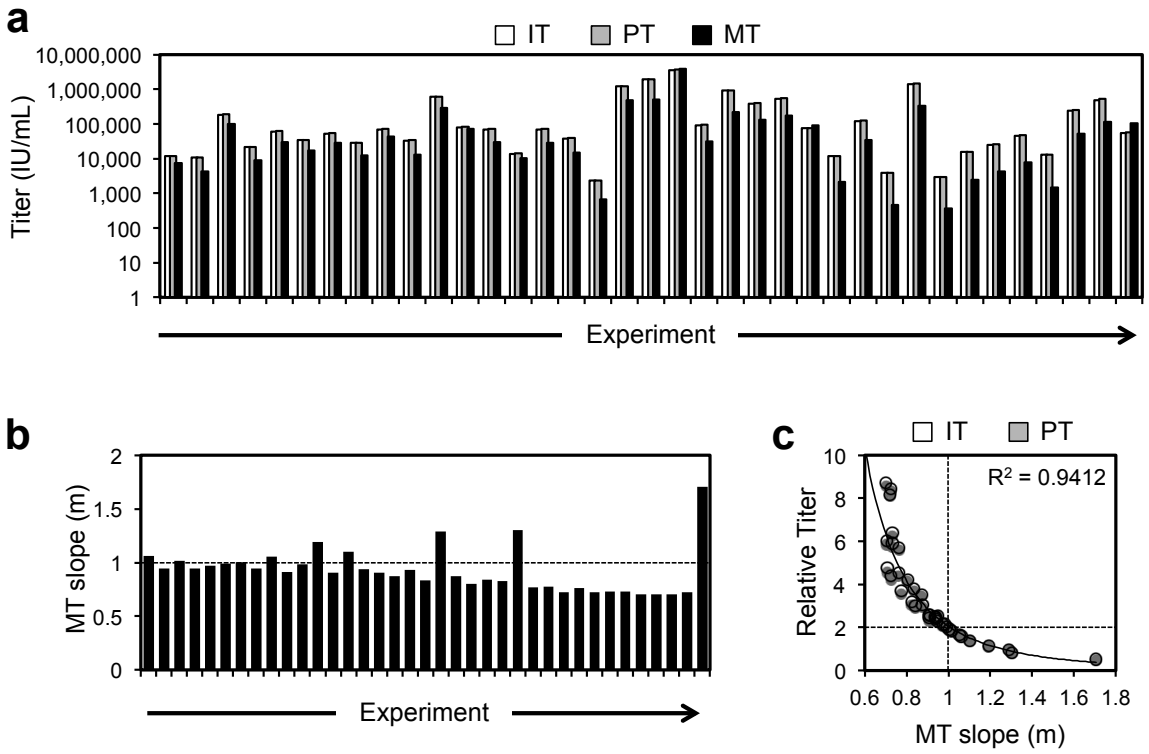

Figure 5.1: Fitting parameter results for IT, PT and MT models. (**a**) Estimated titers for IT, PT and MT models for all 37 HIV titration experiments. (**b**) MT model slope parameters for each titration experiment show a variety of values primarily near or below 1. Although IT and PT model titers were, as expected, 2-fold greater than the MT model on average, the relative titers (IT/MT and PT/MT) were also dependent on MT slope (**c**), where a non-cooperative slope ($m = 1$) resulted in an exact 2-fold difference between IT/PT and MT titers according to power-function estimates (solid line), indicating agreement between all models when non-cooperativity is observed.

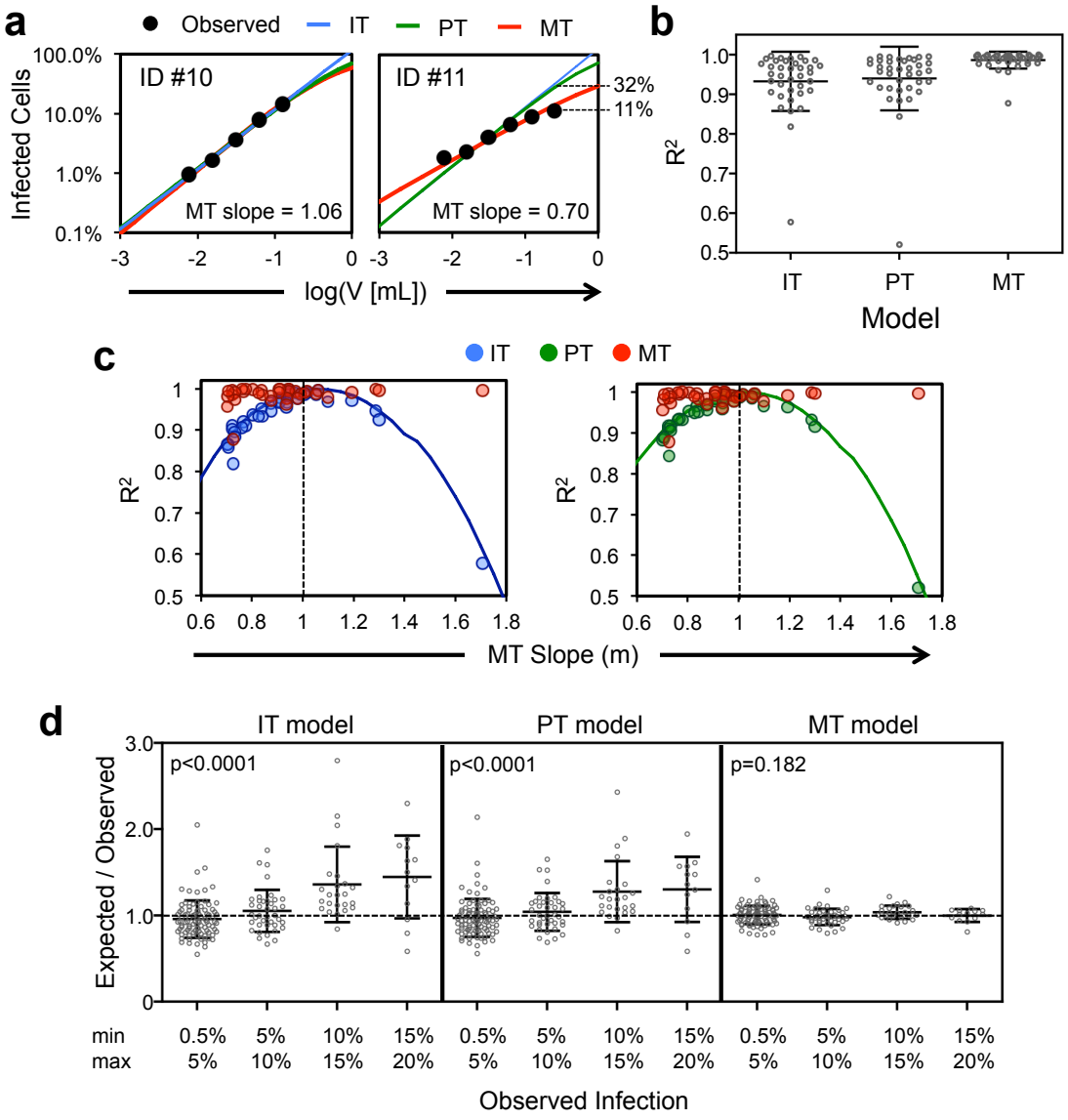

Figure 5.2: Representative accuracy of IT, PT and MT models. (**a**) Titration curves of two representative virus samples exhibiting slopes near 1 (left) or below 1 (right). IT, PT and MT expectations are shown (blue, green and red, respectively) relative to the experimental results (filled circles). (**b**) Correlation coefficients (R^2) of each model to the experimental results of all 37 HIV titration curves. (**c**) The association between MT-model slope (m) and IT (left) and PT (right) model R^2. This association could be directly simulated using the median effect equation and various slopes to generate theoretical titration data (solid lines). (**d**) Ratios of predicted to observed infection for all three models broken into groups of 5% observed infection. In all cases, bars show the mean and standard deviation and p values were calculated using one-way ANOVA.

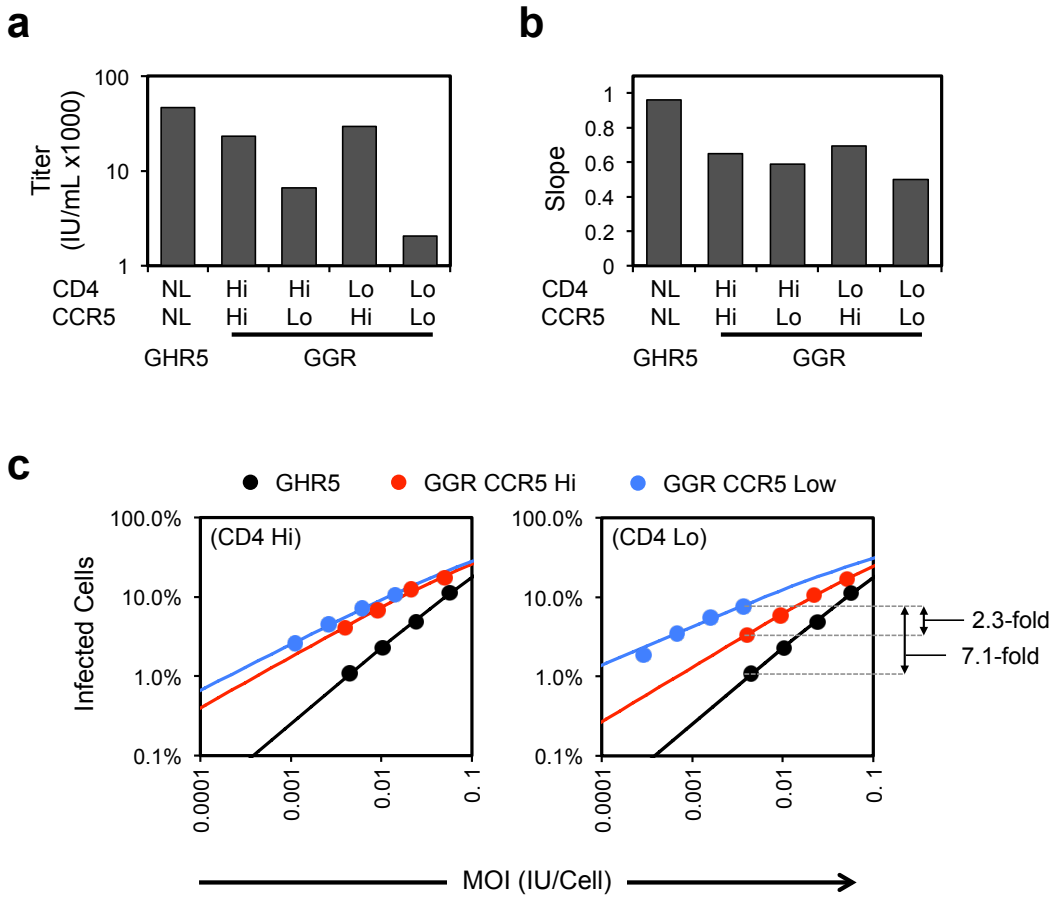

Figure 5.3: Dependence of cooperativity on CD4 and CCR5 expression. (**a**) MT-model titers and (**b**) slopes from titration of of a JRCSF S142N pseudotype on Ghost R5 cells (GHR5) and GGR cells expressing high (Hi) or low (Lo) combinations of CD4 and CCRR5. (**c**) comparison of MOI-normalized infection on GGR cells expressing high (left) or low (right) levels of CD4 across high (red) or low (blue) levels of CCR5 expression. MOI-normalized results using GHR5 cells (black) are shown for reference. Experimental results are shown as filled circles and MT model fits as solid lines. These data represent a single experiment.

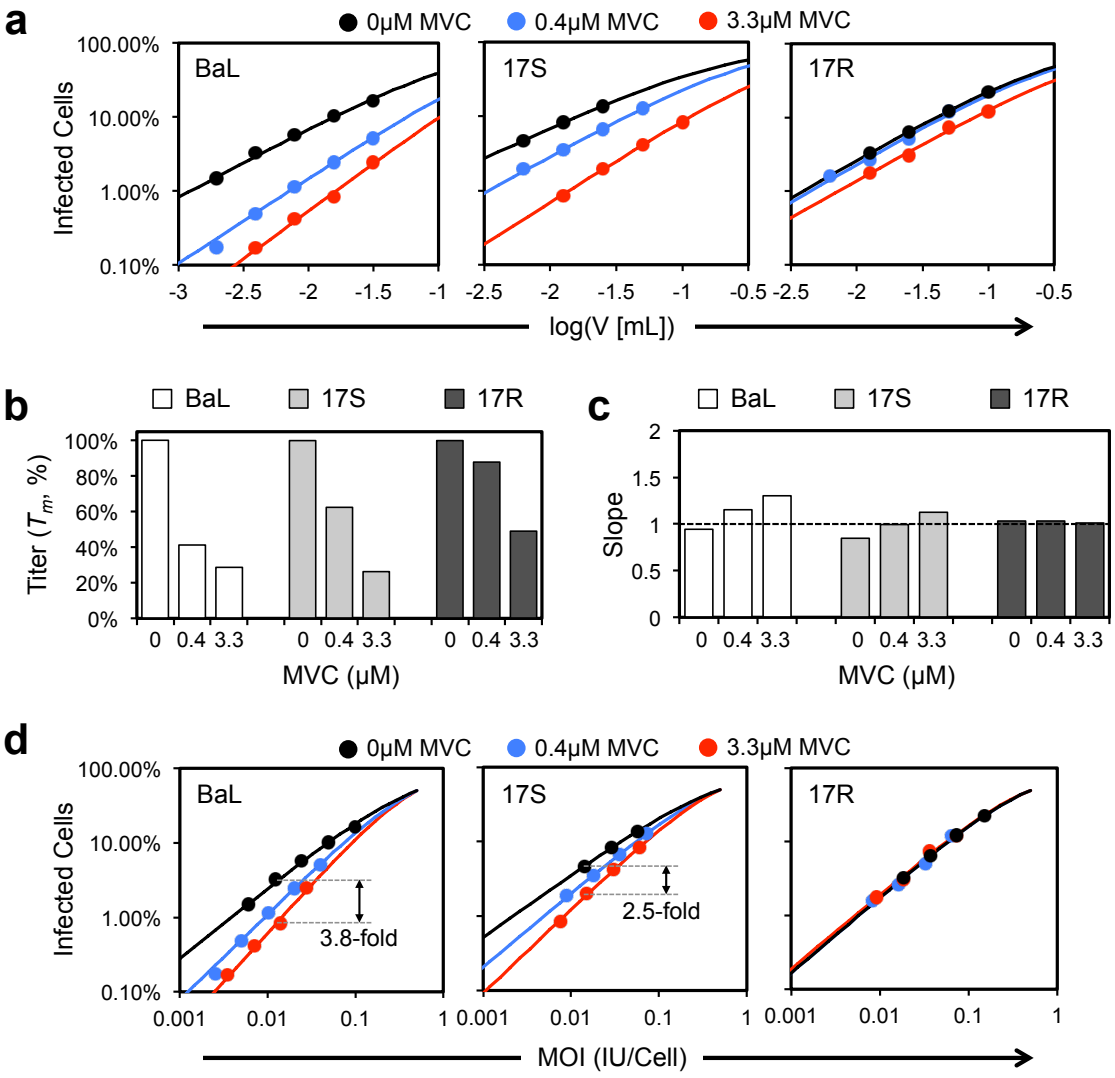

Figure 5.4: Cooperativity in the presence of maraviroc. (**a**) titration curves of BaL, 17S and 17R pseudotype virion in the absence (black) or presence of 0.4 (blue) and 4.4μM (red) MVC. Filled circles show experimental results and solid lines are MT model fits. (**b**) MT-model titers (T_m) from the data shown in panel a. (**c**) MT-model slopes (m) from the data shown in panel a. (**d**) MOI-normalized results from the data shown in panel a, where viral input is described in terms of effective, uninhibited infectious units per cell (IU/Cell). Data are the results of a single experiment.

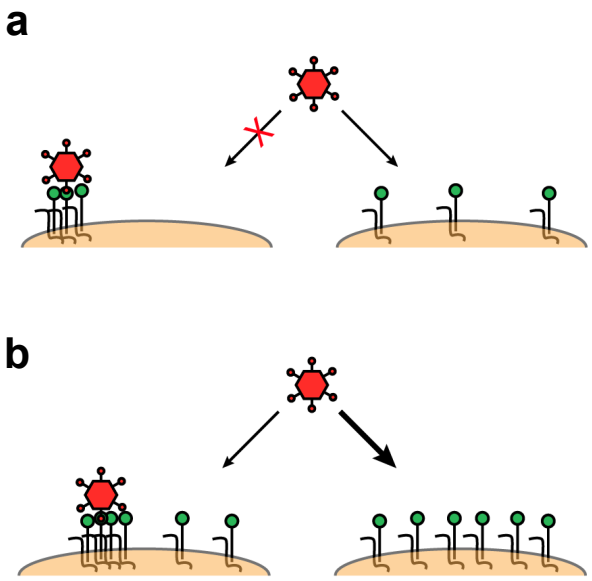

Figure 5.5: Illustration of infectious cooperativity. At low CD4/CCR5 expression (**a**) virion-mediated redistribution of surface CD4 and CCR5 (green circles and black squiggles) can have leave the rest of the cell surface bare, which prevents a virion (red) from attaching to cells that are already engaged by another virion, resulting in strong negative cooperativity. This effect may not be as dramatic when CD4/CCR5 are expressed at high levels (**b**), which may retain a higher avidity resulting in a weaker negative cooperativity.

References

1. Michael Roche, Martin R Jakobsen, Anne Ellett, Hamid Salimiseyedabad, Becky Jubb, Mike Westby, Benhur Lee, Sharon R Lewin, Melissa J Churchill, and Paul R Gorry. HIV-1 predisposed to acquiring resistance to maraviroc (MVC) and other CCR5 antagonists in vitro has an inherent, low-level ability to utilize MVC-bound CCR5 for entry. *Retrovirology*, 8:89, 2011.

2. Michael Roche, Martin R Jakobsen, Jasminka Sterjovski, Anne Ellett, Filippo Posta, Benhur Lee, Becky Jubb, Mike Westby, Sharon R Lewin, Paul A Ramsland, Melissa J Churchill, and Paul R Gorry. HIV-1 escape from the CCR5 antagonist maraviroc associated with an altered and less-efficient mechanism of gp120-CCR5 engagement that attenuates macrophage tropism. *J Virol*, 85(9):4330–42, May 2011.

3. Michael Roche, Hamid Salimi, Renee Duncan, Brendan L Wilkinson, Kelechi Chikere, Miranda S Moore, Nicholas E Webb, Helena Zappi, Jasminka Sterjovski, Jacqueline K Flynn, Anne Ellett, Lachlan R Gray, Benhur Lee, Becky Jubb, Mike Westby, Paul A Ramsland, Sharon R Lewin, Richard J Payne, Melissa J Churchill, and Paul R Gorry. A common mechanism of clinical HIV-1 resistance to the CCR5 antagonist maraviroc despite divergent resistance levels and lack of common gp120 resistance mutations. *Retrovirology*, 10:43, 2013.

4. Jennifer M Pfaff, Craig B Wilen, Jessamina E Harrison, James F Demarest, Benhur Lee, Robert W Doms, and John C Tilton. HIV-1 resistance to CCR5 antagonists associated with highly efficient use of CCR5 and altered tropism on primary CD4+ T cells. *J Virol*, 84(13):6505–14, Jul 2010.

5. John C Tilton, Craig B Wilen, Chukwuka A Didigu, Rohini Sinha, Jessamina E Harrison, Caroline Agrawal-Gamse, Elizabeth A Henning, Frederick D Bushman, Jeffrey N Martin, Steven G Deeks, and Robert W Doms. A maraviroc-resistant HIV-1 with narrow cross-

resistance to other CCR5 antagonists depends on both N-terminal and extracellular loop domains of drug-bound CCR5. *J Virol*, 84(20):10863–76, Oct 2010.

6. J MONOD, J WYMAN, and J P CHANGEUX. ON THE NATURE OF ALLOSTERIC TRANSITIONS: A PLAUSIBLE MODEL. *J Mol Biol*, 12:88–118, May 1965.

7. L.J. Reed and H. Muench. a simple method of estimating fifty per cent endpoints. *The American Journal of Hygiene*, 27(3):493–497, May 1938.

8. C Spearman. The Method of 'Right and Wrong' Cases ('Constant Stimuli') Withut Gauss's Formulae. *Brittish Journal of Psychology*, 2:227–242, 1908.

9. G Karber. Beitrag zur kollektiven Behandlung pharmakologischer Reihenversuche. *Archiv fur Experimentelle Pathologie und Pharmakologie*, 162:480–487, 1931.

10. D.J. Finney. *Statistical Methods in Biological Assay*. Griffin, London, England, 2 edition, 1984.

11. A Gervaix, D West, L M Leoni, D D Richman, F Wong-Staal, and J Corbeil. A new reporter cell line to monitor HIV infection and drug susceptibility in vitro. *Proc Natl Acad Sci U S A*, 94(9):4653–8, Apr 1997.

12. Zengji Li, Loni Ling, Xiaohui Liu, Reiner Laus, and Alain Delcayre. A flow cytometry-based immuno-titration assay for rapid and accurate titer determination of modified vaccinia Ankara virus vectors. *J Virol Methods*, 169(1):87–94, Oct 2010.

13. D C Hitt, J L Booth, V Dandapani, L R Pennington, J M Gimble, and J Metcalf. A flow cytometric protocol for titering recombinant adenoviral vectors containing the green fluorescent protein. *Mol Biotechnol*, 14(3):197–203, Mar 2000.

14. Vincent Gueret, Juan A Negrete-Virgen, Andrew Lyddiatt, and Mohamed Al-Rubeai. Rapid titration of adenoviral infectivity by flow cytometry in batch culture of infected HEK293 cells. *Cytotechnology*, 38(1-3):87–97, Jan 2002.

15. M L Musco, S Cui, D Small, M Nodelman, B Sugarman, and M Grace. Comparison of flow cytometry and laser scanning cytometry for the intracellular evaluation of adenoviral infectivity and p53 protein expression in gene therapy. *Cytometry*, 33(3):290–6, Nov 1998.

16. Jean-Pierre Changeux. Allostery and the Monod-Wyman-Changeux model after 50 years. *Annu Rev Biophys*, 41:103–33, 2012.

17. Hesam N Motlagh, Jing Li, E Brad Thompson, and Vincent J Hilser. Interplay between allostery and intrinsic disorder in an ensemble. *Biochem Soc Trans*, 40(5):975–80, Oct 2012.

18. Hesam N Motlagh, James O Wrabl, Jing Li, and Vincent J Hilser. The ensemble nature of allostery. *Nature*, 508(7496):331–9, Apr 2014.

19. Stephen A Gallo, Catherine M Finnegan, Mathias Viard, Yossef Raviv, Antony Dimitrov, Satinder S Rawat, Anu Puri, Stewart Durell, and Robert Blumenthal. The HIV Env-mediated fusion reaction. *Biochim Biophys Acta*, 1614(1):36–50, Jul 2003.

20. Mark Spear, Jia Guo, and Yuntao Wu. The trinity of the cortical actin in the initiation of HIV-1 infection. *Retrovirology*, 9:45, 2012.

21. Marta Barrero-Villar, José Román Cabrero, Mónica Gordón-Alonso, Jonathan Barroso-González, Susana Alvarez-Losada, M Angeles Muñoz-Fernández, Francisco Sánchez-Madrid, and Agustín Valenzuela-Fernández. Moesin is required for HIV-1-induced CD4-CXCR4 interaction, F-actin redistribution, membrane fusion and viral infection in lymphocytes. *J Cell Sci*, 122(Pt 1):103–13, Jan 2009.

22. Sonia Jiménez-Baranda, Concepción Gómez-Moutón, Ana Rojas, Lorena Martínez-Prats, Emilia Mira, Rosa Ana Lacalle, Alfonso Valencia, Dimiter S Dimitrov, Antonella Viola, Rafael Delgado, Carlos Martínez-A, and Santos Mañes. Filamin-A regulates actin-dependent clustering of HIV receptors. *Nat Cell Biol*, 9(7):838–46, Jul 2007.

23. Paul J Vorster, Jia Guo, Alyson Yoder, Weifeng Wang, Yanfang Zheng, Xuehua Xu, Dongyang Yu, Mark Spear, and Yuntao Wu. LIM kinase 1 modulates cortical actin and CXCR4 cycling and is activated by HIV-1 to initiate viral infection. *J Biol Chem*, 286(14):12554–64, Apr 2011.

24. A.V. Hill. The possible effects of the aggregation of the molecules of hæmoglobin on its dissociation curves. *J. Physiol.*, 40(Suppl.):iv–vii, January 1910.

25. T C Chou and P Talalay. Quantitative analysis of dose-effect relationships: the combined effects of multiple drugs or enzyme inhibitors. *Adv Enzyme Regul*, 22:27–55, 1984.

26. M F Perutz, A J Wilkinson, M Paoli, and G G Dodson. The stereochemical mechanism of the cooperative effects in hemoglobin revisited. *Annu Rev Biophys Biomol Struct*, 27:1–34, 1998.

27. William A Eaton, Eric R Henry, James Hofrichter, Stefano Bettati, Cristiano Viappiani, and Andrea Mozzarelli. Evolution of allosteric models for hemoglobin. *IUBMB Life*, 59(8-9):586–99, 2007.

28. Kelechi Chikere, Nicholas E Webb, Tom Chou, Katharina Borm, Jasminka Sterjovski, Paul R Gorry, and Benhur Lee. Distinct HIV-1 entry phenotypes are associated with transmission, subtype specificity, and resistance to broadly neutralizing antibodies. *Retrovirology*, 11:48, 2014.

29. Samantha H Johnston, Michael A Lobritz, Sandra Nguyen, Kara Lassen, Shirley Delair, Filippo Posta, Yvonne J Bryson, Eric J Arts, Tom Chou, and Benhur Lee. A quantitative affinity-profiling system that reveals distinct CD4/CCR5 usage patterns among human immunodeficiency virus type 1 and simian immunodeficiency virus strains. *J Virol*, 83(21):11016–26, Nov 2009.

30. M T Boyd, G R Simpson, A J Cann, M A Johnson, and R A Weiss. A single amino

acid substitution in the V1 loop of human immunodeficiency virus type 1 gp120 alters cellular tropism. *J Virol*, 67(6):3649–52, Jun 1993.

31. B Lee, M Sharron, L J Montaner, D Weissman, and R W Doms. Quantification of CD4, CCR5, and CXCR4 levels on lymphocyte subsets, dendritic cells, and differentially conditioned monocyte-derived macrophages. *Proc Natl Acad Sci U S A*, 96(9):5215–20, Apr 1999.

32. Christoph Seibert, Weiwen Ying, Svetlana Gavrilov, Fotini Tsamis, Shawn E Kuhmann, Anandan Palani, Jayaram R Tagat, John W Clader, Stuart W McCombie, Bahige M Baroudy, Steven O Smith, Tatjana Dragic, John P Moore, and Thomas P Sakmar. Interaction of small molecule inhibitors of HIV-1 entry with CCR5. *Virology*, 349(1):41–54, May 2006.

33. Fotini Tsamis, Svetlana Gavrilov, Francis Kajumo, Christoph Seibert, Shawn Kuhmann, Tom Ketas, Alexandra Trkola, Anadan Palani, John W Clader, Jayaram R Tagat, Stuart McCombie, Bahige Baroudy, John P Moore, Thomas P Sakmar, and Tatjana Dragic. Analysis of the mechanism by which the small-molecule CCR5 antagonists SCH-351125 and SCH-350581 inhibit human immunodeficiency virus type 1 entry. *J Virol*, 77(9):5201–8, May 2003.

34. S Gartner, P Markovits, D M Markovitz, M H Kaplan, R C Gallo, and M Popovic. The role of mononuclear phagocytes in HTLV-III/LAV infection. *Science*, 233(4760):215–9, Jul 1986.

CHAPTER 6

Conclusion

Over the past three and half decades great strides have been made to contain the HIV pandemic. Global scientific research and public policy efforts have transformed what was a terminal illness into a manageable, chronic condition through the discovery and expedited approval and distribution of highly active antiretroviral therapies (HAART). The goals of HIV research have now turned to finding a cure, vaccination, and the managing HIV infection as a life-long condition. Our successes have also been met with the continued discovery of very unique and complex properties of HIV infection, such as persistent reservoirs, high mutation rates and quasispecies diversity, which present significant challenges to these goals.

Novel therapies targeting highly conserved viral features can provide new options to reduce the propensity of resistance. The host of modern broadly neutralizing antibodies target a wide variety of epitopes on HIV Env that may bring forth combinatorial immunotherapies that are almost as diverse as the HIV Env itself. Indeed, such immunotherapeutic strategies have had promising results in animal models[1–5] and in humans[6–8]. As clinical trials of potential immunotherapies continue over the coming years, it is all the more important to understand how to translate *in vitro* neutralizing activity into predictive clinical expectations. This will likely involve comparisons of both IC_{50} potencies and slopes, where potency describes the baseline strength of neutralization, akin to a binding affinity, and the slope serves as a more dynamic property that is specifically relevant to the high levels of neutralization required to suppress viral replication *in vivo*. Using median effect analysis, we show that bnAbs exhibit epitope-specific slopes (Chapter 2) that have a significant impact on clinical expectations. These slopes also illuminate novel mechanisms, such as heterogeneity and cooperativity that can further assist in the development of more active immunotherapeutic strategies.

Novel inhibitory mechanisms can give rise to new classes of inhibitory compounds with lower manufacturing costs and higher stability for long-term storage and broad distribution. While we are only now beginning to understand the role of disulfide reduction in HIV entry[9–16], the existing compounds that target this highly conserved mechanism are already easy

to manufacture and widely distributed. Furthermore, the connection between cell-surface redox potential and immunological activity[9,17] is an important insight that may facilitate more targeted approaches using this inhibitory mechanism. Our results demonstrate a high clinical potential for DSB inhibitors, which exhibited inhibitory slopes greater than any of the broadly neutralizing antibodies we have investigated (Chapter 3). Our results also provide specific guidelines for the future development of novel DSB inhibitors that target the PDI active site, are more electrophilic and are membrane impermeable.

While the first half of this dissertation focuses on the analysis of inhibitor activities from the perspective of an inhibitor (Chapters 2 and 3), the second half demonstrates the unique effects an inhibitor can have on the inherent properties of a virus (Chatpers 4 and 5). The efficiency with which an isolate uses CD4 and CCR5 is highly relevant in the context of clinical pathology and transmission[18–25], where HIV target cells express a variety of CD4/CCR5 surface densities[26,27] and, therefore, represent a diverse array of unique targets for replication *in vivo*. The novel GGR system and associated VERSA metrics[28,29] presented in Chapter 4 show that these inherent CD4/CCR5 usage properties are unique among transmitter/-founder Envs as well as clade C isolates. We also show the impact of specific mutations that confer resistance to the CD4-binding site and V2-glycan bnAbs VRC01 and PG9/PG16, where resistant isolates exhibited a decrease in overall infectivity that was not associated with changes in CD4/CCR5 usage. These metrics provide important details regarding how the CD4/CCR5 usage and target-cell tropism of an isolate adapt to the presence of an inhibitor, which relate directly to the specific pathologies that patients harboring resistant isolates may face as well as appropriate choices for salvage therapy.

CD4 and CCR5 usage is but one inherent property of viral infection that inhibitors may effect. More fundamental is the way inhibitors might influence the behavior of a virus, as a population, in terms of distribution and infectivity. The dose-dependent activity of many biological systems is commonly measured in terms of potency and slope using the Hill[30] and median effect[31] equations. We show that viral infection *in vitro* is, itself, a

classical dose-response system that is accordingly represented by these equations with high accuracy (Chapter 5). The overall negative infectious cooperativity observed is consistent with the rapid effects an attached virion may have on the distribution of CD4 and CCR5 at its target-cell surface[32–36] and, more importantly, may allow the same population of virion to generate more or less infection under different conditions. While high inhibitor slopes ($m > 1$) drive high levels of inhibition at very high concentrations (relative to IC_{50}), low infectivity slopes ($m < 1$) drive high levels of viral infection at very low viral inputs by increasing the probability that each virion will be distributed to virion-free target cells. This phenomenon has important implications in the context of viral expansion, where transmitted and emerging resistant isolates must grow, as a population, from a very low viral input.

This dissertation introduces and applies novel analytical methods that are important for developing the clinical expectations of treatment strategies based on experimental data *in vitro*. The results presented here reveal novel properties of inhibitor activity from the perspective of the inhibitor and from the perspective of the virus, which will be important for clinical strategies focused on the long-term management of HIV infection, preventing transmission and limiting resistance potential.

References

1. Masashi Shingai, Yoshiaki Nishimura, Florian Klein, Hugo Mouquet, Olivia K Donau, Ronald Plishka, Alicia Buckler-White, Michael Seaman, Michael Piatak, Jr, Jeffrey D Lifson, Dimiter S Dimitrov, Michel C Nussenzweig, and Malcolm A Martin. Antibody-mediated immunotherapy of macaques chronically infected with SHIV suppresses viraemia. *Nature*, 503(7475):277–80, Nov 2013.

2. Dan H Barouch, James B Whitney, Brian Moldt, Florian Klein, Thiago Y Oliveira, Jinyan Liu, Kathryn E Stephenson, Hui-Wen Chang, Karthik Shekhar, Sanjana Gupta, Joseph P Nkolola, Michael S Seaman, Kaitlin M Smith, Erica N Borducchi, Crystal Cabral, Jeffrey Y Smith, Stephen Blackmore, Srisowmya Sanisetty, James R Perry,

Matthew Beck, Mark G Lewis, William Rinaldi, Arup K Chakraborty, Pascal Poignard, Michel C Nussenzweig, and Dennis R Burton. Therapeutic efficacy of potent neutralizing HIV-1-specific monoclonal antibodies in SHIV-infected rhesus monkeys. *Nature*, 503(7475):224–8, Nov 2013.

3. Florian Klein, Ariel Halper-Stromberg, Joshua A Horwitz, Henning Gruell, Johannes F Scheid, Stylianos Bournazos, Hugo Mouquet, Linda A Spatz, Ron Diskin, Alexander Abadir, Trinity Zang, Marcus Dorner, Eva Billerbeck, Rachael N Labitt, Christian Gaebler, Paola M Marcovecchio, Reha-Baris Incesu, Thomas R Eisenreich, Paul D Bieniasz, Michael S Seaman, Pamela J Bjorkman, Jeffrey V Ravetch, Alexander Ploss, and Michel C Nussenzweig. HIV therapy by a combination of broadly neutralizing antibodies in humanized mice. *Nature*, 492(7427):118–22, Dec 2012.

4. Joshua A Horwitz, Ariel Halper-Stromberg, Hugo Mouquet, Alexander D Gitlin, Anna Tretiakova, Thomas R Eisenreich, Marine Malbec, Sophia Gravemann, Eva Billerbeck, Marcus Dorner, Hildegard Büning, Olivier Schwartz, Elena Knops, Rolf Kaiser, Michael S Seaman, James M Wilson, Charles M Rice, Alexander Ploss, Pamela J Bjorkman, Florian Klein, and Michel C Nussenzweig. HIV-1 suppression and durable control by combining single broadly neutralizing antibodies and antiretroviral drugs in humanized mice. *Proc Natl Acad Sci U S A*, 110(41):16538–43, Oct 2013.

5. Florian Klein, Lilian Nogueira, Yoshiaki Nishimura, Ganesh Phad, Anthony P West, Jr, Ariel Halper-Stromberg, Joshua A Horwitz, Anna Gazumyan, Cassie Liu, Thomas R Eisenreich, Clara Lehmann, Gerd Fätkenheuer, Constance Williams, Masashi Shingai, Malcolm A Martin, Pamela J Bjorkman, Michael S Seaman, Susan Zolla-Pazner, Gunilla B Karlsson Hedestam, and Michel C Nussenzweig. Enhanced HIV-1 immunotherapy by commonly arising antibodies that target virus escape variants. *J Exp Med*, 211(12):2361–72, Nov 2014.

6. Marina Caskey, Florian Klein, Julio C C Lorenzi, Michael S Seaman, Anthony P West,

Jr, Noreen Buckley, Gisela Kremer, Lilian Nogueira, Malte Braunschweig, Johannes F Scheid, Joshua A Horwitz, Irina Shimeliovich, Sivan Ben-Avraham, Maggi Witmer-Pack, Martin Platten, Clara Lehmann, Leah A Burke, Thomas Hawthorne, Robert J Gorelick, Bruce D Walker, Tibor Keler, Roy M Gulick, Gerd Fätkenheuer, Sarah J Schlesinger, and Michel C Nussenzweig. Viraemia suppressed in HIV-1-infected humans by broadly neutralizing antibody 3BNC117. *Nature*, Apr 2015.

7. Alexandra Trkola, Herbert Kuster, Peter Rusert, Beda Joos, Marek Fischer, Christine Leemann, Amapola Manrique, Michael Huber, Manuela Rehr, Annette Oxenius, Rainer Weber, Gabriela Stiegler, Brigitta Vcelar, Hermann Katinger, Leonardo Aceto, and Huldrych F Günthard. Delay of HIV-1 rebound after cessation of antiretroviral therapy through passive transfer of human neutralizing antibodies. *Nat Med*, 11(6):615–22, Jun 2005.

8. Alexandra Trkola, Herbert Kuster, Peter Rusert, Viktor von Wyl, Christine Leemann, Rainer Weber, Gabriela Stiegler, Hermann Katinger, Beda Joos, and Huldrych F Günthard. In vivo efficacy of human immunodeficiency virus neutralizing antibodies: estimates for protective titers. *J Virol*, 82(3):1591–9, Feb 2008.

9. Shuguang Bi, Patrick W Hong, Benhur Lee, and Linda G Baum. Galectin-9 binding to cell surface protein disulfide isomerase regulates the redox environment to enhance T-cell migration and HIV entry. *Proc Natl Acad Sci U S A*, 108(26):10650–5, Jun 2011.

10. Z Wang, Z Zhou, ZY Gui, and CW Chi. Snapshot of the interaction between HIV envelope glycoprotein 120 and protein disulfide isomerase. *Acta Biochim. Biophys. Sin.*, 42(5):358, 2010.

11. Ingrid Markovic, Tzanko S Stantchev, Karen H Fields, Linda J Tiffany, Melanija Tomiç, Carol D Weiss, Christopher C Broder, Klaus Strebel, and Kathleen A Clouse. Thi-

ol/disulfide exchange is a prerequisite for CXCR4-tropic HIV-1 envelope-mediated T-cell fusion during viral entry. *Blood*, 103(5):1586–94, Mar 2004.

12. Tzanko S Stantchev, Mark Paciga, Carla R Lankford, Franziska Schwartzkopff, Christopher C Broder, and Kathleen A Clouse. Cell-type specific requirements for thiol/disulfide exchange during HIV-1 entry and infection. *Retrovirology*, 9:97, 2012.

13. HJ Ryser, EM Levy, R Mandel, and GJ DiSciullo. Inhibition of human immunodeficiency virus infection by agents that interfere with thiol-disulfide interchange upon virus-receptor interaction. *Proc. Natl. Acad. Sci. USA*, 91(10):4559–63, May 10 1994.

14. W Ou and J Silver. Role of protein disulfide isomerase and other thiol-reactive proteins in HIV-1 envelope protein-mediated fusion. *Virology*, 350(2):406–417, Jul 5 2006.

15. C Finnegan and R Blumenthal. Dissecting HIV fusion: identifying novel targets for entry inhibitors. *Infect Disord Drug Targets*, 6(4):355–67, Dec 2006.

16. Rym Barbouche, Raymond Miquelis, Ian M Jones, and Emmanuel Fenouillet. Protein-disulfide isomerase-mediated reduction of two disulfide bonds of HIV envelope glycoprotein 120 occurs post-CXCR4 binding and is required for fusion. *J Biol Chem*, 278(5):3131–6, Jan 2003.

17. Shuguang Bi, Lesley A Earl, Linsey Jacobs, and Linda G Baum. Structural features of galectin-9 and galectin-1 that determine distinct T cell death pathways. *J Biol Chem*, 283(18):12248–58, May 2008.

18. Paul R Gorry and Petronela Ancuta. Coreceptors and HIV-1 pathogenesis. *Curr HIV/AIDS Rep*, 8(1):45–53, Mar 2011.

19. Donald E Mosier. How HIV changes its tropism: evolution and adaptation? *Curr Opin HIV AIDS*, 4(2):125–30, Mar 2009.

20. Maria José Duenas-Decamp, Paul J Peters, Alexander Repik, Thomas Musich, Maria Paz Gonzalez-Perez, Catherine Caron, Richard Brown, Jonathan Ball, and Paul R Clapham. Variation in the biological properties of HIV-1 R5 envelopes: implications of envelope structure, transmission and pathogenesis. *Future Virol*, 5(4):435–451, Jul 2010.

21. Paul R Gorry, Nicholas Francella, Sharon R Lewin, and Ronald G Collman. HIV-1 envelope-receptor interactions required for macrophage infection and implications for current HIV-1 cure strategies. *J Leukoc Biol*, 95(1):71–81, Jan 2014.

22. Jessica Wade, Jasminka Sterjovski, Lachlan Gray, Michael Roche, Lisa Chiavaroli, Anne Ellett, Martin R Jakobsen, Daniel Cowley, Candida da Fonseca Pereira, Nitin Saksena, Bin Wang, Damian F J Purcell, Ingrid Karlsson, Eva-Maria Fenyö, Melissa Churchill, and Paul R Gorry. Enhanced CD4+ cellular apoptosis by CCR5-restricted HIV-1 envelope glycoprotein variants from patients with progressive HIV-1 infection. *Virology*, 396(2):246–55, Jan 2010.

23. Paul J Peters, Maria J Dueñas-Decamp, W Matthew Sullivan, and Paul R Clapham. Variation of macrophage tropism among HIV-1 R5 envelopes in brain and other tissues. *J Neuroimmune Pharmacol*, 2(1):32–41, Mar 2007.

24. N Dejucq, G Simmons, and P R Clapham. Expanded tropism of primary human immunodeficiency virus type 1 R5 strains to CD4(+) T-cell lines determined by the capacity to exploit low concentrations of CCR5. *J Virol*, 73(9):7842–7, Sep 1999.

25. Maitree Pakarasang, Chantapong Wasi, Surapol Suwanagool, Amphan Chalermchockcharoenkit, and Prasert Auewarakul. Increased HIV-DNA load in CCR5-negative lymphocytes without viral phenotypic change. *Virology*, 347(2):372–8, Apr 2006.

26. B Lee, M Sharron, L J Montaner, D Weissman, and R W Doms. Quantification of CD4, CCR5, and CXCR4 levels on lymphocyte subsets, dendritic cells, and differentially

conditioned monocyte-derived macrophages. *Proc Natl Acad Sci U S A*, 96(9):5215–20, Apr 1999.

27. Sarah B Joseph, Kathryn T Arrildt, Adrienne E Swanstrom, Gretja Schnell, Benhur Lee, James A Hoxie, and Ronald Swanstrom. Quantification of entry phenotypes of macrophage-tropic HIV-1 across a wide range of CD4 densities. *J Virol*, 88(4):1858–69, Feb 2014.

28. Kelechi Chikere, Nicholas E Webb, Tom Chou, Katharina Borm, Jasminka Sterjovski, Paul R Gorry, and Benhur Lee. Distinct HIV-1 entry phenotypes are associated with transmission, subtype specificity, and resistance to broadly neutralizing antibodies. *Retrovirology*, 11:48, 2014.

29. Samantha H Johnston, Michael A Lobritz, Sandra Nguyen, Kara Lassen, Shirley Delair, Filippo Posta, Yvonne J Bryson, Eric J Arts, Tom Chou, and Benhur Lee. A quantitative affinity-profiling system that reveals distinct CD4/CCR5 usage patterns among human immunodeficiency virus type 1 and simian immunodeficiency virus strains. *J Virol*, 83(21):11016–26, Nov 2009.

30. A.V. Hill. The possible effects of the aggregation of the molecules of hæmoglobin on its dissociation curves. *J. Physiol.*, 40(Suppl.):iv–vii, January 1910.

31. T C Chou and P Talalay. Quantitative analysis of dose-effect relationships: the combined effects of multiple drugs or enzyme inhibitors. *Adv Enzyme Regul*, 22:27–55, 1984.

32. Stephen A Gallo, Catherine M Finnegan, Mathias Viard, Yossef Raviv, Antony Dimitrov, Satinder S Rawat, Anu Puri, Stewart Durell, and Robert Blumenthal. The HIV Env-mediated fusion reaction. *Biochim Biophys Acta*, 1614(1):36–50, Jul 2003.

33. Mark Spear, Jia Guo, and Yuntao Wu. The trinity of the cortical actin in the initiation of HIV-1 infection. *Retrovirology*, 9:45, 2012.

34. Marta Barrero-Villar, José Román Cabrero, Mónica Gordón-Alonso, Jonathan Barroso-González, Susana Alvarez-Losada, M Angeles Muñoz-Fernández, Francisco Sánchez-Madrid, and Agustín Valenzuela-Fernández. Moesin is required for HIV-1-induced CD4-CXCR4 interaction, F-actin redistribution, membrane fusion and viral infection in lymphocytes. *J Cell Sci*, 122(Pt 1):103–13, Jan 2009.

35. Sonia Jiménez-Baranda, Concepción Gómez-Moutón, Ana Rojas, Lorena Martínez-Prats, Emilia Mira, Rosa Ana Lacalle, Alfonso Valencia, Dimiter S Dimitrov, Antonella Viola, Rafael Delgado, Carlos Martínez-A, and Santos Mañes. Filamin-A regulates actin-dependent clustering of HIV receptors. *Nat Cell Biol*, 9(7):838–46, Jul 2007.

36. Paul J Vorster, Jia Guo, Alyson Yoder, Weifeng Wang, Yanfang Zheng, Xuehua Xu, Dongyang Yu, Mark Spear, and Yuntao Wu. LIM kinase 1 modulates cortical actin and CXCR4 cycling and is activated by HIV-1 to initiate viral infection. *J Biol Chem*, 286(14):12554–64, Apr 2011.

Appendices

APPENDIX A

Origin and Use of the median Effect Model

Derivation of the Median Effect Model.

The median effect equation is derived from a target-ligand binding equilibrium (Equation A.1) where the n ligand molecules (L) reversibly bind to a single target (T) to form a target-ligand complex [TL_n].

$$[\mathrm{T}] + \mathrm{n}[\mathrm{L}] \underset{\mathrm{k}_{-1}}{\overset{\mathrm{k}_1}{\rightleftharpoons}} [\mathrm{TL}_n] \tag{A.1}$$

The target-ligand equilibrium is defined by Equation A.2a. Representation of bound and unbound target forms can be simplified and grouped by letting $[\mathrm{TL}_n] = [\mathrm{T}]_0 - [\mathrm{T}]$ (where $[\mathrm{T}]_0$ is the total number of targets) to give Equation A.2b.

$$[\mathrm{TL}_n] = \mathrm{K}[\mathrm{T}][\mathrm{L}]^n \tag{A.2a}$$

$$\frac{[\mathrm{TL}_n]}{[\mathrm{T}]_0 - [\mathrm{TL}_n]} = \mathrm{K}[\mathrm{L}]^n \tag{A.2b}$$

Equation A.2b can then be expressed as Equation A.2c where f_a is the ratio of bound target to total target.

$$\frac{f_a}{1 - f_a} = \mathrm{K}[\mathrm{L}]^n \tag{A.2c}$$

Equation A.2c is further simplified by assuming that the percent of ligands occupying target binding sites is a negligible fraction of total ligands (Equation A.2d). The following substitutions are made (Equations A.2e and A.2f) to give the median effect equation (Equation A.2g).

$$[\mathrm{L}] \approx [\mathrm{L}]_0 \tag{A.2d}$$

$$m = n \tag{A.2e}$$

$$D_m = \mathrm{K}^{-1/n} \tag{A.2f}$$

$$\frac{f_a}{1-f_a} = \left(\frac{D}{D_m}\right)^m \tag{A.2g}$$

Because m is equal to the ligand stoichiometry in this equilibrium (n, Equation A.2e), m is considered a stoichiometric parameter. This interpretation holds true for targets with either a single ligand binding site or multiple ligand binding sites whose affinity are not dependent on the degree of target ligation. Importantly, a purely stoichiometric interpretation of the slope is not valid for multivalent targets whose binding affinity is altered by ligation (e.g. cooperative systems), as these systems cannot be represented by a single equilibrium constant. The relevant assumptions of this model are that 1) the concentration of ligand greatly exceeds the target concentration and 2) a negligible fraction of ligands are bound by their targets (such that Equation A.2d is true).

Fitting the Median Effect Model to Experimental Data.

The median effect equation (Equation A.2g) can be linearized by taking the log of both sides to give Equation A.3, which is of the form $y = mx + b$.

$$\log\left(\frac{f_a}{1-f_a}\right) = m\log(D) - m\log(D_m) \tag{A.3}$$

Linear regression identifies the slope of this line (m) and D_m is associated with the x intercept (b) through Equation A.4.

$$D_m = 10^{-b/m} \tag{A.4}$$

Importantly, experimental effect measurements must be normalized to give f_a before the log transformation and linear regression can be performed. Thus, the parameters m and D_m are sensitive to the appropriate normalization of experimental results.

APPENDIX B

Supplementary Information for Chapter 2

The following chapter includes supplementary information from a submitted draft of the following:

Webb NE, Montefiori DC, Lee B. Dose response curve slope helps predict therapeutic potency and breadth of HIV broadly neutralizing antibodies. *Nature Communications*. (*in press*)

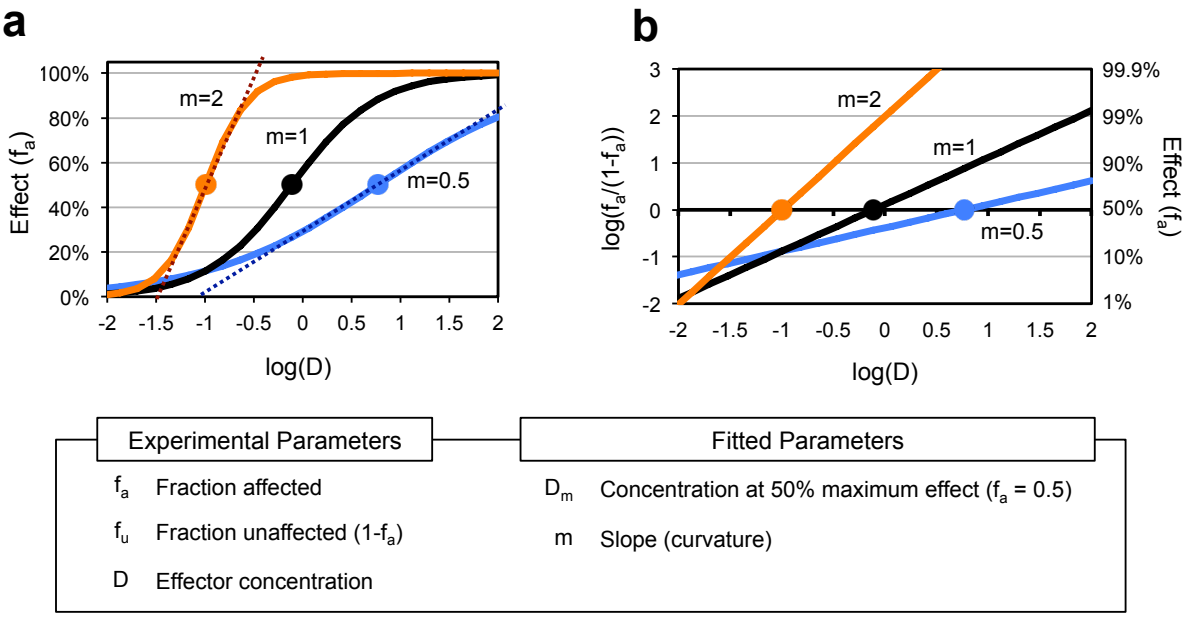

Figure B.1: Example of median effect transformation. (**a**) Standard Hill plot for three theoretical neutralization curves with high (orange), moderate (black) or low (blue) slope (m) and different IC50s (filled circles). (**b**) Log effect ratio transformation (Equation 2.1) of the same curves in panel a. Slope is indicated by the angle of the line relative to x-axis and IC50 is indicated by the x-intercept (filled circles). (**box**) Description of mathematical parameters used for median effect fitting.

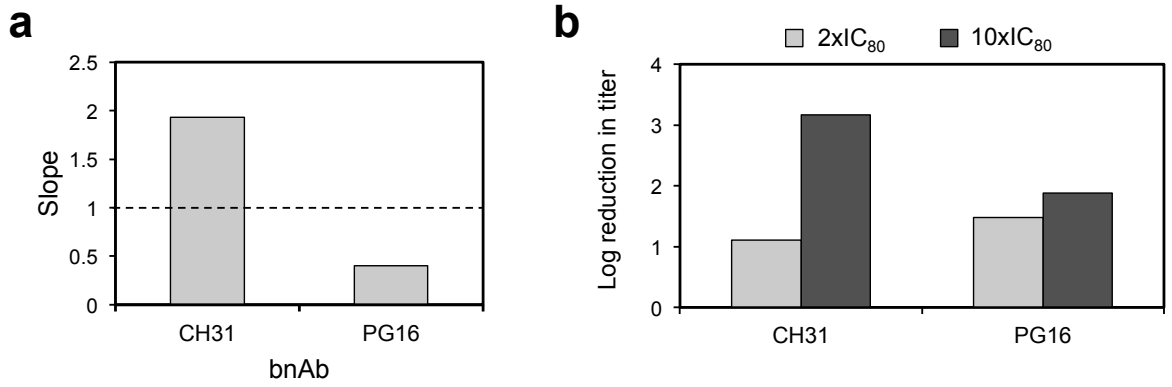

Figure B.2: Validation of median effect extrapolations to extreme neutralization levels. (**a**) Slopes of CH31 and PG16 against Env Ce1176 from standard neutralization assay. (**b**) Log reductions in viral titer using 2x and 10x the IC80 concentrations of CH31 and PG16 determined from titer reduction assay (Methods). A greater reduction in titer was observed for PG16 at 2xIC80, while a more therapeutically relevant reduction in titer was observed for CH31 at 10xIC80.

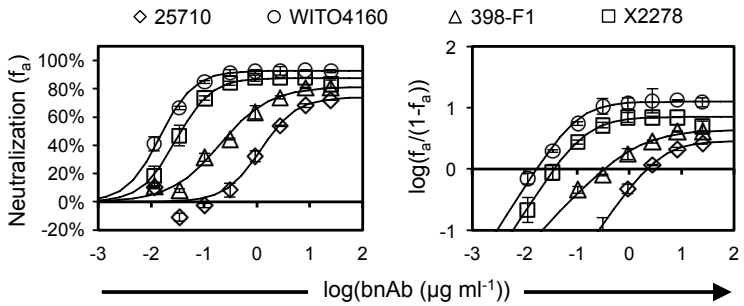

Figure B.3: Examples of neutralization plateaus. Hill (left) and median effect plots (right) of neutralization for representative examples of Envs where plateaus of neutralization were observed with the V2 glycan bnAb CH01 (Table B.2). Symbols show experimental results and solid lines indicate the median effect predictions after fitting to Equation 2.4. Bars show mean and standard deviation from two replicates.

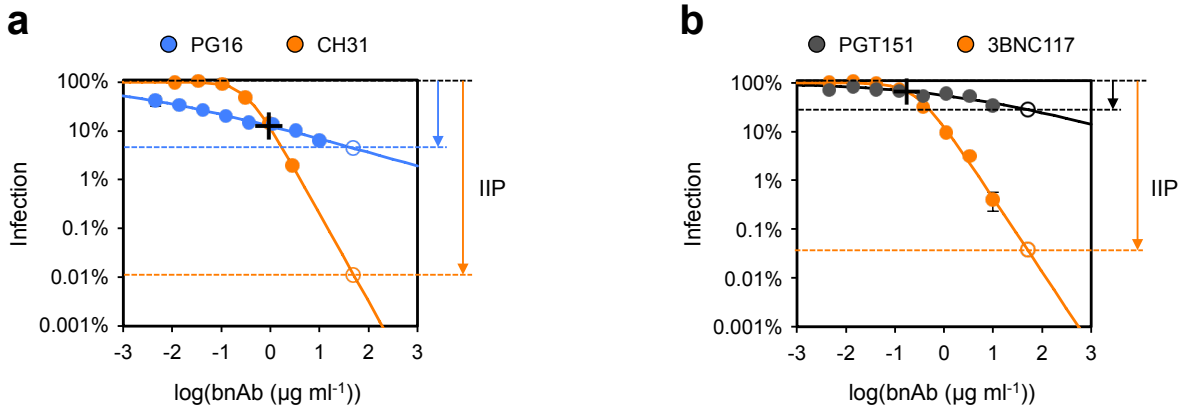

Figure B.4: Illustrative example of IIP. Residual infection at increasing concentrations of (**a**) PG16 and CH31 and (**b**) PGT151 and 3BNC117 against Env 25710 are shown on a log scale (filled circles). IIP describes the log reduction in infection at a given concentration. Extrapolated residual infection at 50 μg mL^{-1} is shown as hollow circles and the corresponding log reduction in infection is illustrated by the arrows. Error bars indicate standard deviation of two replicates.

Table B.1: HIV Envelope Panels.

Global Panel								
Env	**Tier**	**Subtype**	**Country**	**Year**	**Fiebig Stage**	**Mode of Transmission**	**GenBank**	**Ref**
TRO11	2	B	Italy	1995	III	M-M	AY835445	1, 2
25710	2	C	India	1999	V	F-M	EF117271	1, 3
398F1	2	A	Tanzania	2001	Not Available	Heterosexual	HM215312	1
CNE8	2	CRF01_AE	China	2006	Chronic Infection	IVDU	HM215427	1, 4
X2278	2	B	Spain	2007	V/VI	Heterosexual	FJ817366	1
BJOX2000	2	CRF07_BC	China	2007	I /II	IVDU	HM215364	1
X1632	2	G	Spain	2004	Chronic Infection	Heterosexual	FJ817370	1, 5
CE1176	2	C	Malawi	2004	I/II	Sexual	FJ444437	1
246F3	2	AC recomb	Tanzania	2001	VI	Heterosexual	HM215279	1
CH119	2	CRF07_BC	China	2004	Chronic Infection	IVDU	EF117261	1
CE0217	2	C	Malawi	2007	V/VI	Sexual	FJ443575	1
CNE55	2	CRF01_AE	China	2007	Chronic Infection	IVDU	HM215418	1, 4
PVO.4	3	B	Italy	1996	III	M-M	AY835444	2
QH0515.1	2	B	Trinidad	1994	V	F-M	AY835440	2
QH0692	2	B	Trinidad	1994	V	F-M	AY835439	2
SC442661	2	B	Trinidad	1995	IV	F-M	AY835441	2
WITO4160	2	B	U.S.	2000	I	F-M	AY835451	2

REFERENCES

1. DeCamp, A., *et al.* (2014) J.Virol., 88(5): 2489-2507.
2. Li, M., *et al*. (2005) J. Virol., 79(16):10108-10125.
3. Kulkarni, S.S., *et al*. (2009) Virology, 385(2):505-520.
4. Shang, H., *et al*. (2011) J. Biol. CHem., 286(16): 14351-14542.
5. Revilla, A., *et al*. (2011) AIDS Res Hum Retroviruses, 27:889-901.

Table B.2: Summary of Neutralization Parameters.

Epitope	bnAb	Env	Slope	IC_{50}*	IC_{80}*	IC_{90}*	IC_{99}*	Max†
CD4bs	3BNC117	25710	1.51	0.27	0.68	1.16	5.67	>99%
CD4bs	3BNC117	246-F3	1.51	0.099	0.25	0.42	2.09	>99%
CD4bs	3BNC117	398-F1	1.17	0.074	0.24	0.49	3.78	>99%
CD4bs	3BNC117	BJOX002000	NoN	NoN	NoN	NoN	NoN	NoN
CD4bs	3BNC117	Ce1176	1.24	0.14	0.42	0.8	5.49	>99%
CD4bs	3BNC117	Ce0217	1.44	0.043	0.11	0.2	1.06	>99%
CD4bs	3BNC117	CH119	0.90	5.57	25.92	63.72	910	>99%
CD4bs	3BNC117	CNE55	1.63	0.1	0.23	0.39	1.68	>99%
CD4bs	3BNC117	CNE8	1.26	0.16	0.48	0.92	6.15	>99%
CD4bs	3BNC117	PVO4	N.D.	N.D.	N.D.	N.D.	N.D.	N.D.
CD4bs	3BNC117	QH0515	N.D.	N.D.	N.D.	N.D.	N.D.	N.D.
CD4bs	3BNC117	QH0692	N.D.	N.D.	N.D.	N.D.	N.D.	N.D.
CD4bs	3BNC117	SC422661	N.D.	N.D.	N.D.	N.D.	N.D.	N.D.
CD4bs	3BNC117	TRO11	1.52	0.03	0.074	0.13	0.61	>99%
CD4bs	3BNC117	WITO4160	N.D.	N.D.	N.D.	N.D.	N.D.	N.D.
CD4bs	3BNC117	X1632	0.63	2.5	22.94	83.84	>1000	>99%
CD4bs	3BNC117	X2278	1.32	0.012	0.036	0.066	0.41	>99%
CD4bs	CH31	246-F3	1.53	0.054	0.13	0.23	1.09	>99%
CD4bs	CH31	398-F1	1.41	0.059	0.16	0.28	1.52	>99%
CD4bs	CH31	BJOX002000	NoN	NoN	NoN	NoN	NoN	NoN
CD4bs	CH31	Ce1176	1.93	1.23	2.52	3.84	13.3	>99%
CD4bs	CH31	Ce0217	1.93	0.059	0.12	0.18	0.64	>99%
CD4bs	CH31	CH119	1.51	1.48	3.72	6.37	31.2	>99%
CD4bs	CH31	CNE55	1.58	0.057	0.14	0.23	1.04	>99%
CD4bs	CH31	CNE8	1.54	0.13	0.31	0.53	2.53	>99%
CD4bs	CH31	PVO4	1.54	0.51	1.24	2.1	9.94	>99%
CD4bs	CH31	QH0515	1.41	0.14	0.37	0.67	3.64	>99%
CD4bs	CH31	QH0692	1.77	0.84	1.84	2.9	11.27	>99%
CD4bs	CH31	SC422661	1.30	0.15	0.44	0.82	5.2	>99%
CD4bs	CH31	TRO11	1.31	0.11	0.32	0.6	3.73	>99%
CD4bs	CH31	WITO4160	1.14	0.13	0.45	0.92	7.53	>99%
CD4bs	CH31	X1632	1.28	0.043	0.13	0.24	1.56	>99%
CD4bs	CH31	X2278	1.54	0.08	0.2	0.33	1.59	>99%
CD4bs	HJ16_22	25710	NoN	NoN	NoN	NoN	NoN	NoN
CD4bs	HJ16_22	246-F3	NoN	NoN	NoN	NoN	NoN	NoN
CD4bs	HJ16_22	398-F1	0.47	21.16	392	>1000	>1000	>99%
CD4bs	HJ16_22	BJOX002000	NoN	NoN	NoN	NoN	NoN	NoN

Epitope	bnAb	Env	Slope	IC_{50} *	IC_{80} *	IC_{90} *	IC_{99} *	Max †
CD4bs	HJ16_22	Ce1176	1.17	0.3	0.97	1.95	15.23	>99%
CD4bs	HJ16_22	Ce0217	1.54	0.053	0.13	0.22	1.05	>99%
CD4bs	HJ16_22	CH119	1.69	0.14	0.31	0.5	2.08	>99%
CD4bs	HJ16_22	CNE55	NoN	NoN	NoN	NoN	NoN	NoN
CD4bs	HJ16_22	CNE8	0.97	11.61	48.74	113	>1000	>99%
CD4bs	HJ16_22	PVO4	N.D.	N.D.	N.D.	N.D.	N.D.	N.D.
CD4bs	HJ16_22	QH0515	N.D.	N.D.	N.D.	N.D.	N.D.	N.D.
CD4bs	HJ16_22	QH0692	N.D.	N.D.	N.D.	N.D.	N.D.	N.D.
CD4bs	HJ16_22	SC422661	N.D.	N.D.	N.D.	N.D.	N.D.	N.D.
CD4bs	HJ16_22	TRO11	1.14	0.078	0.26	0.54	4.42	>99%
CD4bs	HJ16_22	WITO4160	N.D.	N.D.	N.D.	N.D.	N.D.	N.D.
CD4bs	HJ16_22	X1632	NoN	NoN	NoN	NoN	NoN	NoN
CD4bs	HJ16_22	X2278	NoN	NoN	NoN	NoN	NoN	NoN
CD4bs	sCD4	25710	1.32	1.19	3.4	6.31	39.01	>99%
CD4bs	sCD4	246-F3	1.03	12.21	46.7	102	>1000	>99%
CD4bs	sCD4	398-F1	0.87	8.02	39.22	99.29	>1000	>99%
CD4bs	sCD4	BJOX002000	1.04	1.45	5.46	11.87	118	>99%
CD4bs	sCD4	Ce1176	1.06	4.73	17.51	37.66	362	>99%
CD4bs	sCD4	Ce0217	0.72	13.58	93.47	289	>1000	>99%
CD4bs	sCD4	CH119	0.79	15.75	91.54	256	>1000	>99%
CD4bs	sCD4	CNE55	NoN	NoN	NoN	NoN	NoN	NoN
CD4bs	sCD4	CNE8	NoN	NoN	NoN	NoN	NoN	NoN
CD4bs	sCD4	PVO4	N.D.	N.D.	N.D.	N.D.	N.D.	N.D.
CD4bs	sCD4	QH0515	N.D.	N.D.	N.D.	N.D.	N.D.	N.D.
CD4bs	sCD4	QH0692	N.D.	N.D.	N.D.	N.D.	N.D.	N.D.
CD4bs	sCD4	SC422661	N.D.	N.D.	N.D.	N.D.	N.D.	N.D.
CD4bs	sCD4	TRO11	0.46	33.81	685	>1000	>1000	>99%
CD4bs	sCD4	WITO4160	N.D.	N.D.	N.D.	N.D.	N.D.	N.D.
CD4bs	sCD4	X1632	1.24	1.01	3.09	5.93	40.78	>99%
CD4bs	sCD4	X2278	NoN	NoN	NoN	NoN	NoN	NoN
CD4bs	VRC01	25710	1.14	0.5	1.69	3.45	28.52	>99%
CD4bs	VRC01	246-F3	1.56	0.25	0.6	1.02	4.74	>99%
CD4bs	VRC01	398-F1	1.23	0.17	0.51	0.99	6.92	>99%
CD4bs	VRC01	BJOX002000	NoN	NoN	NoN	NoN	NoN	NoN
CD4bs	VRC01	Ce1176	1.50	2.04	5.15	8.85	43.89	>99%
CD4bs	VRC01	Ce0217	1.15	0.21	0.7	1.42	11.36	>99%
CD4bs	VRC01	CH119	1.64	1.19	2.78	4.55	19.71	>99%
CD4bs	VRC01	CNE55	1.44	0.45	1.17	2.05	10.84	>99%
CD4bs	VRC01	CNE8	1.22	0.95	2.96	5.74	40.78	>99%
CD4bs	VRC01	PVO4	1.53	0.8	1.98	3.36	16.04	>99%

Epitope	bnAb	Env	Slope	IC_{50} *	IC_{80} *	IC_{90} *	IC_{99} *	Max †
CD4bs	VRC01	QH0515	1.43	1	2.65	4.68	25.17	>99%
CD4bs	VRC01	QH0692	1.47	1.13	2.9	5.03	25.61	>99%
CD4bs	VRC01	SC422661	1.34	0.11	0.32	0.58	3.48	>99%
CD4bs	VRC01	TRO11	1.48	0.52	1.32	2.3	11.66	>99%
CD4bs	VRC01	WITO4160	1.37	0.23	0.64	1.15	6.66	>99%
CD4bs	VRC01	X1632	0.71	0.15	1.06	3.29	94.16	>99%
CD4bs	VRC01	X2278	1.06	0.066	0.25	0.53	5.14	>99%
gp120/41	PGT151	25710	0.29	1.93	231	>1000	>1000	>99%
gp120/41	PGT151	246-F3	0.38	0.009	0.34	2.88	>1000	76.2%
gp120/41	PGT151	398-F1	0.88	0.005	0.024	0.062	0.95	>99%
gp120/41	PGT151	BJOX002000	1.13	0.019	0.066	0.14	1.14	>99%
gp120/41	PGT151	Ce1176	0.98	0.009	0.037	0.084	0.98	>99%
gp120/41	PGT151	Ce0217	NoN	NoN	NoN	NoN	NoN	NoN
gp120/41	PGT151	CH119	0.58	0.029	0.32	1.29	79.75	93.8%
gp120/41	PGT151	CNE55	NoN	NoN	NoN	NoN	NoN	NoN
gp120/41	PGT151	CNE8	0.72	15.71	109	339	>1000	>99%
gp120/41	PGT151	PVO4	N.D.	N.D.	N.D.	N.D.	N.D.	N.D.
gp120/41	PGT151	QH0515	N.D.	N.D.	N.D.	N.D.	N.D.	N.D.
gp120/41	PGT151	QH0692	N.D.	N.D.	N.D.	N.D.	N.D.	N.D.
gp120/41	PGT151	SC422661	N.D.	N.D.	N.D.	N.D.	N.D.	N.D.
gp120/41	PGT151	TRO11	0.88	12.5	60.23	151	>1000	>99%
gp120/41	PGT151	WITO4160	N.D.	N.D.	N.D.	N.D.	N.D.	N.D.
gp120/41	PGT151	X1632	0.25	0.97	247	>1000	>1000	>99%
gp120/41	PGT151	X2278	0.88	0.024	0.12	0.29	4.5	>99%
HM cluster	2G12	25710	1.03	46.89	179	393	>1000	>99%
HM cluster	2G12	246-F3	NoN	NoN	NoN	NoN	NoN	NoN
HM cluster	2G12	398-F1	NoN	NoN	NoN	NoN	NoN	NoN
HM cluster	2G12	BJOX002000	NoN	NoN	NoN	NoN	NoN	NoN
HM cluster	2G12	Ce1176	NoN	NoN	NoN	NoN	NoN	NoN
HM cluster	2G12	Ce0217	NoN	NoN	NoN	NoN	NoN	NoN
HM cluster	2G12	CH119	NoN	NoN	NoN	NoN	NoN	NoN
HM cluster	2G12	CNE55	NoN	NoN	NoN	NoN	NoN	NoN
HM cluster	2G12	CNE8	NoN	NoN	NoN	NoN	NoN	NoN
HM cluster	2G12	PVO4	0.99	2.65	10.69	24.2	271	>99%
HM cluster	2G12	QH0515	1.47	0.06	0.15	0.27	1.36	>99%
HM cluster	2G12	QH0692	1.36	3.55	9.87	17.93	105	>99%
HM cluster	2G12	SC422661	1.08	3.28	11.89	25.24	234	94.5%
HM cluster	2G12	TRO11	0.98	0.27	1.13	2.57	29.38	>99%
HM cluster	2G12	WITO4160	0.91	2.11	9.72	23.76	334	>99%
HM cluster	2G12	X1632	NoN	NoN	NoN	NoN	NoN	NoN

Epitope	bnAb	Env	Slope	IC_{50} *	IC_{80} *	IC_{90} *	IC_{99} *	Max †
HM cluster	2G12	X2278	1.22	0.24	0.75	1.46	10.43	>99%
MPER	10E8	25710	0.63	0.015	0.13	0.49	22.7	>99%
MPER	10E8	246-F3	0.75	0.38	2.43	7.21	180	>99%
MPER	10E8	398-F1	0.72	0.54	3.71	11.41	316	>99%
MPER	10E8	BJOX002000	0.81	0.45	2.52	6.87	133	>99%
MPER	10E8	Ce1176	1.04	0.32	1.2	2.62	26.36	>99%
MPER	10E8	Ce0217	0.75	0.2	1.27	3.75	91.28	>99%
MPER	10E8	CH119	0.58	0.31	3.33	13.45	835	>99%
MPER	10E8	CNE55	0.65	0.18	1.56	5.49	226	>99%
MPER	10E8	CNE8	0.68	0.021	0.16	0.53	18.01	>99%
MPER	10E8	PVO4	N.D.	N.D.	N.D.	N.D.	N.D.	N.D.
MPER	10E8	QH0515	N.D.	N.D.	N.D.	N.D.	N.D.	N.D.
MPER	10E8	QH0692	N.D.	N.D.	N.D.	N.D.	N.D.	N.D.
MPER	10E8	SC422661	N.D.	N.D.	N.D.	N.D.	N.D.	N.D.
MPER	10E8	TRO11	0.87	0.026	0.13	0.32	5.05	>99%
MPER	10E8	WITO4160	N.D.	N.D.	N.D.	N.D.	N.D.	N.D.
MPER	10E8	X1632	1.01	0.43	1.71	3.81	40.6	>99%
MPER	10E8	X2278	0.83	0.35	1.85	4.95	90.05	>99%
MPER	2F5	25710	NoN	NoN	NoN	NoN	NoN	NoN
MPER	2F5	246-F3	0.88	1.23	5.9	14.77	223	>99%
MPER	2F5	398-F1	0.72	9.64	66.25	205	>1000	>99%
MPER	2F5	BJOX002000	NoN	NoN	NoN	NoN	NoN	NoN
MPER	2F5	Ce1176	NoN	NoN	NoN	NoN	NoN	NoN
MPER	2F5	Ce0217	NoN	NoN	NoN	NoN	NoN	NoN
MPER	2F5	CH119	NoN	NoN	NoN	NoN	NoN	NoN
MPER	2F5	CNE55	0.66	1.34	10.87	37.04	>1000	>99%
MPER	2F5	CNE8	1.06	3.2	11.9	25.65	249	>99%
MPER	2F5	PVO4	N.D.	N.D.	N.D.	N.D.	N.D.	N.D.
MPER	2F5	QH0515	N.D.	N.D.	N.D.	N.D.	N.D.	N.D.
MPER	2F5	QH0692	N.D.	N.D.	N.D.	N.D.	N.D.	N.D.
MPER	2F5	SC422661	N.D.	N.D.	N.D.	N.D.	N.D.	N.D.
MPER	2F5	TRO11	NoN	NoN	NoN	NoN	NoN	NoN
MPER	2F5	WITO4160	N.D.	N.D.	N.D.	N.D.	N.D.	N.D.
MPER	2F5	X1632	0.84	2.45	12.8	33.66	588	>99%
MPER	2F5	X2278	0.87	16.17	78.91	199	>1000	>99%
MPER	4E10	25710	1.10	1.15	4.03	8.42	74.26	>99%
MPER	4E10	246-F3	0.72	3.74	25.43	78.04	>1000	>99%
MPER	4E10	398-F1	0.76	12.88	78.87	228	>1000	>99%
MPER	4E10	BJOX002000	0.54	4.95	63.61	283	>1000	>99%
MPER	4E10	Ce1176	1.00	6.72	26.88	60.51	666	>99%

Epitope	bnAb	Env	Slope	IC_{50} *	IC_{80} *	IC_{90} *	IC_{99} *	Max †
MPER	4E10	Ce0217	0.81	1.37	7.53	20.42	389	>99%
MPER	4E10	CH119	1.26	6.45	19.38	36.88	247	>99%
MPER	4E10	CNE55	0.60	2.98	30.54	119	>1000	>99%
MPER	4E10	CNE8	0.97	7	29.42	68.17	818	>99%
MPER	4E10	PVO4	N.D.	N.D.	N.D.	N.D.	N.D.	N.D.
MPER	4E10	QH0515	N.D.	N.D.	N.D.	N.D.	N.D.	N.D.
MPER	4E10	QH0692	N.D.	N.D.	N.D.	N.D.	N.D.	N.D.
MPER	4E10	SC422661	N.D.	N.D.	N.D.	N.D.	N.D.	N.D.
MPER	4E10	TRO11	0.88	1.19	5.73	14.33	216	>99%
MPER	4E10	WITO4160	N.D.	N.D.	N.D.	N.D.	N.D.	N.D.
MPER	4E10	X1632	0.64	2.62	22.86	81.19	>1000	>99%
MPER	4E10	X2278	0.57	11.31	127	524	>1000	>99%
V2-glycan	CH01	25710	1.28	1.21	3.55	6.68	43.35	74.1%
V2-glycan	CH01	246-F3	0.82	0.74	4.02	10.85	204	82.9%
V2-glycan	CH01	398-F1	0.93	0.2	0.89	2.14	28.55	81.2%
V2-glycan	CH01	BJOX002000	0.41	29.06	881	>1000	>1000	>99%
V2-glycan	CH01	Ce1176	NoN	NoN	NoN	NoN	NoN	NoN
V2-glycan	CH01	Ce0217	0.87	0.28	1.38	3.51	55.22	93.8%
V2-glycan	CH01	CH119	1.22	1.38	4.31	8.36	59.54	92.3%
V2-glycan	CH01	CNE55	NoN	NoN	NoN	NoN	NoN	NoN
V2-glycan	CH01	CNE8	NoN	NoN	NoN	NoN	NoN	NoN
V2-glycan	CH01	PVO4	N.D.	N.D.	N.D.	N.D.	N.D.	N.D.
V2-glycan	CH01	QH0515	N.D.	N.D.	N.D.	N.D.	N.D.	N.D.
V2-glycan	CH01	QH0692	N.D.	N.D.	N.D.	N.D.	N.D.	N.D.
V2-glycan	CH01	SC422661	N.D.	N.D.	N.D.	N.D.	N.D.	N.D.
V2-glycan	CH01	TRO11	NoN	NoN	NoN	NoN	NoN	NoN
V2-glycan	CH01	WITO4160	N.D.	N.D.	N.D.	N.D.	N.D.	N.D.
V2-glycan	CH01	X1632	0.63	0.58	5.21	18.8	838	73.2%
V2-glycan	CH01	X2278	1.34	0.03	0.084	0.15	0.92	87.6%
V2-glycan	CH31	25710	1.80	0.32	0.69	1.08	4.1	>99%
V2-glycan	PG16	25710	0.29	0.001	0.14	2.37	>1000	>99%
V2-glycan	PG16	246-F3	NoN	NoN	NoN	NoN	NoN	NoN
V2-glycan	PG16	398-F1	NoN	NoN	NoN	NoN	NoN	NoN
V2-glycan	PG16	BJOX002000	NoN	NoN	NoN	NoN	NoN	NoN
V2-glycan	PG16	Ce1176	0.40	0.001	0.024	0.18	70.36	>99%
V2-glycan	PG16	Ce0217	1.69	0.002	0.004	0.006	0.024	>99%
V2-glycan	PG16	CH119	0.61	0.53	5.19	19.8	>1000	>99%
V2-glycan	PG16	CNE55	0.33	1.29	91.36	>1000	>1000	>99%
V2-glycan	PG16	CNE8	0.37	0.5	21.17	188	>1000	>99%
V2-glycan	PG16	PVO4	N.D.	N.D.	N.D.	N.D.	N.D.	N.D.

Epitope	bnAb	Env	Slope	IC_{50} *	IC_{80} *	IC_{90} *	IC_{99} *	Max †
V2-glycan	PG16	QH0515	N.D.	N.D.	N.D.	N.D.	N.D.	N.D.
V2-glycan	PG16	QH0692	N.D.	N.D.	N.D.	N.D.	N.D.	N.D.
V2-glycan	PG16	SC422661	N.D.	N.D.	N.D.	N.D.	N.D.	N.D.
V2-glycan	PG16	TRO11	NoN	NoN	NoN	NoN	NoN	NoN
V2-glycan	PG16	WITO4160	N.D.	N.D.	N.D.	N.D.	N.D.	N.D.
V2-glycan	PG16	X1632	0.34	0.014	0.82	8.8	>1000	>99%
V2-glycan	PG16	X2278	0.79	0.002	0.012	0.033	0.7	>99%
V2-glycan	PG9	25710	0.96	0.04	0.17	0.4	4.87	98.3%
V2-glycan	PG9	246-F3	1.12	0.022	0.076	0.16	1.33	>99%
V2-glycan	PG9	398-F1	NoN	NoN	NoN	NoN	NoN	NoN
V2-glycan	PG9	BJOX002000	0.68	0.079	0.6	1.99	67.89	>99%
V2-glycan	PG9	Ce1176	0.86	0.006	0.028	0.072	1.18	>99%
V2-glycan	PG9	Ce0217	1.13	0.005	0.018	0.036	0.3	>99%
V2-glycan	PG9	CH119	1.33	0.51	1.45	2.67	16.27	>99%
V2-glycan	PG9	CNE55	0.56	0.077	0.93	4.01	301	>99%
V2-glycan	PG9	CNE8	0.69	0.46	3.45	11.25	371	>99%
V2-glycan	PG9	PVO4	N.D.	N.D.	N.D.	N.D.	N.D.	N.D.
V2-glycan	PG9	QH0515	N.D.	N.D.	N.D.	N.D.	N.D.	N.D.
V2-glycan	PG9	QH0692	N.D.	N.D.	N.D.	N.D.	N.D.	N.D.
V2-glycan	PG9	SC422661	N.D.	N.D.	N.D.	N.D.	N.D.	N.D.
V2-glycan	PG9	TRO11	0.90	17.7	82.72	204	>1000	>99%
V2-glycan	PG9	WITO4160	N.D.	N.D.	N.D.	N.D.	N.D.	N.D.
V2-glycan	PG9	X1632	0.77	0.11	0.64	1.85	42.16	89.2%
V2-glycan	PG9	X2278	0.94	0.012	0.054	0.13	1.64	>99%
V3-glycan	10-1074	25710	1.40	0.08	0.21	0.38	2.12	>99%
V3-glycan	10-1074	246-F3	NoN	NoN	NoN	NoN	NoN	NoN
V3-glycan	10-1074	398-F1	1.13	0.011	0.036	0.073	0.61	>99%
V3-glycan	10-1074	BJOX002000	1.46	0.017	0.044	0.076	0.4	>99%
V3-glycan	10-1074	Ce1176	1.76	0.029	0.063	0.099	0.39	>99%
V3-glycan	10-1074	Ce0217	1.11	0.008	0.029	0.061	0.52	>99%
V3-glycan	10-1074	CH119	1.51	0.026	0.064	0.11	0.54	>99%
V3-glycan	10-1074	CNE55	NoN	NoN	NoN	NoN	NoN	NoN
V3-glycan	10-1074	CNE8	NoN	NoN	NoN	NoN	NoN	NoN
V3-glycan	10-1074	PVO4	N.D.	N.D.	N.D.	N.D.	N.D.	N.D.
V3-glycan	10-1074	QH0515	N.D.	N.D.	N.D.	N.D.	N.D.	N.D.
V3-glycan	10-1074	QH0692	N.D.	N.D.	N.D.	N.D.	N.D.	N.D.
V3-glycan	10-1074	SC422661	N.D.	N.D.	N.D.	N.D.	N.D.	N.D.
V3-glycan	10-1074	TRO11	1.23	0.019	0.06	0.12	0.82	>99%
V3-glycan	10-1074	WITO4160	N.D.	N.D.	N.D.	N.D.	N.D.	N.D.
V3-glycan	10-1074	X1632	NoN	NoN	NoN	NoN	NoN	NoN

Epitope	bnAb	Env	Slope	IC_{50} *	IC_{80} *	IC_{90} *	IC_{99} *	Max †
V3-glycan	10-1074	X2278	1.74	0.031	0.07	0.11	0.44	>99%
V3-glycan	PGT121	25710	1.32	0.028	0.081	0.15	0.93	>99%
V3-glycan	PGT121	246-F3	NoN	NoN	NoN	NoN	NoN	NoN
V3-glycan	PGT121	398-F1	1.74	0.03	0.067	0.11	0.42	>99%
V3-glycan	PGT121	BJOX002000	1.40	0.024	0.064	0.11	0.64	>99%
V3-glycan	PGT121	Ce1176	1.58	0.019	0.044	0.074	0.34	>99%
V3-glycan	PGT121	Ce0217	1.17	0.004	0.012	0.024	0.18	>99%
V3-glycan	PGT121	CH119	0.92	0.016	0.072	0.17	2.38	>99%
V3-glycan	PGT121	CNE55	NoN	NoN	NoN	NoN	NoN	NoN
V3-glycan	PGT121	CNE8	NoN	NoN	NoN	NoN	NoN	NoN
V3-glycan	PGT121	PVO4	N.D.	N.D.	N.D.	N.D.	N.D.	N.D.
V3-glycan	PGT121	QH0515	N.D.	N.D.	N.D.	N.D.	N.D.	N.D.
V3-glycan	PGT121	QH0692	N.D.	N.D.	N.D.	N.D.	N.D.	N.D.
V3-glycan	PGT121	SC422661	N.D.	N.D.	N.D.	N.D.	N.D.	N.D.
V3-glycan	PGT121	TRO11	1.44	0.014	0.036	0.062	0.33	>99%
V3-glycan	PGT121	WITO4160	N.D.	N.D.	N.D.	N.D.	N.D.	N.D.
V3-glycan	PGT121	X1632	NoN	NoN	NoN	NoN	NoN	NoN
V3-glycan	PGT121	X2278	1.33	0.023	0.065	0.12	0.73	>99%
V3-glycan	PGT128	25710	1.57	0.029	0.07	0.12	0.54	>99%
V3-glycan	PGT128	246-F3	1.52	0.007	0.017	0.029	0.14	>99%
V3-glycan	PGT128	398-F1	1.33	0.005	0.014	0.026	0.16	>99%
V3-glycan	PGT128	BJOX002000	1.85	0.062	0.13	0.2	0.74	97.4%
V3-glycan	PGT128	Ce1176	NoN	NoN	NoN	NoN	NoN	NoN
V3-glycan	PGT128	Ce0217	0.94	0.063	0.28	0.66	8.63	>99%
V3-glycan	PGT128	CH119	1.80	0.048	0.1	0.16	0.62	>99%
V3-glycan	PGT128	CNE55	NoN	NoN	NoN	NoN	NoN	NoN
V3-glycan	PGT128	CNE8	1.44	0.03	0.079	0.14	0.73	>99%
V3-glycan	PGT128	PVO4	N.D.	N.D.	N.D.	N.D.	N.D.	N.D.
V3-glycan	PGT128	QH0515	N.D.	N.D.	N.D.	N.D.	N.D.	N.D.
V3-glycan	PGT128	QH0692	N.D.	N.D.	N.D.	N.D.	N.D.	N.D.
V3-glycan	PGT128	SC422661	N.D.	N.D.	N.D.	N.D.	N.D.	N.D.
V3-glycan	PGT128	TRO11	1.51	0.028	0.069	0.12	0.58	>99%
V3-glycan	PGT128	WITO4160	N.D.	N.D.	N.D.	N.D.	N.D.	N.D.
V3-glycan	PGT128	X1632	NoN	NoN	NoN	NoN	NoN	NoN
V3-glycan	PGT128	X2278	1.35	0.012	0.033	0.061	0.36	>99%

N.D., Not Done.

NoN, Non Neutralized. Neutralization ≥50% was not observed within the range of bnAb concentrations assayed or median effect predicted IC_{50} was ≥50μg/mL.

* Potencies are determined from median effect fit parameters in units of μg/mL

† Fitted maximum neutralization (see **Methods**)

APPENDIX C

Quantifying CD4/CCR5 Usage Efficiency of HIV-1 ENV Using the Affinofile System

The following chapter includes a reprint of the following:

Webb NE, Lee B. Quantifying CD4/CCR5 Usage Efficiency of HIV-1 Env Using the Affinofile System. *Methods in Moleclar Biology,* 3rd ed. Springer. (*in press*)

Summary

Entry of HIV-1 into target cells involves the interaction of the HIV envelope (Env) with both a primary receptor (CD4) and a coreceptor (CXCR4 or CCR5). The relative efficiency with which a particular Env uses these receptors is a major component of cellular tropism in the context of entry and is related to a variety of pathological Env phenotypes **(1)**. The protocols outlined in this chapter describe the use of the Affinofile system, a 293-based dual-inducible cell line that expresses up to 25 distinct combinations of CD4 and CCR5 as well as the associated Viral Entry Receptor Sensitivity Assay (VERSA) metrics used to summarize the CD4/CCR5-dependent infectivity results. This system allows for high resolution profiling of CD4 and CCR5 usage efficiency in the context of unique viral phenotypes.

1. Introduction

HIV-1 entry is driven by the envelope glycoproteins gp120 and gp41 (Env). Fusion between the viral and cellular membrane is driven by a multi-stage, concerted mechanism that first requires binding of gp120 to cell-surface CD4. This engagement triggers conformational changes in gp120 that expose a coreceptor binding region, which subsequently binds to one of two chemokine coreceptors: CCR5 (R5) or CXCR4 (X4). Coreceptor interactions trigger the release of a fusion peptide in gp41, which induces membrane fusion, ultimately leading to infection.

While HIV Envs can be classified as either R5, X4 or dual R5/X4 tropic based on the coreceptor recognized **(2)**, coreceptor tropism alone does not predict target-cell tropism or pathology. For example, although macrophages express higher levels of CCR5 than CD4+ T cells, many R5-tropic viruses can infect CD4+ T cells but mot macrophages. The majority of transmitted HIV-1 Envs are exclusively R5-tropic **(3-5)**, which persist throughout the course of infection to the onset of clinical AIDS, where nearly half of all subtype B infections evolve X4-tropism **(6-8)**. However, X4-tropism is not a requirement of advanced disease as R5 Envs are also associated with disease progression, T-cell depletion and clinical AIDS **(9,10)**. Indeed, the relative efficiency of CCR5 usage among certain Envs has been linked to transmission **(11,12)**, macrophage tropism **(13-15)**, and neurovirulence **(16-18,13)**, underscoring the importance of CD4 and CCR5 usage efficiency in pathological contexts.

Prior studies of CD4 and CCR5 usage efficiency commonly evaluate infection on multiple cell lines expressing distinct and homogenous CD4/CCR5 surface densities **(19-21)**, which, although informative, offers a limited resolution of CD4 and CCR5 expression combinations. Additionally, differences in post-entry infection susceptibility and viral gene expression can confound interpretations of entry efficiency. We describe the Affinofile system **(22)**, a 293-derived CD4/CCR5 dual-inducible cell line and the associated Viral Entry Receptor Sensitivity Assay (VERSA) metrics used to assess CD4 and CCR5 usage efficiency in an interdependent context on a single clonal cell line.

Affinofile cells express CD4 through the tet-on system where, in the presence of tetracycline, inhibition of CD4 expression by the tet transactivator is released providing concentration-dependent expression of CD4. CCR5 is expressed through the Ecdysone system where ponasterone A promotes dimerization of constitutively expressed VgEcr and RXR nuclear receptor proteins, which drives CCR5 expression in a concentration-dependent manner. A schematic of this inducible system is shown in **Figure 1** and more detail regarding the mechanisms of induction can be found in the literature **(22,1)**. Affinofile cells can be induced to generate up to 25 distinct combinations of CD4 and CCR5 (as measured by CD4/CCR5 antibody epitopes per cell), recapitulating a wide, biologically relevant range of receptor/corecetor surface densities **(14)**. CD4 expression generally ranges between 2,000 and 150,000 CD4 antibody biding sites per cell (ABS/cell) and CCR5 expression ranges between 1,500 and 25,000 ABS/cell. These induction matrices are then infected to profile viral infectivity across the entire range of combined CD4 and CCR5 expression levels. This profile is distilled by the VERSA algorithm into three metrics that describe the overall infectivity of an Env (mean induction, M), the stoichiometric contribution of CD4 and CCR5 to infectivity (angle, θ) and the responsiveness of an Env to the most efficient combination of CD4 and CCR5 expression (amplitude, Δ). These three parameters have been used to identify specific mechanisms of entry inhibitor resistance **(23-28)**, target-cell tropism **(14,29,15,13)**, and transmission **(11,12)** in terms of an Env's response to changing levels of CD4 and CCR5 expression on Affinofile cells. A more in-depth description of these metrics and how they have been applied to specific Env phenotypes is reviewed in **(1)**.

The protocols provided in this chapter are intended as a guide for using the Affinofile system and interpreting the results in any context and, thus, are not specific for analyzing a particular Env phenotype. The experiments described can be easily adjusted to fit specific research needs so long as the fundamental requirements and core concepts discussed are satisfied. The first procedure quantifies CD4 and CCR5 expression in term of induction with doxycycline and ponasterone A, respectively, to calibrate this system and determine the range of induction to be used in further experiments (**Section 3.1**). We then describe the preparation and infection of an Affinofile matrix composed of 25 distinct CD4/CCR5 expression levels (**Section 3.2**). This chapter then closes with an in-depth discussion of the fundamental meaning and derivation of each VERSA metric to provide users with a strong foundation from which to interpret relative differences in CD4 and CCR5 usage efficiency in a wide range of contexts (**Section 3.3**).

2. Materials

2.1. Cell Culture

1. Affinofile Media: Dulbecco's Modified Eagle Medium (DMEM) supplemented with 10% dialyzed fetal bovine serum (**Note 1**) with 50μg/mL Blasticidin S HCl.
2. Affinofiles are normally cultured in 10cm culture dishes and split every 2-3 days at 1/5X for no more than 35 passages.

2.2. Induction, Staining and Quantification

1. One 24-well plate.
2. Doxycycline hyclate (10μM in sterile water). Store in 50-100μL aliquots at -20ºC.
3. Ponasterone A resuspended and stored according to manufacturer's instructions.
4. PE quantification beads. These are used to quantify expression of CCR5 by correlating the geometric mean fluorescence of a variety of bead populations with distinct fluorophore-per-bead quantities to the fluorescence of stained Affinofiles. We routinely use QuantiBrite PE Beads (BD Biosciences, Cat #340495).
5. APC quantification beads. These are used to quantify expression of CD4 by correlating the geometric mean fluorescence of a variety of bead populations with distinct fluorophore-per-bead quantities to the fluorescence of stained Affinofiles. We routinely use Quantum™ APC MESF beads (Bangs Laboratories, Cat #823A).
6. APC mouse anti-human CD4 (Clone RPA-T4) and appropriate isotype (APC isotype for CD4 antibody).
7. PE mouse anti-human CCR5 (Clone 2D7) and appropriate isotype (PE isotype for CCR5 antibody).
8. FACS buffer: 2% FBS in DPBS.
9. FACS buffer supplemented with 5mM EDTA

10. CD4 staining solution: 1/2X APC mouse anti-human CD4 in FACS buffer
11. CCR5 staining solution: 1/2X PE mouse anti-human CCR5 in FACS buffer
12. CD4 isotype staining solution: 1/2X APC mouse IgG1κ isotype in FACS buffer
13. CCR5 isotype staining solution: 1/2X PE mouse IgG2aκ isotype
14. Paraformaldehyde (2%)
15. Flow cytometer with APC (635nm excitation/660-668 emission) and PE (488nm excitation/575-566nm emission) channels

2.3 Infection

1. Two 24-well plates.
2. Doxycycline hyclate (10μM in sterile water). Store in 50-100μL aliquots at -20ºC.
3. Ponasterone A (powder, Invitrogen, Cat #H101-01) resuspended and stored according to manufacturer's instructions.
4. Pseudotyped HIV reporter virus ($5x10^5$ IU minimum per matrix to achieve an MOI of 0.2). Affinofiles express low, basal levels of CXCR4 and can be infected by both R5 and X4-tropic envelopes. Only R5-tropic envelopes will respond to different levels of CCR5 induction. The particular envelope chosen should be relevant to ones specific research purposes.

5. Relevant pseudotype reporter detection reagents.

3. Methods

3.1 Quantitative Determination of CD4 and CCR5 Induction

The induction range of each thawed batch of Affinofiles must be determined before use. This protocol uses a minimized sample set whereby CD4 and CCR5 are measured simultaneously across a range of combined Doxycycline and Ponasterone A serial dilutions. **Figure 2** shows the sample set and plate map for this protocol, where each induction dilution is indicated by samples *1-8* and *U1, U2* (uninduced), isotype controls are indicated by samples *A-D* and cytometer voltage adjustment samples *E–H*. This sample set is intended to provide excess controls for cytometer voltage adjustments. CD4 and CCR5 are measured simultaneously using APC-labeled CD4 antibody (clone RPA-T4) and PE-labeled CCR5 antibody (clone 2D7) such that no fluorescence compensation is necessary. This protocol can be adjusted for single color analysis of both CD4 and CCR5 by doubling the sample set and staining each replicate with CD4 or CCR5 antibodies. Refer to 'Section 3.1: Antibody Usage' for a more thorough description of the CD4/CCR5 antibodies used.

3.1.1 Induction and Staining

1. Seed one 24-well plate with Affinofiles at a minimum density of $1x10^5$ cells/well (see **Figure 2**) using Affinofile media (**Note 2**).

2. Incubate at 37ºC (5% CO_2) until the cells have adhered and wells have reached 70-80% confluency.
3. Prepare 100µL maximum induction solution with 78ng/mL doxycycline and 52µM ponasterone A. (**Note 3**)
4. Prepare seven 0.5X serial dilutions of the maximum induction solution by serial diluting 30µL maximum induction solution through seven additional tubes containing 30µL Affinofile media.
5. Add 20µL of the appropriate induction dilution to wells *1-8* (**Figure 2**).
6. Add 20µL of the maximum induction solution to wells *E–F* (**Figure 2**).
7. Add 20µL Affinofile media to wells *U* and *A-D* (**Figure 2**).
8. Swish plate left-right and up-down gently to mix
9. Incubate at 37ºC (5% CO_2) for 16-20 hours
10. Prepare labeled FACS tubes with 2mL FACS buffer each, one tube for each well in **Figure 2**.
11. Aspirate media from each well and replace with FACS buffer supplemented with 5mM EDTA.
12. Incubate for 2-5 minutes at room temperature and visually confirm cell detachment.
13. Transfer cells to appropriate FACS tubes using a minimum 700µL of FACS buffer from the destination FACS tube to wash the well surface.
14. Pellet cells at 300g for 5 minutes at 4ºC
15. Decant supernatant and break up pellet by vortexing gently

16. Add 2mL FACS buffer without EDTA and pellet cells at 300g for 5 minutes at 4ºC
17. Decant supernatant and break up pellet by vortexing gently
18. Add 2µL CD4 staining solution to tubes *1-8*, *U1, U2* and *E, F.* Vortex immediately after addition.
19. Add 2µL CCR5 staining solution to tubes *1-8*, *U1, U2* and *E, F.* Vortex immediately after addition.
20. Add 2µL CD4 isotype staining solution to tubes *A, B* and 2µL CCR5 isotype staining solution to tubes *C, D*. Vortex immediately after addition.
21. Incubate at 4ºC in the dark for 60 minutes
22. Add 2mL FACS buffer to each tube
23. Pellet cells at 300g for 5 minutes at 4ºC
24. Decant supernatant and break up pellet by vortexing gently
25. Resuspend cells in 200µL paraformaldehyde (2%) and vortex gently to mix
26. Store at 4ºC in the dark until samples can be analyzed using flow cytometry

3.1.2 Flow Cytometry Analysis

Quantitative PE and APC beads are analyzed concurrently with the Affinofile samples described in **Section 3.1 Induction Staining**. These should be prepared according to the manufacturer's specification.

Samples *G, H* are intended for FSC/SSC voltage adjustment and live cell gating while samples *A, B* and *C, D* are CD4 and CCR5 isotype controls, respectively. One replicate of these sets is intended for fluorescence voltage adjustment (it is also recommended that PE and APC voltage should consider the fluorescence of PE and APC quantitative bead populations) while the other will be recorded as an isotype background for subtraction. Samples *E* and *F* are replicates of sample *1* (max CD4/CCR5 induction) for fluorescence channel voltage adjustment. **Figure 3a** shows a sample FSC/SSC plot with a live cell gate. Once the cytometer voltage is adjusted appropriately, a minimum of $5x10^4$ live cell events should be recorded from samples *1-8*, *U1, U2* (induced and uninduced samples), one of *A* or *B* (CD4 isotype control), and one of *C* or *D* (CCR5 isotype control). Once these samples are recorded, the quantitative PE and APC bead samples should be recorded after adjusting FSC/SSC voltage appropriately. Fluorescence channel voltage should not be adjusted to ensure that the bead fluorescence is representative of the fluorescence observed on Affinofile cells.

Quantitative calibration of APC and PE fluorescence is determined by comparing the geometric mean fluorescence of each bead population with the manufacturer indicated APC/PE molecules per bead. **Figures 3 (b and d)** show calibration curves for both the Quantum™ APC MESF (**Figure 3b**) and QuantiBrite PE beads (**Figure 3d**), respectively. Follow the manufacturer's instructions for converting the geometric mean fluorescence of each bead population to fluorophore molecules. This calibration is then applied to the isotype-subtracted geometric mean fluorescence of each Affinofile

induction sample (*1-8, U1* and *U2*) to calculate fluorophore molecules per cell, which is directly equal to antibody binding sites per cell (**Figures 3c and 3e**).

Induction ranges for all future experiments involving this particular batch of Affinofiles may be determined from these induction-response curves. The quantity of antibody binding sites, once determined for an individual thaw of Affinofiles, does not change significantly until late passages (>25-30).

3.1.3 Antibody Usage

We refer the reader to our recent review **(1)** and references therein for the CD4 and CCR5 monoclonal antibodies (MAbs) used. Many anti-CD4 MAbs that bind to the D1-D2 domain of CD4 with low (single digit) nanomolar Kd and compete well for gp120 binding (e.g. clone RPA-T4 and Q4120, etc.) can be used for quantifying CD4 ABS/cell on Affinofiles. However, CCR5 is conformationally heterogeneous and some epitopes recognized by commercially available anti-CCR5 MAbs might not coincide with those necessary for productive gp120-CCR5 interactions **(30)**. The 2D7 anti-CCR5 Mab is most often used for quantifying CCR5 for HIV entry studies, and has been used in almost all Affinofile studies to date. Although some CCR5 MAbs such as PA14 may recognize an even larger spectrum of relevant CCR5 conformations **(30)**. For historical consistency and comparison purposes, we recommend that 2D7 be used for quantifying CCR5 ABS/cell on Affinofiles.

3.2 Induction Matrix and Infection

This protocol describes infection of a 5x5 induction matrix containing 25 distinct combinations of CD4 and CCR5 expression in a 24-well format (**Figure 4**). Doxycycline and ponasterone A concentrations for this matrix should be determined from the quantitative induction responses described in **Section 3.1**. Preparation of induction solutions is greatly simplified when serial dilution can be used, although this is not required. The induction matrix is infected with reporter-pseudotyped HIV virus. We recommend infecting at an MOI of 0.2 (**Note 4**) as determined on GHOST R5 cells which express saturating levels of CD4 and CCR5 **(31)**.

1. Seed two 24-well plates with $8x10^4$ cells/well in Affinofile media (**Note 5**).
2. Incubate at 37ºC (5% CO_2) until the cells have adhered and reached 50-60% confluence.
3. Prepare five doxycycline induction solutions at 52X the final desired concentration, with the fifth solution containing no doxycycline. Each solution should have a minimum, final volume of 60µL.
4. Prepare five ponasterone A induction solutions at 52X the final desired concentration, with the fifth solution containing no ponasterone A. Each solution should have a minimum, final volume of 60µL.
5. Add 10µL of each doxycycline dilution to appropriate wells (see **Figure 4**) and swish plate left-right and up-down gently to mix.
6. Add 10µL of each ponasterone A dilution to appropriate wells (see **Figure 4**) and swish plate left-right and up-down gently to mix.

7. Incubate 16-20 hours at 37ºC (5% CO_2)
8. Trypsinize and count the three *Count* wells. (**Note 6**)
9. Remove media from *Cell* wells (**Figure 4**) and replace with the same media used to dilute viral stock
10. Remove media from all induction wells and add viral inoculant at an MOI of 0.2 to each well. (**Note 7**).
11. Centrifuge plates at 700g for 2 hours at 37ºC.
12. Remove inoculant/media from all wells and replace with fresh Affinofile media.
13. Incubate at 37ºC (5% CO_2) to allow reporter expression (typically 48-72 hours)
14. Measure the reporter signal from each of the induction wells and subtract reporter signal from the background signal obtained from the three *Cell* wells.

VERSA Metric Processing

Using the ABS calibration curve determined in **Section 3.1**, determine the CD4 and CCR5 ABS quantities for each doxycycline and ponasterone A concentration used in the induction matrix (**Section 3.2: Induction Matrix and Infection**). The VERSA algorithm accepts single header (**Figure 5a**) and double header (**Figure 5b**) formats. The single header format correlates CD4/CCR5 ABS to infectivity directly while the double header format includes additional fields for doxycycline and ponasterone A concentrations associated with each CD4/CCR5 ABS value. Example single and double

header formats are shown to the lower left of each format description (**Figure 5a** and **b**, respectively). The infectivity itself may be reported as either background-subtracted reporter signal values or normalized infection (**Note 8**).

The following formatting criteria must be met for VERSA analysis:

1. The data must be converted to CSV format
2. The first (or only) matrix data set must start at the first row of the CSV file
3. Multiple matrices may be included in the same file so long as they are separated by a single empty row and have the same number of headers (**Note 9**).

Open the VERSA website: http://versa.biomath.ucla.edu/ in any browser and click on **DATA ANALYSIS** (upper left hand menu). Select the number of headers and indicate the total number of datasets (matrices) included in the file. Select **Choose File** and locate the appropriate csv file, then click on **Process File** to begin calculation.

Figure 6 shows a sample of the VERSA output that includes the VERSA metric summary (mean induction M, angle θ and vector amplitude Δ) and $F(x,y)$ polynomial fitting parameters (a0–a5). While the metrics summarize each matrix in terms of overall infectivity and CD4/CCR5 usage efficiency, the fitting parameters can be used to reconstruct the surface fit $F(x,y)$.

3.3 Analysis of VERSA Metrics

VERSA metrics are derived by fitting an Env's infectivity profile to a 2nd order polynomial surface function $F(x,y)$ (**Figure 7a**). The mean infectivity across the entire surface (M) describes the overall infectivity of the Env throughout all levels of CD4 and CCR5 expression (**Figure 7b**). The gradient of $F(x,y)$ (S) is defined by a vector anchored at the lowest CD4/CCR5 expression level that points in the direction of the steepest path along the surface (**Figure 7c**). This sensitivity vector (S) is composed of an amplitude of responsiveness (Δ) to a specific stoichiometric combination of CD4 and CCR5 expression defined as an angle (θ, e.g. the direction of S in the *x,y* plane). By convention, low angles (θ<45º) indicate that the path of greatest responsiveness is weighted toward CD4, while high angles (θ>45º) indicate a CCR5-weighted responsiveness.

As the mean level of infection observed across the entire surface, M is generally indicative of overall infection efficiency. This is most evident when comparing infection profiles in the absence and presence of entry inhibitors **(28,25)**.
However, M is inherently bound by the maximum and minimum levels of infection observed. For example, the infectivity profile of YU2 reveals a distinct ability to mediate high levels of infection at low CD4 surface densities compared to JRCSF **(13)**, which necessarily increases the mean infectivity (by increasing the minimum). The dynamic range and steepness of an infectivity surface has a lesser impact on M, for example, a short and dramatic increase in infectivity that plateaus at low levels of CD4 and CCR5 will naturally increase the mean by weighting more CD4/CCR5 expression levels at high

infection. Collectively, these unique effects describe specific mechanistic components of generalized entry efficiency.

The sensitivity vector (S) identifies the path of the greatest increase in infection from the lowest CD4/CCR5 combination, taking into account the curvature of the entire surface (**Figure 7c**). S is more easily visualized as the average of a step-wise path of greatest increase in infectivity starting at the lowest CD4/CCR5 level (shadow arrows in **Figure 7c**). The sensitivity vector has two components: an amplitude (Δ) that describes the vertical slope, and a direction defined by coordinates in the *x,y* (or CD4/CCR5) plane, which is summarized as an angle (θ). The angle is a balance of the CD4 and CCR5 expression associated with the gradient path and as such, is interpreted as the most efficient stoichiometric combination of CD4 and CCR5 used by an Env. By convention, θ is defined off of the CD4 axis, thus, Envs that exhibit a stronger responsiveness to changes in CD4 expression will yield a lower angle (θ<45º) while Envs exhibiting a stronger responsiveness to CCR5 expression will give higher angles (θ>45). For example, a relative increase in θ that is not associated with significant changes in Δ or M indicates that the Env is more responsive to CCR5 (by comparison).

The amplitude (Δ) quantifies the strength of responsiveness to this most efficient, θ-defined combination of CD4/CCR5. In the simplest context, such as comparison of two Envs that exhibit no dramatic differences in θ, a higher Δ suggests a greater efficiency of infection in response to the ideal CD4/CCR5 combination and will necessarily be associated with an increase in M.

The metrics themselves can be represented in a polar format (**Figure 7d**) that clearly illustrates the functional clustering of Envs. Each infectivity profile is represented as a single point surrounded by a circle with radius M, angled off the *x* axis (CD4) by θ at a distance Δ. It is important to note that these three metrics (M, Δ and θ) are derived from a mathematically smoothed surface and describe only the properties of the surface itself. The more intricate details of an Env's response to CD4 and CCR5 expression may not result in significant metric differences due to the fact that the metrics are intended to accommodate the entire surface **(32)**. Alternative representations of these data can offer additional insight without the need for mathematical fitting, such as 2D profiles or 2D infectivity response plots (published in Figure 5g and d, e, respectively **(32)**).

4. Notes

1. Some lots and brands of FBS have residual tetracyclines that may induce CD4 expression. We routinely use Dialyzed FBS, Thermo Scientific, Cat #SH30079.03
2. The growth rate of Affinofile cells can decrease approximately 50-75% under induction. A high density seed or longer pre-induction culture is necessary to ensure a minimum of $5x10^4$ live-cell events during flow cytometry analysis. Some labs routinely seed their Affinofile cells onto polylysine-coated plates to mitigate cell loss. This is appropriate for infectivity experiments (see **Note 5**) but is not recommended when the

cells are to be used for FACS determination of CD4 and CCR5 expression levels.

3. In this protocol, doxycycline and ponasterone A concentrations are prepared at 26X of the final concentration. Alternatively, the culture media can be entirely replaced with Affinofile media containing the proper doxycycline/ponasterone A concentrations, however, as Affinofiles are weakly adherent, some cell loss may occur.
4. An MOI of 0.2 as determined on Ghost R5 cells (which are highly susceptible to HIV infection due to high expression of both CD4 and CCR5) is the upper limit of the linear range of infection. This MOI is used to first ensure that the majority of infected Affinofiles were infected by a single infectious unit and second, to maximize the dynamic range of infection across the CD4/CCR5 expression matrix.
5. As mentioned in **Note 2**, the growth rate of Affinofiles decreases during induction, it is also slower after infection. The cell seed used for an infection matrix should be informed by both this decreased growth rate and the post-infection culture time required for adequate reporter signal. The cell seed provided is optimized for luciferase reporter pseudotype virus requiring a 48 hour post-infection culture period. Longer culture periods will require lower cell seeds to prevent overgrowth. The ultimate goal is to achieve a healthy and adherent cell density on the day of infection that is low enough to prevent overgrowth until infection is measured. Seeding Affinofile cells onto

polylysine coated plates can result in less well-to-well variability, especially when highly passaged Affinofile cells begin to lose their already weak baseline adherence.

6. For the most accurate count, we recommend counting two separate 10μL volumes from each trypsinized well sample.
7. Viral inoculant should be diluted in the same solution the virus was stored/cultured.
8. Both background-subtracted reporter signal and normalized infection are valid for VERSA processing. When normalizing, the subtracted signals should be normalized to the signal observed at saturating or near-saturating CD4 and CCR5 induction levels. When properly normalized, there is little difference in θ, however, the scale of mean induction (M) and amplitude (Δ) is necessarily dependent on whether the data is normalized or not. A more thorough discussion of normalization cab be found in **(1)**. Normalization is our current standard.
9. Multiple matrices may have different CD4 and CCR5 ABS quantities as each matrix is processed independently.

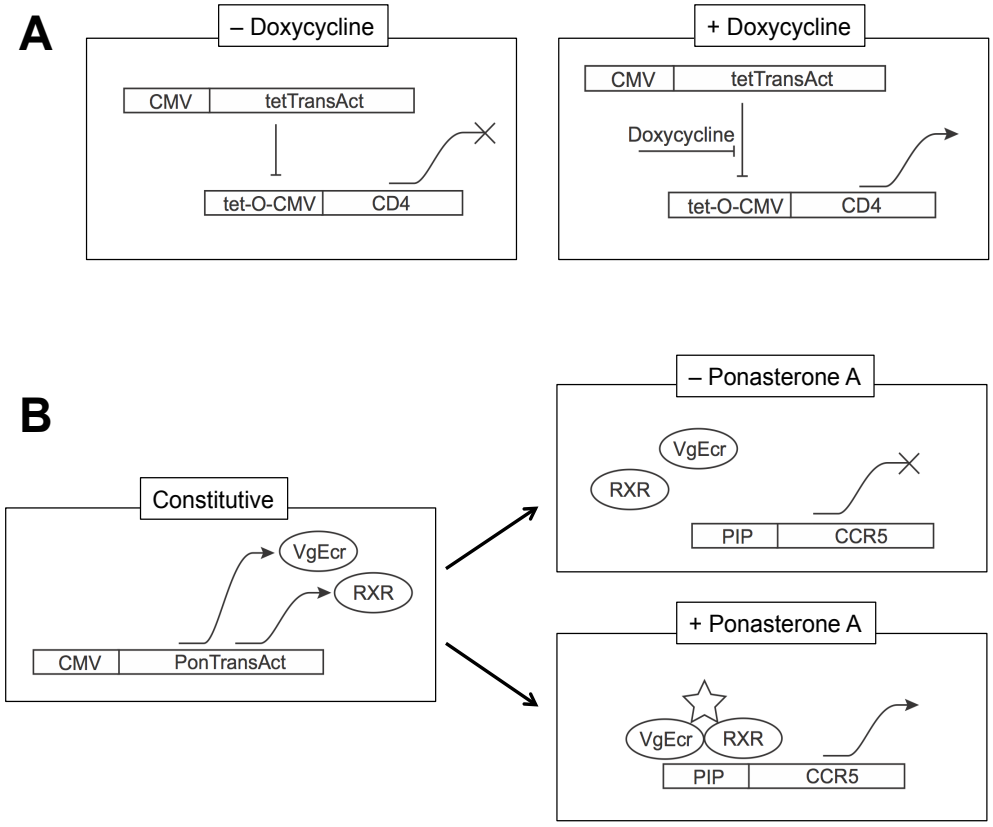

Figure 1: Schematic of the Affinofile System. **(A)** The Tet-On system drives CD4 expression where tetracycline prevents the tet transactivator from repressing CD4 expression in a dose-dependent fashion. **(B)** CCR5 expression is driven by the ecdysone-inducible system. Ponasterone A (star) induces dimerization of the constitutively expressed insect nuclear hormone receptor subunits (VgEcR and RXR, represented as PonTransAct) forming VgRXR, which binds the ponasterone inducible promoter, driving expression of CCR5 in a manner dependent on ponasterone A concentration.

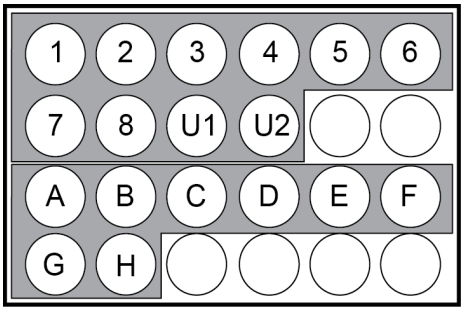

Figure 2: Plate map for quantitative determination of CD4/CCR5 expression. Samples 1-8 are concomitant serial dilutions of doxycycline and ponasterone A with samples U1 and U2 remaining uninduced. Samples A-B and C-D are duplicate CD4/CCR5 isotype staining controls, respectively, while samples E-F are induced for maximum CD4/CCR5 expression for cytometer voltage adjustment. Samples G and H are uninduced Affinofiles used for live cell gating and FSC/SSC voltage calibration.

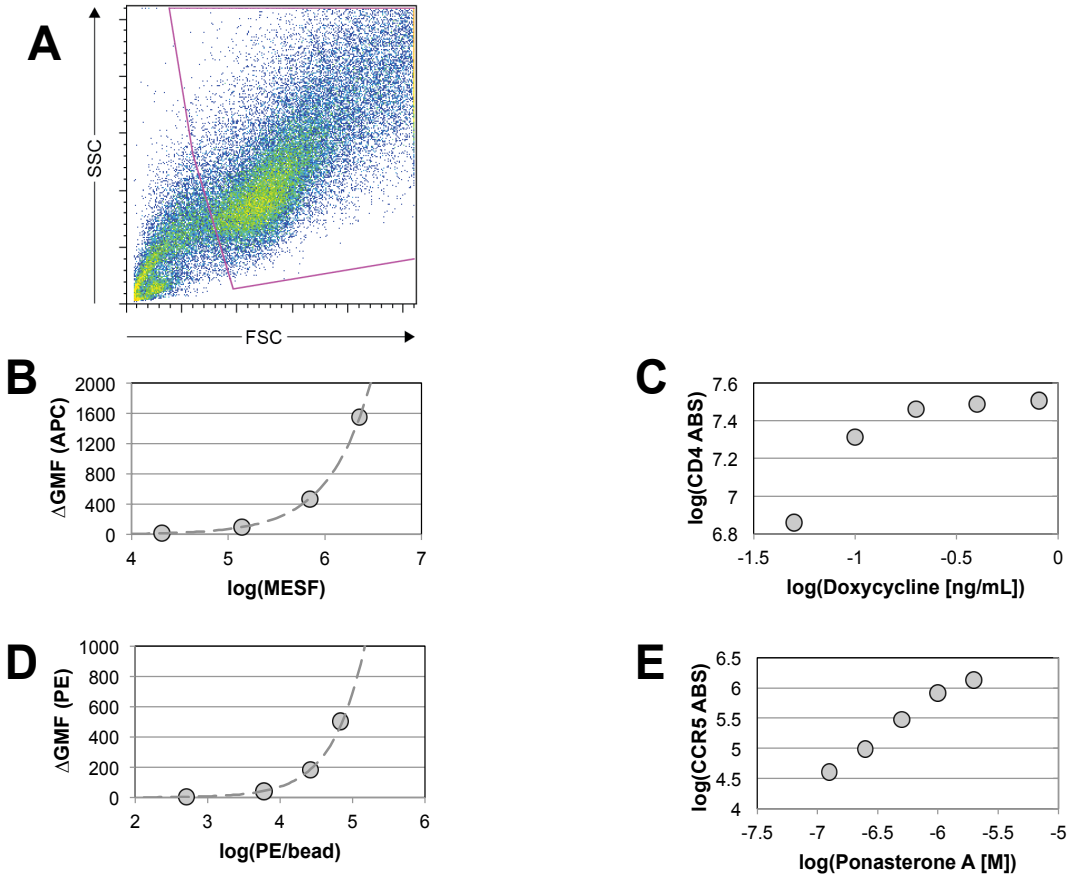

Figure 3: Quantifying CD4 and CCR5 antibody binding sites per cell. Geometric mean fluorescence for PE (CCR5) and APC (CD4) are calculated from live cells **(A)**. Quantitative APC and PE beads are used to correlate geometric mean fluorescence to fluorophore molecules per bead **(B and D)**. These calibration curves are then used to calculate antibody binding sites per cell for each induced Affinofile sample **(C and E)**.

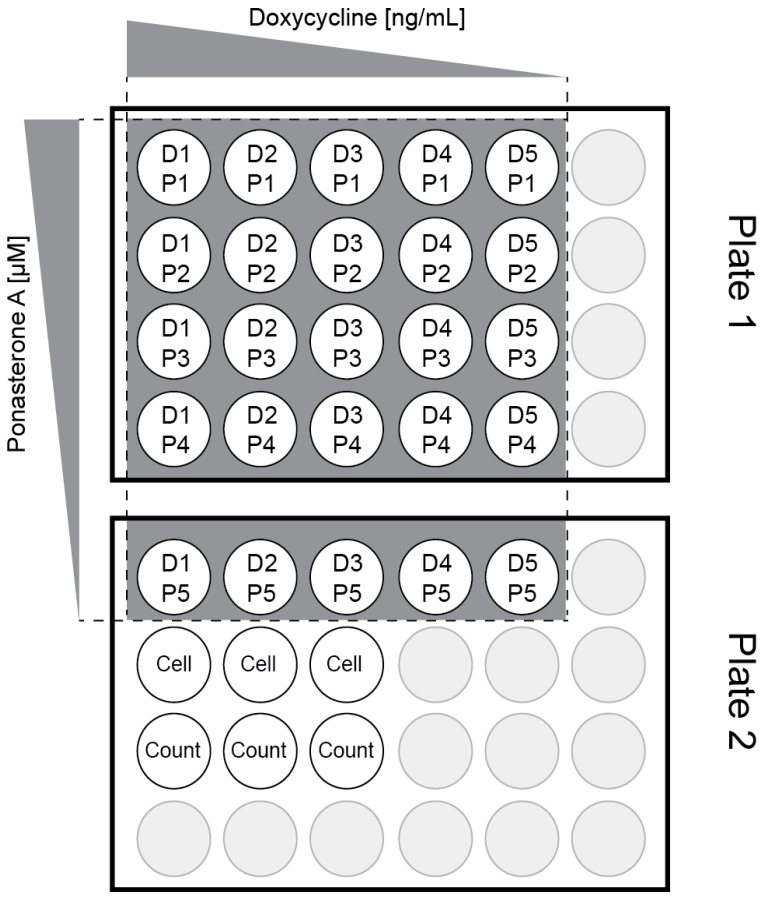

Figure 4: Infection matrix plate map. This matrix consists of 5 doxycycline (D1-D5, high to low) and 5 ponasterone A (P1-P5, high to low) inductions. Uninfected cell samples are included for reporter background measurement **(27)** and additional cell counting wells (Count) are included for proper MOI determination.

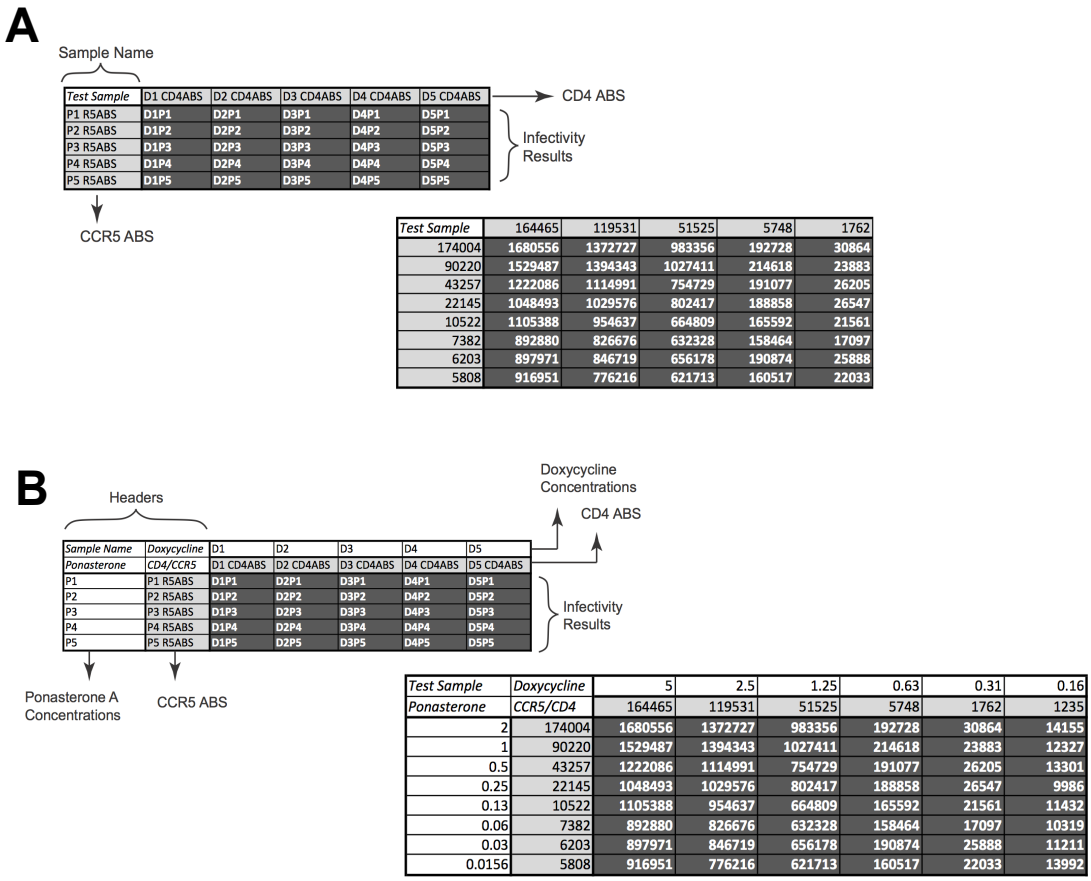

Figure 5: VERSA Format. VERSA includes a single header format **(A)** that associates antibody binding sites to infectivity reporter values and a double header format **(B)** that includes doxycycline and ponasterone A concentrations. Example formats are shown below format descriptions using background-subtracted reporter signals.

These are the Angle, Magnitude and Mean Induction values for each datasets

Strain	Vector Angle	Vector Magnitude	Mean Induction
Matrix 1	13.21	0.76	0.28
Matrix 2	12.59	0.75	0.32
Matrix 3	13.95	0.79	0.35
Matrix 4	13.26	0.77	0.32

These are the fitting polynomials for each datasets.

The polynomials are of the form: $F(X,Y)=a_0 + a_1X + a_2Y + a_3XY + a_4 X^2 + a_5Y^2$.

Strain	a_0	a_1	a_2	a_3	a_4	a_5
Matrix 1	0.02	0.06	-0.09	0.43	0.47	0.05
Matrix 2	0.03	0.21	-0.05	0.39	0.33	0.02
Matrix 3	0.00	0.54	-0.12	0.47	-0.01	0.08
Matrix 4	0.02	0.27	-0.09	0.43	0.26	0.05

Figure 6: VERSA Output. VERSA metrics (vector angle, vector amplitude and mean induction) are reported for each matrix in this 4-matrix data set, along with the polynomial fitting parameters (a_0-a_5) used to construct the surface (boxed rectangle). It is not necessary for the user to know the values of these fitting parameters in order to understand the biological meaning of the VERSA metrics.

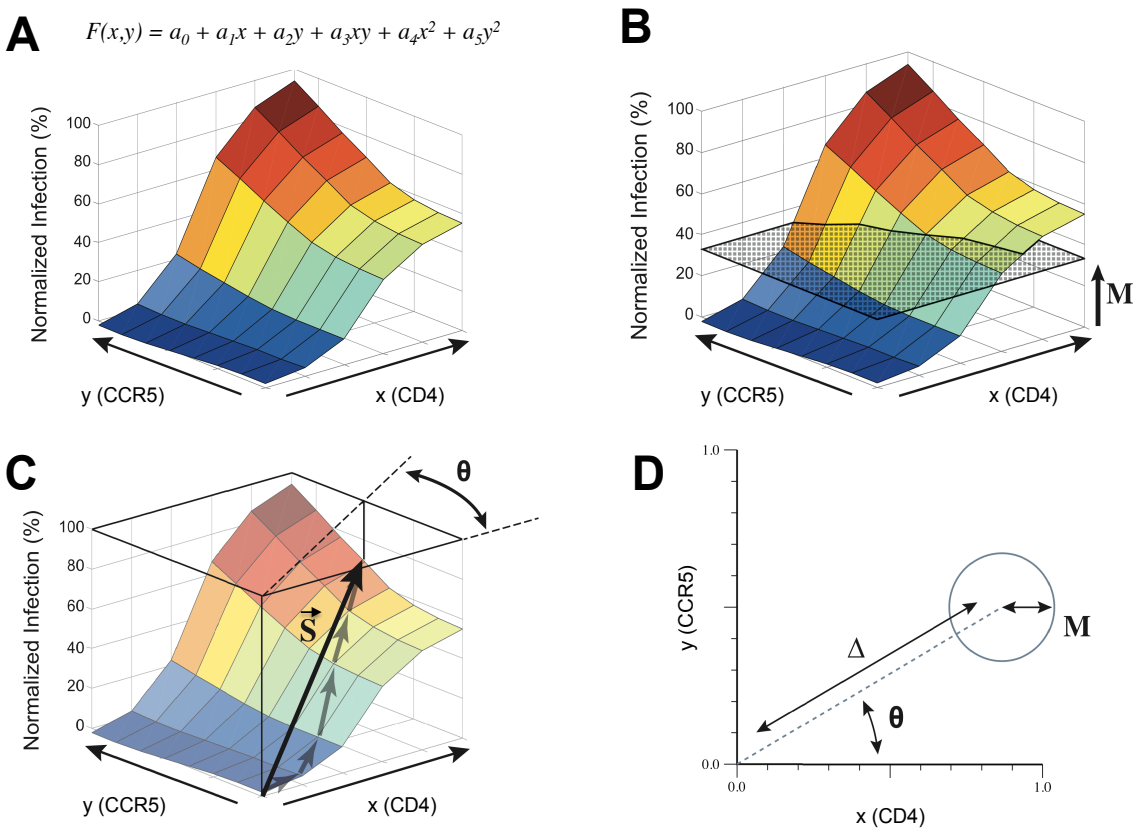

Figure 7: VERSA Metrics. The VERSA metrics θ, Δ and M are calculated by fitting the surface function $f(x, y)$ **(A)** to infectivity data across all combined CD4/CCR5 expression levels. Mean infectivity (M) is the mean infectivity observed across the entire surface **(B)**. A sensitivity vector $(\vec{S})$ is fit to the gradient of $f(x, y)$ **(C)**. The vector is composed of an angle (θ) indicating the direction of greatest infectivity response (in the x,y plane) and the amplitude (Δ) of responsiveness. A polar plot **(D)** summarizes these three metrics where θ is defined as the angle of a line anchored at the origin, Δ is the length of that line and M is the size of the circle set at the end of the line.

References

1. Chikere K, Chou T, Gorry PR, Lee B (2013) Affinofile profiling: how efficiency of CD4/CCR5 usage impacts the biological and pathogenic phenotype of HIV. Virology 435 (1):81-91. doi:10.1016/j.virol.2012.09.043

2. Berger EA, Doms RW, Fenyö EM, Korber BT, Littman DR, Moore JP, Sattentau QJ, Schuitemaker H, Sodroski J, Weiss RA (1998) A new classification for HIV-1. Nature 391 (6664):240. doi:10.1038/34571

3. Long EM, Rainwater SMJ, Lavreys L, Mandaliya K, Overbaugh J (2002) HIV type 1 variants transmitted to women in Kenya require the CCR5 coreceptor for entry, regardless of the genetic complexity of the infecting virus. AIDS Res Hum Retroviruses 18 (8):567-576. doi:10.1089/088922202753747914

4. Salvatori F, Scarlatti G (2001) HIV type 1 chemokine receptor usage in mother-to-child transmission. AIDS Res Hum Retroviruses 17 (10):925-935. doi:10.1089/088922201750290041

5. van't Wout AB, Kootstra NA, Mulder-Kampinga GA, Albrecht-van Lent N, Scherpbier HJ, Veenstra J, Boer K, Coutinho RA, Miedema F, Schuitemaker H (1994) Macrophage-tropic variants initiate human immunodeficiency virus type 1 infection after sexual, parenteral, and vertical transmission. J Clin Invest 94 (5):2060-2067. doi:10.1172/JCI117560

6. Melby T, Despirito M, Demasi R, Heilek-Snyder G, Greenberg ML, Graham N (2006) HIV-1 coreceptor use in triple-class treatment-experienced patients: baseline prevalence, correlates, and relationship to enfuvirtide response. J Infect Dis 194 (2):238-246. doi:10.1086/504693

7. Moyle GJ, Wildfire A, Mandalia S, Mayer H, Goodrich J, Whitcomb J, Gazzard BG (2005) Epidemiology and predictive factors for chemokine receptor use in HIV-1 infection. J Infect Dis 191 (6):866-872. doi:10.1086/428096

8. Wilkin TJ, Su Z, Kuritzkes DR, Hughes M, Flexner C, Gross R, Coakley E, Greaves W, Godfrey C, Skolnik PR, Timpone J, Rodriguez B, Gulick RM (2007) HIV type 1 chemokine coreceptor use among antiretroviral-experienced patients screened for a clinical trial of a CCR5 inhibitor: AIDS Clinical Trial Group A5211. Clin Infect Dis 44 (4):591-595. doi:10.1086/511035

9. Brown BK, Darden JM, Tovanabutra S, Oblander T, Frost J, Sanders-Buell E, de Souza MS, Birx DL, McCutchan FE, Polonis VR (2005) Biologic and genetic characterization of a panel of 60 human immunodeficiency virus type 1 isolates, representing clades A, B, C, D, CRF01_AE, and CRF02_AG, for the development and assessment of candidate vaccines. J Virol 79 (10):6089-6101. doi:10.1128/JVI.79.10.6089-6101.2005

10. Huang W, Eshleman SH, Toma J, Fransen S, Stawiski E, Paxinos EE, Whitcomb JM, Young AM, Donnell D, Mmiro F, Musoke P, Guay LA, Jackson JB, Parkin NT, Petropoulos CJ (2007) Coreceptor tropism in human immunodeficiency virus type 1 subtype D: high prevalence of CXCR4 tropism and heterogeneous composition of viral populations. J Virol 81 (15):7885-7893. doi:10.1128/JVI.00218-07

11. Ping L-H, Joseph SB, Anderson JA, Abrahams M-R, Salazar-Gonzalez JF, Kincer LP, Treurnicht FK, Arney L, Ojeda S, Zhang M, Keys J, Potter EL, Chu H, Moore P, Salazar MG, Iyer S, Jabara C, Kirchherr J, Mapanje C, Ngandu N, Seoighe C, Hoffman I, Gao F, Tang Y, Labranche C, Lee B, Saville A, Vermeulen M, Fiscus S, Morris L, Karim SA, Haynes BF, Shaw GM, Korber BT, Hahn BH, Cohen MS, Montefiori D, Williamson C, Swanstrom R, CAPRISA

Acute Infection Study and the Center for HIV-AIDS Vaccine Immunology Consortium (2013) Comparison of viral Env proteins from acute and chronic infections with subtype C human immunodeficiency virus type 1 identifies differences in glycosylation and CCR5 utilization and suggests a new strategy for immunogen design. J Virol 87 (13):7218-7233. doi:10.1128/JVI.03577-12

12. Parker ZF, Iyer SS, Wilen CB, Parrish NF, Chikere KC, Lee F-H, Didigu CA, Berro R, Klasse PJ, Lee B, Moore JP, Shaw GM, Hahn BH, Doms RW (2013) Transmitted/founder and chronic HIV-1 envelope proteins are distinguished by differential utilization of CCR5. J Virol 87 (5):2401-2411. doi:10.1128/JVI.02964-12

13. Salimi H, Roche M, Webb N, Gray LR, Chikere K, Sterjovski J, Ellett A, Wesselingh SL, Ramsland PA, Lee B, Churchill MJ, Gorry PR (2013) Macrophage-tropic HIV-1 variants from brain demonstrate alterations in the way gp120 engages both CD4 and CCR5. J Leukoc Biol 93 (1):113-126. doi:10.1189/jlb.0612308

14. Joseph SB, Arrildt KT, Swanstrom AE, Schnell G, Lee B, Hoxie JA, Swanstrom R (2014) Quantification of entry phenotypes of macrophage-tropic HIV-1 across a wide range of CD4 densities. J Virol 88 (4):1858-1869. doi:10.1128/JVI.02477-13

15. Sterjovski J, Roche M, Churchill MJ, Ellett A, Farrugia W, Gray LR, Cowley D, Poumbourios P, Lee B, Wesselingh SL, Cunningham AL, Ramsland PA, Gorry PR (2010) An altered and more efficient mechanism of CCR5 engagement contributes to macrophage tropism of CCR5-using HIV-1 envelopes. Virology 404 (2):269-278. doi:10.1016/j.virol.2010.05.006

16. Gorry PR, Bristol G, Zack JA, Ritola K, Swanstrom R, Birch CJ, Bell JE, Bannert N, Crawford K, Wang H, Schols D, De Clercq E, Kunstman K, Wolinsky SM, Gabuzda D (2001)

Macrophage tropism of human immunodeficiency virus type 1 isolates from brain and lymphoid tissues predicts neurotropism independent of coreceptor specificity. J Virol 75 (21):10073-10089. doi:10.1128/JVI.75.21.10073-10089.2001

17. Gorry PR, Taylor J, Holm GH, Mehle A, Morgan T, Cayabyab M, Farzan M, Wang H, Bell JE, Kunstman K, Moore JP, Wolinsky SM, Gabuzda D (2002) Increased CCR5 affinity and reduced CCR5/CD4 dependence of a neurovirulent primary human immunodeficiency virus type 1 isolate. J Virol 76 (12):6277-6292

18. Martín J, LaBranche CC, González-Scarano F (2001) Differential CD4/CCR5 utilization, gp120 conformation, and neutralization sensitivity between envelopes from a microglia-adapted human immunodeficiency virus type 1 and its parental isolate. J Virol 75 (8):3568-3580. doi:10.1128/JVI.75.8.3568-3580.2001

19. Kozak SL, Platt EJ, Madani N, Ferro J, F E, Peden K, Kabat D (1997) CD4, CXCR-4, and CCR-5 dependencies for infections by primary patient and laboratory-adapted isolates of human immunodeficiency virus type 1. J Virol 71 (2):873-882

20. Platt EJ, Madani N, Kozak SL, Kabat D (1997) Infectious properties of human immunodeficiency virus type 1 mutants with distinct affinities for the CD4 receptor. J Virol 71 (2):883-890

21. Platt EJ, Wehrly K, Kuhmann SE, Chesebro B, Kabat D (1998) Effects of CCR5 and CD4 cell surface concentrations on infections by macrophagetropic isolates of human immunodeficiency virus type 1. J Virol 72 (4):2855-2864

22. Johnston SH, Lobritz MA, Nguyen S, Lassen K, Delair S, Posta F, Bryson YJ, Arts EJ, Chou T, Lee B (2009) A quantitative affinity-profiling system that reveals distinct CD4/CCR5

usage patterns among human immunodeficiency virus type 1 and simian immunodeficiency virus strains. J Virol 83 (21):11016-11026. doi:10.1128/JVI.01242-09

23. Pugach P, Ray N, Klasse PJ, Ketas TJ, Michael E, Doms RW, Lee B, Moore JP (2009) Inefficient entry of vicriviroc-resistant HIV-1 via the inhibitor-CCR5 complex at low cell surface CCR5 densities. Virology 387 (2):296-302. doi:10.1016/j.virol.2009.02.044

24. Pfaff JM, Wilen CB, Harrison JE, Demarest JF, Lee B, Doms RW, Tilton JC (2010) HIV-1 resistance to CCR5 antagonists associated with highly efficient use of CCR5 and altered tropism on primary CD4+ T cells. J Virol 84 (13):6505-6514. doi:10.1128/JVI.00374-10

25. Roche M, Jakobsen MR, Sterjovski J, Ellett A, Posta F, Lee B, Jubb B, Westby M, Lewin SR, Ramsland PA, Churchill MJ, Gorry PR (2011) HIV-1 escape from the CCR5 antagonist maraviroc associated with an altered and less-efficient mechanism of gp120-CCR5 engagement that attenuates macrophage tropism. J Virol 85 (9):4330-4342. doi:10.1128/JVI.00106-11

26. Roche M, Jakobsen MR, Ellett A, Salimiseyedabad H, Jubb B, Westby M, Lee B, Lewin SR, Churchill MJ, Gorry PR (2011) HIV-1 predisposed to acquiring resistance to maraviroc (MVC) and other CCR5 antagonists in vitro has an inherent, low-level ability to utilize MVC-bound CCR5 for entry. Retrovirology 8:89. doi:10.1186/1742-4690-8-89

27. Flynn JK, Paukovics G, Moore MS, Ellett A, Gray LR, Duncan R, Salimi H, Jubb B, Westby M, Purcell DFJ, Lewin SR, Lee B, Churchill MJ, Gorry PR, Roche M (2013) The magnitude of HIV-1 resistance to the CCR5 antagonist maraviroc may impart a differential alteration in HIV-1 tropism for macrophages and T-cell subsets. Virology 442 (1):51-58. doi:10.1016/j.virol.2013.03.026

28. Roche M, Salimi H, Duncan R, Wilkinson BL, Chikere K, Moore MS, Webb NE, Zappi H, Sterjovski J, Flynn JK, Ellett A, Gray LR, Lee B, Jubb B, Westby M, Ramsland PA, Lewin SR, Payne RJ, Churchill MJ, Gorry PR (2013) A common mechanism of clinical HIV-1 resistance to the CCR5 antagonist maraviroc despite divergent resistance levels and lack of common gp120 resistance mutations. Retrovirology 10:43. doi:10.1186/1742-4690-10-43

29. Loftin LM, Kienzle MF, Yi Y, Lee B, Lee F-H, Gray L, Gorry PR, Collman RG (2010) Constrained use of CCR5 on CD4+ lymphocytes by R5X4 HIV-1: efficiency of Env-CCR5 interactions and low CCR5 expression determine a range of restricted CCR5-mediated entry. Virology 402 (1):135-148. doi:10.1016/j.virol.2010.03.009

30. Berro R, Klasse PJ, Lascano D, Flegler A, Nagashima KA, Sanders RW, Sakmar TP, Hope TJ, Moore JP (2011) Multiple CCR5 conformations on the cell surface are used differentially by human immunodeficiency viruses resistant or sensitive to CCR5 inhibitors. J Virol 85 (16):8227-8240. doi:10.1128/JVI.00767-11

31. Lee B, Sharron M, Montaner LJ, Weissman D, Doms RW (1999) Quantification of CD4, CCR5, and CXCR4 levels on lymphocyte subsets, dendritic cells, and differentially conditioned monocyte-derived macrophages. Proc Natl Acad Sci U S A 96 (9):5215-5220

32. Chikere K, Webb NE, Chou T, Borm K, Sterjovski J, Gorry PR, Lee B (2014) Distinct HIV-1 entry phenotypes are associated with transmission, subtype specificity, and resistance to broadly neutralizing antibodies. Retrovirology 11 (1):48. doi:10.1186/1742-4690-11-48

APPENDIX D

Supplementary Information for Chapter 4

The following chapter includes the additional files from:

Chikere K*, **Webb NE***, Chou T, Borm K, Sterjovski J, Gorry PR, Lee B. Distinct HIV-1 entry phenotypes are associated with transmission, subtype specificity and resistance to broadly neutralizing antibodies. *Retrovirology* 2015, 11:40.

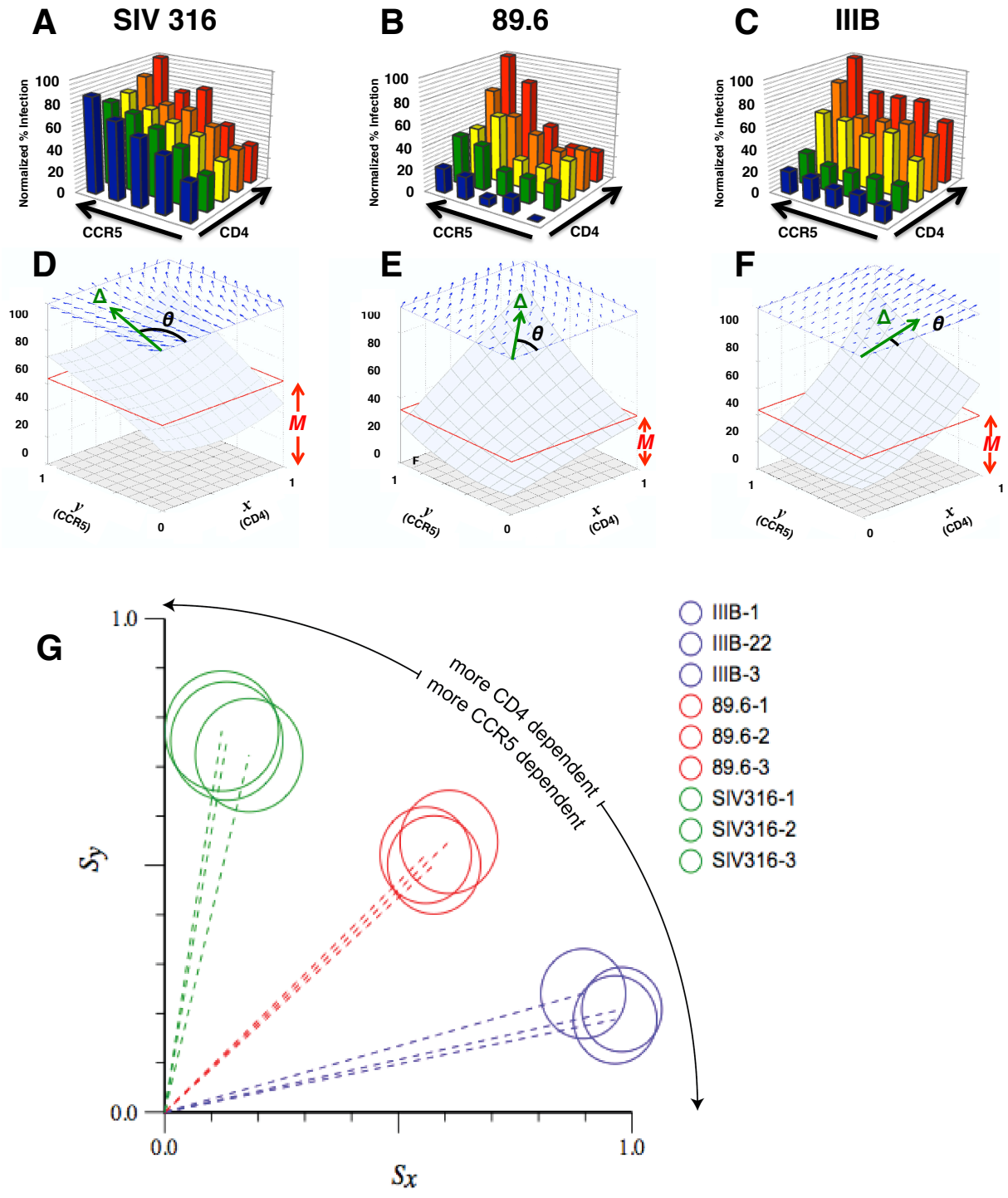
A
SIV 316
B
89.6
C
IIIB
Normalized % Infection
100
80
60
40
20
0
CCR5
CD4
D
E
F
Δ
θ
M
1
0
y (CCR5)
x (CD4)
G
1.0
0.0
Sy
Sx
more CD4 dependent
more CCR5 dependent
IIIB-1
IIIB-22
IIIB-3
89.6-1
89.6-2
89.6-3
SIV316-1
SIV316-2
SIV316-3

Figure D.1: Isolates with different CD4 and CCR5 usage can be represented by distinct 3-D surface plots. GGR Affinofile cells induced to express 25 different combinations of CD4 and CC5 were infected with the (**A**) CD4-independent R5 SIV316, (**B**) R5X4 89.6, or (**C**) X4 III_B pseudotyped viruses. The SIV 316 infection profile indicated that SIV 316 is much more sensitive to changes in CCR5 levels, and is relatively insensitive to varying CD4 levels. Conversely, the HIV III_B infectivity profile indicated a phenotype that was dependent on changes in CD4, but was relatively insensitive to changes in CCR5. This phenotype can be attributed to the use of low levels of CXCR4 present on the HEK293 cells, the parental derivative of GGR Affinofile cells. The 89.6 virus demonstrated an infectivity profile that was equally sensitive to changes in CD4 and CCR5 levels. The distinct infectivity profiles for each Env demonstrated in **A-C** can be mathematically transformed into the corresponding 3-D surface plots shown in **D-F**. These three envelopes represent the diverse range of infectivity profiles that can be demonstrated in GGR Affinofile cells. (**G**) A polar plot representing the three metrics describing the infectivity profiles of the three viruses is shown. SIV316 has a vector angle closest to 90 degrees indicating a greater infective response to CCR5 expression and reflecting the CD4-independence of this Env. Conversely, HIV IIIB has a vector angle closest to zero degrees, endorsing an X4 tropism that is manifested as CCR5 independence. 89.6 has a vector angle of $\approx$45 degrees indicating that it is equally sensitive to changes in CD4 and CCR5 levels. Each circle represents one independent experiment profiling infectivity across 25 distinct CD4/CCR5 expression levels.

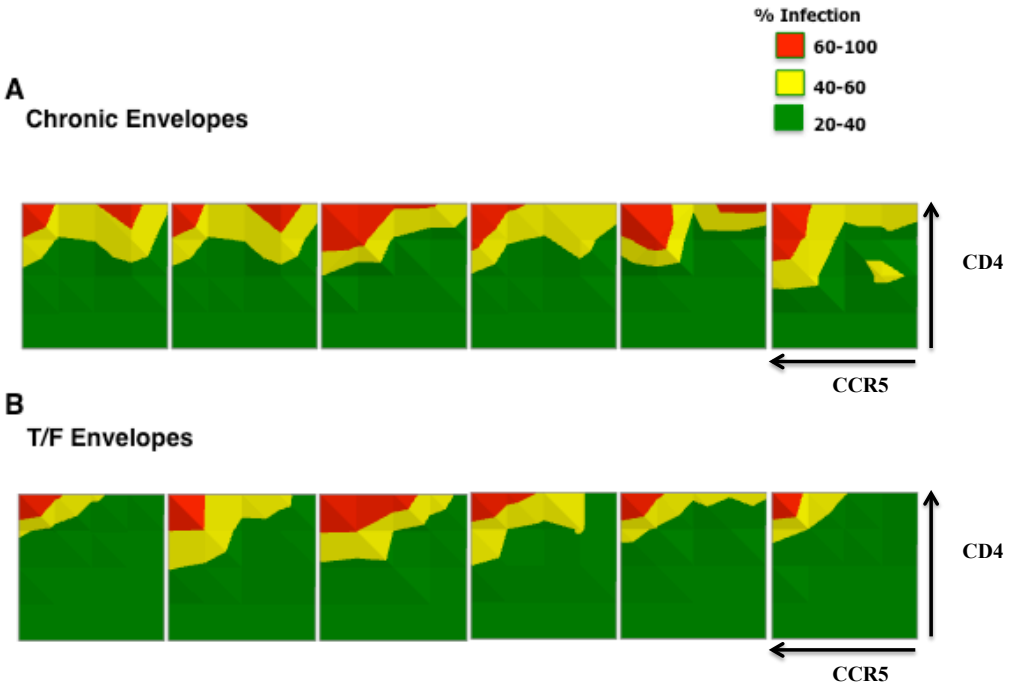

Figure D.2: Infectivity profiles of Chronic and T/F Envelopes. The infectivity profile for individual chronic (**A**) and T/F (**B**) derived envelopes across a spectrum of CD4 and CCR5 expression levels were generated and plotted as described in the Materials and Methods. One representative experiment out of two is shown. Each infectivity data point was performed in triplicate. The contour plots are arranged from highest to lowest mean infectivity (M), from left to right. (**C**) T/F Envs and macrophage tropic (YU2, ADA) and non-macrophage tropic (JRCSF) R5 Envs were used to produce Env pseudotyped luciferase reporter viruses, which were subsequently titrated on JC53 cells. Monocyte derived macrophages were inoculated with equivalent infectious units of each reporter virus, and luciferase activity measured in cell lysates at 72hrs post infection. Results of infection in 3 independent donors are shown. Results are means of triplicate wells, and error bars represent standard deviations.

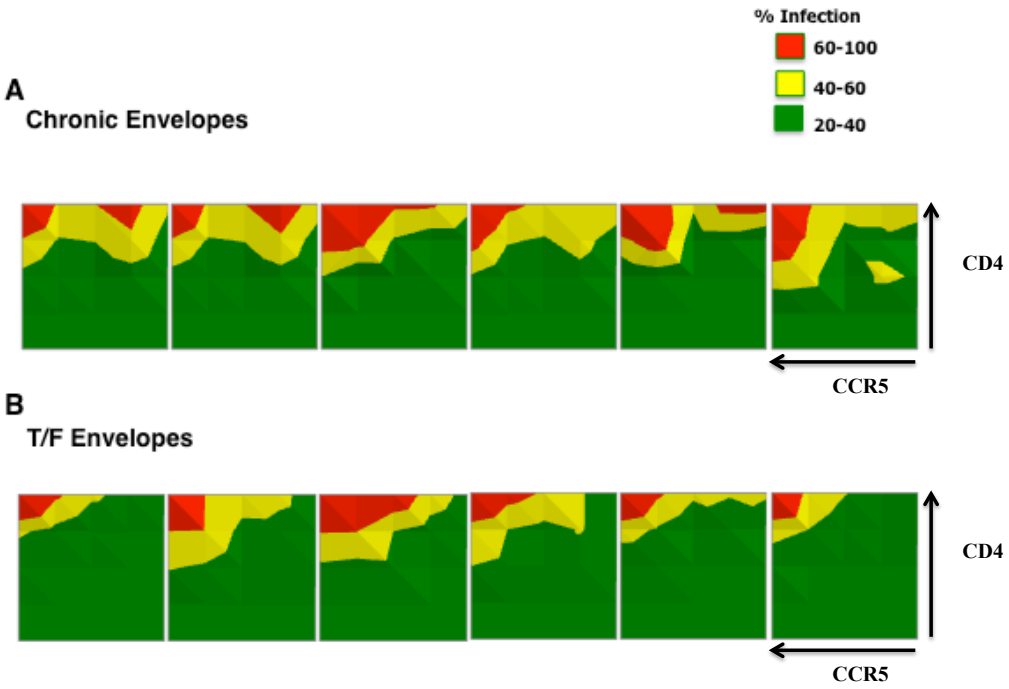

Figure D.3: Infectivity profiles of Subtype A-D Envelopes. The infectivity profile for indivudal Subtype A, Subtype B, Subtype C and Subtype D derived Envs (**A-D**, respectively) across a spectrum of CD4 and CCR5 expression levels were generated and plotted as described in the Materials and Methods. One representative experiment out of at least two is shown. The contour plots are arranged from highest to lowest mean infectivity (M), from left to right.

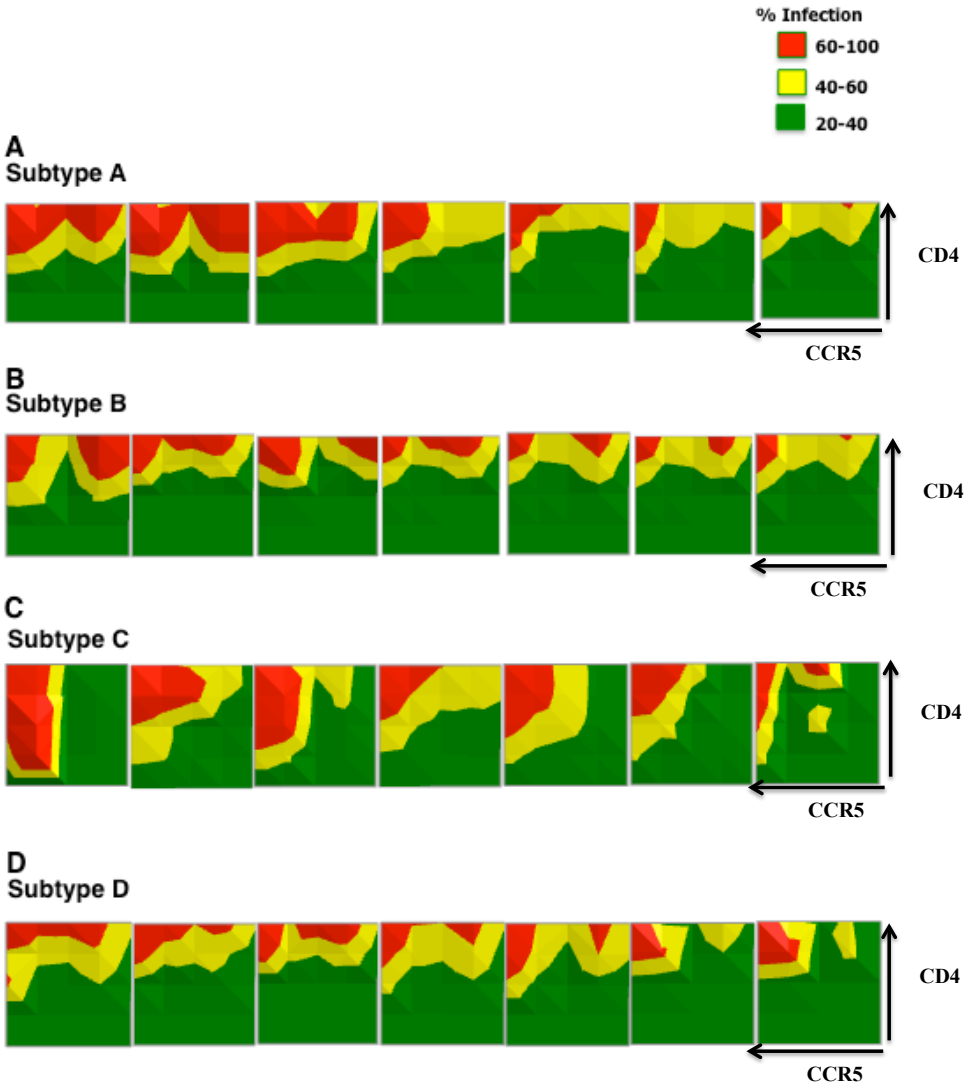

Figure D.4: Infectivity profiles of $(PG9/PG16)^R$ or $(VRC01)^R$ Envs. (**A**) Consensus and/or predicted ancestral Env sequences from subtypes A-D were obtained from the Los Alamos HIV sequence database (http://www.hiv.lanl.gov), and the amino acid sequences from the relevant regions aligned. Arrows highlight location of conserved residues where single point mutations were engineered to confer PG9/16 (N160K) or VRC01 (N279/280A) resistance. (**B-D**) 2-D contour plots of the infectivity profile for individual Envs are shown for the wild-type parental WT (**A**), and the corresponding N160K (**B**), and N279/280A (**C**) mutants. Subtype specific Envs (A1-3, B1-3, C1-3) refer to the Env clones listed in Additional file 4: Table S2. Axes and color-codes are identical to previous contour plots. Contour plots are ordered based on the M values of the parent Env (highest to lowest, from left to right).

Table D.1: List of T/F and chronic envelopes.

Env type	env clone	Gender	Age	Feinberg Stage	Viral Load (copies/ml)	Disease Status	Location	Risk factor	Accession Number	AIDS Repository Designation	b12 IC_{50} (ug/ml)	sCD4 IC_{50} (nM)	T415 (Yes/No)
T/F	p6244_13.B5.4576	M		II	274,000	NA	USA	SPD	EU289191	p6244_13.B5.4576	>50	254	N
	p63358.p3.4013	NR		II	260,000	NA	USA	SPD	EU289192	p63358.p3.4013	>50	538	N
	p700010040.C9.4520	F		II	741,499	NA	USA	IVDU	EU289193	p700010040.C9.4520	0.7	97	N
	p1054.TC4.1499	M		II	320,000	NA	USA	SPD	EU289185	p1054.TC4.1499	4.2	113	Y
	pPRB926_04.A9.4237	NR		II	756,000	NA	USA	SPD	EU289197	pPRB926_04.A9.4237	0.5	93	N
	pSC45.4B5.2631	M		II	6,318,529	NA	Trinidad	Heterosexual	EU289201	pSC45.4B5.2631	0.7	268	N

Env type	env clone	Gender	Age	Time since sero-conversion	CD4 Count (cells/mm^3)	Disease Status	Location	Risk factor	Accession Number	AIDS Repository Designation
Chronic	92TH014.12	M	38	25.6	ND	AS	Bangkok, Thailand	IVDU	U08801	pSVIII-92TH014.12
	92US711.14	M	44	17	853	AS	Baltimore, USA	IVDU	U08448	pBA301711.14
	92US712.4	F	35	15	537	AS	Baltimore, USA	IVDU	U08449	pBA301712.4
	92US714.1	M	28	12	546	AS	Baltimore, USA	IVDU	U08450	pBA301714.1
	92US715.6	M	36	20	470	AS	Baltimore, USA	IVDU	U08451	pBA301715.6
	92US716.6	M	39	4	787	AS	Baltimore, USA	IVDU	U08452	pBA301716.6

NA, non-applicable
AS, asymptomatic
NR, not recorded
**Risk behavior where known. Subjects listed as "SPD" were source plasma donors who denied having sex for money, homosexual activity, IVDU, or receiving a blood transfusion or a tattoo in the preceding year.

Table D.2: List of subtype envelopes.

Env type	Env clone	Approximate length of time of infection	Viral Load (copies/ml)	CD4 Count (cells/mm^3)	Location	Mode of Transmission	Accession Number	Reference	Group PI	b12 IC_{50} (ug/ml)	sCD4 IC_{50} (mg/ml)
A1	Q259env.w6	81 dpi	2,000,000	NA	Kenya	NA	AF407151	1	Overbaugh	>20	NA
A2	QB726.70M.ENV.B3	70 dpi	61,940	NA	Kenya	NA	FJ866111	1	Overbaugh	>20	NA
A3	QH359.21M.ENV.C1	21 dpi	32,120	NA	Kenya	NA	FJ866121	2	Overbaugh	>20	NA
A4	QH209.14M.ENV.A2	14 dpi	28,600	NA	Kenya	NA	FJ866118	2	Overbaugh	>20	NA
A5	QF495.23M.ENV.A3	23 dpi	217,050	NA	Kenya	NA	FJ866114	2	Overbaugh	>20	NA
A6	Q769env.h5	61 dpi	9,000,000	NA	Kenya	NA	AF407159	2	Overbaugh	>20	NA
A7	QH343.21M.ENV.A10	21 dpi	40,750,000	NA	Kenya	NA	FJ866119	2	Overbaugh	>20	NA
B1	SC 422661.8 (SVPB8)	4 wks	1,380,000	ND	Trinidad	F-M	A Y835441	3	Montefiori	4.7	0.2
B2	pCAAN5342 clone A2	NA	>1,000,000	278	USA	M-M	A Y835452	3	Montefiori	>50	16
B3	pREJO4541 clone 67	2 wks	722,349	848	USA	F-M	A Y835449	3	Montefiori	0.7	0.5
B4	pTRJO4551clone 58	1 wks	8122951	NA	USA	M-M	A Y835450	3	Montefiori	>50	20.2
B5	AC10.0, clone 29	4 wks	40,700	919	USA	M-M	A Y835446	3	Montefiori	1.8	8.5
B6	QH0692, clone 42	6 wks	9,611	NA	Trinidad	F-M	A Y835439	3	Montefiori	0.3	0.5
B7	pRHPA4259 clone 7	<8 wks	1,458,354	247	USA	M-F	A Y835447	3	Montefiori	0.1	1.8
C1	HIV-16055-2,	2 dpi	534,557	830	India	F-M	EF117268	4	Montefiori	>50	11.4
C2	HIV-16845-2,	20 dpi	199,655	579	India	M-F	EF117269	4	Montefiori	>50	1
C3	HIV-25710-2,	19 dpi	3523	350	India	F-M	EF117271	4	Montefiori	>50	2.6
C4	HIV-25711-2,	4 dpi	6,633,880	471	India	F-M	EF117272	4	Montefiori	25.9	29
C5	HIV-26191-2,	9 dpi	5,346,070	338	India	F-M	EF117274	4	Montefiori	4.9	17.1
C6	HIV-00836-2,	85 dpi	31,104	ND	India	M-F	EF117265	4	Montefiori	>50	>50
C7	HIV-001428-2, clone 42	11 dpi	217,812	454	India	M-F	EF117266	4	Montefiori	>50	5.2
D1	QA013.70I.ENV.H1	70 dpi	1,527,700	NA	Kenya	NA	FJ866134	2	Overbaugh	>20	NA
D2	QA013.70I.ENV.M12	70 dpi	1,527,700	NA	Kenya	NA	FJ866135	2	Overbaugh	>20	NA
D3	QA465.59M.ENV.D1	59 dpi	37,750	NA	Kenya	NA	FJ866137	2	Overbaugh	17.16	NA
D4	QD435.100M.ENV.B5	100 dpi	17,470	NA	Kenya	NA	FJ866140	2	Overbaugh	>20	NA
D5	QD435.100M.ENV.A4	100 dpi	17,470	NA	Kenya	NA	FJ866139	2	Overbaugh	>20	NA
D6	QD435.100M.ENV.E1	100 dpi	17,470	NA	Kenya	NA	FJ866141	2	Overbaugh	>20	NA
D7	QA465.59M.ENV.A1	59 dpi	37,750	NA	Kenya	NA	FJ866136	2	Overbaugh	9.09	NA

*may be defined differently in different studies; please specify
time since last seronegative test, times since acue retroviral conversion syndrome, combination of clinical parameters

NA, Not available

Reference		Group PI
EM Long et al, ARHR 2002	1	Julie Overbaugh
CA Blish et al, JV 2009	2	Julie Overbaugh
M Li et al, JV 2005	3	David Montefiori
SS Kulkarni et al, Virology 2009	4	David Montefiori

APPENDIX E

Supplementary Information and Mathematical Methods for Chapter 5

Supplementary Material

Table E.1: List of Envelopes.

Env (abbrev.)	Env	Clade	GenBank	Ref
BaL	BaL.26	B	DQ318211	1
24S	24S	B	KC834603	2
24R	24R	B	KC834602	2
17S	17S	B	KC834604	2
17R	17R	B	KC834605	2
MI18	BG505.W6M.ENV.C2	A	DQ208458	3
MI28	MG505.W0M.Env.A2	A	DQ208449	3
MI29	MG505.W0M.ENV.H3	A	DQ208455	3
MI24	BL035.W6M.ENV.C1	D/A	DQ208480	3
MI38	ML035.W0M.ENV.G2	D/A	DQ208474	3
MI39	ML035.W0M.ENV.I2	D/A	DQ208475	3
MI32	MJ412.W0M.ENV.B1	C	DQ208435	3
MI33	MJ412.W0M.ENV.C1	C	DQ208436	3
MI21	BJ613.W6M.ENV.E1	A	DQ208448	3
JRCSF C3	JRCSF S142N	B	S61104	4
JRCSF	JRCSF	B	U45960	5
4051C	4051C	B		6
4051P	4051P	B		6
PVO	PVO	B	AY835444	7
6535	6535	B	AY835438	7
TRJ	TRJ	B	AY835450	7

1. Li et al. J. Virol, 80(3):1414-26, Feb 2006.
2. Roche et al. Retrovirology, 10:43, 2013.
3. Wu et al. J. Virol, 80(2):835-44, Jan 2006.
4. Boyd et al. J. Virol, 67(6):3649-52, Jun 1993.
5. Klasse et al. AIDS Res. Hum. Retroviruses, Mar 1;12(4):347-50, 1996.
6. Joseph et al. J. Virol, 88(4):1858-69, Feb 2014.
7. Li et al. J. Virol, 79(16):10108-25, Aug 2006.

Table E.2: Summary of IT, PT and MT parameters.

ID	Env	Cells	min	max	T	T_P	T_M	m	IT R^2	PT R^2	MT R^2
15	6535	10,000	0.79%	4.53%	2,350	2,379	681	0.873	0.9651	0.9687	0.9831
5	17R	10,000	0.94%	16.74%	15,399	15,780	2,472	0.732	0.8950	0.9162	0.9906
8	17R	10,000	2.58%	17.34%	45,684	47,318	7,824	0.705	0.8660	0.8876	0.9816
4	17S	10,000	0.62%	14.24%	11,660	11,896	2,086	0.766	0.9211	0.9353	0.9930
7	17S	10,000	1.27%	14.54%	25,065	25,784	4,354	0.732	0.8849	0.9062	0.9732
6	24R	10,000	0.84%	6.16%	3,917	3,966	471	0.725	0.9097	0.9169	0.9967
11	24R	10,000	0.61%	11.44%	12,793	13,039	1,492	0.701	0.8643	0.8839	0.9564
10	24S	10,000	0.94%	14.34%	11,652	12,011	7,473	1.062	0.9965	0.9951	0.9964
14	4051C	10,000	1.19%	4.93%	2,972	3,012	368	0.722	0.9023	0.9095	0.9844
9	4051P	10,000	0.93%	11.64%	21,256	21,750	9,066	0.943	0.9903	0.9938	0.9995
48	BaL	140,000	0.58%	16.32%	53,644	56,277	105,611	1.707	0.5778	0.5210	0.9966
51	BaL	157,500	0.57%	8.15%	75,521	77,063	92,739	1.300	0.9251	0.9152	0.9962
64	BaL	77,500	0.85%	19.57%	916,012	941,787	222,347	0.804	0.9375	0.9533	0.9984
1	MI18	10,000	2.29%	13.59%	32,660	33,773	13,189	0.910	0.9778	0.9855	0.9992
66	MI18	100,000	5.76%	18.83%	491,800	520,601	117,587	0.725	0.8184	0.8438	0.8775
33	MI21	80,000	0.54%	6.49%	608,480	617,324	287,939	0.982	0.9767	0.9772	0.9768
34	MI24	80,000	1.06%	13.40%	3,616,000	3,743,823	3,847,215	1.288	0.9461	0.9317	0.9992
30	JR-CSF	70,000	0.73%	11.16%	34,115	34,887	17,254	0.992	0.9860	0.9876	0.9882
31	JR-CSF	70,000	0.51%	14.36%	52,397	53,861	27,985	1.005	0.9847	0.9877	0.9894
32	JR-CSF	70,000	0.67%	11.06%	69,261	70,946	42,886	1.053	0.9844	0.9844	0.9882
52	JR-CSF	157,500	0.70%	15.81%	79,333	82,044	71,963	1.192	0.9718	0.9632	0.9913
19	JR-CSF C3	80,000	2.08%	19.80%	1,434,667	1,490,125	327,931	0.762	0.9052	0.9310	0.9991
21	JR-CSF C3	60,000	1.29%	12.86%	91,342	94,170	30,935	0.875	0.9460	0.9572	0.9707
2	MI28	10,000	1.99%	12.59%	28,034	28,892	12,462	0.944	0.9846	0.9884	0.9937
69	MI28	100,000	3.42%	17.73%	380,360	398,597	131,751	0.841	0.9336	0.9520	0.9841
3	MI29	10,000	4.65%	14.66%	69,207	72,524	29,835	0.908	0.9696	0.9823	0.9997
70	MI29	100,000	4.67%	13.33%	528,235	552,145	172,655	0.826	0.9328	0.9503	0.9894
71	MI32	100,000	0.70%	2.57%	10,925	11,010	4,355	0.947	0.9941	0.9951	0.9986
72	MI33	100,000	0.77%	3.43%	13,896	14,044	10,192	1.100	0.9674	0.9657	0.9789
35	MI38	80,000	0.90%	11.20%	1,204,608	1,235,406	495,709	0.935	0.9548	0.9591	0.9608
73	MI38	100,000	1.15%	14.63%	60,917	62,676	29,357	0.972	0.9897	0.9913	0.9923
74	MI39	100,000	5.24%	19.83%	238,620	251,564	52,548	0.706	0.8575	0.8882	0.9951
12	PVO	10,000	5.65%	14.94%	119,497	125,502	33,905	0.776	0.9101	0.9321	0.9999
20	SVPB8	192,500	0.63%	17.31%	1,903,953	1,954,510	513,139	0.835	0.9512	0.9648	0.9962
22	SVPB8	60,000	0.91%	10.96%	69,614	71,430	29,032	0.938	0.9670	0.9727	0.9768
23	SVPB8	130,000	1.07%	15.27%	180,966	187,554	101,558	1.015	0.9910	0.9939	0.9953
13	TRJ	10,000	1.60%	16.74%	37,774	39,208	15,164	0.905	0.9664	0.9781	0.9917

Expected Differences in Estimated Titers of the IT and MT Models

The infectious titer equation (Equation E.1) was equated with the median effect titer equation (Equation E.2) by substituting f_a from Equation E.1 into Equation E.2 to give Equation E.3, where we let $m = 1$ so that both equations are representing non-cooperativity.

$$f_a = \frac{TV}{C} \tag{E.1}$$

$$\frac{f_a}{1 - f_a} = \left(\frac{2VT_m}{C}\right)^m \tag{E.2}$$

$$\frac{\frac{TV}{C}}{1 - \frac{TV}{C}} = \frac{2VT_m}{C} \tag{E.3}$$

Equation E.3 was solved for T_m in terms of T and simplified as follows:

$$\frac{\frac{TV}{C}}{1 - \frac{TV}{C}} = \frac{2VT_m}{C} \tag{E.4a}$$

$$\frac{1}{\frac{C}{TV} - 1} = \frac{2VT_m}{C} \tag{E.4b}$$

$$\frac{1}{\frac{1}{TV} - \frac{1}{C}} = 2VT_m \tag{E.4c}$$

$$\frac{1}{\frac{1}{T} - \frac{V}{C}} = 2T_m \tag{E.4d}$$

$$\frac{1}{2}\left(\frac{1}{\frac{1}{T} - \frac{V}{C}}\right) = T_m \tag{E.4e}$$

$$\frac{1}{2}\left(\frac{T}{1 - \frac{TV}{C}}\right) = T_m \tag{E.4f}$$

The term $\frac{TV}{C}$ was substituted with f_a in accordance with Equation E.1 to give Equation E.5.

$$T_m = \frac{1}{2}\left(\frac{T}{1-f_a}\right) \tag{E.5}$$

The IT model is not valid when there exists any probability that a single infected cell was infected by more than one virion, thus, the relationship between T and T_m necessarily depends on how much infection was observed (f_a) to accommodate this deficiency. Because this probability is reduced as f_a decreases, we took the limit of Equation E.5 as f_a approaches zero (Equation E.6) to give Equation E.7.

$$\lim_{f_a \to 0}\left[\frac{1}{2}\left(\frac{T}{1-f_a}\right)\right] = \frac{1}{2}T \tag{E.6}$$

$$\frac{1}{2}T = T_m \tag{E.7}$$

Thus, when both models are used to describe a non-cooperative system ($m = 1$) and when the statistical probability of a single cell being infected by multiple virion is eliminated ($\lim_{f_a \to 0}$), the MT model titer (T_m) is expected to be one half the value of an IT model titer (T).

Defining Non-cooperative Slope Boundaries

The infectious titer equations (Equations 5.1a and 5.1b) describe a strict linear proportionality between viral input volume and infection, while the median effect equation (5.7b) is fundamentally non-linear. Our results suggest that viral infection in a non-linear process that is more accurately represented when incorporating the non-linear slope parameter (m) of the MT model and that accordingly, the quality of representation for the IT and PT models is dependent on the degree of cooperativity observed, when $m \neq 1$. To mathematically define the range of m for which the IT and PT models might accurately approximate a non-linear MT-model titration curve, and the range of m that might also be considered non-cooperative, we identified a single point of agreement between the IT and MT models.

While the MT model is non-linear, it does contain a single point of linearity where $\delta f_a/\delta D$ is constant and $\delta^2 f_a/\delta D^2 = 0$. We reasoned that f_a near this point would, accordingly, be *nearly linear*, such that a range of f_a about the linear point could be accurately approximated by the linear IT model. We further reasoned that if this point of linearity fell within the range of f_a used to fit the IT and MT models ($0.5\% \leq f_a \leq 20\%$), then the titration curve itself could be considered *nearly linear* and would be accurately approximated by the IT model.

The following derivation defines the single point of linearity in the MT model in terms of infection, f_a^*, and is a function of slope (m). When f_a^* falls within the range of infection that is observed in an experimental titration curve, then the curve itself may be approximated by a linear model (as points around f_a^* are also nearly linear). When f_a^* falls far outside the observed range of infection, the titration curve is predominantly non-linear and, therefore, cannot be approximated by a linear model. As a function of slope, f_a^* identifies the range of m that can be considered non-cooperative because these slopes correspond to such weak cooperativities that they can be accurately approximated by the linear, non-cooperative IT model.

The median effect equation (Equation E.8) can be solved in terms of f_a to give Equation E.9.

$$\left(\frac{f_a}{1-f_a}\right) = \left(\frac{D}{D_m}\right)^m \tag{E.8}$$

$$f_a = \frac{1}{\left(\frac{D}{D_m}\right)^{-m} + 1} \tag{E.9}$$

The first derivative is then given by Equation E.10.

$$\frac{\delta f_a}{\delta D} = \frac{\frac{m}{D}\left(\frac{D}{D_m}\right)^{-m}}{\left[\left(\frac{D}{D_m}\right)^{-m}+1\right]^2} \tag{E.10}$$

Differentiation by parts can be done by letting

$$A = \frac{m}{D}\left(\frac{D}{D_m}\right)^{-m} \qquad\qquad B = \frac{1}{\left[\left(\frac{D}{D_m}\right)^{-m}+1\right]^2}$$

Differentiation of each part A and B with respect to dose (D) gives

$$\frac{\delta A}{\delta D} = \frac{-m(m+1)\left(\frac{D}{D_m}\right)^{-m}}{D^2} \qquad\qquad \frac{\delta B}{\delta D} = \frac{2m\left(\frac{D}{D_m}\right)^{-m}}{D\left[\left(\frac{D}{D_m}\right)^{-m}+1\right]^3}$$

which is simplified by letting $R = (D/D_m)^{-m}$ to give

$$\frac{\delta A}{\delta D} = \frac{-m(m+1)R}{D^2} \qquad\qquad \frac{\delta B}{\delta D} = \frac{2mR}{D(R+1)^3}$$

The second derivative is then given by

$$\frac{\delta^2 f_a}{\delta D^2} = A\frac{\delta B}{\delta D} + B\frac{\delta A}{\delta D}$$

to obtain Equation E.11.

$$\frac{\delta^2 f_a}{\delta D^2} = \frac{m^2}{D^2}\left[\frac{R}{(R+2)^2}\right]\left[\frac{2R}{R+1} - 1 - \frac{1}{m}\right] \qquad R = \left(\frac{D}{D_m}\right)^{-m} \tag{E.11}$$

Effect (f_a) is inherently non-linear with respect to dose (D) in the median effect and Hill equations, however, both equations do contain an instantaneous point of linearity where $\delta f_a/\delta D$ is constant and $\delta^2 f_a/\delta D^2$ is zero. This point can be solved where the second deriva-

tive (Equation E.11) is equal to zero, as shown in Equation E.12.

$$0 = \frac{m^2}{D^2}\left[\frac{R}{(R+2)^2}\right]\left[\frac{2R}{R+1} - 1 - \frac{1}{m}\right] \qquad R = \left(\frac{D}{D_m}\right)^{-m} \tag{E.12}$$

This gives trivial solutions where $D \to \infty$ for the first two terms

$$0 = \frac{m^2}{D^2} \qquad 0 = \frac{R}{(R+1)^2}$$

and a non-trivial solution for the third term where

$$0 = \frac{2R}{R+1} - 1 - \frac{1}{m}$$

which can be rearranged to give

$$\frac{1}{2}\left(1 + \frac{1}{m}\right) = \frac{R}{R + \frac{1}{R}}$$

which is simplified by letting $R_o = 1/R$ to give

$$\frac{1}{2}\left(1 + \frac{1}{m}\right) = \frac{1}{1 + R_o}$$

which is solved for R_o to give

$$R_o = \frac{1 - \frac{1}{m}}{1 + \frac{1}{m}}$$

where the median effect equation (Equation E.8) can be substituted using

$$R_o = \frac{1}{R} = \left(\frac{D}{D_m}\right)^m = \frac{f_a}{1 - f_a}$$

to give

$$\frac{f_a}{1-f_a} = \frac{1-\frac{1}{m}}{1+\frac{1}{m}}$$

which is further simplified to give

$$f_a^* = \frac{1}{2}\left(1-\frac{1}{m}\right) \tag{E.13}$$

where f_a^* denotes the level of infection where the median effect model is instantaneously linear ($\delta^2 f_a/\delta D^2 = 0$).

The range of experimentally observed infection used to fit the IT, PT and MT models in our data was $1.7 \pm 1.6\%$ to $13 \pm 4.6\%$ infection, where f_a^* falls within this range only for $1.04 < m < 1.35$ (Equation E.13). Experimental titrations having MT slopes within this range gave similar R^2 for both the IT and MT models while titrations having slopes outside this range gave significantly different IT and MT R^2 values ($p = 0.0002$), demonstrating that titration curves whose slopes are within $1.04 < m < 1.35$ can be approximated by the linear IT model as non-cooperative when f_a is restricted to $1.7\% < f_a < 13\%$ infection (the average range of infection observed in our data after filtering the data to exclude $f_a < 0.5\%$ and $f_a > 20\%$). Equation E.13 also suggests that weak degrees of negative cooperativity are not as well approximated by the linear IT model than stronger degrees of positive cooperativity, which is relevant to the that fact the majority of these titrations exhibited $m < 1$.